# Modeling one-dimensional optical turbulence

Clément Colléaux


# MODÉLISATION DE TURBULENCE OPTIQUE UNIDIMENSIONNELLE

**Clément COLLÉAUX**

Institut de Physique de Nice (INPHYNI), CNRS, UMR 7010

**Présentée en vue de l'obtention du grade de :** docteur en physique d'Université Côte d'Azur

**Dirigée par :** Sergey Nazarenko

**Soutenue le :** 23 Octobre 2024

**Devant le jury, composé de :**

*Bérengère Dubrulle*, Directrice de recherche CNRS, Institut IRAMIS, CEA

*Alessandra Lanotte*, Directrice de Recherche, CNR Nanotech

*Sergey Nazarenko*, Directeur de Recherche CNRS, INPHYNI, Université Côte d'Azur

*Miguel Onorato*, Professeur, Université de Turin

*Antonio Picozzi*, Directeur de Recherche CNRS, Laboratoire Interdisciplinaire Carnot de Bourgogne

*Pierre Suret*, Professeur des Universités, PhLAM

# MODÉLISATION DE TURBULENCE OPTIQUE UNIDIMENSIONNELLE

**JURY**

**Rapporteurs**

*Miguel Onorato*
Professeur
Université de Turin, Turin

*Antonio Picozzi*
Directeur de Recherche CNRS
Laboratoire Interdisciplinaire Carnot de Bourgogne, Dijon

**Examinateurs**

*Bérengère Dubrulle*
Directrice de recherche CNRS
Institut IRAMIS, CEA, Gif sur Yvette

*Alessandra Lanotte*
Directrice de Recherche
CNR Nanotech, Lecce

*Pierre Suret*
Professeur des Universités
PhLAM, Lille

**Directeur de thèse**

*Sergey Nazarenko*,
Research Director CNRS,
Institut de Physique de Nice (INPHYNI), Université Côte d'Azur, Nice

*L'impossible recule toujours quand on marche vers lui.*

---

Antoine de Saint-Exupéry

# Abstract

## Résumé en Français

MODÉLISATION DE TURBULENCE OPTIQUE UNIDIMENSIONNELLE

L'étude de l'optique non-linéaire est d'importance pratique car cela désigne des systèmes tels que les fibres optiques et des cristaux liquides mais aussi d'importance théorique car la lumière non-linéaire possède des propriétés très similaires à l'hydrodynamique. Les systèmes optiques non-linéaires sont modélisés par une équation non-intégrable qui contient une physique riche. Dans cette thèse, nous explorons deux aspects de cette équation. Nous analysons d'abord la propagation de structures localisées dans ce système et nous concluons que ce dernier tend vers un état final qui agit comme un attracteur. Nous l'identifions à un état lié, une structure localisée qui oscille en amplitude et en largeur et qui se propage au milieu d'ondes faiblement non-linéaires. Cet état-lié est caractérisé avec différents outils dont le spectre non-linéaire. Ce spectre non-linéaire a été élaboré pour le système intégrable correspondant à notre système non-intégrable, et apparaît comme un outil pertinent pour caracteriser notre système.

Nous étudions aussi les cascades turbulentes de ce système non-intégrable avec l'aide d'un modèle réduit. Ce modèle permet une étude théorique en simplifiant les interactions entre modes qui sont responsables des cascades turbulentes. Avec ce modèle, nous pouvons déterminer les spectres de Kolmogorov-Zakharov des invariants qui cascadent. Pour l'un de ces invariants, l'action d'onde, la prédiction de Kolmogorov-Zakarhov s'avère être non réalisable à cause de flux divergents. Un modèle non-local permet d'obtenir un nouveau spectre. Ces prédictions théoriques sont confrontées à des simulations numériques. Les spectres obtenus numériquement confirment globalement ces prédictions théoriques. Lors de ces simulations, nous avons observé des solitons incohérents, qui sont des structures pouvant se propager dans des systèmes optiques non-intégrables avec la particularité d'avoir une enveloppe globale constante malgré des changements à échelle plus petite. Ces structures ont été observées en coexistence avec des cascades turbulentes.

*Mots clefs*: 1D-NLSE, optique non-linéaire, turbulence, solitons

# Abstract in English

MODELING ONE-DIMENSIONAL OPTICAL TURBULENCE

Studying non-linear optics systems is of practical importance because it applies to systems such as optical fibers and liquid crystals but also of theoretical importance because non-linear light exhibit properties very similar to hydrodynamics. Non-linear optics are modeled by an non-integrable equation which contains a rich physics. In this thesis, we explore two aspects of this equation. We first analyse the propagation of localized structures in this system and we conclude that the system tends to a final state which acts as a statistical attractor. We identify this attractor as a bound-state, a localized structure which oscillates in amplitude and in width and which propagates among weakly non-linear waves.

We also study the turbulent cascades of this system with the help of an reduced model of the wave kinetics. This reduced model allows us to derive the Kolmogorov-Zakharov spectra of cascading quantities. The Kolmogorov-Zakharov spectrum for the wave-action is found to be non-local and replaced by a no-local prediction. These theoretical predictions are then compared to numerical simulations and show an overall good accordance with numerics, particularly for the non-local spectrum of wave-action. Such numerical simulations show the existence of Incoherent Solitons, which are localized structures propagating with an envelope approximately constant but with propagation of smaller structures inside it. Incoherent Solitons have been found in coexistence with cascade, but for different directions in the Fourier space.

*Key words*: 1D-NLSE, non-linear optics, turbulence, solitons

# Acknowledgments

Avec ce manuscrit se terminent trois ans de thèse, trois ans bien remplis pour lequels je me dois de remercier certaines personnes sans qui ce travail n'aurait pas été possible.

En tout premier lieu, je voudrais remercier chaleureusement Sergey pour m'avoir fait découvrir la turbulence d'onde et m'avoir accompagné, scientifiquement et humainement, pendant ces trois ans. Nos discussions m'ont permis de me familiariser avec le domaine et d'être capable d'apporter une modeste contribution. Merci aussi evidemment à Jason et Jon pour notre collaboration, leurs idées, leurs remarques et leurs conseils. Pensée particulière pour Jon qui a eu le courage de relire ma thèse. Un grand merci ! Je remercie aussi Giorgio pour avoir accepté de faire partie de mon comité de suivi de thèse. Enfin, merci à Ying pour ses conseils en code qui m'ont permis de bien commencer ma thèse.

Un grand merci aux chercheuses et chercheurs qui ont accepté de consacrer du temps à l'évaluation de ce manuscrit, mes rapporteurs Miguel Onorato et Antonio Picozzi, et à l'évaluation de la soutenance, les membres du jury : Bérengère Dubrulle, Alessandra Lanotte et Pierre Suret. La défense de ma thèse n'est rendue possible que grâce à vous.

Il m'est très important de remercier le laboratoire InPhyNi qui m'a accueilli en thèse il y a déjà trois ans. Je remercie bien évidemment l'ensemble de la direction, dont le directeur Guillaume Huyet, mais j'aimerais avoir une pensée particulière pour les gestionnaires, sans qui le travail au labo serait bien plus pénible. Merci Magali ! Enfin, un très grand merci à Jérôme et Bernard pour l'aide inestimable que vous m'avez apportée avec mon ordinateur. Il a mis du temps à arriver mais il a bien servi.

Pour les remerciements plus personnels, il me semble évident de te remercier en premier lieu Sophie. Ton soutien et ton accompagnement m'auront été indispensables pendant ces trois années. Je résume tout ceci en seul mot mais il veut dire beaucoup : Merci !

Il va sans dire que vous avez aussi votre paragraphe Benji et Fred. Pour nos années en colocs et pour tout ce qu'on a partagé ensemble, vous comptez beaucoup pour moi. Merci à vous, mes collègues thésards !

Merci aussi à toi, de la Salle, pour les projets lancés ensemble et ton support.

Je me veux aussi remercier toutes les personnes qui ont fait de mes années à Lyon de superbes années, pour des raisons diverses mais toutes essentielles. Un grand merci donc à Manon, Nacim, Lily, Lisa, Valéri. Je ne peux pas citer tout le monde mais vous saurez vous reconnaître dans ces remerciements.

Merci à celles et ceux qui m'accompagnent actuellement, en particulier Alice, Alban, Kiran et Rowan. Merci à vous pour tout.

Impossible de savoir comment cette thèse se serait passé si je n'avais pas été invité dans le bureau 2-5b. J'ai beaucoup aimé travailler dans ce bureau avec des docteurs et doctorants incroyables. Un grand merci à l'équipe PIQ pour la bonne ambiance qu'elle a mise dans ce bureau : Mathis, Romain, Tess, Yoann, Adrien et Antoine. Il me faut bien évidemment remercier mon co-bureau, celui que j'ai eu devant moi pendant tout ce temps, l'irremplaçable Léo. Merci pour ta bonne humeur et tes goûts musicaux.

Je finis par remercier ma famille qui m'a soutenu et encouragé depuis le début de mes études qui vont enfin se terminer. Merci à mes parents de croire en moi et à mes frère et soeur pour leur aide pendant cette thèse. Ces remerciements précis ne doivent pas faire oublier les autres membres de ma famille qui ont tous eu un grand role dans ma vie pendant ces trois années. Enfin, je veux aussi avoir une pensée pour les membres de ma famille partis récemment et qui ont été de très grande importance dans ma vie de manière générale. Je leur dédie cette thèse.

Bonne lecture à quiconque souhaiterait lire cette thèse, j'espère que vous trouverez ce que vous cherchez !

# Abbreviations

- 1D-, 2D-, 3D- : one dimensional, two dimensional, three dimensional
- (1D-)NLSE : (one dimensional) Non-Linear Schrödinger Equation
- (1D-)SHE : (one dimensional) Schrödinger-Helmholtz Equation
- CT : Canonical Transform
- DAM : Differential Approximation Model
- DC : Direct Cascade
- DST : Direct Scattering Transform
- IS : Incoherent Soliton
- IST : Inverse Scattering Transform
- KE : Kinetic Equation
- KZ : Kolmogorov-Zakharov
- PDE : Partial Differential Equation
- PSD : Power Spectral Density
- (q)ST : (quasi-)Soliton Turbulence
- RJ : Rayleigh-Jeans
- SLAM : Semi-Local Approximation Model
- SWL : Short-Wave Limit
- WT : Wave Turbulence
- ZT : Zakharov Transform

# Contents

# List of Figures

# General Introduction

*Using a term like nonlinear science is like referring to the bulk of zoology as the study of non-el ephant animals.*

**Stanisław Ulam**,
Co-author of one of the very first numerical simulations

It is well known that the number of physical systems that can be perfectly described by linear physics is quite small. Assuming that the response of a system is proportional to its perturbation may allow simple computations, but very often lets aside important characteristics of a real system. Non-linear equations are almost always required to represent concrete systems, such as the oscillation of a pendulum, hydrodynamics or non-linear optics. In this thesis, we will focus on the last example, realized, for instance, in optical fibers or liquid crystals.

Even among the non-linear equations, some of them are easier to grasp, as they conserve an infinity of quantities during time evolution. These are said integrable and have the property to have particular solutions propagating with constant speed and profile, the solitons. In contrast to the linear and non-linear equations, the non-integrable non-linear equations are more difficult to deal with but reflect richer and more realistic physics.

Optical solitons have been considered as a way to propagate information through optical fibers. Indeed, as they keep their shape during the propagation, they can represent bits and we could use trains of solitons to send binary messages. However, the integrable equation for which we can define solitons is only a model to describe real systems. Concrete systems are found to be more complex, with higher-order terms or dissipation which can make the integrable case a poor model. In these real and non-integrable systems, the solitons undergo changes of amplitudes and profile which can cause loss of information. It is thus crucial to understand how solitons propagate and collide in non-integrable systems.

Another aspect of non-integrable systems is cascade, allowed with the interaction of waves whose mixing can propagate quantities, such as energy, through scales. Such cascades can occur when the system is weakly non-linear. Their study improves our understanding of non-linear optics system but also of hydrodynamics, as fluid flows and non-linear light share common properties.

Wave turbulence can be defined as the statistically study of ensembles of interacting non-linear random waves. This framework allows the study of non-equilibrium systems. We can define two different regimes, strong wave turbulence, with the solitons and localized structures, and weak wave turbulence, which studies the cascades of invariants through scales, due to the interaction of weakly non-linear waves. Real physical system appear to be characterized by both regimes of wave turbulence. for similar time and length scales. These two aspects are entangled and can not be considered separately. It is thus necessary to describe properly both phenomena to have a realistic model of concrete experiments with non-integrable equations. More practically, a better understanding of the interactions between coherent structures and waves is necessary to limit the creation of waves, and thus, the loss of information during the sharing of information via solitons. Consequently, the complete study of non-integrable equations is of interest for both fundamental and applied physics.

During this thesis, we will analyse the properties of a non-integrable equation which models non-linear optics : the one-dimensional Schrödinger-Helmholtz equation. This equation models systems such as optical fiber and liquid crystals, taking into account non-local effects. In chapter 1 we will present this equation and its properties. We will also introduce the corresponding integrable equation and discuss the solutions of these two equations.

Then, we will present a complete study of the propagation of different coherent structures into this non-integrable equation, with the comparison of numerical simulations. The latter will suggest the existence of a universal attractor. This attractor has been observed in the literature for other non-integrable systems, and we will confirm its existence with different types of initial conditions. With the help of different diagnostics, it will be characterized as a pulsating localized structure, oscillating in amplitude and width. These results are reported in chapter 2.

Finally, in the chapter 3 we will detail the approximation model that we have used to study theoretically the cascades in the one-dimensional Schrödinger-Helmholtz equation, and to derive the associated spectra. These predictions will then be confronted with numerical simulations. These simulations will be carefully analysed and will give important information about the cascades in this non-integrable system.

# CHAPTER 1

# Theoretical introduction

## 1.1 Equations studied

### 1.1.1 1D Non-Linear Schrödinger Equation (NLSE)

**State of the art**

We first introduce the one dimensional non-linear Schrödinger equation (1D-NLSE) for a function $u(x,t)$, defined in $\mathbb{R} \times [0, +\infty[ \to \mathbb{C}$,

$$i\frac{\partial}{\partial t}u + \frac{1}{2}\frac{\partial^2}{\partial x^2}u + u|u|^2 = 0. \tag{1.1}$$

This equation is a particular case of the 1D Schrödinger equation

$$i\frac{\partial}{\partial t}u + \frac{1}{2}\frac{\partial^2}{\partial x^2}u + V[u,x,t]u = 0, \tag{1.2}$$

where $V \in \mathbb{R}$ is referred to as the potential. If $V$ is a function of $u$, the equation is said *non-linear* because of the term $Vu$ which is not only proportional to $u$. Such equations are called NLS-type equations and are defined by their potential $V$.

The NLSE (not only the one-dimensional version) is widely used in different physics fields to model non-linear systems such as the propagation of light in optical fibers with the recent development of optical solitons for communication [1], [2]. The 1D-NLSE also describes the Bose-Einstein Condensation of dilute gases [3] [4], non-linear optics [5] [6] and gravity waves in deep water [7]. In the next pages, more examples of applications of NLSE-derived equations will be provided. The 1D-NLSE appears in so many physical contexts because it is a universal equation that can be derived under very general conditions. This importance of the 1D-NLSE can be explained by the following observation. It is the leading order equation for the complex envelope of a quasi-monochromatic wave-train propagating inside a dispersive, non-linear medium in the paraxial approximation [8]. Due to the universal aspect of the NLSE, understanding its properties and its solutions

helps us understanding non-linear physics generally, and shed light on the phenomenology exhibited by a wide variety of non-linear systems. This variety of systems corresponds to a variety of potentials $V$.

### The Direct and Inverse Scattering Transform

The 1D-NLSE (1.1) has been found to be integrable by Zakharov and Shabat in 1970 [9], using the Direct and Inverse Scattering Transforms (DST and IST). By integrability, we refer to the property of an equation of having an infinite number of quantities conserved through time. The DST and IST are mathematical tools developed by Gardner et al. in 1967 [10] to solve another non-linear equation, the Korteweg-de Vries (KdV) equation

$$\frac{\partial}{\partial t}u + \frac{\partial^3}{\partial x^3} + 6u\frac{\partial}{\partial x}u = 0. \tag{1.3}$$

The method DST/IST is often referred to as the non-linear Fourier Transform (FT) [11] because both methods are very similar. To solve a Partial Differential Equation (PDE), linear (*e.g.* diffusion equation) or non-linear, one can compute the spatial Fourier Transform of the function at a given time $t_i$, make it evolve in time by taking the FT of the equation until a further time $t_f$ and take the inverse FT to get back to the real space. Similarly, the DST computes a non-linear spectrum for the function $u$ at a given time $t_i$, this spectrum is evolved in time up to $t_f$ and then, the IST transforms this spectrum back into the function in the real space. This analogy is illustrated in FIGURE 1.1.

In both cases, the temporal evolution of the spectrum has a weaker computational cost than the numerical resolution of the differential equation. For a linear PDE, the FT spectrum evolution is trivial, and for non-linear PDE, the evolution is straightforward if one takes a particular caution (see the numerics section 2.3). With the DST/IST, the evolution of the spectrum is always trivial, even for non-linear PDEs. Finally, these methods can compute $u(x, t_f)$ directly from $u(x, t_i)$ without the necessity of calculating the function for the intermediate times.

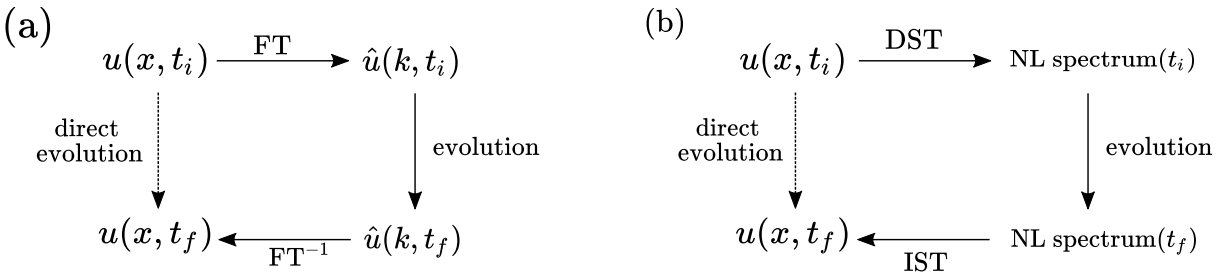


Figure 1.1: **Analogy between the FT** (a) **and the DST/IST** (b) **methods to solve differential equations** - DST/IST methods are often referred to as the non-linear FT due to the parallel between the two solving methods.

More precisely, the main idea of the DST/IST is to write the studied equation as the compatibility condition $\partial_x\partial_t\phi = \partial_t\partial_x\phi$ for a $2 \times 1$ vector $\phi$. This vector $\phi$ solves the Zakharov-Shabat (ZS) system (1.4) specific to the 1D-NLSE [12] [13].

$$\partial_x \phi = \begin{pmatrix} -i\zeta & u \\ -u^* & i\zeta \end{pmatrix} \phi \tag{1.4a}$$

$$\partial_t \phi = \begin{pmatrix} -i\zeta^2 + \frac{i}{2}|u|^2 & \zeta u + \frac{i}{2}\partial_x u \\ -\zeta u^* + \frac{i}{2}\partial_x u^* & i\zeta^2 - \frac{i}{2}|u|^2 \end{pmatrix} \phi. \tag{1.4b}$$

In the general theory of the DST/IST, the matrix operators in the ZS system (1.4) depend on the studied non-linear PDE. We denote as $u$ a function solution of the 1D-NLSE and which appears here as a potential. The function $u$ is taken at a given $t_i$ but as a function of $x$. We also introduce the complex parameter $\zeta \in \mathbb{C}$ [12]. This situation is similar to quantum physics when a wave function (here $\phi$) encounters a potential (here $u$).

The complex parameter $\xi$ can be computed by formulating the first equation (1.4a) as an eigenvalue problem [13] [12],

$$\mathcal{L}\phi = i\left[\begin{pmatrix} \partial_x & 0 \\ 0 & -\partial_x \end{pmatrix} - \begin{pmatrix} 0 & u \\ u^* & 0 \end{pmatrix}\right]\phi = \zeta\phi. \tag{1.5}$$

This operator $\mathcal{L}$ is called the Lax operator of the 1D-NLSE [13], and we can find an anti-symmetric operator $\mathcal{B}$ such that

$$\frac{\mathrm{d}}{\mathrm{d}t}\mathcal{L} = \big[\mathcal{B}, \mathcal{L}\big]. \tag{1.6}$$

This operator is found to be

$$\mathcal{B} = \begin{pmatrix} i\partial_x^2 + \frac{i}{2}|u|^2 & -iu\partial_x - \frac{i}{2}\partial_x u \\ -iu^*\partial_x - \frac{i}{2}\partial_x u^* & -i\partial_x^2 - \frac{i}{2}|u|^2 \end{pmatrix}. \tag{1.7}$$

The operators $\mathcal{L}$ and $\mathcal{B}$ define the Lax pair of the 1D-NLSE. In the Lax theory [14], the existence of this Lax pair proves the integrability of the 1D-NLSE. More generally, a non-linear equation is integrable if and only if it has a Lax pair, which defines the conserved quantities. In the literature [15], the Lax pair of the 1D-NLSE sometimes refers to the matrix operators of the ZS system (1.4) but the latter are just another writing of the operators $\mathcal{L}$ and $\mathcal{B}$. Besides, this is only a terminology point and the core of the DST/IST method, detailed in the coming pages, does not depend on this choice.

With equation (1.5), we can compute the complex parameter $\zeta$ as the eigenvalues of the matrix $\mathcal{L}$. This matrix is fully known as the function $u$ is the analyzed function. More precisely, $\mathcal{L}$ depends on $t$ as its dependence on $u(x,t)$. If the space is discretized into $N_\mathrm{c}$ points, then the matrix $\mathcal{L}$ is $2N_\mathrm{c} \times 2N_\mathrm{c}$ and thus has $2N_\mathrm{c}$ complex eigenvalues. We denote them $\{\zeta_p\}_{p\in[\![1,2N_\mathrm{c}]\!]}$. These eigenvalues have an important physical meaning which will be made explicit in the coming pages.

Each eigenvalue $\zeta_p$ defines an eigenvector $\phi_p$ via $\mathcal{L}\phi_p = \zeta_p\phi_p$. As they are not of a main interest in our work, the determination of these eigenvectors will not be detailed here but can be found in [9] [16]. The study of these eigenvectors defines a constant $C_p$,

the norming constant, for each eigenvalue, as well as a continuous function $r(\xi), \xi \in \mathbb{R}$, the reflection coefficient.

Combined with the eigenvalues $\zeta_p$, the norming constant $C_p$ and the continuous function $r(\xi)$ define the non-linear spectrum of the function, also called scattering data :

$$\text{non-linear spectrum} = \begin{cases} \zeta_p, C_p \text{ for } p \in [\![1, 2N_c]\!] & \rightarrow \text{discrete spectrum} \\ \\ r(\xi), \xi \in \mathbb{R} & \rightarrow \text{continuous spectrum.} \end{cases} \tag{1.8}$$

As in the case of the Fourier spectrum, the non-linear spectrum embeds all the information of the function. The discrete spectrum represents the localized structures of the system, the solitons, introduced in the next subsection, while the continuous spectrum gives access to the waves. The discrete spectrum will be more detailed section 2.2. This non-linear spectrum is the outcome of the DST step. We would like to highlight that the DST computes the non-linear spectrum for $u(x, t_i)$ at a fixed time $t_i$ and thus, the non-linear spectrum only gives information on the components of $u$ at this given time, without any link with the previous times.

Once the non-linear spectrum has been computed for a time $t_i$, the core of the DST/IST method relies on the trivial time evolution for $\zeta_p, C_p$ and $r(\xi)$. Indeed, the eigenvalues $\zeta_p$ of the Lax operator $\mathcal{L}$ are constant in time. This property, called *isospectrality*, is a characteristic of the integrability of an equation, as a consequence of the Lax theory [14]. The evolutions of $C_p$ and $r(\xi)$ are given by the second equation of the ZS system (1.4b) [9] [17]:

$$\zeta_p = \text{const. } \forall p \ , \quad C_p(t_f) = C_p(t_i) e^{2i\zeta_p^2 (t_f - t_i)} \ , \quad r(\xi, t_f) = r(\xi, t_i) e^{2i\xi^2 (t_f - t_i)}. \tag{1.9}$$

Then, the IST step maps this non-linear spectrum back to the function in the real space at the same time. This requires solving integral Gelfand-Levitan-Marchenko equations [9] [18], which is a complicated task. Mostly often, the IST step is performed numerically or in simple or asymptotic cases. An effective alternative is the Darboux transform [18] [19], used when the waves are absent from the system ($r(\xi) = 0$) and which builds the function $u(x, t_i)$ recursively and from a known custom spectrum.

In all this thesis, each time the DST procedure or the DST spectrum are mentioned, they refer to the DST framework devised for the 1D-NLSE from the Lax operator (1.5).

**Solitonic solutions**

The 1D-NLSE has two types of solutions : linear waves and asymptotically localized structures. The nature of these localized structures depends on the sign of the non-linearity. If the non-linear term has the same sign as the linear part, the 1D-NLSE is said to be the focusing 1D-NLSE and admits *bright* solitons, in the other case, the defocusing

1D-NLSE admits *dark* solitons. Both types of solution are particular examples of a general class of non-linear PDEs solutions, *solitons*.

Solitons are solitary waves exhibited as solutions of non-linear equations such as 1D-NLSE or KdV equation. More precisely, a soliton propagates with a constant profile in space, keeping the same form without dissipation nor alteration. Its speed of propagation is also constant. For bright solitons, these unique characteristics are allowed by a balance between the focusing non-linearity of the system, which tends to concentrate the energy in one point, and the dispersion, which causes a localized structure, as a wave-packet, to lose its coherence. As we will see later, the constant amplitude and velocity are directly linked with the isospectrality property of the discrete DST spectrum.

Solitons were first experimentally reported by John Scott Russell in 1843 with the observation of a solitary unperturbed wave created by a boat drawn by horses in a canal [20]. In 1955, the FPUT numerics showed energy cycles in a non-linear chain of oscillators, contrary to the expected equipartition of energy. This was explained by Zabusky and Kruskal in 1965 with their introduction of *solitary-waves pulses* which they eventually named *solitons* [21]. Up to now, the solitons have been discovered for many non-linear PDEs, like 1D-NLSE [9], 1D-KdV equation [10], sine-Gordon equation [22] and Boussinesq equation [23].

Solitons collide elastically no matter their characteristics, meaning that the collision changes neither the solitons' amplitudes nor their speeds. The solitons' positions and phases may be shifted but their profiles are unchanged. This observation can be generalized : all solitons of an integrable non-linear PDEs collide elastically.

The explicit formula of solitons depends on the corresponding non-linear equation. For the focusing 1D-NLSE, the bright solitons are given by

$$u_{\text{sol}}^{\text{NLSE}}(x,t) = A \text{ sech}\left[A(x-s-vt)\right] e^{iv(x-s)} e^{-i(v^2-A^2)t/2} e^{i\phi}, \tag{1.10}$$

with the amplitude $A$, the velocity $v$, the initial position $s$ and the phase $\phi$. For the 1D-NLSE bright solitons, the parameters are independent but this is not a general observation for all solitons. For instance, KdV solitons are characterized by a relation between the amplitude and the velocity : the bigger the soliton, the faster.

FIGURE 1.2(a) presents this profile (1.10) for $A = 20, v = 4, s = 0, \phi = 0$ and $t = 0$. With the amplitude $A$ being a multiplying factor inside the sech function, the higher the soliton, the wider. The bright solitons are characterized by the localization of the function into a peak, while dark solitons represent localized dips in a continuous background [24]. This qualitative difference explains the adjective focusing and defocusing. From now on, the terms 1D-NLSE and 1D-NLSE solitons will refer respectively to the focusing 1D-NLSE, and bright solitons. As such, we will omit the adjectives focusing and bright.

The main result of the DST applied to the 1D-NLSE is the explicit link between the characteristics of the solitons and the positions of the eigenvalues in the complex

plane [17]. Each soliton of amplitude $A$ and velocity $v$ is identified by an unique eigenvalue $\zeta = \zeta^{\mathrm{Re}} + i\zeta^{\mathrm{Im}} = -v/2 + iA/2$, as illustrated FIGURE 1.2(b). This identification can be seen as a definition of a soliton for an integrable system. The isospectrality property constrains the eigenvalues $\zeta_p$ to be constant in time, which also imposes the constancy of $A$ and $v$. This directly corresponds to the collisions between solitons being elastic.

Coherent structures balancing dispersion with self-focusing non-linearity can also exist for non-integrable equations (see for instance 1.22), we will call such structures *solitary waves*. However, for non-integrable equations, we can not find a Lax pair and we can not apply a DST and, thus, these coherent structures can not be defined as eigenvalues of a discrete DST spectrum. Given that, nothing prevents the amplitudes and speeds of solitary waves from changing in time, leading to inelastic collisions. For the rest of this thesis, a soliton is a coherent structure with constant amplitude and speed, undergoing elastic collisions, solution of an integrable non-linear PDE and represented by a single eigenvalue in the corresponding DST spectrum. On the contrary, solitary waves are also coherent structures with steady amplitude and speed during free propagation, but undergoing inelastic collisions. These solitary waves are solutions of non-integrable non-linear PDE.

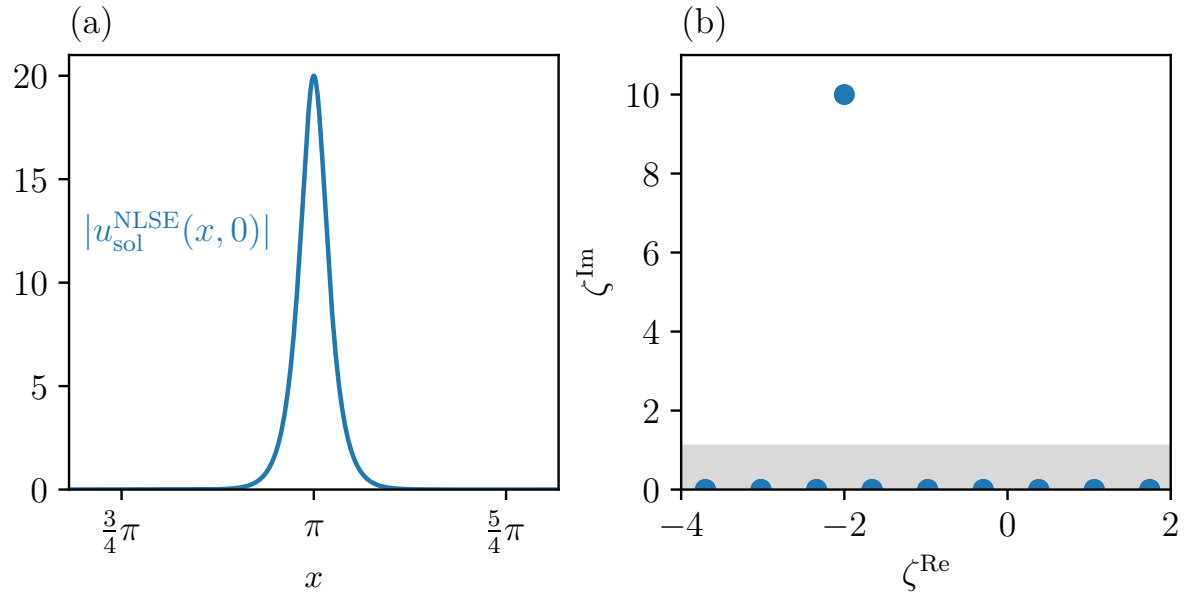


Figure 1.2: **Pure soliton profile and discrete DST spectrum -** (a) Plot of the function (1.10) with $A = 20, v = 4, s = 0$ and $\phi = 0$. (b) Corresponding discrete DST spectrum. The soliton is represented by an unique eigenvalue $\zeta$ which position is given by its characteristics, $\zeta = -v/2 + i20/2 = -2 + 10i$.

From a terminology point of view, this what differentiates the solitons (elastic collisions) from solitary waves (inelastic collisions). This property is a direct consequence of the integrability of the equation as it comes from the isospectrality property of the Lax operator spectrum $\{\zeta_p\}_p$.

To summarize, the 1D-NLSE is integrable because one we associate a Lax pair with it. The spectrum of the Lax operator defines moving localized structures, the solitons. The integrability of 1D-NLSE ensures that these solitons collide elastically, keeping their amplitudes and velocities constant.

**Hamiltonian formalism and conserved quantities**

The 1D-NLSE (1.1) can be derived from a Hamiltonian formalism

$$i\frac{\partial}{\partial t}u = \frac{\delta}{\delta u^*}\mathcal{H}. \tag{1.11}$$

For 1D-NLSE, one can easily verify that the Hamiltonian $\mathcal{H}^{\text{NLSE}}$ is

$$\mathcal{H}^{\text{NLSE}} = \int_{\text{domain}} \frac{1}{2}\left|\frac{\partial u}{\partial x}\right|^2 \mathrm{d}x - \int_{\text{domain}} \frac{1}{2}|u|^4 \mathrm{d}x, \tag{1.12}$$

which can be divided in two Hamiltonians, $\mathcal{H}_2^{\text{NLSE}} = \int \frac{1}{2}\left|\frac{\partial u}{\partial x}\right|^2 \mathrm{d}x$ and $\mathcal{H}_4^{\text{NLSE}} = -\int \frac{1}{2}|u|^4 \mathrm{d}x$.

The Hamiltonians can be written as functions of $\hat{u}_{\mathbf{k}}(t)$ the Fourier components of $u(x,t)$, given in 1D by

$$\hat{u}_{\mathbf{k}}(t) \equiv \hat{u}(\mathbf{k},t) = \frac{1}{L}\int_{\text{domain}} u(x,t)e^{-i\mathbf{k}x}\mathrm{d}x \qquad \Leftrightarrow \qquad u(x,t) = \sum_{\mathbf{k}=-\infty}^{\infty} \hat{u}_{\mathbf{k}} e^{i\mathbf{k}x}. \tag{1.13}$$

Notice that we denote the wave-vector $\mathbf{k} \in \mathbb{R}$ and $k \in \mathbb{R}^+$ its norm. The $x$-integration is performed over the 1D domain of length $L$ in which the system is defined. In numerics, this often corresponds to a discretized box with different boundary conditions. This discretization also truncates the $\mathbf{k}$-sum to a maximum and gives discrete values for $\mathbf{k}$. With this decomposition into Fourier coefficients, we obtain

$$\mathcal{H}^{\text{NLSE}} = \underbrace{\sum_{\mathbf{k}=-\infty}^{\infty} \frac{1}{2}\mathbf{k}^2|\hat{u}_{\mathbf{k}}|^2}_{\mathcal{H}_{2,\mathbf{k}}^{\text{NLSE}}} \underbrace{-\frac{1}{2}\sum_{\mathbf{k}_{1-4}=-\infty}^{\infty} \hat{u}_{\mathbf{k}_1}\hat{u}_{\mathbf{k}_2}\hat{u}^*_{\mathbf{k}_3}\hat{u}^*_{\mathbf{k}_4}\ \delta^{\mathbf{k}_1,\mathbf{k}_2}_{\mathbf{k}_3,\mathbf{k}_4}}_{\mathcal{H}_{4,\mathbf{k}}^{\text{NLSE}}}, \tag{1.14}$$

where $\delta^{\mathbf{k}_1,\mathbf{k}_2}_{\mathbf{k}_3,\mathbf{k}_4} = \delta(\mathbf{k}_1+\mathbf{k}_2-\mathbf{k}_3-\mathbf{k}_4)$ is the Kronecker delta, equal to 1 if the argument is equal to 0 and 0 otherwise.

The Hamiltonian $\mathcal{H}_{2,\mathbf{k}}^{\text{NLSE}}$ is a quadratic Hamiltonian, representing the linear waves propagating without any interaction. Setting it equal with the standard form $\sum_{\mathbf{k}} \omega_{\mathbf{k}}|\hat{u}_{\mathbf{k}}|^2$, we obtain the following linear dispersion relation

$$\omega_{\mathbf{k}} = \frac{1}{2}\mathbf{k}^2. \tag{1.15}$$

This dispersion relation is not linear in $\mathbf{k}$ and thus shows that 1D-NLSE is a dispersive system : waves defined by two different wave-vectors $\mathbf{k}_1 \neq \mathbf{k}_2$ will propagate with different

phase velocities $v_{\mathrm{p},\mathbf{k}_1} \neq v_{\mathrm{p},\mathbf{k}_2}$.

$\mathcal{H}^{\mathrm{NLSE}}_{4,\mathbf{k}}$ represents an interaction Hamiltonian which represents non-linear interactions between four modes. More precisely, it describes $2 \leftrightarrow 2$-type interactions, between two in-coming modes, with Fourier coefficients $\hat{u}_{\mathbf{k}_{1,2}}$, and two out-going modes, with Fourier coefficients $\hat{u}^*_{\mathbf{k}_{3,4}}$. These modes must satisfy the condition $\mathbf{k}_1 + \mathbf{k}_2 = \mathbf{k}_3 + \mathbf{k}_4$ for the interaction to happen, due to the Kronecker delta in the expression of the Hamiltonian. Such waves are said in *wave-number resonance*. FIGURE 1.3 illustrates, in 2D for visibility, such a process. This interaction is characterized by a coefficient $T^{\mathbf{k}_1,\mathbf{k}_2}_{\mathbf{k}_3,\mathbf{k}_4}$, depending on the four modes, called interaction coefficient. This coefficient represents the strength of the considered interaction. With the latter, the interacting Hamiltonian can be written as

$$\mathcal{H}_{4,\mathbf{k}} = \frac{1}{2} \sum_{\mathbf{k}_{1-4}=-\infty}^{\infty} T^{\mathbf{k}_1,\mathbf{k}_2}_{\mathbf{k}_3,\mathbf{k}_4}\, \hat{u}_{\mathbf{k}_1} \hat{u}_{\mathbf{k}_2} \hat{u}^*_{\mathbf{k}_3} \hat{u}^*_{\mathbf{k}_4}\, \delta^{\mathbf{k}_1,\mathbf{k}_2}_{\mathbf{k}_3,\mathbf{k}_4}. \tag{1.16}$$

For the 1D-NLSE, the interaction coefficient for $2 \leftrightarrow 2$ interactions is found to be

$$T^{\mathbf{k}_1,\mathbf{k}_2}_{\mathbf{k}_3,\mathbf{k}_4} = -1.. \tag{1.17}$$

Note that the factor $\frac{1}{2}$ has been let out of the sum in the expression of $\mathcal{H}^{\mathrm{NLSE}}_{4,\mathbf{k}}$ to take into account the symmetry factor. The property of all Hamiltonian to be real quantities implies relations for $T$

$$T^{\mathbf{k}_1,\mathbf{k}_2}_{\mathbf{k}_3,\mathbf{k}_4} = T^{\mathbf{k}_2,\mathbf{k}_1}_{\mathbf{k}_3,\mathbf{k}_4} = T^{\mathbf{k}_1,\mathbf{k}_2}_{\mathbf{k}_4,\mathbf{k}_3} = \left(T^{\mathbf{k}_3,\mathbf{k}_4}_{\mathbf{k}_1,\mathbf{k}_2}\right)^*. \tag{1.18}$$

The underscript $_i$ in $\mathcal{H}_i$ represents the order of the interaction by counting the number of interacting modes. In particular, for $\mathcal{H}_2$, $1 \leftrightarrow 1$ "interactions" just represent the free propagation of linear waves.

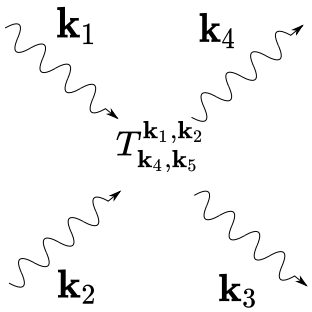


Figure 1.3: **2D visualization of a $2 \leftrightarrow 2$-type interaction**

The 1D-NLSE is a conservative system which conserves exactly the total energy $\mathcal{H}^{\mathrm{NLSE}}$ as long as forcing or dissipating terms are not added. Another quantity is conserved, the wave-action, denoted $\mathcal{N}$

$$\mathcal{N} \equiv \int_{\mathrm{domain}} |u|^2 \mathrm{d}x = \frac{L}{2\pi} \sum_{\mathbf{k}=-\infty}^{\infty} |\hat{u}_{\mathbf{k}}|^2. \tag{1.19}$$

The equality between the two integrals is ensured by the Parseval theorem. Wave-action $\mathcal{N}$ can be interpreted as the number of particles when the 1D-NLSE describes a dilute Bose gas or the total light intensity in an optical system without any loss. Exact conservations of $\mathcal{H}$ and $\mathcal{N}$ are not limited to the 1D-NLSE, they are also valid in more dimensions and for NLS-type equations for which the potential $V$ only depends on $|u|^2$. Finally, we can note than an equation which conserves $\mathcal{N}$ can only have even-order interaction Hamiltonians with $M \leftrightarrow M$-type interactions, with $M$ an integer. For such interactions, the number of in-coming waves is equal to the number of out-coming waves, ensuring the conservation of the total number of waves, *ie* the wave-action $\mathcal{N}$.

The 1D-NLSE also conserves exactly the total momentum

$$\mathbf{P} = -i \int_{\text{domain}} \left( u^* \partial_x u - u \partial_x u^* \right) \mathrm{d}x, \tag{1.20}$$

which has the property not to be sign definite. Contrary to the wave-action which is a positive quantity by definition, the sign of $\mathbf{P}$ is not fixed.

We can note that the 1D-NLSE is only integrable in 1D. The 2D- and 3D- NLSE are non-integrable and, consequently, do not exhibit soliton solutions. Moreover, the integrability of the NLSE in 1D is an important characteristic as it implies that 1D-NLSE can not exhibit a turbulent behaviour. To observe a turbulent evolution, we need to consider the NLSE in more dimensions [25] or to break the integrability by adding terms, as we describe next in section 1.1.2. Alternate means of breaking integrability have been studied, such as pumping or damping in optical fibers [5]. Such pumped and damped systems do not conserve $\mathcal{H}$ or $\mathcal{N}$, unless the damping exactly matches the forcing.

### 1.1.2 1D Schrödinger-Helmholtz Equation (SHE)

The equation we will focus on in this work is an NLS-type equation for a particular potential $V$, the one-dimensional Schrödinger-Helmholtz equation (1D-SHE),

$$i \frac{\partial}{\partial t} u + \frac{1}{2} \frac{\partial^2}{\partial x^2} u - V[u] u = 0 \tag{1.21a}$$

$$\beta \frac{\partial^2}{\partial x^2} V - V = |u|^2, \tag{1.21b}$$

with $u(x,t)$ a $\mathbb{R} \times [0, +\infty[ \to \mathbb{C}$ function and $\beta$ a real and positive physical constant. The potential $V$ is defined by a differential equation 1.21(b). The 1D-SHE arises in non-linear optics where sub-leading corrections to the 1D-NLSE need to be taken into account in order to accurately describe the dynamics. In particular, the 1D-SHE describes optical medium responds to the propagation of a light beam of intensity $|u|^2$ by modifying its refractive index (denoted here as $V$). This modification involves both local and non-local mechanisms. The local mechanism is the Kerr effect, represented by the term $-V$ in the Left-Hand-Side (LHS) of 1.21(b). If we consider only this local Kerr effect, we would recover the 1D-NLSE. The non-local mechanism can be thermo-optic with the

heating of the medium by the input beam which spreads through the crystals by diffusion [26] [27] [28]. The non-local mechanism can also be, in elasto-optic medium such as the liquid crystals, due to long-range elastic forces which spread the reorientation of the molecules with the input beam [29] [30]. In both cases, the Schrödinger Equation 1.21(a) for the variable $u$ is coupled to a Helmholtz equation 1.21(b) for $V$. This motivates the name Schrödinger-Helmholtz equation for the system. This coupling also means that the value of the function $u$ at a position $x_0$ depends on its values at the other positions $x \neq x_0$.

We can combine both equations of the system (1.21) to have a single equation for $u(x,t)$.

$$i\frac{\partial}{\partial t}u + \frac{1}{2}\frac{\partial^2}{\partial x^2}u + u\left(1-\beta\frac{\partial^2}{\partial x^2}\right)^{-1}|u|^2 = 0. \tag{1.22}$$

Taking $\beta = 0$, we recover the integrable 1D-NLSE but it has been shown that the 1D-SHE is not integrable for $\beta > 0$ [5]. Thus, the parameter $\beta$ controls how much non-integrable the system is. This non-integrability implies that the 1D-SHE can not be associated to a Lax pair and, thus, does not admit solitons solutions as defined above.

**Solitary wave solution**

Despite its non-integrability and the absence of solitons as eigenvalues of a discrete DST spectrum, the 1D-SHE also has a solitary wave solution, in the sense of a localized structure propagating in straight line keeping the same profile but which does not collide elastically. The solitary wave solution $u^{\text{SHE}}_{\text{sol w}}$ of equation (1.22) has been found by [31],

$$u^{\text{SHE}}_{\text{sol w}}(x,t) = \frac{3}{2}\frac{1}{\sqrt{2\beta}}\ \text{sech}\Big[\frac{1}{2\sqrt{\beta}}(x-vt)\Big]^2 e^{-i(\frac{v^2}{2}-\frac{1}{2\beta})t}e^{ivx}. \tag{1.23}$$

The main differences with the soliton solution of the 1D-NLSE is firstly the exponent 2 of the sech-function. This changes the width of the localized structure. Secondly, the amplitude is now fixed by the non-integrability parameter $\beta$ : the amplitude is not a free variable in the SHE. However, the solitary wave speed is still is independent from its amplitude. The final difference is the different coefficients multiplying the sech, inside the sech and in the exponential phase.

In FIGURE 1.4 we compare the profiles of a 1D-NLSE soliton and a 1D-SHE solitary wave. $u^{\text{SHE}}_{\text{solw.}}$ is plotted for $\beta = 10^{-2}$ and the amplitude $A$ of $u^{\text{NLSE}}_{\text{sol}}$ is chosen for both structures to have the same maximum 10.607. Both structures also have the same velocity $v = -1$. The NLSE soliton is found to be slightly more narrow, due to the difference of exponent for the sech-function. In (b) we also compute the DST spectrum of this solitary wave. Here we use the DST procedure corresponding to the integrable 1D-NLSE and that applying it to the non-integrable 1D-SHE does not presume any coherent results. However, the solitary wave is still characterized by only one eigenvalue, like the 1D-NLSE soliton, with the same real part as the 1D-NLSE eigenvalue $0.5 = -v/2$. The difference lies in the imaginary part, with $A/\zeta^{\text{Im}} = 2$ for the 1D-NLSE soliton and 1.535 for the 1D-SHE solitary wave. This difference can be explained by the non-integrability of the

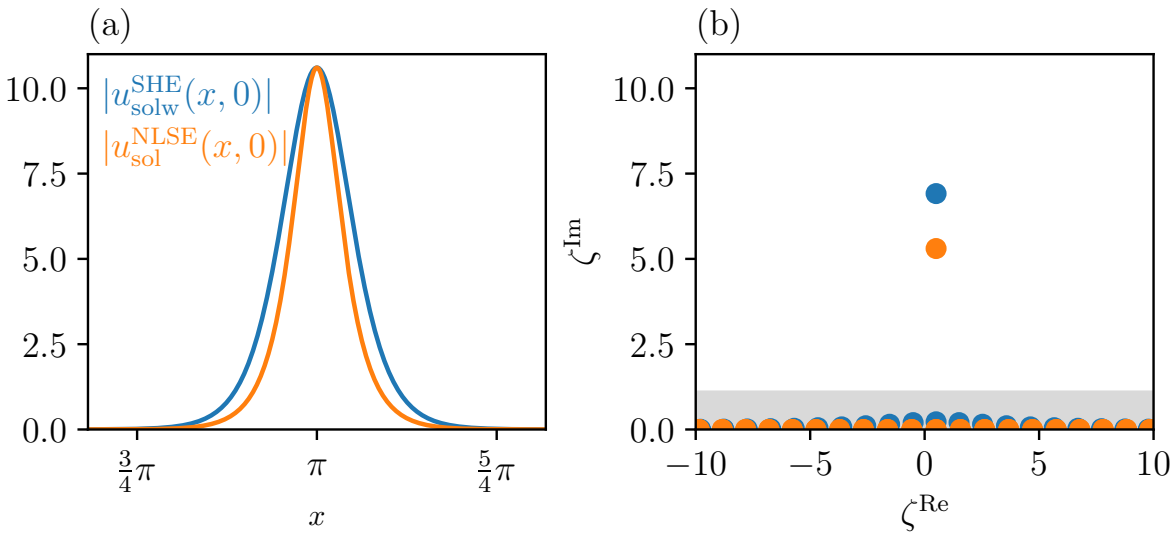


Figure 1.4: **SHE solitary wave profile and DST spectrum -** (a) We compare 1D-SHE solitary waves ($\beta = 10^{-2}$) and 1D-NLSE soliton adjusted to have the same maximum. The 1D-SHE solitary wave appears to be slightly wider, corresponding to a bigger wave-action. (b) For each function plotted, we compute the discrete DST spectrum. They are both represented by a unique eigenvalue, with the expected value for $\zeta^{\mathrm{Im}} = A/2$ for the 1D-NLSE soliton, as opposed to $A/1.535$ for the 1D-SHE solitary wave.

1D-SHE, while the DST is supposed to be applied on the integrable 1D-NLSE. The grey region is a threshold which will be explained in section 2.2.

**Hamiltonian formalism and conserved quantities**

As for the 1D-NLSE, the 1D-SHE can be described with the Hamiltonian formalism (1.11) with the following Hamiltonian, written with the Fourier components,

$$\mathcal{H}^{\mathrm{SHE}} = \sum_{\mathbf{k}=-\infty}^{\infty} \frac{1}{2}\mathbf{k}^2|\hat{u}_{\mathbf{k}}|^2 + \frac{1}{2}\sum_{\mathbf{k}_{1-4}=-\infty}^{\infty} {}^{\mathrm{SHE}}T^{k_1,k_2}_{k_3,k_4}\ \hat{u}_{k_1}\hat{u}_{k_2}\hat{u}^*_{k_3}\hat{u}^*_{k_4}\delta^{k_1,k_2}_{k_3,k_4}, \tag{1.24}$$

with the 4-modes interaction coefficient defined as a function of the scattering modes [25]

$${}^{\mathrm{SHE}}T^{\mathbf{k}_1,\mathbf{k}_2}_{\mathbf{k}_3,\mathbf{k}_4} = \frac{-1}{4}\Big(A_{1234}+A_{2134}+A_{1243}+A_{2143}\Big),\ A_{1234} = \frac{1}{\beta(\mathbf{k}_1-\mathbf{k}_4)(\mathbf{k}_3-\mathbf{k}_2)+1}. \tag{1.25}$$

The 1D-NLSE and 1D-SHE have the same linear dispersion relation $\omega_{\mathbf{k}} = \mathbf{k}^2/2$, which was expected because both equations share the same linear part. Similarly, the interaction coefficient represents interactions between four modes, this time with a coefficient depending on the wave-numbers. The 1D-SHE also conserves exactly the Hamiltonian $\mathcal{H}$ and the wave-action $\mathcal{N}$. It will be useful to write the 1D-SHE (1.22) in terms of Fourier coefficients,

$$i\frac{\partial \hat{u}_{\mathbf{k}}}{\partial t} = \omega_{\mathbf{k}}\hat{u}_{\mathbf{k}} + \sum_{\mathbf{k}_{1-3}} {}^{\mathrm{SHE}}T^{\mathbf{k}_1,\mathbf{k}_2}_{\mathbf{k}_3,\mathbf{k}}\ \hat{u}_1\hat{u}_2\hat{u}^*_3\,\delta^{\mathbf{k}_1,\mathbf{k}_2}_{\mathbf{k}_3,\mathbf{k}}. \tag{1.26}$$

The 1D-SHE also conserves the impulsion $\mathbf{P}$ as defined in (1.20).

### 1.1.3 Other limits of the 1D-SHE

As said before, taking $\beta = 0$ in the 1D-SHE system (1.21), we obtain the 1D-NLSE. However, the 1D-SHE has other limits. The non-linear term of the 1D-SHE contains two terms, the constant 1 and the second spatial derivative $\beta\frac{\partial^2}{\partial x^2}$. The global equation thus has two limits, corresponding to either of these terms dominating. In Fourier space, the non-linear operator becomes $(1+\beta k^2)^{-1}$ for which we can define a particular wave-vector $k^* = 1/\sqrt{\beta}$ to have $(1+k^2/k^{*2})^{-1}$. With this, the two limits correspond to $k^2 \ll k^{*2}$, the Long Wave limit (LW limit) and $k^2 \gg k^{*2}$, the Short Wave limit (SW limit).

As we want to characterize turbulence in 1D-SHE systems, one needs to consider the next order term in the Taylor expansion of the non-linear term $(1-\beta\frac{\partial^2}{\partial x^2})^{-1}$ in the LW limit $\beta\frac{\partial^2}{\partial x^2} \ll 1$ (equivalent to $k \ll k^*$) :

$$\left(1-\beta\frac{\partial^2}{\partial x^2}\right)^{-1} \sim \left(1+\beta\frac{\partial^2}{\partial x^2}\right) + \mathcal{O}\left(\beta\frac{\partial^2}{\partial x^2}\right). \tag{1.27}$$

With this expansion, the 1D-SHE becomes

$$i\frac{\partial}{\partial t}u + \frac{1}{2}\frac{\partial^2}{\partial x^2}u + u\left(1+\beta\frac{\partial^2}{\partial x^2}\right)|u|^2 = 0. \tag{1.28}$$

This equation will be referred to as the one dimensional Long-Wave Equation (1D-LWE) and has also been found to be not integrable [5]. The expansion (1.27) needs to be done up to the second term because stopping at the first term we end up with the 1D-NLSE.

In the Short-Wave limit ($k^2 \gg k^{*2}$), the dominant term in the non-linearity is $\beta\frac{\partial^2}{\partial x^2}$. This time, we can stop the Taylor expansion at the first order

$$\left(1-\beta\frac{\partial^2}{\partial x^2}\right)^{-1} \sim -\left(\beta\frac{\partial^2}{\partial x^2}\right)^{-1} + \mathcal{O}(1). \tag{1.29}$$

This condition may be satisfied only for a certain range of $k$, this point will be discussed with the numerical results section 3.5. The equation obtained with this expansion in the Short-Wave limit is known as the one dimensional Schrödinger-Newton Equation (1D-SNE) :

$$i\frac{\partial}{\partial t}u + \frac{1}{2}\frac{\partial^2}{\partial x^2}u - u\left(\beta\frac{\partial^2}{\partial x^2}\right)^{-1}|u|^2 = 0 \tag{1.30}$$

We stopped the Taylor expansion (1.29) at the first order because the obtained 1D-SNE is non-integrable and can, thus, exhibit turbulent behaviour. It has been also studied by Laurie et al. [5].

Both 1D-LWE and 1D-SWE corresponds to limit case of the 1D-SHE and thus model the same systems, as non-linear optics, in their respective limits. Both are also are also conservative systems which conserve the wave-action $\mathcal{N}$ and the Hamiltonian $\mathcal{H}$

$$\mathcal{H} = \sum_{\mathbf{k}=-\infty}^{\infty} \frac{1}{2}\mathbf{k}^2 |\hat{u}_{\mathbf{k}}|^2 + \frac{1}{2} \sum_{\mathbf{k}_{1-4}=0}^{\infty} T^{\mathbf{k}_1,\mathbf{k}_2}_{\mathbf{k}_3,\mathbf{k}_4}\, \hat{u}_{\mathbf{k}_1} \hat{u}_{\mathbf{k}_2} \hat{u}^*_{\mathbf{k}_3} \hat{u}^*_{\mathbf{k}_4}\, \delta^{\mathbf{k}_1,\mathbf{k}_2}_{\mathbf{k}_3,\mathbf{k}_4}. \tag{1.31}$$

They both represent $2 \leftrightarrow 2$-type interactions, yet with different interaction coefficients

$${}^{\text{LWE}}T^{\mathbf{k}_1,\mathbf{k}_2}_{\mathbf{k}_3,\mathbf{k}_4} = -1 + \frac{\beta}{2}\Big(\mathbf{k}_1\mathbf{k}_4 + \mathbf{k}_2\mathbf{k}_3 + \mathbf{k}_1\mathbf{k}_3 + \mathbf{k}_2\mathbf{k}_4 - 2\mathbf{k}_1\mathbf{k}_2 - 2\mathbf{k}_3\mathbf{k}_4\Big) \tag{1.32}$$

and

$${}^{\text{SNE}}T^{\mathbf{k}_1,\mathbf{k}_2}_{\mathbf{k}_3,\mathbf{k}_4} = \frac{1}{2\beta}\Big(\frac{1}{\mathbf{k}_1\mathbf{k}_4} + \frac{1}{\mathbf{k}_2\mathbf{k}_3} + \frac{1}{\mathbf{k}_1\mathbf{k}_3} + \frac{1}{\mathbf{k}_2\mathbf{k}_4} - \frac{2}{\mathbf{k}_1\mathbf{k}_2} - \frac{2}{\mathbf{k}_3\mathbf{k}_4}\Big) \tag{1.33}$$

We can note that the interaction coefficient for the LWE has two contributions coming from the non-linear terms of (1.28).

## 1.2 Wave Turbulence

Wave Turbulence (WT) is the study of non-linear, random, and non-equilibrium interacting waves. WT can be described as the statistical mechanics of non-linear waves. It is applied to a large variety of non-linear systems : water waves with both gravity and capillary waves [32], [33], internal waves [34], Kelvin waves in superfluid Helium [35], Alfvén waves in hot plasma [36], non-linear optics [37], vibrating plates [38]. These systems are often open, with forcing (like the wind forcing the surface water waves) and dissipation (viscous dissipation, dissipation in optial fibers, ...). Such external interactions move the system away from potential equilibrium states and classical thermodynamics can not be applied anymore. It is more relevant to define and work with the flux of cascading quantities.

### 1.2.1 Hydrodynamic Turbulence

In 1926, [39], L. F. Richardson imagined the idea of the energy cascading through scales with a succession of hydrodynamic vortices, each vortex creating a smaller one. According to Richardson, the big vortices are created by external forcing at the largest scale in the system, and this scheme will continue until the vortices are so small that they are dissipated by viscosity.

*Big whirls have little whirls*
*that feed on their velocity,*
*And little whirls have lesser whirls*
*and so on to viscosity*

**Lewis Fry Richardson, 1922**

In this example, the energy is transferred from large length-scales to small length-scales, but we can also consider the same cascade in the Fourier space, towards large

wave-numbers. In Fourier space, denoting the forcing scale as $k_f$ and the dissipation scale as $k_\nu$, the cascade occurs for scales $k$ such that $k_f \ll k \ll k_\nu$, called the *inertial range*. This cascade, as imagined by Richardson, is local in the sense that a very big vortex will create a vortex slightly smaller than itself. In a local cascade, a vortex interacts with vortices with similar sizes, contrary to a non-local cascade for which there can be interactions between vortices of very different sizes.

In 1941, Kolmogorov and Obukhov, [40] [41], introduced the hypothesis of similarity : in the inertial range, the turbulence properties do not depend on the details of the forcing nor the dissipation. Particularly, the energy spectrum does not depend on the viscosity $\nu$. With this assumption, a dimensional analysis lead to an expression of the one dimensional energy spectrum for isotropic 3D hydrodynamic turbulence

$$E^{(1\mathrm{D})}(\mathbf{k}) = \mathcal{C}\varepsilon^{\frac{2}{3}}k^{-\frac{5}{3}} \tag{1.34}$$

with $\varepsilon$ the energy flux and $\mathcal{C}$ a dimensionless constant. Denoting $\mathbf{u}$ the velocity field of the fluid, the one dimensional energy spectrum $E^{(1\mathrm{D})}(\mathbf{k})$ is defined as the kinetic energy density $\langle \mathbf{u}^2/2 \rangle = \int_{\mathbf{k}} E^{(1\mathrm{D})}(\mathbf{k})\mathrm{d}\mathbf{k}$. The spectrum (1.34) is known as the Kolmogorov-Obukhov spectrum. Even though this spectrum is quite easy to obtain, it has been validated by different numerics and experiments. $\mathcal{C}$ has been experimentally found to be $\mathcal{C} \simeq 1.6$. The deviations from the Kolmogorov-Obukhov spectrum are small for the spectrum itself but are non-negligible for higher-order moments. These deviations are responsible for the intermittency phenomenon. The intermittency is the property of some systems to contain waves of very-large amplitude, with a probability higher than expected with the Kolmogorov-Obukhov model.

2D hydrodynamic turbulence has also been studied the same way, and it exhibits a dual-cascade behaviour. Indeed, 2D hydrodynamic systems conserve two distinct quantities, the kinetic energy and the enstrophy, which is the total vorticity squared $\Omega = \int_{\mathbf{k}} \mathbf{k}^2 E^{(1\mathrm{D})}(\mathbf{k})\mathrm{d}\mathbf{k}$. Fjørtoft showed in 1953 [42] that these two quantities have to cascade in opposite directions in $k$-space. This argument is detailed section 1.3.4. He found that energy is transferred to small scales (*inverse energy cascade*) and enstrophy to large scales (*direct enstrophy cascade*). Kraichnan found in 1967 [43] that each cascade can be described by a Kolmogorov-Obukhov-like spectrum, if we write enstrophy flux by $\eta$ the , Kraichnan found

$$E^{(1\mathrm{D})}(\mathbf{k}) = \mathcal{C}'\varepsilon^{\frac{2}{3}}k^{-\frac{5}{3}} \quad \text{for the inverse energy cascade,} \tag{1.35a}$$

$$E^{(1\mathrm{D})}(\mathbf{k}) = \mathcal{C}''\eta^{\frac{2}{3}}k^{-3} \quad \text{for the direct enstrophy cascade.} \tag{1.35b}$$

with the apostrophes to underline that these constants are different from the one obtained in 3D. These spectra have been obtained experimentally and numerically [44]. DNS have even **showed** the dual cascade behaviour , [45] [46], by forcing in the middle of the $k$ range. DNS and experiments found $C' \simeq 6$ [45] and $C'' \simeq 1.6$.

2D hydrodynamic systems conserve two invariants (energy and enstrophy) and are characterized by a dual cascade. This result can be generalized, $M$ conserved quantities will be transferred with $M$ cascades happening in the same time.

### 1.2.2 Wave Turbulence

In hydrodynamic turbulence, the mechanism of energy transfer is the creation of new vortices. The Wave Turbulence (WT) is characterized by the interaction of waves, which is here responsible for the cascade of quantities. The different waves are defined by their wave-vectors $\mathbf{k}_i$ and they interact if the $\mathbf{k}_i \in \mathbb{R}$ are in resonance.

#### Resonances

A set of modes $\{\mathbf{k}_i\}_{i\in[\![1,N]\!]}$ is said to be resonant if it satisfies the following equalities

$$\mathbf{k}_1 \pm \mathbf{k}_2 \pm ... \pm \mathbf{k}_N = 0 \qquad \text{wave} - \text{vector resonance,} \tag{1.36a}$$

$$\omega_{\mathbf{k}_1} \pm \omega_{\mathbf{k}_2} \pm ... \pm \omega_{\mathbf{k}_N} = 0 \qquad \text{frequency resonance.} \tag{1.36b}$$

In this case, this set $\{\mathbf{k}_i\}_{i\in[\![1,N]\!]}$ defines an $N$-mode interaction. $\omega_{\mathbf{k}}$ is the linear dispersion relation, which depends on the studied equation. Particularly, the condition for wave-vector resonance (1.36a) will always the same while the condition for frequency resonance (1.36b) may differ between two equations having different non-linear terms. Together, conditions (1.36a) and (1.36b) define a surface in the joint $(\mathbf{k}_i, \omega_{\mathbf{k}_i})$ space, known as the resonant manifold.

Resonances are at the center of turbulence because it is resonances between modes that allow the propagation of conserved quantities through scales, and thus, cascades. The relative signs define the in-coming and the out-going modes of the interaction. For instance, at $N = 4$, one can have three non-trivial sorts of interactions; $1 \leftrightarrow 3, 3 \leftrightarrow 1$ and $2 \leftrightarrow 2$. The nature of the interactions happening in a system is given by the non-linear term in the equation of motion.

The $\mathbf{k}$-equation (1.36a) encodes the conservation of linear energy and the $\omega-$equation (1.36b) encodes the conservation of momentum. The particular even $N = 2M$ case conserves the number of particles during a $N$-modes interaction : $M$ modes are created from $M$ modes, so there is no loss nor gain. If the system only contains such $2M$-modes interactions, then it conserves total wave-action $\mathcal{N} = (L/2\pi)^d \sum_{\mathbf{k}} a_{\mathbf{k}} a^*_{\mathbf{k}}$ in $d$ dimensions.

To each resonance is associated an interaction coefficient which represents the strength of the interaction. This interaction coefficient depends on the equation and on the resonance studied, and is determined by writing the equation in the Hamiltonian formalism. For a resonance to be physically possible, the resonant conditions (1.36) need to be satisfied and the interaction coefficient needs to be non-zero. An important result is that integrable equations do not have any resonant manifold, *ie* the resonant conditions (1.36) can not be satisfied for any $N$. As these interactions of waves ares responsible for the cascade of quantities, it implies that integrable equations can not exhibit turbulent behaviour. For instance, the 1D-NLSE is integrable and thus can not be analyzed in the WT framework, on the contrary to the 2D- and 3D-NLSE which are not integrable.

**Weak Wave Turbulence**

The WT framework and predictions can be divided into two limits depending on the relative strength of the non-linearity. Quantitatively, we compare the quadratic and interaction Hamiltonians $\mathcal{H}_2$ and $\mathcal{H}_4$ with the ratio

$$\chi = \frac{|\mathcal{H}_4|}{\mathcal{H}_2}. \tag{1.37}$$

The regime $\chi \ll 1$ is called *weak* WT (for weakly non-linear), contrary to the *strong* WT $\chi \gg 1$. In the strong limit, the system is dominated by coherent structures such as solitons or solitary waves, which are strongly non-linear objects the non-linearity. Inversely, in the weak limit we can observe cascades of conserved quantities such as energy KZ spectra. In this thesis, we will study these two limits : the chapter 2 focuses on the strong WT with the propagation of coherent structures in the 1D-SHE while the chapter 3 studies the cascades in the 1D-SHE in the weak WT framework.

## 1.3 Kinetic Equation and solutions

### 1.3.1 Derivation of the Kinetic Equation

In this section, we will just outline the important steps of the derivation of the Kinetic Equation (KE) as this equation is the core of our work. For a full and detailed derivation of the KE, see [3] [37]. The goal is to derive the KE for the 1D-SHE, which is the evolution equation for the wave-action spectrum (or wave-action density) defined, in 1D, as

$$n_{\mathbf{k}}(t) = \frac{L}{2\pi} \langle |\hat{u}_{\mathbf{k}}(t)|^2 \rangle_{\text{i.r.}}. \tag{1.38}$$

where $\langle \, . \, \rangle_{\text{i.r.}}$, represents the average over independent realisations. If we assume ergodicity for the system, then this ensemble average can be replaced by a temporal average over a single realisation. If we assume the isotropy of the system, the wave-action spectrum $n_{\mathbf{k}}$ becomes a function of the norm $k$, $n_{\mathbf{k}}(k)$. Assuming this isotropy, the symmetric wave-action spectrum can be computed in 1D as $n_{\mathbf{k}}(k) = n_{\mathbf{k}} + n_{-\mathbf{k}}$.

We start from a non-linear equation, the 1D-SHE for our study of one dimensional optical turbulence, and we write it in Fourier space. Next, we assume that the non-linear terms are weak compared to the linear one to separate linear and non-linear time-scales. This step corresponds to consider the weak WT regime. Then, we perform a weak non-linearity expansion of the Fourier variable. We use this expansion to write the one-mode generating function. The following step is a particular average, the Random Phases and Amplitudes (RPA) average. It consists of assuming that the complex amplitudes of Fourier variables (more precisely their components in the weak non-linear expansion) are characterized by independent and random amplitudes and phases, the phases being uniformously distributed on the unit circle.

At this point, the generating function is defined, for an intermediate time $T$ between the linear and non-linear time scales, with the Fourier coefficients $\hat{u}_{\mathbf{k}}$ of the initial function

$u$. The sum over these Fourier coefficient will be turned into the integral over the Fourier transforms after the *large-box* limit. Then, the limit of weak non-linearity is applied, to finally obtain the evolution equation for the wave-action spectrum $n_{\mathbf{k}}$ for the 1D-SHE in

$$\frac{\partial n_{\mathbf{k}}}{\partial t} = 24\pi \int \left|{}^{\mathrm{SHE}}T^{\mathbf{k}_1,\mathbf{k}_2}_{\mathbf{k}_3,\mathbf{k}}\right|^2 \left[\frac{1}{n_{\mathbf{k}}} + \frac{1}{n_3} - \frac{1}{n_2} - \frac{1}{n_1}\right] n_1 n_2 n_3 n_{\mathbf{k}}\ \delta^{1,2}_{3,\mathbf{k}}\ \delta(\omega^{1,2}_{3,\mathbf{k}})\ \mathrm{d}\mathbf{k}_1\,\mathrm{d}\mathbf{k}_2\,\mathrm{d}\mathbf{k}_3. \tag{1.39}$$

with the interaction coefficient ${}^{\mathrm{SHE}}T$ defined in (1.25). This Kinetic Equation relies on $2 \leftrightarrow 2$ interactions. The wave-action densities $n_{\mathbf{k}_i}$ are denoted $n_i$. The delta-functions $\delta^{1,2}_{3,\mathbf{k}}$ and $\delta(\omega^{1,2}_{3,\mathbf{k}})$ stand respectively for $\delta(\mathbf{k}_1 + \mathbf{k}_2 - \mathbf{k}_3 - \mathbf{k})$ and $\delta(\omega_1 + \omega_2 - \omega_3 - \omega_{\mathbf{k}})$.

The 1D-SHE, and its versions in 2D or 3D, are all characterized by the dispersion relation $\omega_{\mathbf{k}} = \mathbf{k}^2/2$, which is a particular case of $\omega_{\mathbf{k}} = C\mathbf{k}^\alpha$ with $\alpha > 1$. However, we can show graphically that the four-mode resonance conditions can not satisfied in 1D. The four-mode interaction that we want to study is

$$\begin{cases} \omega_{\mathbf{k}_1} + \omega_{\mathbf{k}_2} = \omega_{\mathbf{k}_3} + \omega_{\mathbf{k}_4} \\ \\ \mathbf{k}_1 + \mathbf{k}_2 = \mathbf{k}_3 + \mathbf{k}_4. \end{cases}$$

This graphical demonstration is illustrated Figure 1.5. First, we plot $\omega_{\mathbf{k}} = \mathbf{k}^2/2$ and we identify $\mathbf{k}_1$ and $\mathbf{k}_3$ on the $\mathbf{k}-$axis. Then, we plot twice again the $\mathbf{k}^2/2$ parabola but starting from the points $(\mathbf{k}_1, \mathbf{k}_1^2/2)$ (plotted in blue) and $(\mathbf{k}_3, \mathbf{k}_3^2/2)$ (plotted in red). The variables $\mathbf{k}_2$ and $\mathbf{k}_4$ can be defined, respectively, from $\mathbf{k}_1$ and $\mathbf{k}_4$. Thus, a point on the blue curve has the coordinates $(\mathbf{k}_1 + \mathbf{k}_2, (\mathbf{k}_1^2 + \mathbf{k}_2^2)/2)$ and a point in the red curve is $(\mathbf{k}_3 + \mathbf{k}_4, (\mathbf{k}_3^2 + \mathbf{k}_4^2)/2)$. With this construction, the four-mode interaction conditions are verified for each intersection of the blue and red curves. One can check on the figure that such a point is possible only for $\mathbf{k}_1 = \mathbf{k}_4$ and $\mathbf{k}_2 = \mathbf{k}_3$ which corresponds to a trivial interaction without any energy transfer between wave modes. Excluding this trivial set of modes, one can conclude that four-mode resonant interaction are absent in a 1D system with a dispersion relation $\omega_{\mathbf{k}} = C\mathbf{k}^2$. This result holds for dispersion relation $\omega_{\mathbf{k}} = C\mathbf{k}^\alpha, \alpha > 1$, due to the convexity of the parabola.

### 1.3.2 Canonical Transform

If a system does not allow four-mode interactions, the expansion of $\mathcal{H}$ needs to be taken to the next order. As said before, there is no odd-order term in a Hamiltonian for a system which conserves the total wave-action $\mathcal{N}$. Thus, the next term is at the $6^{\mathrm{th}}$-order. In this case, we need to apply a Canonical Transform (CT) to remove the non-resonant leading non-linear order (here the fourth) and obtain a new resonant order (here the sixth). This mathematical procedure is detailled by Zakharov et al. in [47] and already used in KW [35], [48], water waves [49] and particularly in optical turbulence [5].

Hence, we will apply a CT to the 1D-SHE to remove the non-resonant four-modes interactions. Namely, we perform a change of variables $\hat{u}_{\mathbf{k}}(t) \to \hat{a}_{\mathbf{k}}(t)$ with a Taylor expansion as a quasi-linear transformation

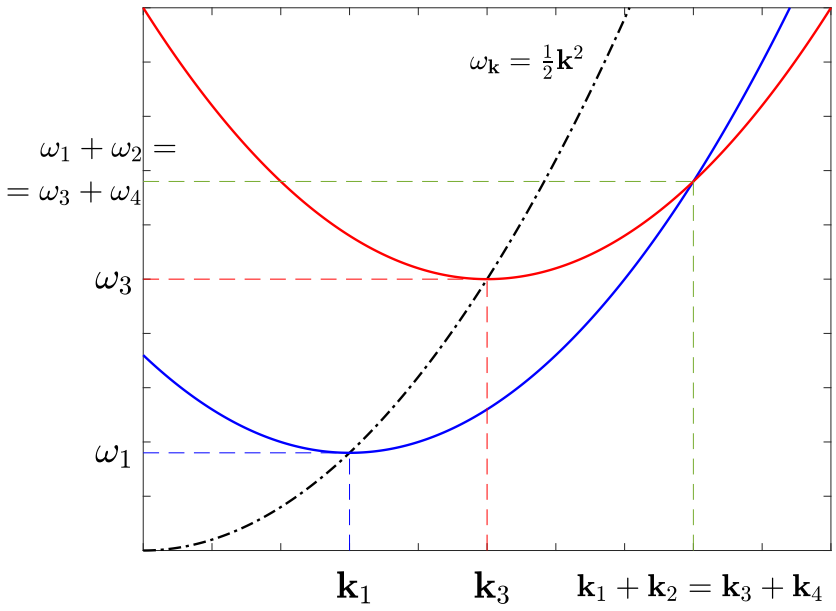


Figure 1.5: **Graphical point to show that non-trivial four-modes interactions are impossible for dispersion relation $\omega_{\mathbf{k}} = \mathbf{k}^2/2$**

$$\hat{u}_{\mathbf{k}}(t) = \hat{a}_{\mathbf{k}}(t,\tau)\Big|_{\tau=0} + \tau\,\frac{\partial \hat{a}_{\mathbf{k}}(t,\tau)}{\partial\tau}\Big|_{\tau=0} + \frac{\tau^2}{2}\,\frac{\partial^2 \hat{a}_{\mathbf{k}}(t,\tau)}{\partial\tau^2}\Big|_{\tau=0} + \mathcal{O}(\tau^2). \tag{1.40}$$

The new variable $\hat{a}_{\mathbf{k}}(t,\tau)$ depends on both physical time $t$ and an "auxiliary" time $\tau$. It corresponds to a new Hamiltonian, labelled auxiliary $\mathcal{H}_{\text{aux}}$, which defines its time evolution of $a_{\mathbf{k}}$ with $\partial a_{\mathbf{k}}/\partial\tau = -i\delta\mathcal{H}_{\text{aux}}/\delta a^*_{\mathbf{k}}$. This auxiliary Hamiltonian only contains interacting terms, *ie*

$$\mathcal{H}_{\text{aux}} = \frac{1}{2}\sum_{\mathbf{k}_1-\mathbf{k}_4} \tilde{T}^{\mathbf{k}_1,\mathbf{k}_2}_{\mathbf{k}_3,\mathbf{k}_4}\,\hat{a}_1\hat{a}_2\hat{a}^*_3\hat{a}^*_4\,\delta^{\mathbf{k}_1,\mathbf{k}_2}_{\mathbf{k}_3,\mathbf{k}_4} + \frac{1}{3}\sum_{\mathbf{k}_1-\mathbf{k}_4} \tilde{W}^{\mathbf{k}_1,\mathbf{k}_2,\mathbf{k}_3}_{\mathbf{k}_4,\mathbf{k}_5,\mathbf{k}_6}\,\hat{a}_1\hat{a}_2\hat{a}_3\hat{a}^*_4\hat{a}^*_5\hat{a}^*_6\,\delta^{\mathbf{k}_1,\mathbf{k}_2,\mathbf{k}_3}_{\mathbf{k}_4,\mathbf{k}_5,\mathbf{k}_6}, \tag{1.41}$$

and its coefficient $\tilde{T}^{\mathbf{k}_1,\mathbf{k}_2}_{\mathbf{k}_3,\mathbf{k}_4}$ and $\tilde{W}^{\mathbf{k}_1,\mathbf{k}_2,\mathbf{k}_3}_{\mathbf{k}_4,\mathbf{k}_5,\mathbf{k}_6}$ will be defined in order to cancel the non-resonant four-waves interactions in the 1D-SHE (see [5] for details). This cancellation creates a new non-linear term of the sixth order from the now-removed fourth order, as illustrated FIGURE 1.6, with the six-modes interaction coefficient

$$W^{\mathbf{k}_1,\mathbf{k}_2,\mathbf{k}_3}_{\mathbf{k}_4,\mathbf{k}_5,\mathbf{k}_6} = \frac{1}{24}\sum_{\substack{i,j,k=1\\ i\neq j\neq k\neq i}}^{3}\ \sum_{\substack{p,q,r=4\\ p\neq q\neq r\neq p}}^{6}\left[\frac{1}{\omega^{i,j}_{r,i+j-r}} - \frac{1}{\omega^{p+q-j,j}_{p.q}}\right]\ {}^{\text{SHE}}T^{i,k}_{r,i+k-r}\ {}^{\text{SHE}}T^{q+p-j,j}_{q,p}. \tag{1.42}$$

where $\omega^{a,b}_{c,d}$ stands for $\omega_{\mathbf{k}_a} + \omega_{\mathbf{k}_b} - \omega_{\mathbf{k}_c} - \omega_{\mathbf{k}_d}$. We have also used the simplified for $T$, as $T^{a,b}_{c,d} = T^{\mathbf{k}_a,\mathbf{k}_b}_{\mathbf{k}_c,\mathbf{k}_d}$. The explicit expression of $W^{\mathbf{k}_1,\mathbf{k}_2,\mathbf{k}_3}_{\mathbf{k}_4,\mathbf{k}_5,\mathbf{k}_6}$ will be given section 3.2, where we study the cascades in this 1D-SHE system.

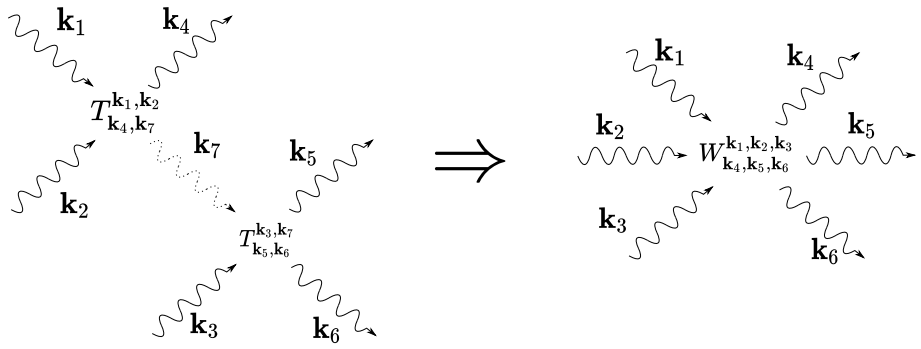


Figure 1.6: **2D illustration of the canonical transform -** In this example, two four-mode interactions are combined, with the exchange of a *virtual* mode $\mathbf{k}_7$, to create a six-mode interaction.

### 1.3.3 Kinetic Equation

With this CT, we finally have the KE for 1D-SHE, as a system with $3 \leftrightarrow 3$-type interactions,

$$\begin{aligned}\frac{\partial n_{\mathbf{k}}}{\partial t} = 24\pi \int \left|W^{1,2,3}_{4,5,\mathbf{k}}\right|^2 \left[\frac{1}{n_{\mathbf{k}}} + \frac{1}{n_5} + \frac{1}{n_4} - \frac{1}{n_1} - \frac{1}{n_2} - \frac{1}{n_3}\right] \\ \times\, n_1 n_2 n_3 n_4 n_5 n_{\mathbf{k}}\ \delta^{1,2,3}_{4,5,\mathbf{k}}\ \delta(\omega^{1,2,3}_{4,5,\mathbf{k}})\ \mathrm{d}\mathbf{k}_1\, \mathrm{d}\mathbf{k}_2\, \mathrm{d}\mathbf{k}_3\, \mathrm{d}\mathbf{k}_4\, \mathrm{d}\mathbf{k}_5,\end{aligned} \tag{1.43}$$

where, for convenience, we denote $W^{\mathbf{k}_1,\mathbf{k}_2,\mathbf{k}_3}_{\mathbf{k}_4,\mathbf{k}_5,\mathbf{k}}$ as $W^{1,2,3}_{4,5,\mathbf{k}}$. In the same way as for the four-mode KE, the delta-functions $\delta^{1,2,3}_{4,5,\mathbf{k}}$ and $\delta(\omega^{1,2,3}_{4,5,\mathbf{k}})$ stand respectively for $\delta(\mathbf{k}_1 + \mathbf{k}_2 + \mathbf{k}_3 - \mathbf{k}_4 - \mathbf{k}_5 - \mathbf{k})$ and $\delta(\omega_1 + \omega_2 + \omega_3 - \omega_4 - \omega_5 - \omega_{\mathbf{k}})$.

#### Conserved quantities

Now that we have the full expression of the KE, we can have a look at its conserved quantities and see if the invariants of 1D-SHE found in section 1.1.2 are still conserved. To this end, we define an arbitrary quantity $\Psi$, with its $\mathbf{k}$-space density $\rho_{\mathbf{k}}$, such that

$$\Psi = \int_{\mathbf{k}} \rho_{\mathbf{k}} n_{\mathbf{k}} \mathrm{d}\mathbf{k}. \tag{1.44}$$

For the quantity $\Psi$ to be conserved, we can show that it implies a relation over its density $\rho_{\mathbf{k}}$ by computing $\dot{\Psi} = \int_{\mathbf{k}} \rho_{\mathbf{k}} \dot{n}_{\mathbf{k}} \mathrm{d}\mathbf{k}$. With the symmetries of interaction coefficient $W$, we get the condition

$$\Psi \text{ conserved} \Leftrightarrow \rho_{\mathbf{k}} + \rho_{\mathbf{k}_5} + \rho_{\mathbf{k}_4} - \rho_{\mathbf{k}_1} - \rho_{\mathbf{k}_2} - \rho_{\mathbf{k}_3} = 0 \text{ on the resonant manifold} \tag{1.45}$$

To check if the wave-action $\mathcal{N}$ and the total energy $\mathcal{H}$ are still conserved by the KE, we need to check whether their densities $\rho_{\mathbf{k}}$ verify the latter condition.

For the wave-action, we saw that it could be written as $\mathcal{N} = (2\pi/L)\int_{\mathbf{k}} |\hat{u}_{\mathbf{k}}|^2 \mathrm{d}\mathbf{k}$. Thus, the $\mathbf{k}$-space density is equal to $\rho_{\mathbf{k}} = 1$. It trivially verifies the condition (1.45) and the wave-action is indeed exactly conserved by the KE.

For the total energy $\mathcal{H}$, we find that only the quadratic energy $\mathcal{H}_2 = \sum_{\mathbf{k}} \mathbf{k}^2/2|\hat{u}_{\mathbf{k}}|^2$ can be expressed like $\Psi$ with a density $\rho_{\mathbf{k}} = \mathbf{k}^2/2 = \omega_{\mathbf{k}}$ which verifies condition (1.45) on the resonant manifold. That means that the KE only conserves the linear equation $\mathcal{H}_2$ and not the total energy $\mathcal{H}_2 + \mathcal{H}_4$. This can be understood with the assumption of weak non-linearity used to derive the KE. In weak WT, we assume $\mathcal{H} \simeq \mathcal{H}_2$ and we denote this approximate value as $E$ in this context,

$$E = \int_{\mathbf{k}} \omega_{\mathbf{k}} n_{\mathbf{k}} \mathrm{d}\mathbf{k}. \tag{1.46}$$

This energy $E$ defines the energy density $E^{(1\mathrm{D})}_{\mathbf{k}} = \omega_{\mathbf{k}} n_{\mathbf{k}}$.

### 1.3.4 Steady states : Rayleigh-Jeans and Kolmogorov-Zakharov spectra

The integral on the Right Hand Side (RHS) of the equation (1.43) is called the collision integral. A wave-action spectrum $n_{\mathbf{k}}$ which makes this collision integral null is a stationary solution of the KE. There are two main types of stationary spectra, the thermodynamic equilibrium and the Kolmogorov-Zakharov (KZ) spectrum.

In a steady state, all the energy injected in the system is dissipated, which implies that the energy dissipation rate is equal to the energy injection rate. The same reasoning works for the wave-action.

#### Rayleigh-Jeans spectrum

The thermodynamic equilibrium is a state in which all modes have defined energy or wave-action without any net exchange between them. Thus, there are no fluxes of energy nor wave-action. The corresponding wave-action spectrum is called the Rayleigh-Jeans (RJ) spectrum,

$$n^{\mathrm{RJ}}_{\mathbf{k}} = \frac{1}{\omega_{\mathbf{k}} + \mu} \tag{1.47}$$

with $\mu$ being the equivalent of the chemical potential and $\omega_{\mathbf{k}} = \mathbf{k}^2/2$ for the equations we study. This spectrum corresponds to the equipartition of an invariant with the $k$-space density $\omega_{\mathbf{k}} + \mu$.

Such a spectrum is physically unmeaningful in a system unbounded in $k$-space because it implies an infinite total energy, as the integral of $n^{\mathrm{RJ}}_{\mathbf{k}}$ diverges at $k \to \infty$. This problem is called the "Ultraviolet Catastrophe", in reference to the similar divergence of the classical spectrum proposed to explain the black body radiation. This problem can be solved by a cut-off at large $k$ [50] [51]. However, RJ spectrum can be considered for a finite zone of the $\mathbf{k}$-space, removing the problem of the divergence at $k \to \infty$. It can

occur near a dissipative scale when the dissipation is not large enough to compensate the forcing and waves accumulation. With this bottleneck effect, the energy tends to locally thermalize, which creates a spectrum close to the RJ spectrum.

### Kolmogorov-Zakharov spectrum

In 1965 [52], Zakharov found mathematically a new type of statistically steady but *non-equilibrium* states, the Kolmogorov-Zakharov (KZ) spectra, defined by a conserved quantity of the system cascading through scales with a constant flux. It is precisely these fluxes which put the system out of equilibrium. KZ spectra are named after the spectrum found by Kolmogorov in 1941 [40] for hydrodynamics, regarded the strong parallel between these two spectra.

A system with $N$ sign-definite invariants will have $N$ KZ spectra. The 1D-SHE conserves the total energy, the wave-action and the impulsion. However, the latter is not of a constant sign while energy and wave-action are always positive. Hence, only quadratic energy and wave-action do cascade on KZ spectra.

When one invariant is transferred through scales on a KZ spectrum, the other invariants do not cascade, their fluxes are null. For instance, in a system with a dual cascade of energy and wave-action, like the 1D-SHE, the Fjørtoft argument (detailled in next section 1.3.4 predicts that energy will cascade from the forcing scale to be dissipated at large $k$, while the wave-action will be dissipated at low $k$. This will be realised by a KZ spectrum when such a KZ spectrum is physically viable (see section 1.4.4 regarding the locality of the KZ spectrum). In between the forcing and the high $k$-dissipation scales, in the so-called *direct cascade inertial range* where energy is cascading, the steady-state spectrum will be the KZ spectrum for the energy cascade. The flux of wave-action will be null on this spectrum. Conversely, in the lower $k$- *inverse cascade inertial cascade*, the spectrum will be the KZ wave-action cascade spectrum, on which the energy flux is null. KZ spectra can be observed in systems forced at a given scale and dissipating at another scale, exactly like in the Kolmogorov theory.

Let us define important quantities which characterize a KZ spectrum. For a dual cascade of energy and wave-action (for instance), we define $P_k = P(k)$ and $Q_k = Q(k)$ respectively as the energy and the wave-action fluxes. In the isotropy assumption, these fluxes depend on the norm $k$ and not the vector $\mathbf{k}$. These fluxes follow the conservation laws with the energy and wave-action spectra

$$\partial_t\Big(\omega_{\mathbf{k}} n_{\mathbf{k}}(k)\Big) + \partial_k P_k = 0 \tag{1.48a}$$

$$\partial_t n_{\mathbf{k}}(k) + \partial_k Q_k = 0, \tag{1.48b}$$

for which we have used the expression of the energy density $E^{(1\mathrm{D})}_{\mathbf{k}} = \omega_{\mathbf{k}} n_{\mathbf{k}}$ defined in (1.46). Particularly, relations (1.48a) and (1.48b) imply that, for the cascade of a given

conserved quantity, the corresponding flux is independent from $k$.

If a system is forced in the middle of the available modes, the dissipation can occur either at big $k$ or at small $k$. For a system which is defined by two conserved quantities, like the 1D-NLSE or the 1D-SHE with energy and wave-action, one needs to find where each quantity is dissipated. The Fjørtoft argument answers this.

**The Fjørtoft argument**

The original Fjørtoft argument [42] is an *ad absurdum* argument which gives the direction of cascade for each quantity. We will present it for a dual cascade for simplicity but the Fjørtoft argument is not limited to two invariants cascading, see [53] for example of triple cascade.

When the system has reached a steady state, all the energy put in the system is dissipated, thus, $\int P_k \mathrm{d}k = 0$. Equivalently, $\int Q_k \mathrm{d}k = 0$. We assume that the system is forced in some modes around a particular one $k_f$ in the middle of the $k$-range. Energy and wave-action enter the system at $k_f$, at rates $P_f$ and $Q_f$ respectively. Let us assume that both quantities can be dissipated in two different parts of the spectrum, there exists dissipation in small scales at $k_- \ll k_f$ and at large scales at $k_+ \gg k_f$. The dissipation rates are respectively $P_-, Q_-$ and $P_+, Q_+$, with $P_f = P_- + P_+$ and $Q_f = Q_- + Q_+$. With these assumptions, there are two different ranges in $k$-space for the energy and wave action to be spread from the forcing scale to (at least one) dissipation scale. In these ranges, called *inertial ranges*, we also assume, like Kolmogorov, that neither forcing nor dissipation occur. If the system is weakly non-linear (to allow KZ cascades), fluxes verify $P_k \simeq \omega_{\mathbf{k}} Q_k \simeq Q_k \mathbf{k}^2/2$.

If wave-action was dissipated at $k_+$, at a rate comparable to the injection rate $Q_f$ because the system is in steady state, that would correspond to an energy dissipation rate equal to $1/2k_+^2 Q_f$. However, the energy injection rate was $1/2k_f^2 Q_{\{}$ which is smaller than the dissipation rate due to the condition $k_f \ll k_+$. This is absurd, implying that the assumption of the wave-action being dissipated at $k_+$ is not possible and, thus, can only be dissipated at $k_-$ after an *inverse* cascade. With the same reasoning, we can show that the energy can only be dissipated at $k_+$. This represents a *direct* energy cascade. This dual cascade behaviour is illustrated Figure 1.7.

## 1.4 KZ spectra

To characterize a KZ spectrum, we need to find the expression wave-action spectra as function of $\mathbf{k}$. More precisely, these spectra are assumed to be self-similar, so we work with power-laws ansatz $n_{\mathbf{k}} = Ck^x$, with a constant $C$ and where the exponent $x$ needs to be determined. Finally, we make the assumption of isotropy, so that the system only depends on the amplitude $k$. We present here two methods to obtain the KZ prediction : from the KE itself and from dimensional analysis.

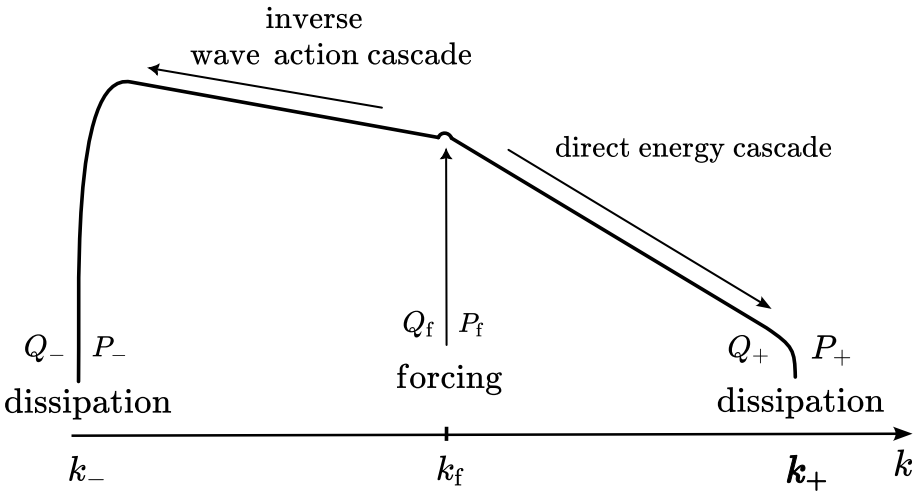


Figure 1.7: **Illustration of the dual cascade** - If the forcing occurs in the middle of the $k$-space, then a dual cascade will develop, with an inverse wave-action cascade and a direct energy cascade.

### 1.4.1 KZ spectra by Zakharov Transform

The Zakharov Transform (ZT) is a mathematical method to obtain the KZ prediction for a given KE, in our case the six-modes KE (3.10). This method relies on the interaction coefficient being *scale invariant*. Mathematically, that means that

$$W(\lambda\mathbf{k}_1, \lambda\mathbf{k}_2, \lambda\mathbf{k}_3, \lambda\mathbf{k}_4, \lambda\mathbf{k}_5, \lambda\mathbf{k}) = \lambda^\gamma W(\mathbf{k}_1, \mathbf{k}_2, \mathbf{k}_3, \mathbf{k}_4, \mathbf{k}_5, \mathbf{k}), \quad \forall\lambda \in \mathbb{R}. \tag{1.49}$$

If such a $\gamma \in \mathbb{R}$ exists, it is called an *homogeneity coefficient*. The ZT method also requires the scale invariance of the linear dispersion relation $\omega_k$

$$\omega(\lambda\mathbf{k}) = \lambda^\alpha \omega(\mathbf{k}) \tag{1.50}$$

with $\alpha$ the homogeneity coefficient. For the dispersion relation $\omega_\mathbf{k} = \mathbf{k}^2/2$ we have $\alpha = 2$. We will take a power-law ansatz for the spectrum $n_\mathbf{k} = Ck^x$ with $C$ a constant and $x$ the exponent to find.

We will separate the KE into six integrals and perform different changes of variables in five of them. We will show the computations for we change of variable and generalize its result. In one sixth of the collision integral, we will perform the following change of variable $\mathbf{k}_i \to \tilde{\mathbf{k}}_i$

$$\mathbf{k}_1 = \frac{\mathbf{k}\tilde{\mathbf{k}}_1}{\tilde{\mathbf{k}}_3}, \ \mathbf{k}_2 = \frac{\mathbf{k}\tilde{\mathbf{k}}_2}{\tilde{\mathbf{k}}_3}, \ \mathbf{k}_3 = \frac{\mathbf{k}^2}{\tilde{\mathbf{k}}_3}, \ \mathbf{k}_4 = \frac{\mathbf{k}\tilde{\mathbf{k}}_4}{\tilde{\mathbf{k}}_3}, \ \mathbf{k}_5 = \frac{\mathbf{k}\tilde{\mathbf{k}}_5}{\tilde{\mathbf{k}}_3}. \tag{1.51}$$

with the Jacobian $J = -\left(\frac{\mathbf{k}}{\tilde{\mathbf{k}}_2}\right)^6$.

The computations are detailed in [3] and we here only give the result, as one example of ZT will be detailed section 3.4.

$$\begin{aligned}\frac{\partial n_{\mathbf{k}}}{\partial t} &= C^5 4\pi \int |W^{1,2,3}_{4,5,\mathbf{k}}|^2 \; \delta^{1,2,3}_{4,5,\mathbf{k}} \; \delta\left(\omega^{1,2,3}_{4,5,\mathbf{k}}\right) {k_1}^x {k_2}^x {k_3}^x {k_4}^x {k_5}^x k^x \\ &\times \left[1 + \left(\frac{k_5}{k}\right)^y + \left(\frac{k_4}{k}\right)^y - \left(\frac{k_1}{k}\right)^y - \left(\frac{k_2}{k}\right)^y - \left(\frac{k_3}{k}\right)^y\right] \\ &\times \left[k^{-x} + {k_5}^{-x} + {k_4}^{-x} - {k_1}^{-x} - {k_2}^{-x} - {k_3}^{-x}\right] \mathrm{d}\mathbf{k}_1 \mathrm{d}\mathbf{k}_2 \mathrm{d}\mathbf{k}_3 \mathrm{d}\mathbf{k}_4 \mathrm{d}\mathbf{k}_5\end{aligned} \tag{1.52}$$

with $y = -5x - 3 - 2\gamma$. We note than taking $y = 0$ or $y = -2$ cancels the corresponding square bracket. For $y = 0$ it is trivial and for $y = 2$ it comes by using $\delta(\omega^{1,2,3}_{4,5,\mathbf{k}})$ that ensures the frequency resonance. Hence, these values of $y$ cancel the collision integral. They give two values of $x$, the exponent of the wave-action spectrum, corresponding to the inverse wave-action cascade and to the direct energy cascade.

Consequently, with the assumption of the interaction coefficient being self-similar, we can compute the exponents of the direct and inverse cascades with the Zakharov Transform from the KE.

### 1.4.2 KZ spectrum by dimensional analysis

For a dimensional derivation of the spectrum of energy density $E^{(1\mathrm{D})}_{\mathbf{k}}$, we need to write down the dimensions of the parameters. First, we obviously have $[\mathbf{k}] = [l]^{-1}$. The dimension of the total energy of the system $E$ is equal by definition to that of its kinetic energy $E_c = \frac{1}{2}mv^2$. For an incompressible fluid, the density $\rho = \frac{m}{V}$ is constant. This suggests a change of units to have $\rho = 1$ without any unit, $m$ and $V$ having the same dimension $[l]^3$. With this, the dimension of $E$ is

$$[E] = \frac{[l]^5}{[t]^2} \tag{1.53}$$

The density of energy in $d$ dimensions $\frac{\mathrm{d}E}{\mathrm{d}V_d}$ defines the energy spectrum $E^{(1\mathrm{D})}_{\mathbf{k}}$ via $\frac{\mathrm{d}E}{\mathrm{d}V_d} = \int \mathrm{d}\mathbf{k} E^{(1\mathrm{D})}_{\mathbf{k}}$. For the dimensions, this gives

$$\frac{[E]}{[l]^d} = \left[E^{1\mathrm{D}}_k\right][l]^{-1} \Rightarrow \left[E^{(1\mathrm{D})}_k\right] = \frac{[l]^{6-d}}{[t]^2}. \tag{1.54}$$

As the energy spectrum $E^{(1\mathrm{D})}_{\mathbf{k}}$ and the energy flux $\varepsilon$ verify the energy conservation $\frac{\partial}{\partial t}E^{(1\mathrm{D})}_{\mathbf{k}} + \frac{\partial}{\partial k}\varepsilon$, we have the dimension of $\varepsilon$ :

$$[\varepsilon] = \frac{[l]^{5-d}}{[t]^3}. \tag{1.55}$$

Up to now, the considered dimensions do not depend on the studied system. The particularity of a system will be set in its dispersion relation and in the nature of the resonant modes.

Let us consider a dispersion relation

$$\omega_{\mathbf{k}} = \lambda \mathbf{k}^{\alpha} \tag{1.56}$$

with $\lambda, \alpha$ real constants which characterize the system. This anzatz may seem too specific but it describes many systems, systems whose dynamics is qualitatively controlled by one dimensional parameter. We can list the capillary waves driven by the surface tension $\gamma$ ($\omega_{\mathbf{k}} = \sqrt{\gamma/\rho}\mathbf{k}^{\frac{3}{2}}$), the water gravity waves controlled by the gravitational acceleration $g$ ($\omega_{\mathbf{k}} = \sqrt{g}\mathbf{k}^{\frac{1}{2}}$), the Kelvin waves in superfluids driven by the quantum of circulation $\kappa$ ($\omega_{\mathbf{k}} = \kappa\mathbf{k}^2$ linearized), ...

$\lambda$ can play the role of the important dimensional parameter and its dimension is given by

$$[\lambda] = \frac{[l]^{\alpha}}{[t]^{1}}. \tag{1.57}$$

The system is also characterized by the resonant modes and particularly by the order of resonances $N$, *ie* the number of waves involved in the resonance. We assume that $N$ connects the energy flux $\varepsilon$ and the total energy $E$,

$$\varepsilon \sim \frac{\mathrm{d}}{\mathrm{d}t}\left(\frac{\partial}{\partial t}\right) E \sim E^{N-1}. \tag{1.58}$$

In the energy cascade (and its direction does not matter), the energy flux $\varepsilon$ is expected not to depend on $k$. Then, the $k$- dependence must come from an explicit $k$ term. Finally, the spectrum must depend on $\lambda$ which represent the particularity of the system.

We can now express the KZ energy spectrum $E_{\mathbf{k}}^{(1\mathrm{D})}$ as powers of $k$ and $\lambda$,

$$E_{\mathbf{k}}^{(1\mathrm{D})} = \varepsilon^{\frac{1}{N-1}} k^{x} \lambda^{y}, \tag{1.59}$$

and obtain the powers $y$ and $x$ with the dimensional analysis and the equations (1.57) and (1.58). We obtain

$$x = d - 6 + 2\alpha + \frac{5 - d - 3\alpha}{N-1} \qquad y = 2 - \frac{3}{N-1}. \tag{1.60}$$

Spectrum (1.60) implies that we can predict an energy KZ spectrum for a system from no more than the numbers of dimensions $d$, the order of interaction $N$ and the characteristics $\lambda, \alpha$ of the dispersion relation.

The same reasoning goes for the wave-action cascade (or the other quantity cascading, no matter its direction), the only change being the dimension of the (wave-action) flux $\eta$

$$[\eta] = \frac{[\varepsilon]}{[\omega]} = \frac{[l]^{5-d}}{[t]^{2}}. \tag{1.61}$$

The dimensional analysis gives

$$E_{\mathbf{k}}^{(1\mathrm{D})} = \eta^{\frac{1}{N-1}} k^{X} \lambda^{Y}, \tag{1.62}$$

$$X = d - 6 + \frac{5 - d + 3\alpha(N-2)}{N-1} \qquad Y = 2 - \frac{2}{N-1} \ . \tag{1.63}$$

It is important to notice that spectrum (1.62) is the *energy* spectrum corresponding to the cascade of the conserved quantity *which is not the energy*. It will be more convenient to write the energy spectrum (1.62) as the energy of the actually cascading quantity. For instance, we remind that quadratic energy and wave-action spectra $E_{\mathbf{k}}^{(1D)}$ and $n_{\mathbf{k}}$ are linked by $E_{\mathbf{k}}^{(1D)} = \omega_{\mathbf{k}} n_{\mathbf{k}}$.

Another dimensional analysis can be performed once we have the expression of the fluxes $P(k)$ and $Q(k)$. We remember, for instance, the definition of the wave-action KZ spectrum which makes the wave-action flux independent of $k$. With the explicit formula for $P(k)$ depending on the wave-action spectrum $n_{\mathbf{k}}$, a dimensional analysis with a count of the powers of $k$ allows us to find the wave-action exponent $x$ which cancels the $k-$dependence. This this exponent $x$ would correspond to the wave-action KZ spectrum. This method will be used and detailed in section 3.4.

### 1.4.3 Applications of weak Wave Turbulence

Weak WT can be applied to a wide variety of dispersive non-linear systems.

#### Gravity-capillary waves

Gravity-capillary waves are the waves evolving at the free surface of a fluid. They are defined by the dispersion relation $\omega_{\mathbf{k}}^2 = \left(gk + \frac{\gamma}{\rho}k^3\right)\tanh(kh)$ with $g$ the gravitational field strength, $\rho$ the density of the fluid, $\gamma$ its surface tension and $h$ its depth. This dispersion relation gets simplified in two limits, in the capillary limit $\omega_{\mathbf{k}} = \sqrt{\gamma/\rho}\ k^{\frac{3}{2}}$, and in the gravity waves limit with $\omega_{\mathbf{k}} = \sqrt{gk}$. In these two limits, the waves are dispersive and the system is non-linear given the hydrodynamics.

For capillary waves, if we use notations of the dimensional derivation section 1.4.2, we have $d = 2, N = 3, \alpha = \frac{3}{2}$ and $\lambda = \sqrt{\gamma/\rho}$. These values give the Zakharov-Filonenko spectrum for the direct energy cascade [54], [55]

$$E_{\mathbf{k}}^{(1D)} = C_0\ \varepsilon^{\frac{1}{2}}(\gamma/\rho)^{-\frac{1}{4}}k^{\frac{7}{4}}. \tag{1.64}$$

This spectrum can also be derived from the 3-modes KE [56]. It has been verified numerically [57] and experimentally [33].

The KE of water waves has been written first by Hasselman in 1967 [58] and implies 4-modes resonances. A KZ spectrum, the Zakharov-Filonenko [54] has been derived from this KE. This spectrum has been observed experimentally first in 1972 [59] and numerically [32] . We can notice than the dimensionally-derived energy spectrum ($\sim \omega^{-5}$ by Philips in 1958 [60] differs from the Zakharov-Filonenko spectrum in $\omega^{-4}$).

**Internal waves**

Internal waves are a crucial mechanism for the mixing of seas and the transport of heat. First energy spectrum for internal waves has been proposed by Garrett and Munk in 1975, [61] [34], with the hypothesis of horizontal isotropy. This spectrum links the vertical and the horizontal wave-vectors and can be written as a function of the frequency and one of these wave-vectors. WT formalism has been applied to internal ocean waves to obtain a KE with 3-modes interactions, [62] [63]. Such 3-modes interactions have been observed in stratified media by Davis et al. [64]. It appeared that the short-wave Garrett-Munk spectrum corresponds to the KZ spectrum derived from the KE with KZ transform [63].

**Kelvin waves**

WT can also be applied to Kelvin waves propagating in superfluids like Helium. In superfluids, the waves responsible for the cascades are supported by vortex filaments. Such waves are called Kelvin waves and their interaction via six-mode resonances. Their spectrum has been obtained via dimensional analysis and verified numerically by Kozik and Svistunov [65] [66]. While it has also been observed by Boffetta et al. [35], the Kozik-Svistunov spectrum appeared to be non-local and thus, unphysical [48]. Superfluid turbulence is governed by the Biot-Savart equation.

### 1.4.4 Locality of KZ spectra

KZ predictions assume the locality of the interactions. This implies resonances between wave-vectors close to each other. This supports the idea of cascade; the excited wave-vectors will transfer energy to neighbouring wave-vectors and so on, on a continuous process. Such interactions are called *local*. This is to be compared to the hydrodynamical vortices of Richardson which create slightly smaller vortices. By contrast, non-local interactions involve wave-vectors well separated in the Fourier space.

Mathematically, locality corresponds to the convergence of the KE in both $k \to 0$ and $k \to \infty$ limits [3]. If there is a divergence in one of these limits for a KZ spectrum, it implies that this spectrum can not occur in real systems. KZ spectra can be derived for many weak WT systems but this does not mean that these spectra are physical. For instance, the Kozik-Svistunov spectrum derived for Kelvin waves, spectrum $E_k \sim \kappa^{\frac{7}{5}} \epsilon^{\frac{1}{5}} k^{-\frac{7}{5}}$ [65] (with $\kappa$ the quantum of circulation) was found to be non physical as the KE diverges in the IR limit [48]. This problem can be solved with a log correction [25].

# CHAPTER 2

# Propagation of coherent structures into the SHE

## 2.1 Introduction

Now that we have defined the concepts of solitons and integrable (or not) equations, we can introduce some concepts which will be at the core of our work for this chapter.

The Modulation Instability (MI) is the evolution, of a slightly-perturbed condensate, under a non-linear equation which tends to create localized structures from this uniform initial state. The MI is a linear instability corresponding to the growth rate of certain modes being positive. The created localized structures grow until saturation, when the non-linear physics becomes more important than the linear. This particular behaviour is proposed to explain the appearance of extreme events. For instance, the special case of Benjamin-Feir instability [67] [68] for gravity water waves was found out as an explanation for the rogue waves [69]. Experimental evidences of MI were also found in non-linear optical systems [70].

The concept of Soliton Gas (SG) was proposed by Zakharov in 1971 [71] with the idea of an ensemble of solitons (for a given non-linear equation) weakly interacting. This corresponds to a rarefied gas, with a small density of solitons, mostly non-overlapping. This definition has been generalized more recently to dense gases with overlapping and strongly interacting solitons [13]. Links have been found between solitons gas and hydrodynamics, making the soliton gas an interesting object of study. An $N$-Soliton Gas can be constructed with the DST/IST method and more precisely with the dressing method [7], the characteristics of the solitons are defined by the values chosen for the discrete spectrum. A recent achievement of the soliton gas model is the is a possible explanation of the MI final state with a SG made of 128 solitons [72].

A soliton gas in an integrable systems, like the 1D-NLSE, evolves with elastic collisions imposed by the integrability of the equation. The solitons' positions and phases can change but their number, amplitudes and speeds are constant. Richer dynamics are

obtained for non-integrable equations. As we mentioned when discussing solitary waves in the 1D-SHE, non-integrable systems can exhibit localized structures created by the balance between dispersion and focusing non-linearity and which propagate without alteration of their profile. However, collisions between such structures are non-elastic and, thus, the system does not conserve the number of structures through its evolution. This evolution of many localized structures in non-integrable systems exhibit an interesting final state. It has been observed by Zakharov et al. [73] that this final state is a unique large localized structure propagating on top of a weak gaussian field of random linear waves. Their first numerical evidence has been obtained for different potentials in the focusing 1D-NLSE, making the equation non-integrable. Since then, this particular final state has been observed in non-linear optics experiments and numerics [74] [5].

Let us make a terminology point. The term *solitons* is restricted to solutions of integrable non-linear equations which propagate with a constant shape and collide elastically. The numerous studies of non-integrable systems showed the existence of propagating localized structures in such systems, but we can not name them solitons. Besides, it is the very fact that these structures do not collide elastically which provides the final structure. For the following of this work, they will be referred to as *quasi-solitons*, to illustrate their obvious similarity with the pure solitons. Then, the study of localized structures interacting in a non-integrable equation will be denoted as *quasi-soliton turbulence* (qST) in our work.

Thermodynamic and statistical arguments were proposed to describe this final organization into a super quasi-soliton [75] [76]. This final super quasi-soliton acts like a statistical attractor for the system by minimizing locally the energy with the weak waves ensuring the conservation of the total energy. This gaussian field is necessary to increase the entropy of the initial field, as the transformation of all the waves into a localized structure corresponds to a decrease of the disorder.

The qST has been extensively studied for different potentials $V(|u|)$ for focusing 1D-NLS-type equations

- $V(|u|) = |u|$ in [77] [73],
- $V(|u|) = (1 - a|u|^2)/(1 - b|u|^2),\ a, b \in \mathbb{R}$ in [73]
- $V(|u|) = (1 + \beta\partial^2/\partial x^2)|u|^2$ and $(\beta\partial^2/\partial x^2)^{-1}$ in [5].

In this chapter, we study the potential, derived from non-linear optics,

$$V(|u|, \beta) = \left(1 - \beta\frac{\partial^2}{\partial x^2}\right)^{-1}|u|^2 \tag{2.1}$$

which defines the SHE (1.22). As said earlier, this equation is non-integrable for $\beta > 0$ and, thus, can exhibit quasi-Soliton Turbulence (qST) features. This qST evolution will be examined with different types of initial conditions and characterized with two diagnostics, the DST and spatio-temporal spectra. These diagnostics are detailed section 2.2.

Firstly, we observe the proper qST behaviour by setting initial energy in only a few Fourier modes and letting the system evolve without forcing nor dissipation. Under some conditions, its evolution leads to a final localized structure which will be characterized. This qST behaviour is allowed by the interactions between localized structures which are not elastic, due to the non-integrability of the SHE. This evolution is reported in section 2.3. Given that, we next study these collisions by initializing the system as two 1D-SHE solitary waves (section 2.4) and then 1D-NLSE solitons (section 2.5). This allows us to examine the collisions between the localized structures of the SHE and to draw some conclusions about their final state.

Finally, in section 2.6, we analyse precisely the localized structure that appears during the evolution of the initial flat top spectrum. This is done by launching a single 1D-NLSE soliton into the conservative 1D-SHE system and following its characteristics with the diagnostics specified above. This simulation is performed at different non-integrability factor $\beta$ to conclude over the importance of the non-integrability in the reported observations.

## 2.2 Numerical strategy and diagnostics

### 2.2.1 Integration of the 1D-SHE

The 1D-SHE

$$i\frac{\partial}{\partial t}u + \frac{1}{2}\frac{\partial^2}{\partial x^2}u + u\left(1-\beta\frac{\partial^2}{\partial x^2}\right)^{-1}|u|^2 = 0 \tag{2.2}$$

will be integrated numerically over a a periodical box of length $L = 2\pi$ divided in $N_x = 4096$ points (sometimes, $N_x = 2048$ where stated) corresponding to $x$-discretization $\Delta x = L/N_x = 1.5 \times 10^{-3}$ (or $\Delta x = 3 \times 10^{-3}$ for $N_x = 2048$). Such values of $L$ and $N_x$ also determine $\Delta k = 2\pi/L = 1$ and $k_{\max} = \Delta k N_x/2 = 2048$ (1024 for $N_x = 2048$).

To deal with the non-linearity, we chose a pseudo-spectral method [78] [79] for the integration scheme. This scheme integrates the equation in Fourier space with a particular caution for the non-linear term. In order to avoid the expensive convolutions, the multiplications in the non-linear term are done back in the physical space. An three-halves anti-aliasing procedure [80] is applied to prevent the apparition of un-physical modes with the multiplications in real space. We implemented a fourth-order exponential time-differencing Runge-Kutta method [81] with a time step denoted $\Delta t$. $\Delta t$ is chosen sufficiently small so that the fastest resolvable wave packet does not cross more than one grid point between two timesteps. This is equivalent to the Courant-Friedrichs-Lewy (CFL) condition

$$\Delta t < \frac{\Delta x}{\max_k v_g} \tag{2.3}$$

with $v_g = \mathrm{d}\omega_{\mathbf{k}}/\mathrm{d}\mathbf{k}$ the group velocity. This condition ensures that the fastest group velocity in the system is well-resolved. With the dispersion relation $\omega_{\mathbf{k}} = \mathbf{k}^2/2$, the upper limit of $\Delta t$ is $\Delta x/k_{\max} = 2L_x/N_x^2 = 7.49 \times 10^{-7}$ ($3 \times 10^{-6}$ for $N_x = 2048$). Then, to satisfy the

CFL-like condition we choose $\Delta t = 5\times10^{-7}$ for $N_x = 4096$ ($\Delta t = 1\times10^{-6}$ for $N_x = 2048$).

Another way to verify that the $\Delta t$ used is appropriate is the conservation of the total energy $\mathcal{H}$ and the wave-action $\mathcal{N}$. If we do not add forcing nor dissipation terms to equation (2.2), this system is conservative. With the choice of $\Delta t$ explained previously, the values of $\mathcal{H}$ and $\mathcal{N}$ are found to remain constant for both choices of $N_x = 4096$ or $N_x = 2048$. For instance, for $N_x = 4096$, their relative changes are smaller than $10^{-11}\%$.

### 2.2.2 Diagnostics

#### DST spectrum

As defined section 1.1.1, the DST spectrum contains notably a solitonic part made of a discrete set of eigenvalues and corresponding norming constants. These eigenvalues are computed from the matrix (1.5) and we use the Fourier collocation method to find them [82], [83], [13], [84]. This method is based on the Fourier expression of matrix (1.5) and, thus, decomposes the studied function $u(t_i, x)$ at a given time $t_i$ into $N_c$ Fourier spatial modes. Eigenvalues $\zeta_p$ are computed from a $2N_c$ matrix. The collocation method is pertinent for periodical systems and, thus, is adapted for the system we study. The used number of Fourier modes $N_c$ is determined from a balance between the precision and the computation time. We used $N_c = 513$ modes, after a convergence study to make sure that this number of modes gives accurate results for 1D-NLSE solitons.

The result of the collocation method is a set of $2N_c$ complex eigenvalues $\zeta_p = \zeta_p^{\mathrm{Re}} + i\zeta_p^{\mathrm{Im}}$ which are complex conjugate pairs. With this symmetry, we can consider only the eigenvalues with positive imaginary parts. For a soliton of the NLSE, its amplitude $A_p$ and speed $v_p$ are encrypted in the eigenvalue $\zeta_p$ with $A_p = 2\zeta_p^{\mathrm{Im}}$ and $v_p = -2\zeta_p^{\mathrm{Re}}$. These relations are illustrated schematically on an example spectrum Figure 2.1(a).

An important fact about the Fourier collocation is that it only computes the eigenvalues of the DST spectrum : it does not give access to either the norming constants nor to the continuous spectrum. Consequently, the Fourier collocation method can only access the number of solitons, their amplitudes, and their speeds. Solitons' phase and positions can not be determined with this method. The same goes for the wave components of the systems, encoded in the continuous spectrum. With the Fourier collocation we do not have the entirety of the DST spectrum so we can not reconstruct the function with IST. In our studies, DST is only used as a tool to characterize the soliton part of the system. Given that we can not access the rest of the spectrum, the term DST spectrum will always refer to the *discrete* DST spectrum in the following.

In the example of a DST output Figure 2.1(a), some eigenvalues are included in a grey area near to the real axis. This area defines a theoretical and numerical threshold : eigenvalues below this threshold can not be trusted as physical solitons. First, as we study a periodic system, we can not consider solitons whose width is comparable with the length of the box. If we denote $d$ the mid-height size of the soliton and $L = 2\pi$ the length of the box, we chose to eliminate solitons characterized by $d > \frac{1}{4}L$ to make sure that the solitons we consider are really contained in the box. With the characteristics of

a soliton, this maximal value for the width can be translated into a minimal value for the amplitude and, thus, for the imaginary part, namely $\zeta^{\mathrm{Im}} > T_{\mathrm{width}}$.

A threshold also can be determined from numerical considerations. The Fourier collocation method is known to create spurious eigenvalues with small imaginary part from the continuous spectrum due to the decomposition in Fourier modes [13] [83]. To identify these artificially created eigenvalues, we change the length of the function and look for the eigenvalues which change. For a function defined for $x \in [-L/2, L/2]$, we create two expanded functions with arrays of zero to create functions defined for $x \in [-3/4L, 3/4L]$ and for $x \in [-L, L]$ [13] [83]. We define a spectrum-based threshold $T_{\mathrm{spectrum}}$ above which all eigenvalues are the same for the spectra of the two functions, up to relative differences of 2.5%. The width-related threshold $T_{\mathrm{width}}$ only depends on the length $L$ of the box and can be used for every kind of initial conditions. For $L = 2\pi$, we have $T_{\mathrm{width}} = 1.1$. Inversely, $T_{\mathrm{spectrum}}$ is computed for each initial condition type. We always find $T_{\mathrm{spectrum}} \simeq 1.1$, meaning both thresholds are relevant. We would like to emphasize that, below $T_{\mathrm{width}} = 1.1$, the three DST spectra are qualitatively similar and only differs by small quantitative discrepancies.

There are other methods to compute the discrete DST spectrum, the main one being the Boffetta and Obsorne transfer algorithm which computes the whole scattering matrix and finds the spectrum as the zeros of the Jost function $a(\zeta)$ [85], [86]. This method is more complex than the Fourier collocation, however it is complete and provides the total DST spectrum with both discrete and continuous parts. We can also cite the Ablowitz-Ladik method [87] [88]. We use the Fourier collocation for its simplicity to implement and its speed.

It is important to notice than the equations of the DST presented section 1.1.1 were found to be applied to the pure 1D-NLSE only, which is different from the 1D-SHE that we study. So, from a strict theoretical point of view, we can not apply the presented DST to the 1D-SHE. However, there are some points which suggest its use to characterize our system. First, the 1D-SHE has been found non-integrable and, thus, it is not possible to find a Lax pair such as the one found for NLSE. Consequently, there is no DST theory made explicitly for the 1D-SHE. Secondly, the 1D-SHE can be seen as a non-integrable version of 1D-NLSE with the parameter $\beta$ controlling this deviation from integrability. For a sufficiently small $\beta$, the system can be considered as close to integrability and thus, we can expect consistent results from the DST analysis.

Even with these quantitative changes, we have carefully checked that the DST spectrum is in accordance with the function profile in the real space, as well as with the $(\mathbf{k} - \omega)$ plots (see below). The main difference between the DST spectra for the 1D-SHE and the 1D-NLSE is the isospectrality property which is not ensured for SHE, while it was for NLSE. The eigenvalues composing the DST spectrum of a function evolving with the 1D-SHE can move in the complex plane. This behaviour, consequence of the non-integrability of the 1D-SHE, will be interpreted as localized structures with time-evolving characteristics. However, it is important to notice that the computation of the DST spectrum requires the function $u(x, t_i)$ for a single time $t_i$. Thus, the DST algorithm does

not *know* the equation which governs the temporal evolution of $u$. If a pure sech-profile soliton, solution of the NLSE, appears during a non-integrable evolution, then the DST spectrum will contain only the corresponding eigenvalue. The problem of non-integrable equations is that pure sech-profile solitons will never appear because they are not solutions of the equation. Consequently, their non-zero vicinity will alter the DST spectrum. .

Finally, it is interesting to apply the DST to non-integrable systems because integrable systems are often approximations and neglect higher-order effects. For instance, dissipation, losses or Raman scattering, like in optical fibers, are not taken into account by integrable models. If we restrain our scope to integrable systems, we can not analyse data collected from real experiments, because a lot of experiments can not be described by integrable models. In the literature, we have examples of DST being applied to reals systems such as soliton gas in water tank [89], solitonic laser pulses in optical fiber [90] [91] or the modelling of a laser system [11].

### $(\mathbf{k}-\omega)$ spectrum

We can compare the results given by the DST with the Fourier analysis of the system with the basis function $e^{i(\omega t-\mathbf{k}x)}$. More precisely, we compute the spatio-temporal Fourier spectrum over a time window and represent this density $|\hat{u}(\mathbf{k},\omega)|^2$ on a $(\mathbf{k},\omega)$ plot. The structures expected in the system, solitons and waves, have a specific signature with this Fourier analysis. Thus, we can use these $(\mathbf{k}-\omega)$ plots to identify the main components in our function and obtain their characteristics.

Linear waves are represented by the linear dispersion relation $\omega_k$. For the SHE, we expect a parabola $\omega_{\mathbf{k}} = \mathbf{k}^2/2$ (white dashed line in FIGURE 2.1(b)). As the system is not linear, this parabola is altered by non-linear effects. A non-linear Bogoliubov correction shifts the parabola towards negative $\omega$ by a factor related to the squared amplitude of the function. Its precise expression is given as $\sum_{\mathbf{k},\mathbf{k}_1} T^{\mathbf{k},\mathbf{k}}_{\mathbf{k}_1,\mathbf{k}_1}|\hat{u}_{\mathbf{k}_1}|^2$ but will not be used in this thesis. As linear waves are represented by the parabola, slightly non-linear waves are localized closely around this parabola, making the dispersion relation wider (blue width in FIGURE 2.1(b).

Solitons signatures in $(\mathbf{k}-\omega)$ plots are straight lines with positions and slopes related to the solitons speeds and amplitudes. Each soliton gives a unique line and Fourier theory gives the position of this line center $(\mathbf{k}^* = v, \omega^* = \frac{v^2-A^2}{2})$, denoting $v$ and $A$ the soliton speed and amplitude. These values are obtained directly from the expression of the soliton (1.10) as $\omega^*$ is identified in the time-dependent phase term. Also, the slope of the straight is equal to the speed of the corresponding soliton, as illustrated FIGURE 2.1(b). 1D-SHE solitary waves are also represented by straight lines, for which the link between the slope of the line and the velocity of the structure stands. That means that with the $(\mathbf{k}-\omega)$ spectrum we can deduce the number of solitons, as well as their speeds and amplitudes. We use this method to double-check the results given by the DST in all our simulations. Note that this method does not allow us to recover their phases and positions.

The parameters of the time window used to compute the spatio-temporal spectrum

(a) Direct Scattering Transform Eigenvalues (b) Spatiotemporal $(k, \omega)$ Spectrum

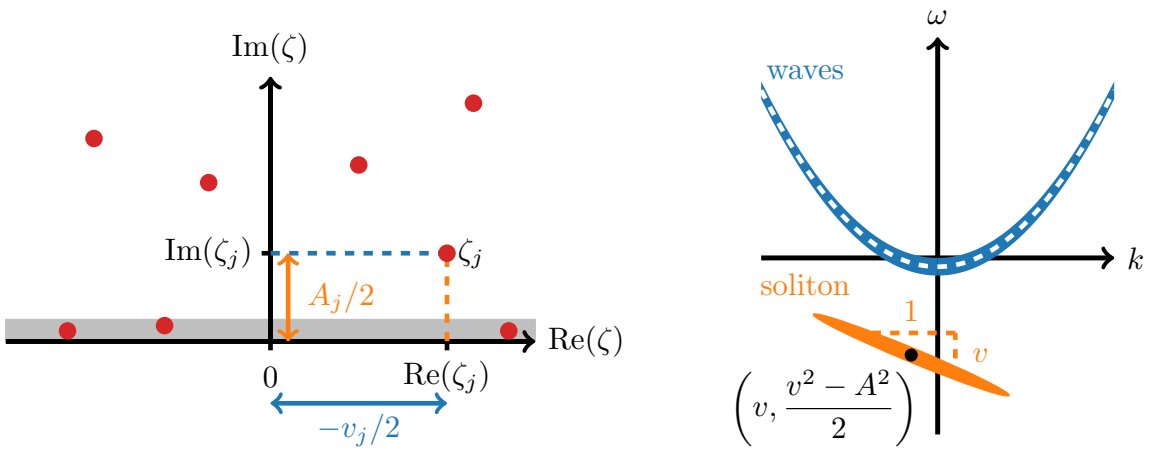


Figure 2.1: **Diagnostics used to characterize the numerical simulations -** (a) Example of a DST spectrum. Each eigenvalue (red dot) represents a soliton and its position in the complex plane defines the soliton amplitude (twice the imaginary part in the NLSE) and speed (minus twice the real part in the NLSE). The grey part box denotes the threshold, below which the eigenvalues are unphysical (soliton wider than the box or numerical artefacts). (b) Example of a $(\mathbf{k} - \omega)$ plot which contains signatures of linear waves (white dashed parabola), weakly non-linear waves (blue width of the parabola) and a soliton (orange straight line). The amplitude and speed of the soliton can be deduced from the characteristics of this line.

are crucial to identify the spectral signatures. These are the total time $T$ of this windows and the *output* time interval $dt_o$ between two times slices (note that it is not necessarily equal to the $dt$ of the numerical integration). $T$ and $dt_o$ determine important quantities of the $(\mathbf{k} - \omega)$ plot, the maximum frequency resolved $\omega_{\max} = 2\pi/(2dt_o)$ and the frequency precision $\Delta\omega = 2\pi/T$. The factor $1/2$ in $\omega_{\max}$ is added to take into account the Nyquist-Shannon sampling theorem. According to this theorem, to resolve a signal up to a frequency $f$ we need to sample it with a frequency $f_s$ which satisfies $f_s > 2f$. That implies that, sampling every $dt_o$, the biggest frequency resolved is $1/(2dt_o)$, which gives $\omega_{\max} = 2\pi/(2dt_o)$. This value of $\omega_{\max}$ gives $k_{\max} = \sqrt{2\omega_{\max}}$ with the dispersion relation. Therefore, for a sufficient precision we want a long time window with data output very frequently. However, that can create very big arrays and slow down the computation, a compromise needs to be found. Finally, we recall that $\Delta k = 1$ is fixed by the choice of $L = 2\pi$.

Contrary to the DST, the $(\mathbf{k} - \omega)$ spectra do not provide information for a given time but over a time window. Computing $(\mathbf{k} - \omega)$ plots for subsequent windows creates a movie which allows to visualize the time evolution of solitons. It has been observed in [5] that solitons created via Modulational Instability (MI) are found to peel off from the dispersion relation at a $k_s$ where the associated straight line is tangential to the parabola. That means that the speed of the created soliton is equal to the group speed of the wave, $\left.\frac{\mathrm{d}\omega_k}{\mathrm{d}k}\right|_{k_s} = v$.

## 2.3 Quasi-Soliton Turbulence

### 2.3.1 Initial Conditions

To study the quasi-Soliton Turbulence, we create an initial flat-top Fourier spectrum, as in [5],

$$\hat{u}_k = \begin{cases} \text{Amp } e^{i\varphi_{\mathbf{k}}} & \text{if } \ k \in [\![k_i - dk_i, k_i + dk_i]\!] \\ 0 & \text{else} \end{cases} \tag{2.4}$$

where $k_i$ and $dk_i$ stand respectively for the middle of the initially excited modes and $dk_i$ the half-width of the top-hat spectrum. Amp stands for the amplitude, equal for all the modes and $\varphi_{\mathbf{k}} \in \mathcal{U}([-\pi, \pi[)$ are the phases, by definition random. Notice that this spectrum is statistically symmetric in $\mathbf{k} \leftrightarrow -\mathbf{k}$ as the only difference between positive and negative $\mathbf{k}$ is the random phases. With a flat-top Fourier spectrum, the function in real space is initially a set of random waves of amplitude Amp and wave-vectors distributed around $k_i$.

To these initial conditions are attributed initial wave-action $\mathcal{N}$ and energies $\mathcal{H}_2, \mathcal{H}_4$ and $\mathcal{H} = \mathcal{H}_2 + \mathcal{H}_4$. For our box of length $L = 2\pi$ with $\Delta k = 1$, $\mathcal{N}$ is given by

$$\mathcal{N} = L \sum_{\mathbf{k}} |\hat{u}_{\mathbf{k}}|^2 = 4Lk_i \text{Amp}^2. \tag{2.5}$$

For the initial conditions (2.4), $\mathcal{N}$ does not depend on the mean position $k_i$ of these modes in the Fourier space. Conversely, the energy terms do depend on which modes are excited. For instance, the initial quadratic energy $\mathcal{H}_2$ is given by

$$\mathcal{H}_2 = \frac{1}{2} \sum_{\mathbf{k} \in \text{excited modes}} \mathbf{k}^2 \text{Amp}^2. \tag{2.6}$$

By changing $k_i$ while keeping $dk_i$ constant it is thus possible to change the total energy $\mathcal{H}$ while keeping the same wave-action $\mathcal{N}$. This is an important property as $\mathcal{H}$ and $\mathcal{N}$ will be constant in time, as conserved quantities of the 1D-SHE.

### 2.3.2 Numerical Results

We report FIGURE 2.2 the evolution of the 1D-SHE system for the initial conditions (2.4) with Amp $\simeq 2.8$, $k_i = 7.5$ and $dk_i = 1.5$. These values correspond the excited modes $6 \leq k \leq 9$, a total wave-action $\mathcal{N} = 400$ and the total energy $\mathcal{H} = -1192.5$. The box is here divided in 4096 grid points.

In the left panels, we plot the spatio-temporal dynamics of the system, first for small times $0 \leq t \leq 26$ and then for very large times $989 \leq t \leq 1000$. On its $t-$axis, four time intervals (a) to (d) of length $T = \pi$ are highlighted in white. The system is studied at these time intervals with the diagnostics, snapshot and DST spectrum (middle panels) and $(\mathbf{k} - \omega)$ spectrum (right panels). More precisely, for the time intervals (a) and (b), the snapshots and DST spectra are computed for only specified time while for (c) and

(d) they are showed for two different times of the interval to show the short-time evolution.

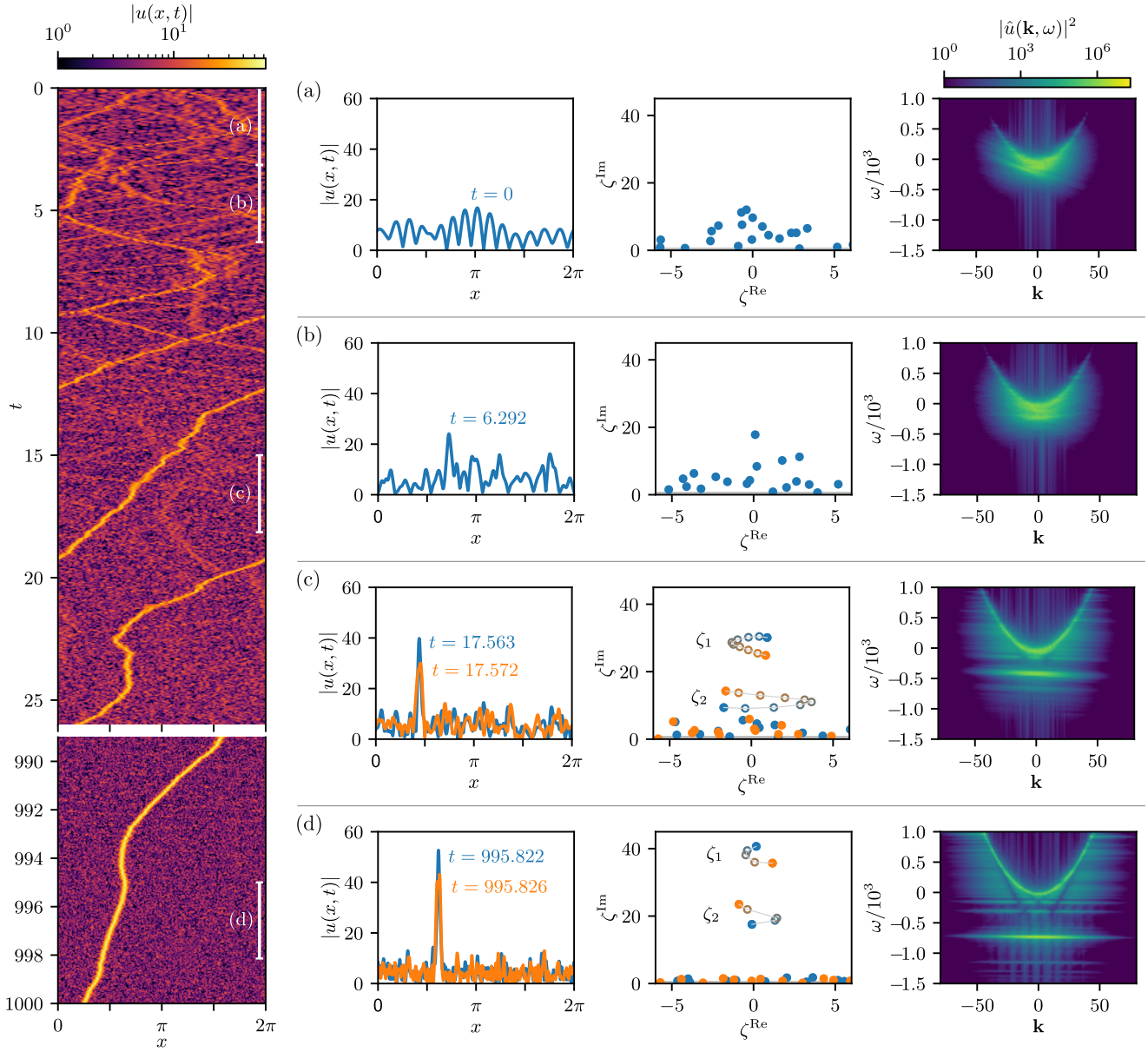


Figure 2.2: **Evolution of the 1D-SHE system for flat-top initial conditions** - The system is studied at different times with the DST and $(\mathbf{k}-\omega)$ spectra. The comparisons of these spectra with the $(x-t)$ plot shows the creation of one large isolated propagating structure, characterized by oscillating amplitude and width.

The initial function in the real-space, directly computed from the initial flat-top spectrum, and its DST spectrum are plotted in (a). The function is a superposition of random waves, as seen in the $|u|$ snapshot, however, the DST spectrum, computed for this initial condition, identifies quite a large number of solitons in the system corresponding to the eigenvalues above the threshold represented by the gray area. We stress that no solitons have been embedded in the initial conditions but some have been detected, as eigenval-

ues of the DST defined for the 1D-NLSE. In the complex plane which contains the DST spectrum, the eigenvalues "swarm" during time evolution, and do not keep a constant position. As the position of the eigenvalues are directly related to their corresponding solitons, this indicates that the solitons characteristics drastically change in time, which is contradictory with the definition of solitons in integrable systems. Given the abrupt changes of the DST spectrum and the absence of solitons traces in the $(x-t)$ plot (a), we assume that, in early times, there are no exact solitons in the system. However, in the $(x-t)$ dynamics we observe localized structures propagating and interacting, which may correspond to the eigenvalues obtained in the DST spectrum. It is important to notice than the eigenvalues stay grouped together and that no one grows alone in stage (a).

The system rapidly organizes itself in clearer and larger localized structures. As we clearly see in (b) for the time $t = 6.292$, the function has now four different recognizable structures in the $x$-space, with one remarkably larger than the three others. This situation is also seen on the DST spectrum, as four eigenvalues can be identified with the largest imaginary parts (this latter being proportional to the soliton amplitude in the DST framework for the 1D-NLSE). Besides, one eigenvalue is isolated in the complex plane with an imaginary part almost twice bigger than the other eigenvalues, corresponding to the biggest structure on the snapshot. These structures are solitons according to the DST and they are indeed visible on the $(x-t)$ plot, particularly during the time interval (b) where we can see two isolated structures propagating on top of a smaller one and waves. We highlight once again that, as the 1D-SHE is non-integrable, proper solitons can not be found in this system. Hence, localized structures will be referred to as *quasi*-solitons to, nonetheless, underline their localized propagation. We can notice that these quasi-solitons do not propagate in straight lines, as solitons normally do. Hence, with the presented system, we study indeed the quasi-Soliton Turbulence as defined in introduction 2.1.

The $(\mathbf{k}-\omega)$ plot 2.2(b) confirms the presence of linear waves with the parabola which can very modelled with a very good accuracy by the expected dispersion relation $\omega_{\mathbf{k}} = \mathbf{k}^2/2$ (model not plotted for clarity). We can also observe straight lines in the $\omega < 0$ region, as the spectral signature of the quasi-solitons. These lines are quite blurry because theirs slopes are supposed to be equal to quasi-soliton speeds, but these speeds are not constant. The minimum of the parabola contains a lot of energy which comes from the interaction between the linear waves and the quasi-solitons created. A movie of successive $(\mathbf{k}-\omega)$ spectra would show these straight lines going down in the $(\mathbf{k},\omega)$ plane, which corresponds to quasi-solitons growing. As observed in [5], the straight lines are peeling off from the dispersion relation.

Now that some quasi-solitons are clearly distinguishable from the wave background, they will collide numerous times in the periodic box. As said before, such collisions are not elastic because the 1D-SHE is not integrable. Consequently, colliding quasi-solitons can undergo changes of amplitudes and/or speeds. More importantly, the number of quasi-solitons is not fixed, some can disappear. The number of DST eigenvalues found by the collocation method is fixed but we mean that the number of eigenvalues above the threshold diminishes. Between the time intervals (b) and (c), the number of quasi-solitons

decreases because of these non-elastic collisions. Moreover, the amplitude of the biggest quasi-soliton keeps increasing as seen on the $(x-t)$ plot between (b) and (c). Comparing the snapshots of $|u|$ for close times in (c), we realise that the quasi-soliton amplitude changes in time. For the two times showed, the amplitude drops. We can also observe a change of its width, the quasi-soliton being wider while smaller. The actual evolution is an oscillation of the quasi-soliton between these two states, between tall-and-thin and small-and-wide. The analysis of the DST spectrum confirms this oscillation. We highlight in particular two eigenvalues with the two biggest imaginary parts, $\zeta_1 = \zeta_1^{\mathrm{Re}} + i\zeta_1^{\mathrm{Im}}$ and $\zeta_2 = \zeta_2^{\mathrm{Re}} + i\zeta_2^{\mathrm{Im}}$, such that $\zeta_1^{\mathrm{Im}} > \zeta_2^{\mathrm{Im}}$. Their evolutions between the two times are given by the dots with the progressive colors (only shown for these two eigenvalues). The corresponding trajectories in the complex plane are highlighted by gray lines. For simplicity we only plot a half of the periodical behaviour. For the rest of the thesis, comparing the eigenvalues, such as in "biggest eigenvalues" explicitly refers to comparing their imaginary parts.

With this detailed evolution, we understand that the two different states of the quasi-soliton are characterized by two qualitatively different DST spectra. When the quasi-soliton is tall and thin, $\zeta_1$ and $\zeta_2$ are the most separated, $\zeta_1^{\mathrm{Im}}$ is at its maximum while $\zeta_2^{\mathrm{Im}}$ is at its minimum, and conversely when the quasi-soliton is small and wide. The precise time evolutions of $\zeta_{1,2}^{\mathrm{Im}}$ is plotted FIGURE 2.5(a) and will be analysed in the coming paragraphs. As we will show, $\zeta_1^{\mathrm{Im}}$ and $\zeta_2^{\mathrm{Im}}$ oscillate in phase opposition, as do $\zeta_1^{\mathrm{Re}}$ and $\zeta_2^{\mathrm{Re}}$.

Similarly to the DST spectrum, the $(\mathbf{k}-\omega)$ spectrum also changes qualitatively between (b) and (c). The parabola for linear waves is still present but the quasi-solitonic trace is now a set of three parallel lines centered around a main one near $\omega = 400$. This main line is surrounded by two weaker lines with the same slope, with a considerable drop of energy between the main and the secondary lines. The considered slope is measured and appears to be indeed equal to the mean speed of the quasi-soliton during the time interval, such as it is expected for soliton in the 1D-NLSE. Lines with the same slope are also visible decorating the linear dispersion relation, standing for the non-linear interactions between the linear waves and the quasi-soliton. We recall that such interactions are made possible by the non-integrability of the 1D-SHE . There is one such decoration for each resolved $\mathbf{k}$. Noting that $\Delta k = 1$ in our simulation, we suggest this could be a finite-size effect. We predict that in an infinitely resolved system, this effect would manifest as a non-linear broadening of the linear dispersion relation.

In the (c) region of the $(x-t)$ plot, we still find some low-amplitude structures propagating. During the time evolution between (c) and (d), these small structures have disappeared through non-elastic collisions with the big oscillating quasi-soliton. Notice that the time interval between (c) and (d) is considerably larger than between (b) and (c). In (d), the oscillating quasi-soliton propagates alone on top of the small wave background, with a larger (mean) amplitude than in (c). This can be seen in the comparison of snapshots for close times. This average increase appears in the DST spectrum as an average increase of the imaginary parts $\zeta_{1,2}^{\mathrm{Im}}$. The time evolution of the latter is qualitatively the same as in (c), but with oscillations around a larger mean value. Indeed, the quasi-soliton still has two *extreme states*, tall-and-thin with two main eigenvalues spread

in their imaginary parts and shorter and wider with the two eigenvalues closer. Note that the oscillations of these eigenvalues happen far above the threshold, suggesting that this indeed represents a physical behaviour. Another important result from the comparison of DST spectra of (c) and (d) is the the growth of the two biggest eigenvalues which have risen in the complex plane, while all the other eigenvalues have significantly reduced. Now, the other eigenvalues lie down in the threshold region, meaning that they are not physically recognisable within the box.

The same observation can be made for the $(\mathbf{k}-\omega)$ spectrum of (d), the region $\omega < 0$ is still dominated by a main line and two surrounding parallels ones but one can also notice tertiary lines, still with the same slope, particularly visible near the parabola. Moreover, two straight lines of energy depletion cut these parallel lines in the extension of the dispersion relation. As yet, we have no explanation for this phenomenon. Finally, comparing the four $(\mathbf{k}-\omega)$ spectra, one can remark that the parabola corresponding to weakly nonlinear waves goes to higher and higher $k$ as the system evolves. This corresponds to large-$k$ waves appearing in the system, as a consequence of inverse cascade. This excitation of large-$k$ waves can be verified by comparing the snapshots of $|u|$.

### 2.3.3 Study of the final state

It appears from the study of the evolution of the system that the final state of an ensemble of quasi-solitons in the 1D-SHE is a single oscillating quasi-soliton, characterized by oscillating eigenvalues in the DST spectrum and parallel lines in $(\mathbf{k}-\omega)$ spectrum.

To verify that the parallel lines are indeed the signature of the final quasi-soliton, we can separate these structures from the linear waves background by filtering the $(\mathbf{k}-\omega)$ spectrum for the steady state in the time interval (d) of the FIGURE 2.2. Isolating the parabola and then performing a double inverse FT, we should recover the wave field in the real space. Similarly, taking only the parallel lines, lying below the dispersion relation, is expected to give the dominant coherent structure. Here, *coherent* means that the structure keeps its coherence by staying localized during the propagation. Due to the non-linear correction to the linear dispersion relation, the filtering will not be done around $\omega = 0$ but around $\omega = -40$. Finally, the filterings will be done by taking only a non-inclined rectangle in the $(\mathbf{k}-\omega)$ plot, *ie* only $\omega^- < \omega < \omega^+$ for all $\mathbf{k}$. The results of these filterings are presented FIGURE 2.3.

If we isolate the part of the spectrum corresponding to $\omega \leqslant -40$, the double inverse FT gives the $(x-t)$ of a function we call $u_{\text{coh}}(x,t)$, the coherent part of $u$, and which contains the quasi-soliton, proving that the three parallel lines in the $(\mathbf{k}-\omega)$ spectrum are indeed its spectral signature. Indeed, the obtained function is made of a localized structure oscillating in width and in amplitude, signifying that these characteristics are encoded in the parallel lines. Moreover, its trajectory is exactly the same as the quasi-soliton of the full function.

We also verify explicitly that the main and secondary lines in the $(\mathbf{k}-\omega)$ spectrum,

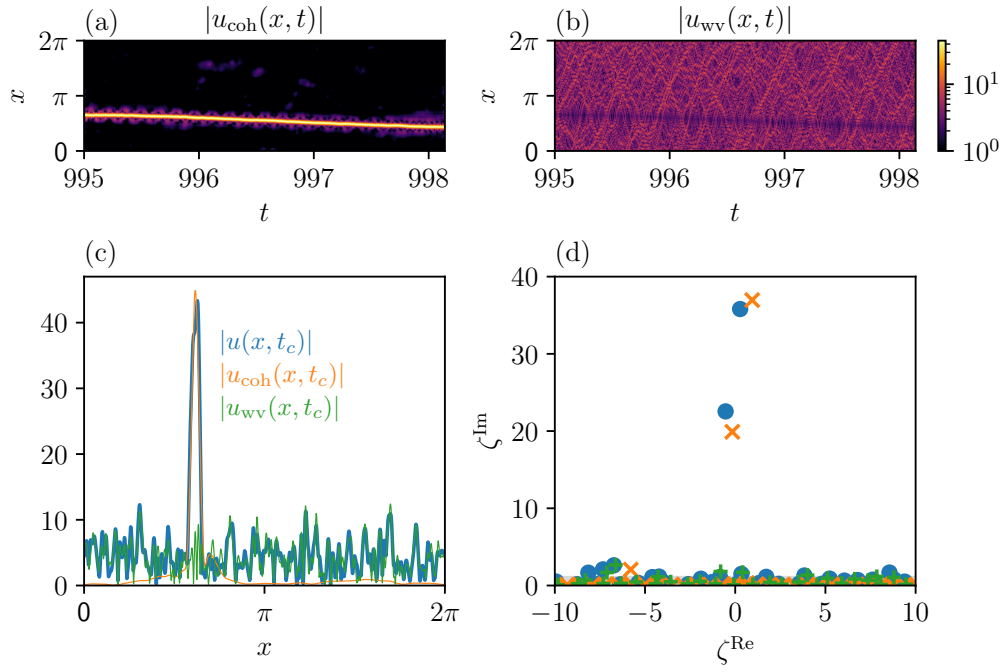


Figure 2.3: **Decomposition study of the $(\mathbf{k}-\omega)$ plot in the final state-** (a) Inverse FT of the $\omega \leqslant -40$ part. The system only contains the oscillating structure with dispersed very small waves. (b) Inverse FT of the $\omega > -40$ part. Only waves are present in the system, with almost nothing in the coherent structure's trajectory. (c) Comparison of the different parts of the function in the real space at $t = 995.8252$. Far away from the structure, the system is modelled by the linear sum of the wave and the localized parts. (d) DST comparison of the full function and its parts. The two eigenvalues of the bound state are also found for the localized part, while slightly modified. Notice that the wave part does not contain any eigenvalue.

each isolated separately, recreate the same trajectory with differences of amplitudes. This confirms that the secondary lines in the $(\mathbf{k}-\omega)$ plot are not associated with a soliton or quasi-soliton with another trajectory. We can notice that isolating only the main line reduces the frequency and the amplitude of the quasi-soliton's oscillation. The quasi-soliton part of the function corresponds to a time-averaged wave-action of 245.089. This shows that 61.3 % of the total wave-action $\mathcal{N} = 400$ is concentrated inside the final structure.

The snapshot of $u_{\mathrm{coh}}$ at $t_{\mathrm{c}} = 995.8252$ shows clearly the coherent structure, with some other local maxima. We assume that these smaller maxima would disappear with a better isolation of the lines in the $(\mathbf{k}-\omega)$ spectrum. Besides, even with these bumps, we see that $|u|$ tends to a null constant value asymptotically around the structure. This observation confirms the idea that the coherent structure is not simply a breather for which the function is constant away from the structure [84]. The DST spectrum of this same time finds only two eigenvalues above the threshold and these eigenvalues are close, in the complex plane, to the ones characterizing the quasi-soliton. We only present here a snapshot of the DST spectrum but we have verified that it has the same qualitative bound state-like evolution as the full function. To summarize, we have found that the

real-space part of the function corresponding to the parallel lines in the $(\mathbf{k}-\omega)$ spectrum is the manifestation of the oscillating evolution of $\zeta_1$ and $\zeta_2$ in the DST spectrum.

In FIGURE 2.3(b), we present the result of the filtered inverse FT done by isolating the spectrum for $\omega > -40$, which gives $u_{\rm wv}$, the wave-part of $u$. $u_{\rm wv}$ corresponds to a system filled with waves almost in the whole box except on the trajectory of the structure, clearly visible with waves of lower amplitude. The mean amplitude of these waves is 4.4088, averaged on the whole $(x-t)$ plot. The wave-action computed for $u_{\rm wv}(x,t)$, averaged in time over the interval (d), is $\simeq 154.911$, which represents 38.7% of the total wave-action of the system $\mathcal{N} = 400$. On the subplot (c), which plots $|u_{\rm wv}(x,t_c)|$, we can see that at the position of the structure the waves have a particular behaviour with constant amplitude and a frequency lower than anywhere else. On the subplot (d) we see that the DST spectrum computed for the wave part, again at the time $t_{\rm c}$, does not show any eigenvalue above the threshold and, thus, no physically meaningful eigenvalues. This result was expected for $u_{\rm wv}$ which only contains the wave component of $u$.

On the comparison (c) of $|u(x,t_{\rm c})|$ with its wave and coherent parts $|u_{\rm wv}(x,t_{\rm c})|$ and $|u_{\rm coh}(x,t_{\rm c})|$, we see that the full field $|u(x,t_c)|$ is relatively well modelled by the linear sum of $|u_{\rm wv}(x,t_{\rm c})|$ and $|u_{\rm coh}(x,t_{\rm c})|$ in the full box apart from at the structure position. At the position of the quasi-soliton, all the local maxima of the wave part are not visible on the total function. These two observations indicate the non-linear interaction of the localized structure with the linear waves. With the same idea, we can see on the DST spectrum that two eigenvalues slightly above the threshold are not captured by a part of $u$, contrary to the eigenvalues of the bound-state. This may suggest that these eigenvalues can represent the result of a non-linear interaction between coherent and wave parts but this requires further studies. Finally, as seen in the snapshot for $t_c$, $u$ and $u_{\rm coh}$ have very close maxima during the evolution. Quantitatively, their time-averaged maxima are respectively equal to 48.865 and 48.197, while it is 12.150 for the wave part. This supports the determination of the quasi-soliton amplitude $A$ as the maximum of the whole function.

To make sure that the second eigenvalue is indeed a characteristic of the oscillating structure and not an artefact, we truncate the function around this structure by putting the function to zero everywhere else. If the second eigenvalue corresponds to the structure, we expect the DST spectrum to barely change. In FIGURE 2.4, we compare, at $t_{\rm c}$ the DST spectrum for the function defined the whole box and the truncated function. It appears that the two eigenvalues which makes the bound state in the spectrum of the full function are also found in the spectrum of the truncated function. That implies that the second eigenvalue is indeed directly linked with the structure. For simplicity, we only show this result for one extreme case of the bound state, but the other one with $\zeta_2^{\rm Im}$ minimum has also been checked and the observation stands. We can also observe in FIGURE 2.4 that the spectrum of the truncated function does not contain other eigenvalues than the two of the bound state.

To study more precisely this final coherent structure, we plot FIGURE 2.5(a) the time series of the imaginary parts $\zeta_{1,2}^{\rm Im}$ and the maximum of the function $\max_x(|u(x,t)|)$ for a short time window in the interval (d). This maximum is taken as the amplitude of the

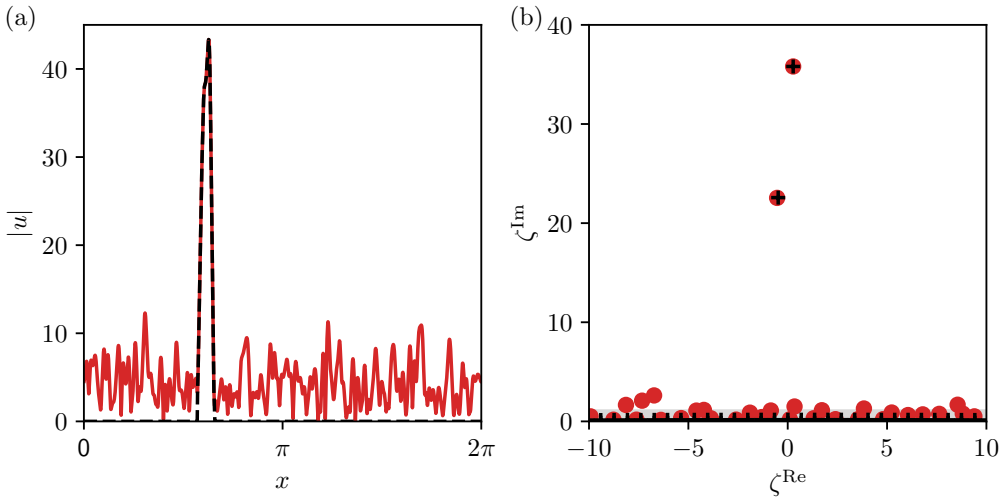


Figure 2.4: **DST spectrum of the function truncated around the structure -** (a) Snapshot of the truncated function. (b) DST spectrum and comparison with the spectrum of the full function. The two eigenvalues creating the bound state are also found for the truncated function.

main quasi-soliton. The comparison suggests indeed that the imaginary parts oscillate with the same frequency as the maximum of $|u|$. More precisely, $\max_x(|u(x,t|)$ and $\zeta_1^{\mathrm{Im}}(t)$ seem to evolve in-phase and the two imaginary parts in phase opposition. The correlation of the evolutions of $\zeta_{1,2}^{\mathrm{Im}}$ is confirmed by the study of the cross-correlation functions $\rho[\max|u(x)|, \zeta_1^{\mathrm{Im}}]$ and $\rho[\zeta_1^{\mathrm{Im}}, \zeta_2^{\mathrm{Im}}]$, presented FIGURE 2.5(b). The cross correlation function is given by

$$\rho[f,g](\tau) = \frac{\int \left(f(t+\tau) - \mu_f\right)\left(g^*(t) - \mu_g^*\right) \mathrm{d}t}{\sigma_f \sigma_g}, \tag{2.7}$$

where $\mu$ and $\sigma$ represent respectively the mean value and standard deviation obtained empirically for the function $f(t)$ and $g(t)$. The positive for $\rho[\max|u(x)|, \zeta_1^{\mathrm{Im}}]$ and negative peaks for $\rho[\zeta_1^{\mathrm{Im}}, \zeta_2^{\mathrm{Im}}]$ for $\tau = 0$ indicate clearly the in phase evolutions of the bound-state amplitude $\max|u(x)|$ and the biggest imaginary part $\zeta_1^{\mathrm{Im}}$ as well as the phase-opposition evolutions for $\zeta_1^{\mathrm{Im}}$ and $\zeta_2^{\mathrm{Im}}$. The same comparison has been done for $\zeta_1^{\mathrm{Re}}$ and $\zeta_2^{\mathrm{Re}}$ and shows the same result, the real parts of the biggest eigenvalues evolve in phase opposition.

Now that the correlation between the amplitude of the quasi-soliton, denoted $A(t)$ and the biggest imaginary part $\zeta_1^{\mathrm{Im}}(t)$ is ensured, we can have a look at the proportionality coefficient. recall that for the integrable 1D-NLSE, the ratio $A/\ \zeta_1^{\mathrm{Im}}$ is constant and equal to 2, with the two quantities being constant. For the 1D-SHE , we now have time-dependant quantities. Denoting $\langle . \rangle_t$ the time averaging, we can compute $\langle A(t)/\zeta_1^{\mathrm{Im}}(t)\rangle_t$ for the two time intervals where the coherent structure has been spotted, (c) and (d). For (c) we obtain $\simeq 1.30$ and $\simeq 1.25$ for (d). To summarize, the biggest imaginary part in the DST spectrum is correlated with the amplitude of the structure, with a ratio close to the value expected in the linear case. We interpret this similarity as a sign that DST is still a precise tool to study a non-integrable system, even if it is not perfectly accurate.

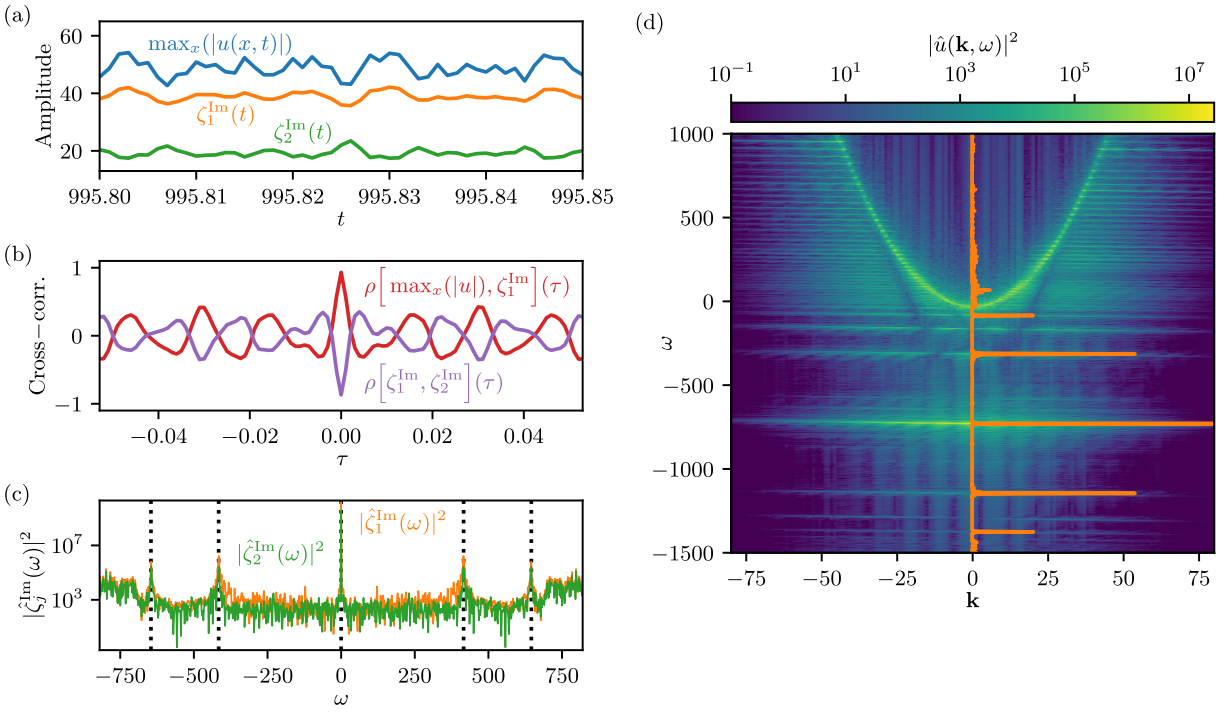


Figure 2.5: **Time evolution of the DST spectrum biggest eigenvalues $\zeta_{1,2}^{\mathrm{Im}}$ for time interval (d) in Figure 2.2 -** (a) Times series of $\zeta_{1,2}^{\mathrm{Im}}$ compared with the maximum of $|u|$. The imaginary parts oscillate around two well-separated values with the same frequency and in phase opposition. $\zeta_1^{\mathrm{Im}}(t)$ evolves in phase with the maximum of the function. (b) Cross-correlation functions between the time-series. $\max_x(|u|)$ and $\zeta_1^{\mathrm{Im}}$ are found in phase while $\zeta_2^{\mathrm{Im}}$ and $\zeta_2^{\mathrm{Im}}$ are in phase opposition. (c) PSD of the times series $|\hat{\zeta}_{1,2}^{\mathrm{Im}}(\omega)|^2$. Both spectra have maxima for the same frequencies, which proves that the times series have correlated evolutions. (d) Superimposition of the PSD $|\hat{\zeta}_1^{\mathrm{Im}}(\omega)|^2$ on the $(\mathbf{k}-\omega)$ spectrum, placing the $\omega = 0$ peak on top of the main straight line. The secondary peaks of the PSD correspond to the parallel lines of the $(\mathbf{k}-\omega)$ spectrum.

The decrease of this ratio between the time intervals (c) and (d) (highly separated in time scale) can be interpreted with the growth of the coherent structure. Indeed, the increase of its amplitude implies a consolidation of this structure, driving the system further away from integrability. Thus, the DST spectrum is expected to be less precise. It is important to notice that the relation $A/\zeta^{\mathrm{Im}} = 2$ in the integrable case stands when the soliton is described by only one eigenvalue (as the definition of solitons) while in our case, there is always another eigenvalue ($\zeta_2$) which could inhibit the proportionality between $A$ and $\zeta_1^{\mathrm{Im}}$. It is indeed observed that the ratio $A/\zeta_1^{\mathrm{Im}}$ oscillates in time, being maximum when $\zeta_2^{\mathrm{Im}}$ is minimum and inversely. The relation between the structure velocity and the real part $\zeta_1^{\mathrm{Re}}$ shows an even better accordance : denoting $v(t)$ the speed of the coherent structure, we obtain $\langle v(t)/\zeta_1^{\mathrm{Re}}(t)\rangle_t \simeq -2.19$ in (c) and $\simeq -2.12$ in (d), to be compared with the constant value -2 in the integrable case.

The correlation between the imaginary parts can also be observed by comparing their corresponding Power Spectral Densities (PSDs) $|\hat{\zeta}_{1,2}^{\mathrm{Im}}(\omega)|^2$. Both spectra have the same peaks, a primary one at $\omega = 0$, corresponding to the mean value of each time series,

and secondary and tertiary ones, respectively at $\omega = \pm 415.814$ and $\omega = \pm 645.711$. The difference in amplitudes for the $\omega = 0$ peak captures the factor 2 between the mean values of the time series. The same secondary peaks are the peaks of lowest $|\omega|$ and thus correspond to the lowest frequency in the $t$-evolution. Both spectra having their secondary peaks located at the same $\omega$ confirms that $\zeta_{1,2}^{\mathrm{Im}}$ oscillate with the same frequency denoted $\Omega = 415.814$. The PSD of $\max_x(|u(x,t|)$, not shown for visibility, displays the same primary and smaller peaks. All the PSDs are symmetric functions of $\omega$ because the related time series are real.

To this point, it is now clear that the coherent structure created by the evolution of the system with 1D-SHE is associated with the oscillations of the main eigenvalues $\zeta_1$ and $\zeta_2$ in the DST spectrum and parallel lines in the $(\mathbf{k} - \omega)$ spectrum. We propose to name this coherent structure a *bound-state* to illustrate the correlated and oscillating evolutions of $\zeta_1$ and $\zeta_2$. More precisely, a bound-state denotes a coherent structure, oscillating in amplitude and in width, characterized by two DST eigenvalues oscillating in phase opposition and with a spectral signature of parallel lines. Remark that no conditions are set on its speed nor trajectory.

We recall that, for a 1D-NLSE soliton characterized by $A$ and $v$, the center $(\mathbf{k}^*, \omega^*)$ of its straight line in the $(\mathbf{k} - \omega)$ spectrum is given by $(\mathbf{k}^* = v, \omega^* = (v^2 - A^2)/2)$. As the 1D-SHE is galilean invariant, we expect the relation $\mathbf{k}^* = v$ to stand. This was verified in the time interval (d) as $\mathbf{k}^*$ was located between $\mathbf{k} = 0$ and $-1$ for a mean speed $\langle v \rangle_t = -0.21$ (below the resolution $\Delta k = 1$ of our simulation). A very important result can be obtained by superimposing the PSD $|\hat{\zeta}_{1,2}^{\mathrm{Im}}(\omega)|^2$ on top of the $(\mathbf{k} - \omega)$ spectrum of the corresponding time window, as it is done FIGURE 2.5(d). $|\hat{\zeta}_{1,2}^{\mathrm{Im}}(\omega)|^2$ is placed in such a way that the primary peak at $\omega = 0$ is aligned with the main line of the $(\mathbf{k} - \omega)$ plot, whose center is found at $(k^* = -0.21, \omega^* = -730)$ by searching for the maximum at $\mathbf{k} \simeq \langle v \rangle_t$. We observe a good correspondence between the secondary peaks of $|\hat{\zeta}_{1,2}^{\mathrm{Im}}(\omega)|^2$ and the secondary lines of the $(\mathbf{k} - \omega)$, for both time intervals (c) and (d), *ie* when the final quasi-soliton has been formed. As the secondary peaks in the PSD are the direct sign of the oscillations of the amplitude and the imaginary parts, we conclude that the secondary lines in the $(k - \omega)$ spectrum represent the same phenomenon. This result is of great importance as it also shows that the two diagnostics that we use are consistent together.

Finally, we can try to interpret the $\omega$-position of the main line, $\omega^* = -730$, by comparing it to the frequency of 1D-SHE solitary waves or 1D-NLSE solitons. In the time interval (d), the bound-state has averaged amplitude $\bar{A} \simeq 48.9$ and velocity $\bar{v} \simeq -0.21$. As the secondary lines of the $(\mathbf{k} - \omega)$ spectrum have been identified as linked with the amplitude oscillations, we will only take the mean values into account to try to recover the position of the main line. If we consider a 1D-NLSE soliton, we would expect a frequency $\omega_{\mathrm{sol}}(\bar{A}, \bar{v}) = -(\bar{v}^2 - \bar{A}^2)/2 \simeq -1194$ given its expression (1.10), quite different from the observed value of -730. Similarly, with a 1D-SHE solitary wave (1.23), we expect a frequency $\omega_{\mathrm{sol.w.}}(\bar{v}) = (1/\beta - \bar{v}^2) \simeq= -100$, even less consistent with the numerical value. We can also remember that the 1D-SHE solitary wave has an amplitude fixed by the non-linearity parameter $\beta$, which is 10.6 for the value $\beta = 10^{-2}$, also far from the

mean amplitude observed $\simeq 48.9$.

**Discussion**

We have made different tests to make sure that the parallel lines observed in the $(\mathbf{k}-\omega)$ plot are actually the spectral signature of the bound-state. Similarly, we have checked that the two evolving eigenvalues found in the DST spectrum correspond to the bound-state.

The nature of the bound-state is a delicate question. The second eigenvalue identified by the DST, clearly above the threshold, can hardly be considered as a second independent soliton, as shown by the different tests realized. If this smaller soliton existed, we would suppose that it would always be *hidden* inside the main one. Indeed, as $\zeta_1^{\mathrm{Re}} \neq \zeta_2^{\mathrm{Re}}$, these solitons would have have different speeds and the smaller soliton would propagate inside the bigger one. According to this assumption, the oscillating quasi-soliton would be the non-linear sum of the two eigenvalues. However, as the 1D-SHE is non-integrable, solitons are not stable and particularly the 1D-NLSE solitons, which are only stable in the 1D-NLSE, as we will show section 3.1. We prefer to see this solitonic bound state as an non-integrable version of the one described by Zakharov and Shabat [9] for the 1D-NLSE . They describe this bound state as made of two eigenvalues (constant for the 1D-NLSE ) with the same real part and two different imaginary parts $\zeta_1^{\mathrm{Im}}$ and $\zeta_2^{\mathrm{Im}} < \zeta_1^{\mathrm{Im}}$. According to them, the structure resulting from these eigenvalues will oscillate in amplitude at the frequency $\omega = 4\left(\zeta_1^{\mathrm{Im}^2} - \zeta_2^{\mathrm{Im}^2}\right)$ (the difference between the factor 4 in their article and 2 in our work corresponds to the difference of coefficient for the studied equations). Contrary to the 1D-NLSE , in our case the imaginary parts are not constant but we can compute $\omega = 2\left(\langle\zeta_1^{\mathrm{Im}}\rangle_t^{\,2} - \langle\zeta_2^{\mathrm{Im}}\rangle_t^{\,2}\right) \simeq 2250$, a factor 5 higher that the value found at $\Omega \simeq 416$. We will see in section 3.1 that this model gives more consistent results for a simpler system.

The observed bound-state can be found similar to Kuznetsov-Ma breathers which are also time-periodic solutions of the focusing 1D-NLSE [84]. However, as mentioned before, these breathers are characterized by constant values far away from the central peak. As we have shown, isolating the bound-state and putting to zero its wave background does not change nor its characteristics nor spectral signatures. Besides, the DST spectrum of a Kuznetsov-Ma breather contains a branchcut, which is a continuous vertical line of eigenvalues at $\zeta^{\mathrm{Re}} = 0$, plus a singe eigenvalue. This DST spectrum is qualitatively different from the one we have observed for the bound-state. Finally, Kuznetsov-Ma breathers, and breathers in general, are observed in the integrable 1D-NLSE so we can not expect to observe them in the non-integrable SHE. The bound-state may perhaps be seen as an non-integrable version of breathers but this question is left open.

We have noticed that the DST framework of the integrable 1D-NLSE, even when applied to a non-integrable system, gives predictions which are qualitatively in great accordance with the spatio-temporal and Fourier dynamics. The oscillations of the two eigenvalues capture the evolution of the quasi-soliton : we prefer to see the DST spectrum of the bound state as a signature of this final state rather than as an exact definition

of the system (as it is in integrable case). The ability of the DST to describe qualitatively well the 1D-SHE system may be considered as a first numerical result.

### 2.3.4 Condition of existence for the bound-state

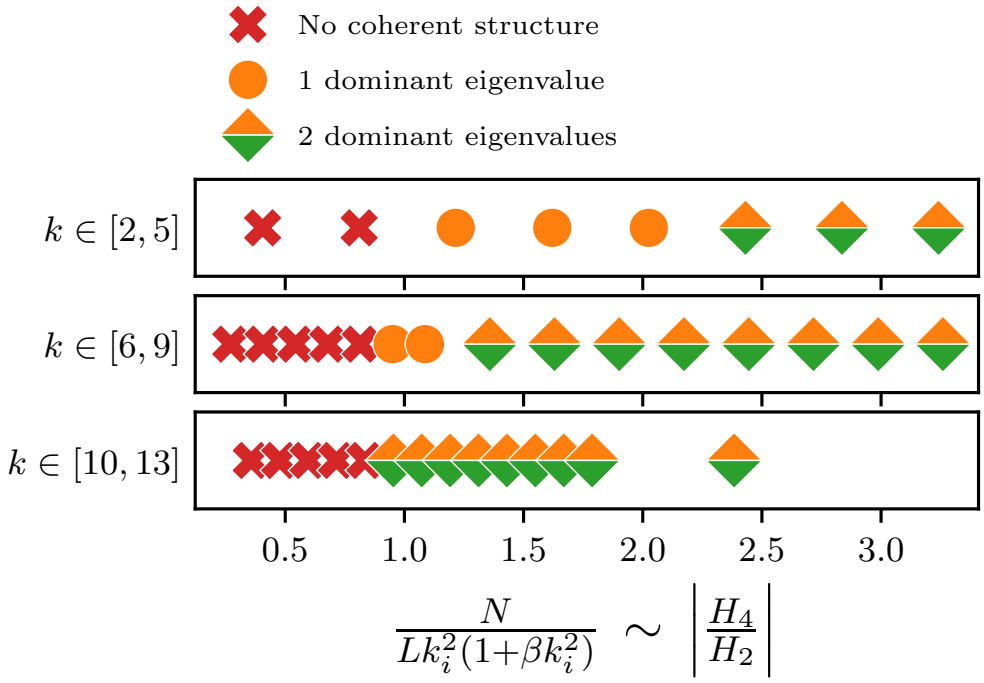


Figure 2.6: **Quasi-Soliton Turbulence phase diagram -** For different initial flat-top spectra , we identify the simulations which lead to a bound-state for different non-linearity ratios. We observe that if the system is too linear, the bound-state does not appear.

In the previous section, we identified a bound-state for a single simulation, starting from a flat-top spectrum with Amp $= 3, k_i = 7.5$ and $dk_i = 1.5$, see (2.4). To see if there were any conditions for its existence, we ran sets of qST simulations like detailed before but with varying the initial conditions. Specifically, we prepare the system with an initial flat-top spectrum of random waves and we scan the amplitude Amp of this initial spectrum. We repeat this scan of Amp by placing the spectrum at larger and larger lengthscales by increasing $k_i$. We keep $dk_i = 1.5$ the same in these experiments. We evolve the system for a very long time (up to $t = 6000$) in order to observe whether dominant coherent structure emerges and what its DST characteristics are. To be able to reach such a large time, we reduced the resolution to $N_x = 1024$ and increase the time-step up to $\Delta t = 5 \times 10^{-6}$, to reduce the computation time. We ensure that these simulations are correctly resolved by checking that the wave-action spectrum does not reach the biggest wave-number resolved. However, we still repeated certain runs at higher resolution and find exactly the same qualitative behaviour. Finally, notice that simulating the system up to $t = 6000$ allows us to confirm that the bound-state, when it exists, is indeed the

final state of the system.

The FIGURE 2.6 summarizes the results of this study. It is a phase diagram for which we plot a proxy for the initial non-linearity ratio of the system as abscissa, and the wave-numbers which contain the initial spectrum as ordinates. Each simulation is represented by a marker which depends on its the final state : a red cross if no coherent structure is observed, an orange circle if a coherent structure is observed with only one dominant eigenvalue found in the DST spectrum and an orange-and-green square if a coherent structure is observed with two dominant eigenvalues. The cases when one dominant structure is obtained correspond to a bound-state and we hypothesise that the wave-action $\mathcal{N}$ is not always large enough to exhibit a second eigenvalue $\zeta_2$. This is notably the case for the orange circles. The orange-and-green squares correspond exactly to the bound-states as characterized in the previous section.

A result can be easily drawn for this phase diagram : when the system is too linear, no coherent structures, and consequently no bound-state are observed. This observation was expected given the properties of solitons. Solitons correspond to a balance between non-linearity and dispersion and changing the amplitude of the spectrum does not affect the dispersion. Hence, below a certain threshold, the system is too linear for the non-linearities to match the dispersion and the solitonic structures, such as the bound-state, can not develop. Moreover, this threshold seems to be independent from the position of the initial spectrum in the **k**-space : if the non-linearity ratio is below 0.9, the system will not develop any coherent structures, no matter the excited modes.

Conversely, a bound-state is always observed when the system is very non-linear. The simulation whose results are presented in section 2.3.2 corresponds to an abscissa $|\mathcal{H}_4/\mathcal{H}_2| \simeq 4.6$ for initially excited modes $k \in [6, 9]$. From FIGURE 2.6 we see that we still obtain a bound-state if we reduce the non-linearity ratio down to 1.35, which corresponds to divide by four the wave-action in the system.

For $k \in [2, 5]$ and $k \in [6, 9]$, we observe a transitional state between the absence of any solitonic structures and the existence of a clear bound-state. That corresponds to a solitonic structures characterized by only one dominant eigenvalue in the DST spectrum. We assume that the system *tries* to create a bound-state but that its amplitude is not large enough to make a second eigenvalue grow above the other eigenvalues. More precisely, $\zeta_2^{\mathrm{Im}}$ is not clearly distinguishable from the other imaginary parts. We observe that the range of non-linearity ratios corresponding to this transitional state diminishes when we initially excite larger and larger modes. This observation needs further investigation.

This study of the conditions of existence for the bound-state brings interesting results and confirms the link between the small non-linearity ratio and the absence of bound-state and any coherent structures. Further study are required to complete this phase diagram but we hypothesise that new points in this diagram will not endanger the conclusions we have just drawn.

**Summary of the section**

- We have found that the function, initialised as random waves organizes into an unique coherent structure, named *bound-state*,
- this bound-state has oscillating amplitude and width,
- its DST spectrum finds two eigenvalues with large imaginary parts oscillating in phase opposition,
- parallel lines represent its $(\mathbf{k} - \omega)$ spectrum signature.
- It appears that the bound-state can not exist if the system is too linear.

## 2.4 Two 1D-SHE solitary waves collisions

To have a better understanding of the quasi-Soliton Turbulence behaviour detailed above, we will now study the collisions between two localized structures that we see propagating during the ST evolution. To be precise, we study two 1D-SHE solitary waves collisions to illustrate clearly the conditions under which coherent solitonic structures can merge. Indeed, the creation of the final structure as a bound-state is possible because the 1D-SHE is non integrable and, thus, the occurring collisions are not elastic. Such non-elastic collisions will be studied by preparing the system initially as two 1D-SHE solitary waves (1.23) with speeds of opposite signs and initially located in $s_1 = L/4 = \pi/2$ and $s_2 = 3L/4 = 3\pi/2$. The solitary waves are set as distant as each other to minimize the overlapping of the exponentially decaying tails of the structures. The non-integrability parameter is kept at $\beta = 10^{-2}$ which sets the 1D-SHE solitary waves amplitude as $A \simeq 10.6$. The system studied is the same box of length $L = 2\pi$ with periodic boundary conditions and discretized with $N = 2048$ points. This number of points ensures the conservation of $\mathcal{N} = 60$ and $\mathcal{H} = -1193$ over time with a reasonable time of computation. The periodic boundary conditions force the two solitary waves to recirculate through the box and collide numerous times. This simulates the behaviour of a rarefied gas of interacting solitary waves in an infinite system.

### 2.4.1 Study of simulations with different initial phase differences

**Same final state**

We present the results of simulations obtained for two initial 1D-SHE solitary waves with opposite initial speeds $\pm 0.5$ and different initial phases. The range of initial phase differences $]-\pi, \pi]$ is explored with eight values, equally distributed $\Delta\phi_i = \Delta\phi(t = 0) = m\pi/4, m \in [\![-3, 4]\!]$. The Figure 2.7 compares the spatio-temporal dynamics for these values.

All these different dynamics share two interesting features. The first one is the existence, for large times, of a unique coherent structure, with oscillating width and amplitude,

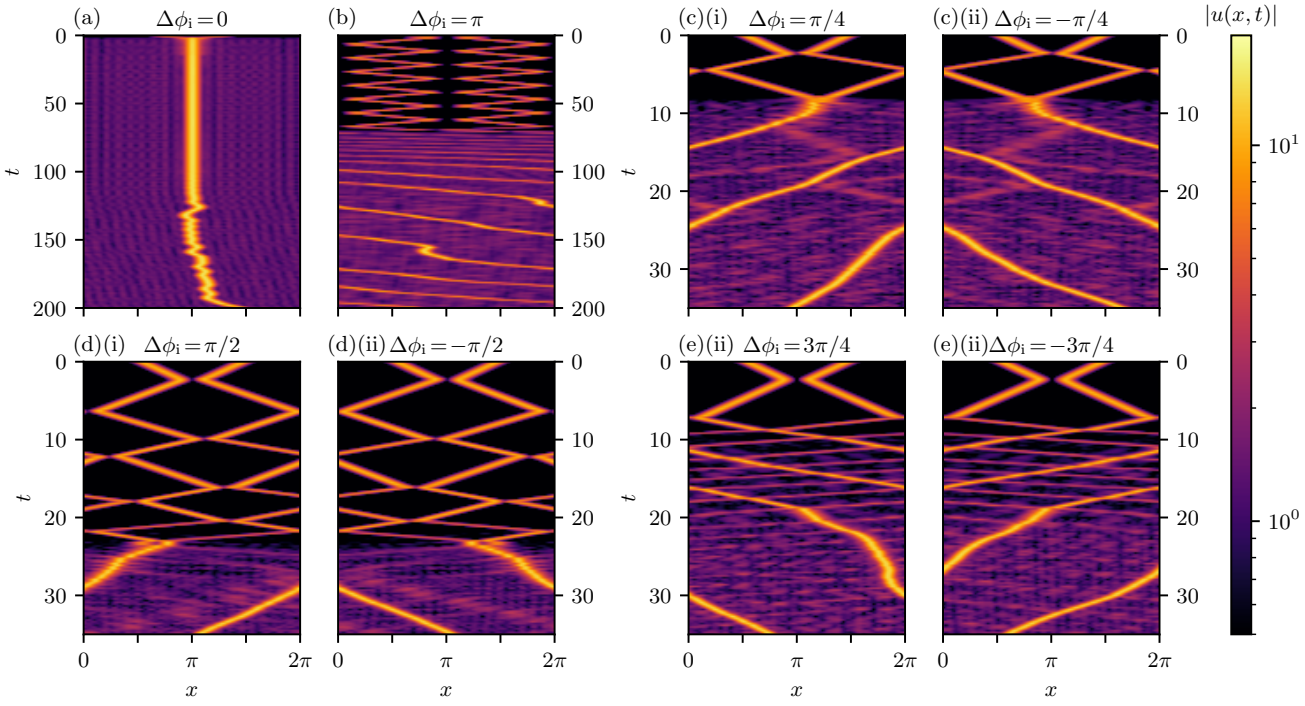


Figure 2.7: **Spatio-temporal dynamics of colliding 1D-SHE solitary waves for different initial phase differences** - The final state is the same for all initial phase difference : a coherent structure propagating on top of linear waves. The initial phase difference $\Delta\phi_i$ plays a role in the evolution, by determining the time at which the two solitary waves merge.

propagating on top of a wave field background, and the second one is the impact of the phase difference, dealt with later. The coherent structures oscillates both in amplitude and in width, it is more convenient to observe this for zoomed $(x-t)$ dynamics, see FIGURE 2.10(a) for instance. Moreover, it appears to be stable in time, as it is observed for large times, until $t = 200$ for $\Delta\phi_i = 0$ and $\pi$. This coherent structure also stands to these times for the other simulations but we only show early times to highlight the process which leads to such a final state. The trajectory of this coherent structure starts to wander at some time. We hypothesise that this is due to the structure itself exchanging momentum with the waves in the system. This final state is qualitatively the same for all of these simulations, with only the trajectory of the final structure seeming quite random.

This final coherent structure is characterized by the DST and $(\mathbf{k}-\omega)$ spectra diagnostics. The DST spectrum shows two main eigenvalues above the threshold, $\zeta^{\mathrm{Im}}_{1,2}$, for all the simulations. We observe oscillating and in phase oppositions evolutions for $\zeta^{\mathrm{Im}}_1(t)$ and $\zeta^{\mathrm{Im}}_2(t)$. These oscillations also have the same frequency that $\max_x|u(x,t)|$, the latter being in phase with $\zeta^{\mathrm{Im}}_1(t)$. These observations are the same as the ones made for the bound-state of the quasi-Soliton Turbulence. This suggests that the final state of the solitary waves collisions also is a bound-state.

In FIGURE 2.8, we compare, for the $\Delta\phi_i = 3\pi/4$ simulation, the $(\mathbf{k}-\omega)$ spectra

computed for this same system but for different time windows, $0 \leqslant t \leqslant 7$ for 2.8(a) and $25 \leqslant t \leqslant 32$ for 2.8(b). The initial stage of the evolution (up to $t = 7$) contains only two solitary waves in the $(x - t)$ plot. These two coherent structures can be clearly seen on the $(\mathbf{k} - \omega)$ plot, as the two crossing straight lines. We can even distinguish the two sub-lines with different but similar slopes, which correspond to the speeds of the solitary waves before and after the first collision. The absence of the parabola shows that the system does not contain linear waves in early times. This observation is in accordance with the $(x - t)$ plot.

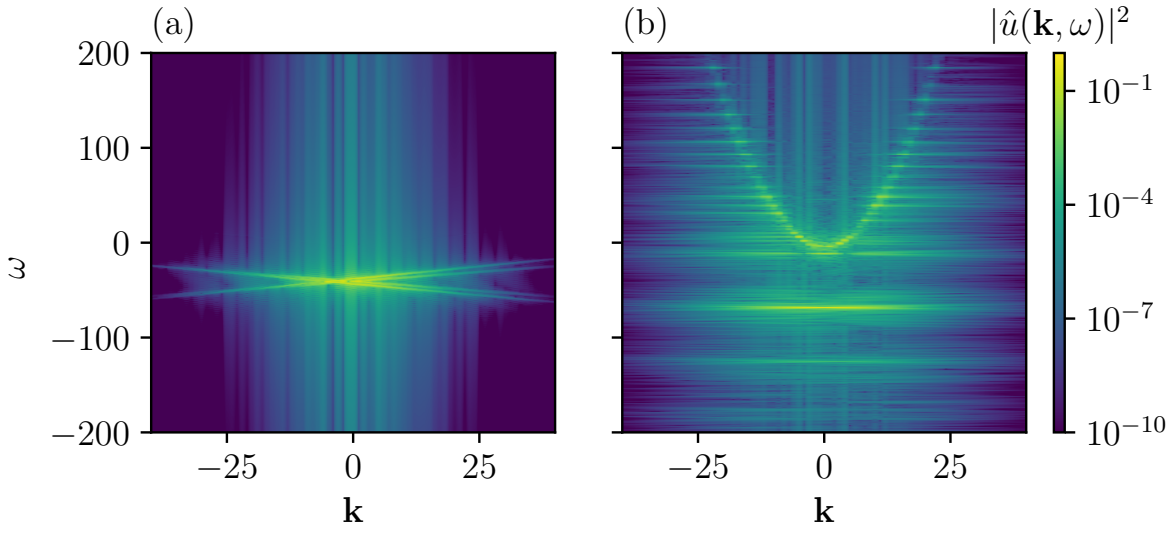


Figure 2.8: $(\mathbf{k} - \omega)$ **spectra computed for the initial state (a)** $(0 \leqslant t \leqslant 7)$ **and for the final state (b)** $(25 \leqslant t \leqslant 32)$ **of the** $\Delta\phi = 3\pi/4$ **simulation.** - Early times are characterized by two crossing lines in the $(\mathbf{k} - \omega)$ plot while parallel lines stand for the late times. This big quantitative difference illustrates the difference in the $(x - t)$ plot.

The $(\mathbf{k} - \omega)$ spectrum of the final stage is qualitatively different. It shows three parallel lines with a slope corresponding to the speed of the final structure. These lines form the spectral signature observed for the bound-state in the quasi-Soliton Turbulence. The PSD $|\hat{\zeta}_1^{\mathrm{Im}}(\omega)|^2$ (not shown here) also superimpose on top of the $(\mathbf{k} - \omega)$ spectrum, with the same accordance than for the final state of the qST. Finally, the parabola shows the presence of linear waves in the system.

Given the strong similarities between the results of the diagnostics for this final coherent structure and the bound-state observed in the quasi-Soliton Turbulence, we conclude that the final coherent structure of the solitary waves collisions also is a bound-state. We can also notice that all the final bound-states (for the different simulations) have very close mean amplitude, that we could link with the same wave-action and energy for all the simulations.

**Short-times evolution**

The different initial conditions of the FIGURE 2.7 display the same final state but with different behaviours for short times. These different behaviours will be described and analyzed in the coming section.

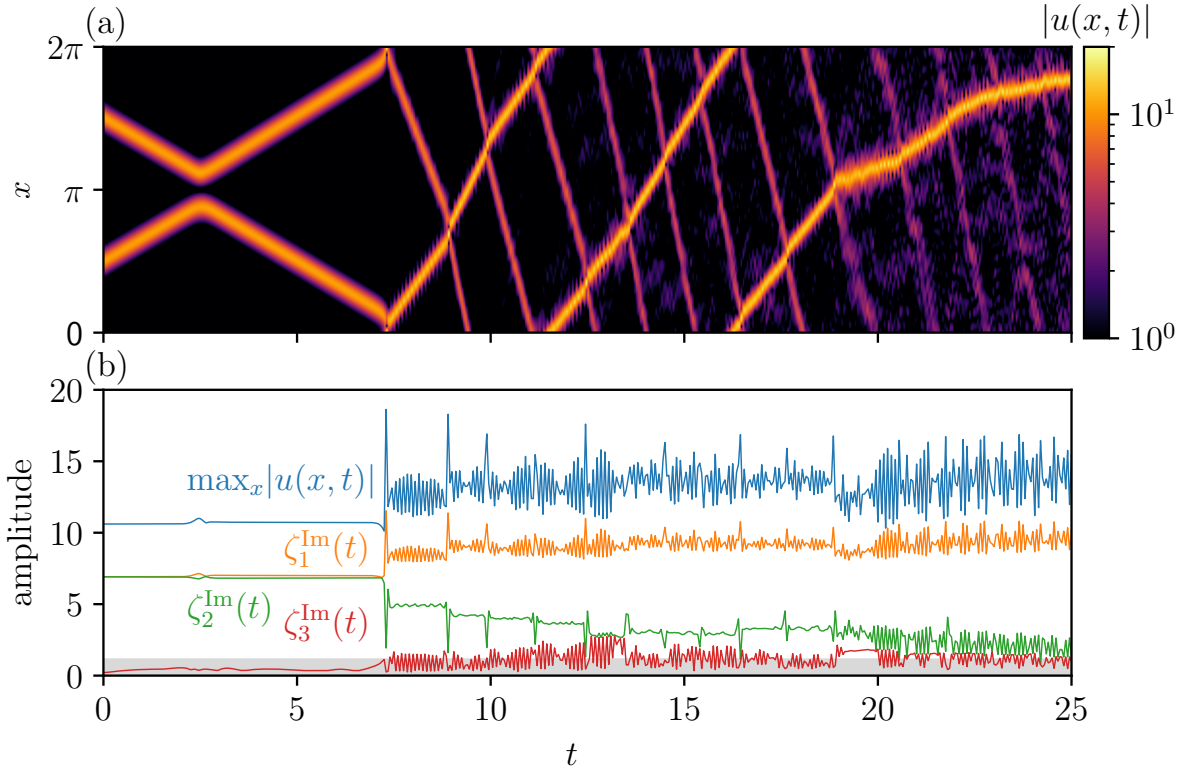


Figure 2.9: **DST spectrum of the $\Delta\phi_i = 3\pi/4$ collision -** (a) Spatio-temporal dynamics. After some collisions, the amplitude of the smaller solitary wave progressively decreases. (b) Evolution of the DST spectrum. $\zeta_{1,2}^{\mathrm{Im}}(t)$ illustrate the non-elastic collisions and is in accordance with the $(x-t)$ dynamics.

The few first collisions are almost elastic as they change the solitons velocities but only slightly alter their amplitudes (the $\Delta\phi_i = 0$ simulation is an exception and we will come back to it later). For instance, FIGURE 2.9 details the early times dynamics of the $\Delta\phi_i = 3\pi/4$ simulation. We observe that the first collision at $t \simeq 2.5$ is quasi-elastic in the sense that the solitary waves speeds and amplitudes barely change. This is seen on the DST evolution as $\zeta_{1,2}^{\mathrm{Im}}$ slightly change, showing the (small) change of solitary waves amplitudes due to the first collision, with one increasing and the other decreasing. More precisely, before the first collision, the two solitary waves have the same amplitude 10.606 while after this collision, their amplitudes are 10.980 and 10.225. The values of $\zeta_1^{\mathrm{Im}} = 7.010$ and $\zeta_2^{\mathrm{Im}} = 6.812$, corresponding to the ratios $A/\zeta^{\mathrm{Im}} = 1.566$ and 1.501, indicate clearly that the DST spectrum tracks correctly the evolution of the amplitudes. For the rest of this chapter we will admit this as a result, and only compare the qualitative evolutions of amplitudes and imaginary parts. Finally, we can observe the large bumps of $\zeta^{\mathrm{Im}}$ at the

collisions. This underlines the non-elasticity of the collisions, because elastic collisions occurring in the NLSE are characterized by a constant DST spectrum, even at collisions.

The subsequent collisions have the same impact on the solitons : at each collision, the overall tendency is for $\zeta_1^{\mathrm{Im}}$ to increase while $\zeta_2^{\mathrm{Im}}$ decreases, with some exceptions visible on FIGURE 2.9 (see the collision at $t \simeq 14$). This evolution can be followed with the DST. For the same figure, after the second collision at $t \simeq 7$, $\zeta_{1,2}^{\mathrm{Im}}$ oscillate even during the propagation, which we interpret as solitary waves with oscillating amplitude, as suggested with snapshots of $|u(x,t)|$ and the $(x-t)$ dynamics. However, looking at $\zeta_3$, the eigenvalue with the third biggest imaginary part, we observe its imaginary part $\zeta_3^{\mathrm{Im}}$ grow from 0 to slightly above the threshold. More importantly, it also oscillates and in phase opposition with $\zeta_1^{\mathrm{Im}}$ and thus in phase opposition with $\max_x|u|$. This indicates that $\zeta_1$ and $\zeta_3$ form a bound-state, corresponding to the larger coherent structure in the system and totally independent from the smaller one. Between the second collision at $t \simeq 7.5$ and the sixth one at $t \simeq 12.5$, the mean values of $\zeta_{1,3}^{\mathrm{Im}}$ increase, corresponding to the growth of the bound-state. We hypothesise that the smaller structure also becomes a bound-state but the study of $\zeta_4^{\mathrm{Im}}$ does not show any conclusive result as the latter stays very small. Then, we assume that this smaller structure is not large enough to really display bound-state characteristics after the collision and, as this structures fades with time, it will never do so. This observation can be linked to the transitional state of the phase diagram for the qST study FIGURE 2.6.

With this evolution, at a certain time, the second eigenvalue of the bound-state $\zeta_3$ starts to have an imaginary part larger than the eigenvalue of the second coherent structure $\zeta_2$. Thus, the second eigenvalue of the bound-state becomes $\zeta_2$, in the sense of the eigenvalue with the second largest imaginary part. For instance, after $t = 20$, it is $\zeta_1^{\mathrm{Im}}$ and $\zeta_2^{\mathrm{Im}}$ which oscillate in phase opposition and thus, form the bound-state. The further evolution is the reinforcement of this bound-state, as seen in the FIGURE 2.7(e)(ii). It is important to understand that we order the eigenvalues according to the size of their imaginary parts, so that the nature of $\zeta_2$ changes during the evolution : it represents a solitary wave for very early times and is the second eigenvalue of a bound-state for late times.

To summarize, the second collision at $t \simeq 7.5$ not only changes the amplitudes of the solitary waves but also creates two bound-states, one of which is too small to display a second eigenvalue. Notice that the oscillations of $\zeta_2^{\mathrm{Im}}$ after the second collision can also suggest that $\zeta_4^{\mathrm{Im}}$, not displayed here for simplicity, lays inside the threshold and, thus, does not represent a physically realisable structure inside the domain. We suggest that the amplitude of the smaller coherent structure is not large enough to create a bound-state. From now on, we will assume that he oscillating structures created by the collisions are indeed bound-states. Hence, the initial structures remain 1D-SHE solitary waves until the first collision which creates bound-states (apart from the $\Delta\phi_i = \pi$ simulation, which will be discussed later).

It is interesting to notice that between collisions, the mean values of $\zeta_i^{\mathrm{Im}}$ do not change; it is indeed the collisions that affect the mean amplitudes, not the propagation itself. Moreover, some waves of non-marginal amplitude are created, showing that the initial

solitary waves have lost some of their coherence through the non-integrable evolution and the non-elastic collisions.

For certain simulations like $\Delta\phi_i = \pm\pi/4$ or $\pm\pi/2$, these quasi-elastic collisions end suddenly with one strongly non-elastic collision which drastically changes the system (see the detailed $(x-t)$ dynamics for $\Delta\phi_i = \pi/4$, FIGURE 2.10(a)). First, linear waves are created during this collision at $t \simeq 8$ which quickly fill up the box : the coherent structures do not contain all the wave-action anymore. With the conservation of this latter, the solitary waves must shrink to release some wave action. More precisely, both initial solitary waves merge into the single coherent structure propagating on top of the linear waves. This structure has oscillating amplitude and width, and a speed which seems to evolve quite randomly. We also assume that it is a bound-state.

Although all the simulations detailed above share the same final state, we just saw that the evolution leading towards it depends on the simulation. As the only difference between these simulations is the initial phase difference, we will now study the role of the phase difference and see if it can explain the difference observed in early times.

**Impact of the phase difference**

The initial phase difference appears to play an important role as the single bound-state is created very early for the $\Delta\phi_i = 0$ simulation (here at the very first collision) and very late for the $\Delta\phi_i = \pi$ one. More particularly, for the $\Delta\phi_i = \pi$ simulation, the collisions do not affect the solitary waves until $t \simeq 65$, which keep their amplitudes and speeds, exactly as if the collisions were symmetric. The absolute value of the initial condition is symmetric with respect to the $\{x \leftrightarrow 2\pi - x, v \leftrightarrow -v\}$ change and the system stays symmetric until the creation of the coherent structure.

This observation seems to indicate that collision between bound-states with a phase-difference of $0[2\pi]$ would create a single bound-state from the two colliding, while two bound-states colliding with a phase difference of $\pi$ undergo an elastic collision. To study this link between the phase difference and the nature of a collision, we need to be able to track the the phase difference during all the simulation, not knowing only its initial value. The phase difference is measured with the following procedure. We localize the coherent structures (1D-SHE solitary waves or bound-state) with the two biggest local maxima of the function, denoted $u_{m,1}(t)$ and $u_{m,2}(t)$, and we compute the phase difference $\Delta\phi(t) = \arg[u_{m,1}(t)] - \arg[u_{m,2}(t)]$. This method does not requires a large computation time but needs to localize properly the coherent structures in the $x$-axis. Near the collisions this is not always possible, so we decided to let blank $\Delta\phi$ for the times when the structures are not distinguishable.

In FIGURE 2.10(b), we present the time evolution of $\Delta\phi(t)$ for the beginning of the $\Delta\phi_i = \pi/4$ simulation. The first observation is the phase difference being constant and equal to $\pi/4$ before the first collision at $t \simeq 2.5$. During this period, the initial 1D-SHE solitary waves have not collided at all and, thus, are still solutions of the 1D-SHE, with the same initial amplitude $A = 10.606$, as verified experimentally. However, after the first collision, $\Delta\phi$ evolves linearly with $t$. This evolution coincides with the breaking of

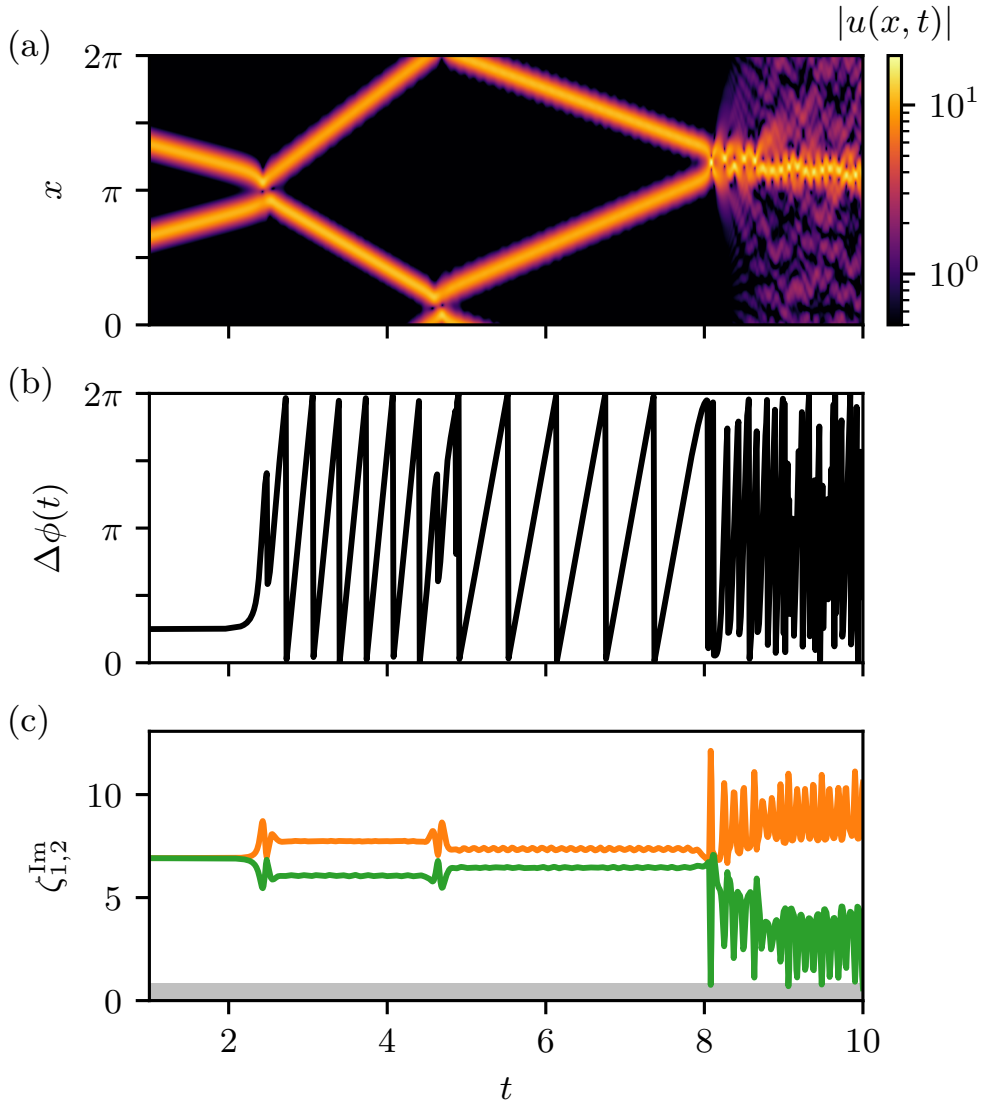


Figure 2.10: **Evolution of $\Delta\phi(t)$ and $\zeta^{\mathrm{Im}}_{1,2}$ for early times of the $\Delta\phi_i = \pi/4$ simulation -** The phase is observed to evolve linearly when the coherent structures have different amplitudes (as testified by the DST). The non-linear collision leading to a merging event occurs with a phase difference very close to $0[2\pi]$.

symmetry between the solitary waves as their mean amplitudes before the second collision are $A_1 = 11.685$ and $A_2 = 9.480$. After the second collision at $t \simeq 4.5$, the asymmetry is less pronounced as the mean amplitudes are now $A_1 = 11.188$ and $A_2 = 10.002$ and $\Delta\phi(t)$ is still a linear function but with a smaller slope. We present here only two examples of this link between asymmetry in amplitude and phase difference evolution, but this link has been observed for all the individual collisions for which we have tracked the phase difference. In the next section 2.5, we will propose a model to explain it. Notice that the value of $\Delta\phi$ after the merging event has not the expected signification because the system now displays a bound-state which is a unique structure : the phase difference between the latter and the second biggest local maxima of the function, found in the background

waves, does not have any sense. For this simulation, the second collision creates a new eigenvalue in the sense that $\zeta_3^{\mathrm{Im}}$ grows from zero to above the threshold while oscillating in phase opposition with $\zeta_1^{\mathrm{Im}}$. However, we can not identify another eigenvalue, which would be $\zeta_4$, and thus we assume that the other coherent structure is too small to exhibit the bound-state characteristics. Finally, we also notice that before the non-elastic collision at $t \simeq 8$, $\zeta_2$ represents an independent coherent structure while, after, it is part of a bound-state.

Another important observation can be made about the evolution of the phase difference. When the bound states collide at $t \simeq 8$, and merge into the bound-state, we found $\Delta\phi = 6.044 \simeq 0[2\pi]$. This supports the initial observations about the $\Delta\phi_i = 0$ simulation : coherent structures colliding in phase which merge into a bound-state.

We also study $\Delta\phi(t)$ for the $\Delta\phi_i = \pi$ simulation and we observed that the $\Delta\phi$ stays very close to $\pi$ until the collisions start to be non-elastic. This study is illustrated FIGURE 2.11 with the constancy of $\zeta_{1,2}^{\mathrm{Im}}$ attesting the absence of non-elastic collisions before $t \simeq 57$. After the first non-elastic collision, the evolutions of $\zeta_{1,2}^{\mathrm{Im}}$ are very similar to what we observed for the $\Delta\phi_i = 3\pi/4$ simulation FIGURE 2.9 This result also supports the initial observation about the $\Delta\phi_i = \pi$ simulation : solitary waves colliding in phase opposition which undergo an elastic collision.

**Phase condition for coherent structures to merge**

Now, we can propose an explanation to the difference of short-times behaviours between the different simulations showed. We have noticed that for two coherent structures propagating with different (mean) amplitudes, their phase difference was a linear function of $t$. We now assume that a collision occurring when the phase difference is equal to, or very close to, $0[2\pi]$ will merge the colliding structures into a single bound-state. Then, we can suggest that the solitary waves propagate and collide (hence with different phase difference each time) until they collide in phase and then merge. During this process, the solitary waves are transformed into bound-states due to non-elastic collisions.

We also assume that a collision with a random phase difference between 0 and $2\pi$ is non-elastic and affect the amplitudes of the solitary waves but further study are required to have a more precise idea. For instance, given the study of few other collisions, we can suggest that the closer to $0[2\pi]$ the phase difference is, the more non-elastic the collision is.

We can also propose a reasoning to explain why the $\Delta\phi_i = \pi$ simulation takes so long to create a unique bound-state. According to our reasoning, with an initial phase difference of $\pi$, all the collisions are elastic and then the solitary waves amplitudes do not change, which implies that the phase difference is still constant equal to $\pi$. For this cycle to end, something, other that collisions which are elastic, must slightly affect the solitary waves amplitudes. We assume that the finite discretization of the box breaks the $x$-symmetry of the system at some point, which causes an asymmetry between the solitary waves and eventually creates non-elastic collisions.

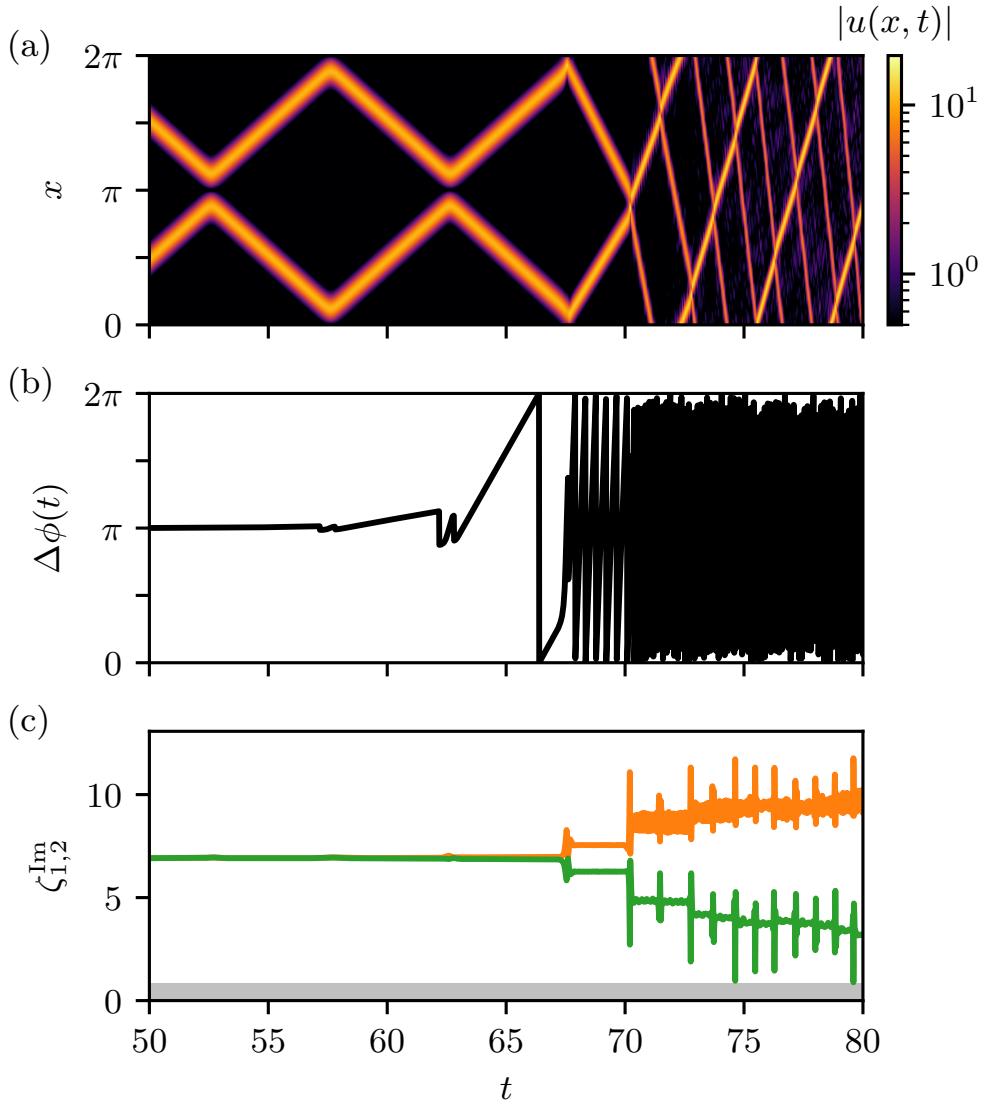


Figure 2.11: **Evolution of $\Delta\phi(t)$ and $\zeta_{1,2}^{\mathrm{Im}}$ for the merging event of the $\Delta\phi_i = \pi$ simulation -** The phase is constant to $\pi$ from $t = 0$ and so are the amplitudes of the solitary waves, attested by $\zeta_{1,2}^{\mathrm{Im}}$ equal to their initial value. The drift of $\Delta\phi$ away from $\pi$ coincide with the first non-elastic collisions.

We do not have yet a definite explanation for this link but a parallel may perhaps be drawn with the conditions for constructive interference. In linear optics, two coherent waves with the same wavelength will interfere in a constructive way if they are in phase and in a destructive way if they are in phase opposition. Given the results of our simulations, we propose that two structures collide inelastically if they are in phase and elastically if they are in phase opposition. The parallel can be easily drawn for the "in-phase" collisions because the inelastic collision leading to a unique structure can be seen as a constructive interference. The "phase opposition" collisions are harder to link with destructive interference because the solitons are not modified by the collisions, which would better correspond to an absence of interference.

There are some limits to our phase difference study. For instance, we highlight the role of the phase difference for, and only for, collisions between structures with the same amplitude and opposite speeds. We recall that keeping $\beta$ fixed constrains the amplitude of the solitary waves. Symmetrical collisions can occur in a quasi-Soliton Turbulence evolution but they are rare compared to collisions between structures of different sizes. Thus, we can say that the phase difference plays a role in the nature of the collisions but its importance has to be compared to the role of the difference of amplitudes and of velocities. More simulations are required to really validate our assumption

**Summary of the section**

- Two 1D-SHE solitary waves launched into a periodic box will undergo inelastic collisions until they merge into a unique coherent structure,
- this coherent structure is found to be a bound-state, with its DST and $(\mathbf{k}-\omega)$ plots signature.
- Solitary waves are transformed into bound-states by undergoing non-elastic collisions.
- The phase difference at a collision controls the nature of this latter, $\Delta\phi = 0$ implies a merging into a bound-state while collisions are elastic for $\Delta\phi = \pi$.

## 2.5 Two 1D-NLSE solitons collisions

We have seen that two 1D-SHE solitary waves in a periodic system will end up in a final bound-state quasi-soliton, with an important role played by the phase difference. To test the universality of this final state, we now initialize the system as two 1D-NLSE solitons (1.10) to see if the system ends up in the same final state. These solitons are defined by $(A_1, v_1 > 0, s_1 = \pi/2, \phi_1)$ and $(A_2, v_2 < 0, s_2 = 3\pi/2, \phi_2)$ which will be precised for each simulation. The positions $s_1 = \pi/2$ and $s_2 = 3\pi/2$ were chosen to maximise the distance between solitons and legitimate the approximation of the double-solitons solution by the linear summation of two solitons. The combination of having $\Delta s$ maximal and solitons tall and thin minimizes the overlapping of the exponential tails. For a single soliton, the amplitude of the tail at $s \pm x = \pi/4$ is less than $10^{-11}$ for the amplitudes $A \gtrsim 10$ we used. All the presented simulations were done with $\beta = 10^{-2}$. The system is kept as a box of length $L = 2\pi$ with periodic boundary conditions and discretized in 2048 points. No forcing nor dissipation are added, thus the system is still conservative which means that total energy $\mathcal{H}$ and the wave-action $\mathcal{N}$ are exactly conserved, respectively to -332 and 80.

The Figure 2.12 presents a set of collisions for $A_1 = A_2 = A = 15$ and $v_1 = -v_2 = 0.5$ and different initial phase differences. The phase differences tested are the same as previously, $\Delta\phi_i = p\pi/4, p \in [\![-3, 4]\!]$.

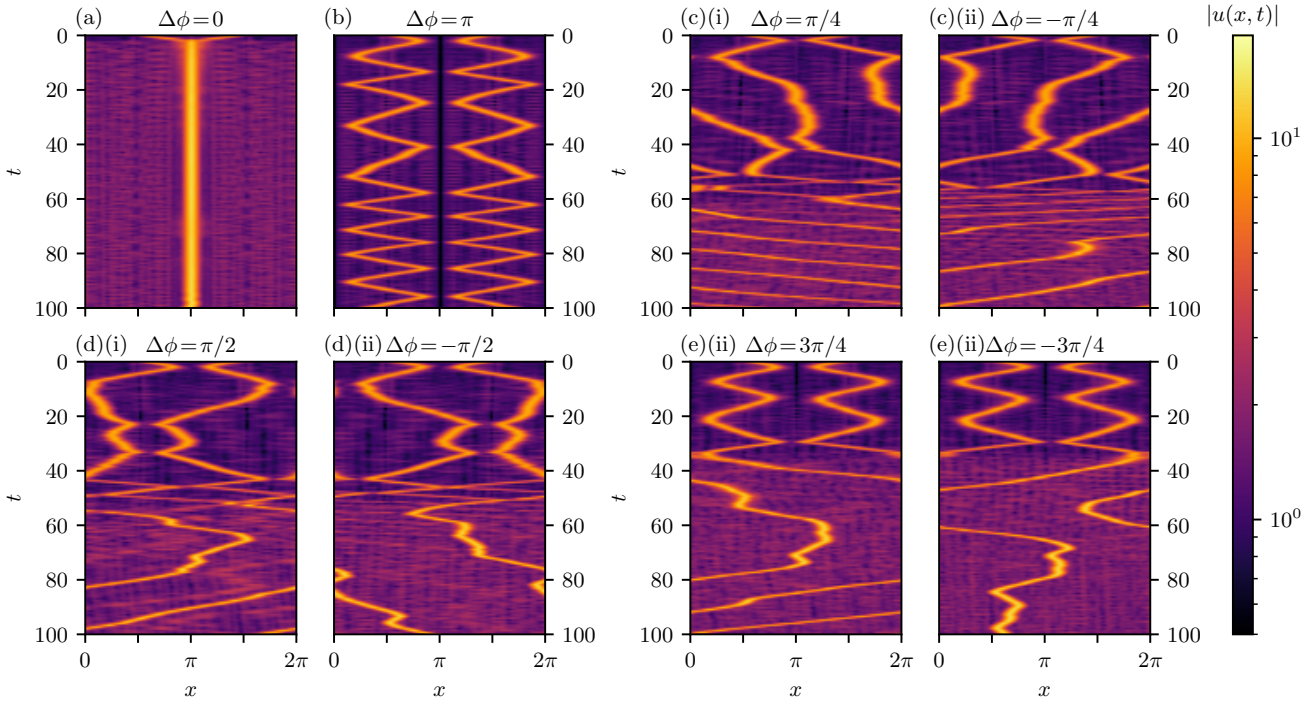


Figure 2.12: **Spatio-temporal dynamics of colliding 1D-NLSE solitons for different initial phase differences** - The colliding initial solitons finally end up in a coherent structure propagating on top of linear waves, exactly like the 1D-SHE solitary waves. The phase difference $\Delta\phi_i$ appears to also play the same role, as the collisions

### 2.5.1 Similar final state than solitary waves collisions

Firstly, we can observe that all the dynamics presented share the same final state (for the simulation $\Delta\phi_i = \pi$ it has not been reached for the time interval displayed), a coherent structure oscillating in width and amplitude, propagating through a box filled up with weakly non-linear waves. Qualitatively, it is the same final state as the bound state observed for both quasi-Soliton Turbulence and colliding solitary waves simulations. The evolution leading to this unique structure strongly recalls the systems studied previously : a series of non-elastic collisions between two oscillating structures leading to the near disappearance of one of the initial structures. We do not name the localized structures *solitons* (apart from $t = 0$ when they really are 1D-NLSE solitons) because these latter are not present in a non-integrable system like the 1D-SHE. The sech-profile 1D-NLSE soliton is not even a solitary wave, it relaxes and emits waves immediately. This phenomenon will be studied more in details in the next section.

As in the previous section, the final structure does not seem to have a constant speed. We still assume that its sudden changes of speeds are due to exchange of momentum with the waves in the system. Moreover, the initial $\{x \to 2\pi - x, v \leftrightarrow -v, \Delta\phi_i \leftrightarrow -\Delta\phi_i\}$ symmetry is broken when the final structure propagates. We again conjecture it is due to the high amplitudes creating differences, at the numerical precision used, between the two simulations. Such differences lead to the simulations being compared ($\Delta\phi_i$ vs $-\Delta\phi_i$) showing different trajectories.

The final structure obtained is characterized with the DST and the double Fourier Transform. The two spectra identify this final state as a bound-state. The $(\mathbf{k} - \omega)$ plot finds parallel lines and the DST spectrum contains two oscillating eigenvalues with large imaginary parts. The correlation between these features and the final oscillating structure is verified with the tests detailed for the qST, *ie* truncation of the function and filtering the $(\mathbf{k} - \omega)$ plot. Obtaining the same final state for now three different types of initial conditions (flat-top spectrum, 1D-SHE solitary waves and 1D-NLSE solitons) suggests the universality of this bound state. To test this universality, we have produced different tableau like FIGURE 2.12 varying the common amplitude $A$ and the speeds $\pm v$. The results we will describe have been observed for many more cases, including initial solitons with different norms of speed.

### 2.5.2 Role of the phase difference

The phase difference appears to play the same role as in 1D-SHE solitary waves collisions. We track the phase difference for the simulations and some results obtained with the study of solitary waves collisions still stand. For instance, two solitons initialized in phase opposition stay in phase opposition until they undergo inelastic collisions and finally merge. We also notice the linear evolution of $\Delta\phi$ between propagating structures. In FIGURE 2.13, we plot $\Delta\phi(t)$ for the times before the final merging for a system initialized as two solitons with amplitudes $A = 14$, speeds $v_i = \pm 3$ and a phase difference $\Delta\phi_i = 3\pi/5$.

The evolution of the phase difference can also be examined theoretically by modelling the structures as oscillating solitons, in resonance with the initial solitons. With the exact formula of the 1D-NLSE soliton (1.10), the phase of a soliton evolves as $\phi(t) = (v^2 - A^2)t/2$, the constant phase being taken null. For a 1D-NLSE soliton, its amplitude and speed $A$ and $v$ are constant, which makes the phase $\phi(t)$ a linear function of time. Then, for two solitons, the phase difference $\Delta\phi$ evolves also linearly as $\Delta\phi(t) = [(v_1^2 - A_1^2) - (v_2^2 - A_2^2)] \times t/2$. To the first order, the colliding structures can be seen as solitons characterized by their mean amplitude and their constant speed. Thus, if the two structures have the same mean amplitude and speed (modulo the sign of their speed), we expect the phase difference not to change in time, more precisely, to keep its initial value. This model appears to describe quite well the simulation with the initial structure in phase opposition. In the general case, when amplitudes and velocities are different, the phase difference evolves linearly in time with a rate which depends on the characteristics of the structures. This conclusion has been observed numerically for all the simulations for which we analyzed the phase difference evolution.

Before analysing precisely this evolution, we need to remind that the method used to detect numerically the structures is very sensitive to the changes of amplitude. More precisely, this method does not work properly when the smallest structure becomes temporarily the biggest one during an oscillation. That is why the phase difference $\Delta\phi$ is not plotted for every time step in FIGURE 2.13, as we only show the times for which the

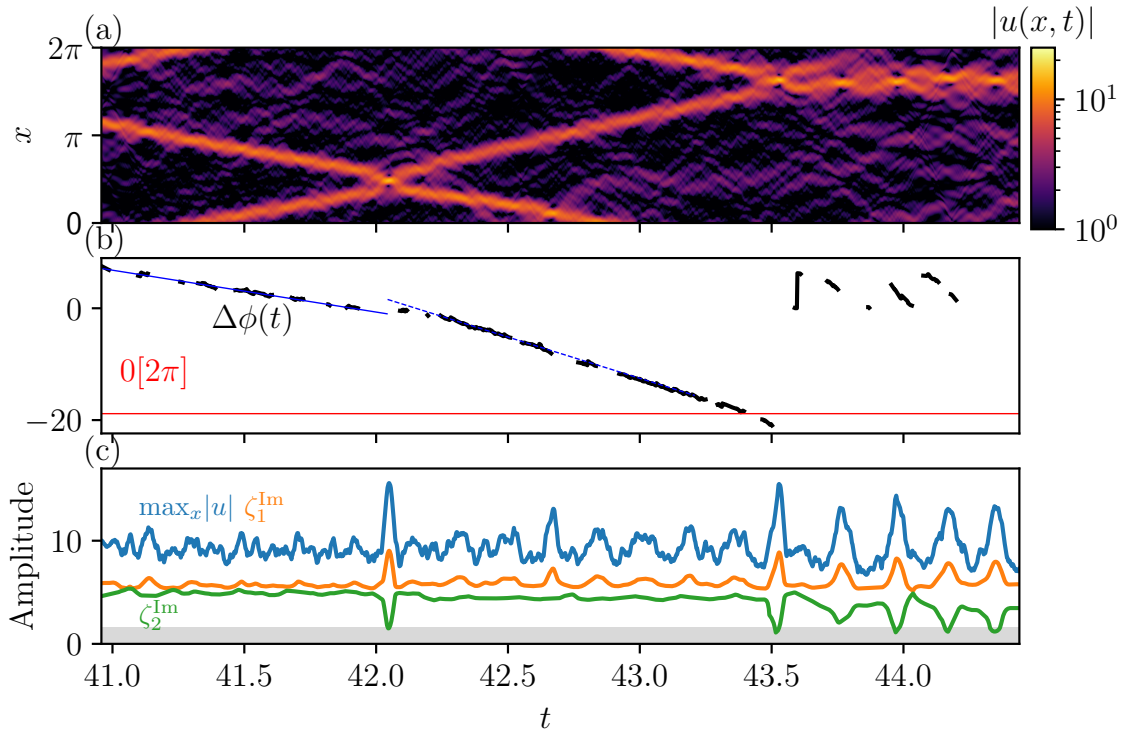


Figure 2.13: **Evolution of $\Delta\phi(t)$ and $\zeta_{1,2}^{\mathrm{Im}}$ for a colliding 1D-NLSE solitons simulation -** During the studied time window, the structures undergo a quasi-elastic collision at $t \simeq 42$ followed by a merging event at $t \simeq 43.5$. Between these interactions, the structures propagate in straight line with oscillating amplitudes and $\Delta\phi(t)$ evolves linearly, with the expected change of slope due to the change of structures amplitudes. With the linear model, the phase difference is very close to 0 modulo $2\pi$ when the structures collide, consistent with the merging happening. Near the merging event, the DST spectrum has the same evolution than it had for 1D-SHE solitary waves merging.

recognition of the structures was good. The phase is computed between 0 and $2\pi$ but is presented here without this modulo restriction to highlight its linear evolutions.

When the structures propagate between collisions, the phase difference is linear function of $t$ as expected. The quasi-elastic collision at $t \simeq 42$ in Figure 2.13 slightly changes the characteristics of the structures, particularly by reducing the amplitude of the structure with positive speed. Thus, we expect the ratio $\Delta\phi/t$ to change at the collision. Indeed, these ratio does change, being measured to, in absolute values, 7.49 before and 14.74 after (slopes of the linear models in plain and dashed blue lines). Assuming that the changes in the speed can be neglected and that only the changes of amplitude counts for $|\Delta\phi/t| \sim |A_1^2 - A_2^2|$, this increase of the slope was expected as the collisions (slightly) increases the amplitude of one of the coherent structure and decreases the other one. However, if we model these structures by solitons having their speed and their mean amplitudes, we obtain the ratios 11.08 and 17.78. These theoretical ratios overestimate the ones found numerically but they have the same increasing evolution. Thus, the theoretical model seems qualitatively accurate but lacks the quantitative precision.

Another important result of this phase difference evolution is the phase difference found at the merging event near 43.5. For this collision, the structures cease to be distinguishable at $t = 43.4135$ At this time, we can not measure the phase difference exactly but the linear model finds $|\Delta\phi(t = 43.4135)| = -18.93 \equiv -0.08[2\pi]$. This value is very close to 0. This result supports our hypothesis that, in the non-integrable 1D-SHE system, a necessary condition for two coherent waves to merge is that their phase difference must be zero.

Modelling the interacting structures as solitons with their mean amplitudes and velocities may seem quite naive but is able to predict qualitatively the evolution of the phase difference. In next section we will detail more results obtained with this model.

### 2.5.3 Differences

Even if colliding 1D-SHE solitary waves and 1D-NLSE solitons lead to a single bound-state as the final state with non-elastic collisions of localized structures, there are some differences between these two initial conditions. First, we can notice that the initial solitons emit linear waves than can be seen on the $(x - t)$ plot, contrary to 1D-SHE solitary waves which create substantial waves only at the non-elastic collisions. Moreover, with the DST and $(\mathbf{k} - \omega)$ spectra, we can show that the interaction structures are always bound-states. Contrary to 1D-SHE solitary waves staying solitary waves until the first substantially non-elastic collision, the 1D-NLSE solitons immediately turn into bound-states and then propagate and interact as bound-states until they merge into a final one. The final bound-state is larger than the colliding ones so it is easier to characterize as such, but we can still observe the properties of these latter. As we will see in the next section, these two phenomena (emission of waves and transformation into bound-states) are intrasically linked.

**Summary of the section**

- Initial 1D-NLSE solitons collide ineslatically to create a single bound-state, exactly like the 1D-SHE solitary waves.
- Again, the merging of coherent structures seems only possible for $\Delta\phi = 0$.
- The main difference with 1D-SHE solitary waves collisions is the immediate transformation of 1D-NLSE into bound-states.

## 2.6 Study of the bound-state

### 2.6.1 Relaxation of the 1D-NLSE soliton into a bound-state

Given the results of our previous studies, we now hypothesise that a bound-state propagating on top of linear waves is the universal final state for all initial conditions for the 1D-SHE. We quickly recall what we define as a bound-state : a coherent structure, oscillating in amplitude and in width, characterized by two DST eigenvalues oscillating

in phase opposition and parallel lines in the $(\mathbf{k}-\omega)$ spectrum. To study this particular structure, we will study the evolution of an initial single 1D-NLSE soliton in the 1D-SHE system, still characterized by the non-integrability parameter $\beta = 10^{-2}$. The 1D-NLSE soliton is defined by $A = 20, v = 4, s = 0, \phi = 0$, which set $\mathcal{H} = 388$ and $\mathcal{N} = 40$, quantities again conserved by the dynamics. The box is discretized with 4096 points.

**Identification of the bound-state**

In FIGURE 2.14(a) we plot the $(x-t)$ evolution the soliton. On this spatio-temporal dynamics, the times $t = 0, 0.056, 0.432, 0.504$ are indicated with grey lines and the corresponding profile snapshots are compared FIGURE 2.14(b). The amplitude $A$ of the structure falls from its initial value 20 to 8.52, reached at $t = 0.056$. Then, the amplitude oscillates periodically around $\bar{A} \simeq 10.5$. Its oscillating width is also clearly visible on the snapshots profiles in FIGURE 2.14(b) and this oscillation is correlated with the amplitude evolution. We only plot here snapshots at four different times but detailed evolution of the structure amplitude $A$ and width $\ell_{1/2}$ (defined as the full-width at half-amplitude) are displayed for $\beta = 10^{-2}$ in FIGURE 2.18.

The bound-state nature of the oscillating structure for $t > 0.056$ is verified by analysing the DST spectrum, particularly the time series of $\zeta_{1,2}^{\mathrm{Im}}$ (displayed FIGURE 2.15(a),(b), and the $(\mathbf{k}-\omega)$ spectrum FIGURE 2.15(c), with the exact overlap of the secondary peaks of the PSD $|\hat{\zeta}_1(\omega)|^2$ with the parallel lines of the $(\mathbf{k}-\omega)$ dynamics (we can even notice observe the good overlap for the tiny tertiary peaks). The oscillating structure is indeed a bound-state. The frequency of $A$ and $\zeta_{1,2}^{\mathrm{Im}}$ was measured at $\Omega = 45.0$.

We can also notice the creation of small waves, visible on the $(x-t)$ dynamics, on the snapshots profiles and on the $(\mathbf{k}-\omega)$ spectrum. These waves propagate in the whole box and go through the quasi-soliton, disrupting the evolution of its maximum. Waves are emitted for very small times, suggesting that they are due to the relaxation of the initial soliton, and from $x \equiv 0[2\pi]$. Finally, we also observe that the bound-state propagates in straight line, with a constant speed. This is the case up to the biggest time reached in simulations $t = 1000$.

**Analysis of the bound-state**

Now that that we have established that the relaxation of an 1D-NLSE soliton leads to a bound-state, we can study it more in detail.

First, the DST spectra displayed in FIGURE 2.14(c) show that when $\zeta_2^{\mathrm{Im}}$ is minimal, it is null. We can even observe that $\zeta_2^{\mathrm{Im}}$ does not exactly oscillate as a sine function, but alternates between being constant equal to 0 and having a sine evolution during a half-period (this behaviour is clear in the FIGURE 2.15(a)). We can suppose that this is due to the amplitude of the bound-state being not large enough.

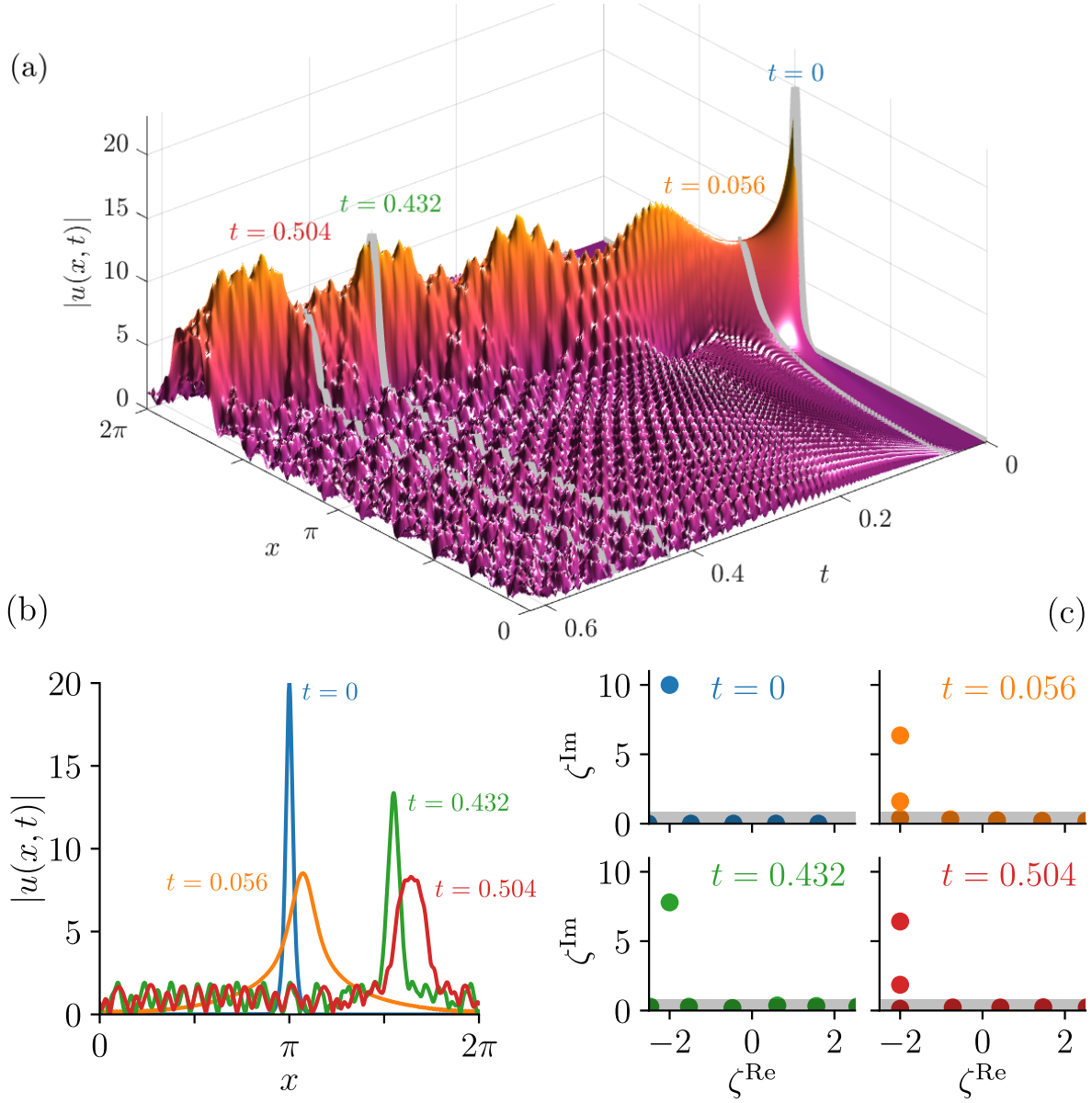


Figure 2.14: **Propagation of a 1D-NLSE soliton in the 1D-SHE** - The 1D-SHE is characterized by $\beta = 10^{-2}$ (a) $(x-t)$ plot : the soliton amplitude drops down and starts to oscillate around approximately the half of its initial value. This amplitude oscillations comes with an oscillation of its width, both oscillations being with the same frequency. This is the sign of a bound-state (b) Snapshots of $|u(x,t)|$ for different times $t$ highlighted on the $(x-t)$ plot. Amplitude and width oscillations are clearly visible. (c) DST spectrum for these times. The phase opposition oscillations of $\zeta^{\mathrm{Im}}_{1,2}$ confirm the bound-state nature of the structure.

Secondly, an interesting specificity of this bound-state can be seen with the DST spectra displayed FIGURE 2.14(c) : the equality, for each time when $\zeta^{\mathrm{Im}}_2$ is above the threshold, $\zeta^{\mathrm{Re}}_1 = \zeta^{\mathrm{Re}}_2$. We recall that for the bound-states observed with the previous initial conditions (flat top spectrum and colliding structures), $\zeta^{\mathrm{Re}}_2$ was evolving in time, even displaying oscillations in phase opposition with $\zeta^{\mathrm{Re}}_1$ in the flat-top simulations. For the bound-state

created by an initial 1D-NLSE soliton, the two eigenvalues $\zeta_1$ and $\zeta_2$ have the same real part. We recall that the real part is directly proportional to the speed of the soliton in the integrable DST framework. Given this, the terminology *bound*-state is even more appropriated in this case because the two solitons expected in the integrable case would have the same speed at same time and thus would constantly overlap. Moreover, that correspond to what Zakharov and Shabat call a bound-state in their pioneering article [9]. In this article, the authors define what a bound-state is for the 1D-NLSE : two eigenvalues with the same real part and different imaginary parts $\eta_1$ and $\eta_2 < \eta_1$. They prove that these two eigenvalues would create a coherent structure oscillating in amplitude with the frequency $2(\eta_1^2 - \eta_2^2) = 2({\zeta_1^{\mathrm{Im}}}^2 - {\zeta^{\mathrm{Im}}}^2)$, taking into account our factor 1/2 for the laplacian.

As we study the 1D-SHE, which is not integrable, $\zeta_1^{\mathrm{Im}}$ and $\zeta_2^{\mathrm{Im}}$ are functions of time but we can compute $2(\langle\zeta_1^{\mathrm{Im}}\rangle_t^2 - \langle\zeta_2^{\mathrm{Im}}\rangle_t^2) \simeq 94.3$. This value needs to be compared to the frequency of the evolution of $\max_x|u(x,t)|$ and $\zeta_{1,2}^{\mathrm{Im}}$, $\Omega \simeq 45$. These values are obviously not equal but the factor $\simeq 2$ indicates that a more subtle link may exist.

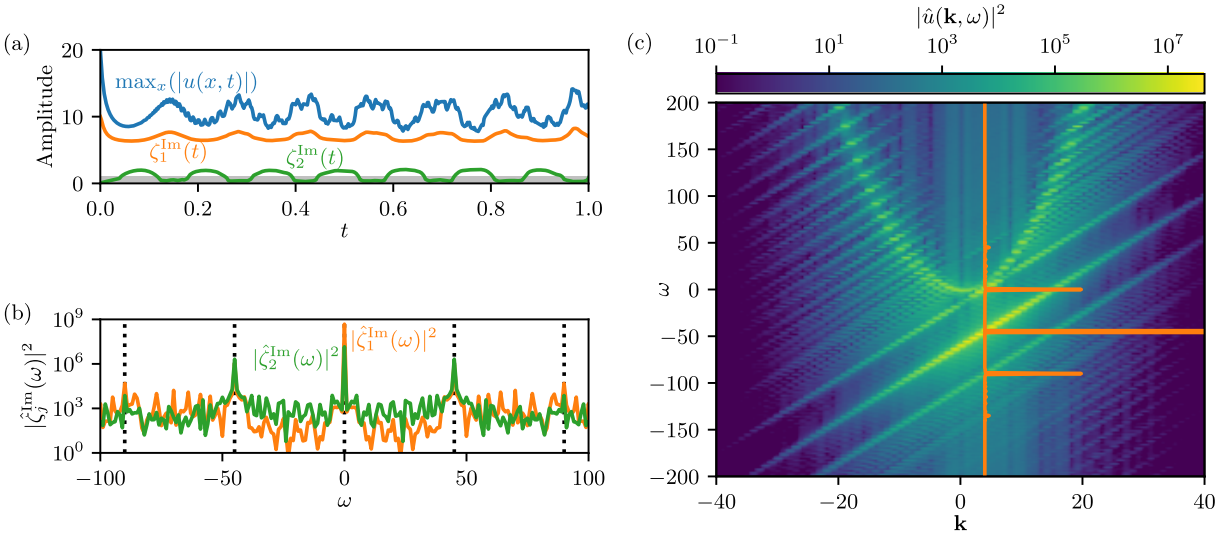


Figure 2.15: **Diagnostic analysis of the bound-state -** (a) Time series of $\zeta_{1,2}^{\mathrm{Im}}$ compared to the amplitude. These evolutions are characteristic of a bound-state. (b) PSD $|\hat{\zeta}_{1,2}^{\mathrm{Im}}(\omega)|^2$. $\zeta_{1,2}^{\mathrm{Im}}(t)$ oscillate with the same frequency $\Omega = 45$. (c) $(\mathbf{k},\omega)$ spectrum. The parallel lines are the signature of the the bound-state and the PSD of $\zeta_1$ perfectly superimposes on it.

In the last section, we modelled the colliding bound-states by solitons characterized by their mean amplitude $\bar{A}$ and mean velocity $\bar{v}$ and this simple model predicted qualitatively well the evolution of the phase difference after a non-elastic collision. We will now use this model to interpret the $(\mathbf{k}-\omega)$ spectrum obtained with this bound-state, displayed Figure 2.15(c). This $(\mathbf{k}-\omega)$ spectrum can be understood in a self-consistent way if we model the quasi-soliton by a pure soliton with a constant speed $v = 4$ but an oscillating amplitude $A(t)$. To compute the position $(\mathbf{k}^*, \omega_{\mathrm{sol}}^*)$ of the straight line for this solitonic model, we consider its averaged amplitude $\bar{A}$. The center is thus computed at $(\mathbf{k}^* = v = 4, \omega_{\mathrm{sol}}^*(\bar{A}) = \frac{v^2 - \bar{A}^2}{2} \simeq -47.1)$ which is find in good accordance with the mea-

sured position ($\mathbf{k}^* = 4, \omega^*_{\text{b.-s.}} - 45$). We can conclude, firstly, that a soliton representing the average bound-state would have the same main line in the $(\mathbf{k} - \omega)$ spectrum and secondly, that the frequency $\omega^*_{\text{b.-s.}}$ of the bound-state is well approximated by the same frequency computed for a soliton characterized by $\bar{A}$, meaning $\omega^*_{\text{sol}}(\bar{A})$.

Thus, the main line in the $(\mathbf{k} - \omega)$ spectrum is assumed to be the leading-order effect of the bound-state with its averaged amplitude. However, this single consideration of the main line does not take into account the oscillating amplitude of the solitonic model. To do so, let us write the pure soliton profile $u^{\text{NLSE}}_{\text{sol}}$ (1.10) in the moving frame $x - vt$, ignoring the sech-term and constant phase terms

$$u^{\text{NLSE}}_{\text{sol}}(x,t) \sim Ae^{-i\omega^*_{\text{sol}}t}. \tag{2.8}$$

The phase of the soliton rotates in the complex plane with the frequency $\omega^*_{\text{sol}} = \frac{v^2 - A^2}{2}$ which is equal to $\omega^*_{\text{b.s.}}$ at the lowest order (*ie* for $A = \bar{A}$) according to the previous result. For an oscillating amplitude, as we have found that $A$ oscillates with the same frequency $\Omega$ as the eigenvalues $\zeta_{1,2}$, we modulate $A$ which becomes $A = \bar{A} + 2\Delta A \cos(\Omega t)$ with $\Delta A$ the strength of the modulation. The main point of this computation it to realize that the frequency of the amplitude oscillations, $\Omega = 45.0$ is very close to the frequency of the phase evolution $\omega^*_{\text{sol}}(\bar{A}) = 47.1$ for a soliton defined by $\bar{A}$. We assume that they are equal, $\omega^*_{\text{sol}} = \Omega$. With the Euler formula, we now have

$$u^{\text{NLSE}}_{\text{sol}}(x,t) \sim \bar{A}e^{-i\Omega t} + \Delta A + \Delta A e^{-i2\Omega t} \tag{2.9}$$

As we have $\bar{A} > \Delta A$, this function has a main component oscillating at $\Omega$ and two sidebands at 0 and $2\Omega$, as observed experimentally. Consequently, this model of a pure soliton with an amplitude oscillating with the same frequency as the soliton phase itself succeeds to explain the three solitonic traces in the $(\mathbf{k} - \omega)$ spectrum.

To complete the study, we can have a look at the two states of the bound-state, displayed Figure 2.16 compared to soliton models with the same maximum. We observe that when the bound-state is tall-and-thin (a), with only $\zeta_1$ above the threshold, the function is modelled accurately by the soliton model, which is consistent with the unicity of $\zeta_1$. We also computed that this state of the bound-state maximizes the non-linearity ratio $|\mathcal{H}_4|/\mathcal{H}_2$ of the function, which is again consistent with the function showing a profile close to a soliton. On the contrary, when the second eigenvalue is also above the threshold and $\zeta_2^{\text{Im}}$ maximum, the profile $|u|$ does not correspond to a solitonic model. As expected, this state minimizes the non-linearity ratio.

We only present here the detailed results of the diagnostics for the initial soliton characterized by $A = 20$ and $v = 4$ but this studied has been performed for other $(A, v)$ at $\beta = 10^{-2}$. Note that the speed of the soliton does not affect at all the behaviour of the initial soliton. For all the tested velocities, the quasi-soliton keeps the initial speed during the relaxation and the shape of the bound-state stays unchanged. Such a result was expected, given the galilean invariance of the 1D-SHE. The results are quantitatively the same for solitons amplitudes between 15 and 30 but further studies (such as the phase

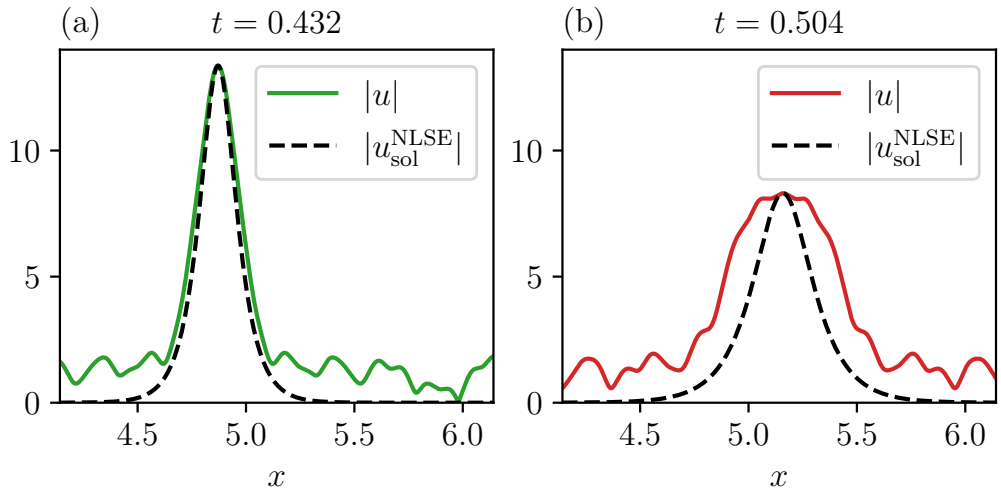


Figure 2.16: **NLSE soliton model of the bound-state -** For the times specified, we compare the bound-state with an 1D-NLSE soliton with the same amplitude. At $t = 0.432$, the function shows a great concordance with the sech model, which is consistent with the DST spectrum at this time being very close to one pure soliton. At $t = 0.504$, the function is considerably wider than the sech profile. This observation is also supported by the DST spectrum, found with two eigenvalues instead of an unique one.

diagram for the qST in section 2.3.4) are required to have a more precise understanding.

**Discussion**

We would like now to summarize our results, discuss some explanations and link them with systems studied in the literature.

We have found that a pure soliton solution of the 1D-NLSE, launched into the 1D-SHE immediately relaxes, emits waves and ends up in a bound-state, which exhibits the same properties than the bound-states obtained with other initial conditions. This bound-state is robust and is the final state of the system. The instantaneous relaxation of the initial pure soliton was expected as it is not a stationary solution of the 1D-SHE. The emitted waves are not damped and, thus, propagate freely in the system and can interact with the bound-state. This interaction is possible because the system is not integrable, in the 1D-NLSE, solitons and waves do not interact. These waves-quasi-soliton interactions can particularly be seen on the $(\mathbf{k} - \omega)$ spectrum with the upper secondary soliton being tangential to the parabola. In this region, the upper secondary line is more intense than the lower one. We assume that this is due to the waves-quasi-soliton interaction because at this point, the waves and the quasi-soliton have the same group speed, making the interaction resonant. We make the hypothesis that these interaction are responsible for the modulation of the amplitude. For now, we do not have a clear mathematical explanation for this link. This is left to future work. Similarly, we do not know yet the mechanism which turns the 1D-NLSE soliton into a bound-state.

Given that all the different tested initial conditions converge towards this bound-state, we assume that it really represents a statistical attractor for the 1D-SHE.

It is not the first time that DST is applied to a non-integrable system. In [89], the authors study the propagation and interaction of an ensemble of soliton with random amplitudes and speeds (called a soliton gas) numerically and experimentally in a 1D water tank with the help of DST analysis. The propagation of waves in this tank is governed by the 1D-NLSE to the lowest order but the experiment takes into account next-order terms. A soliton gas is created and is let to evolve in both a simulation with 1D-NLSE and an experiment. As 1D-NLSE is integrable, the DST spectrum does not change in time. On the contrary, the DST analysis of the experimental data show that the eigenvalues drift in the complex plane. More precisely, the imaginary parts decrease, corresponding to solitons getting smaller. As in our study, the DST is found to be qualitatively accurate to characterize the non-integrable system.

In [90], the DST is also used to characterize a laser beam propagating through an optical fiber. Once again, studying experimental data implies to take into account the losses of the fiber and the gain of the laser. Such effects break down the integrability of the 1D-NLSE model. Under some conditions, if the gain value is sufficiently small, the laser profile shrinks periodically with an increase of the amplitude. This phenomenon is observed in the DST spectrum with the eigenvalues oscillating in both real and imaginary parts (corresponding to solitons speeds and amplitudes) with the same period as the laser profile. Such results are extremely close to the ones we reported earlier, and have also been reported by [91], for solitonic propagation in mode-locked fiber laser and in [11] for a given non-integrable model of a laser system. Finally, this bound-state is also observed (and named so) in [83]. The initial state is prepared by adding a pumping term to the 1D-NLSE which creates quasi-solitons, which is possible because the presence of the pumping breaks the integrability of the 1D-NLSE. When the pumping is turned down, the system comes back to integrability and the spatio-temporal dynamics shows several bound-states.

In order to make the DST analysis more rigorous, a possibility is to develop a perturbation theory. As non-integrable equation can be seen as a perturbation to an integrable equation, one can apply a perturbation theory to the Lax pair of the integrable equation and derive equations for the evolution of the DST spectrum. Such a theory is developed in [92] for different non-linear equations such as 1D-NLSE. More precisely, the integrable non-linear equations are modified by various ways (higher order dispersion term, dissipation terms,...) and the perturbation theory predicts the evolution of the DST spectrum. An interesting case for the 1D-NLSE taken out of integrability by dissipative terms is the decrease of real and imaginary parts of eigenvalues, corresponding to slowed and shrinking solitons.

Finally, "oscillating solitons" have already been reported. In [93], the authors study the relaxation of an initial amplified sech-profile solitons in the 1D-NLSE. The amplitude of this soliton is found to oscillate around an average value bigger than its initial one.

These oscillations are characterized by an exponentially decreasing amplitude. Thus, the final state is an oscillating structure on top small wave fluctuations. A variational approach developed in this article found this final state to be a minimizer of energy in a microcanonical ensemble. More precisely, the authors precise than having an initial amplification factor $\gamma$ below 0.5 or above 1.5 changes the number of eigenvalues found with the DST. For $\gamma > 1.5$, the DST spectrum is made of two eigenvalues with the same real part but with well-separated imaginary parts. Since the equation studied here is pure 1D-NLSE, this DST spectrum is constant in time and the second eigenvalue survives.

To the best of our knowledge, our work is new on its approach, as we study a non-integrable system with both DST and spatio-temporal spectra. Comparing these two methods has the advantage of verifying the results given by the DST with another method and to characterize the system in different ways. For instance, the bound-state, as final state of the relaxation of the initial pure soliton, is characterized by the parallel lines in $(\mathbf{k} - \omega)$ plot and with the two oscillating eigenvalues in the DST spectrum. The exact overlap of the PSD $|\hat{\zeta}_1^{\mathrm{Im}}(\omega)|^2$ with the parallel lines of the $(\mathbf{k} - \omega)$ spectrum is a strong result which indicates that both diagnosis are consistent which other.

### 2.6.2 Comparison for different $\beta$ for early times

We highlight again the fact that, given the expression of the 1D-SHE, the equation is integrable for $\beta = 0$ as it becomes the 1D-NLSE and the non-integrability measurement increases with $\beta$. We will compare simulations done for values of $\beta$ between 0 and 1 to find a tendency. We expect the differences between the initial pure soliton and the final bound-state to fade for $\beta \to 0$.

#### Comparison of the dynamics

In Figure 2.17, we compare the spatio-temporal dynamics for different values of $\beta$ and for early times $0 \leqslant t \leqslant 1$. As expected, the larger $\beta$ is, the stronger the effects of non-integrability are. At $\beta = 0$, the pure soliton propagates without any modification, in accordance with the equation being integrable. For $\beta = 10^{-4}$, the impacts of the non-integrability are not easily visible, the solitons oscillations and the created waves have a very small amplitude. Such effects are so important for $\beta = 5 \times 10^{-2}$ that the trace of the initial soliton is barely visible, it has almost entirely collapsed. The initial radiation of waves is very clear and their maximum speed appears to be independant from $\beta$. For $\beta = 1$, the soliton seems to have disappeared at $t = 1$, fully converted into waves which are bigger than for $\beta = 10^{-2}$. The early quasi-disappearance of the initial soliton can be confirmed by the DST analysis of the function and its spatio-temporal spectrum. For $\beta = 1$, at $t = 0.129$, the system is organized as waves propagating on top of a small and large bump which is likely to be the remnant of the initial soliton. However, the DST spectrum contains no eigenvalues above the threshold.

It is clear with the comparison of the $(x-t)$ plots, that the frequency and the strength of the amplitude oscillation depends on $\beta$. Figure 2.18(a) plots the time evolution of

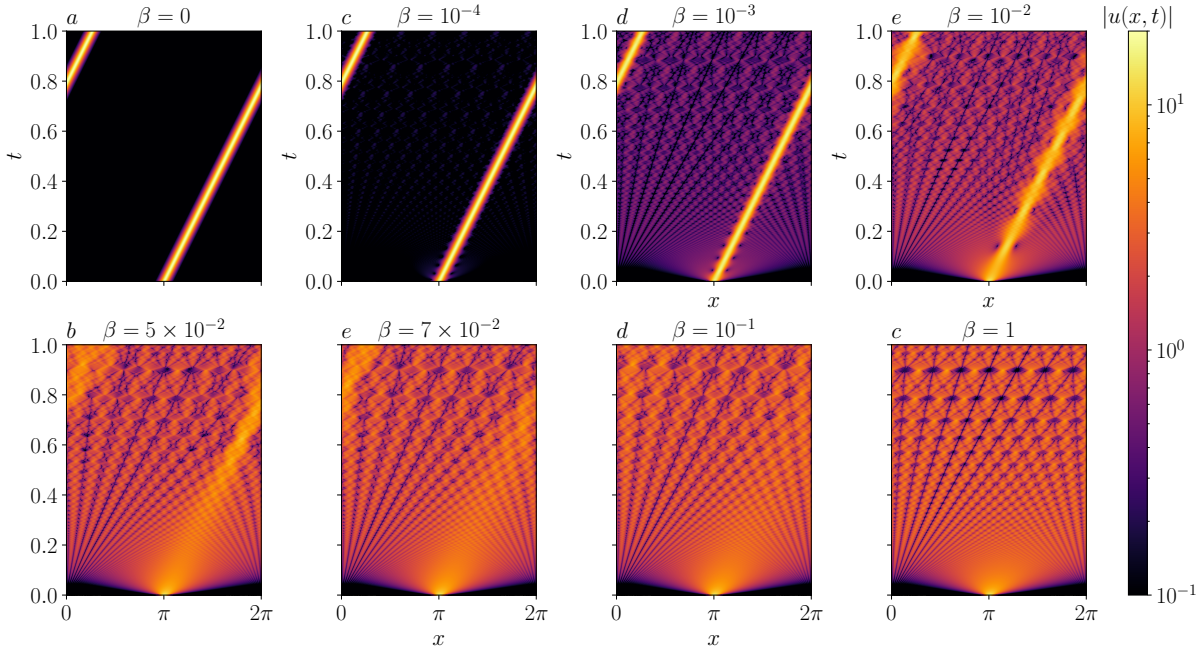


Figure 2.17: **Spatio-temporal dynamics of an NLSE-soliton launched in the 1D-SHE for different non-integrability parameter** $\beta$ - For $\beta = 0$, the soliton propagates without alteration as the equation. For $\beta > 0$, the higher $\beta$ is, the more the initial soliton relaxes. This relaxation comes with larger waves. For $\beta = 1$ the initial soliton seems to have been completely disintegrated into weakly non-linear waves.

$\max_x(|u(x,t)|)$, which is assumed to be the amplitude $A(t)$ of the bound-state, for different values of $\beta$. Decreasing $\beta$ (*ie* going back to integrability) has two effects, the averaged amplitude $\bar{A}$ increases and the amplitude of its oscillations diminishes. As these initial relaxation of amplitude and its oscillations are the effects of non-integrability, their attenuation is consistent, as the system gets closer to integrability. $\beta = 0$ features a constant amplitude, as expected for the propagation of an 1D-NLSE soliton in the 1D-NLSE.

**Re-appearance of the initial solitonic structure**

The initial solitonic structure will re-appear for larger times. As we see on the large-time $(x-t)$ plot FIGURE 2.19, solitonic structures are visible very temporarily near $t = 6.28$. Corresponding snapshot profiles are plotted FIGURE 2.20 with their DST spectrum. For $t = 6.053$, the function does not show any solitonic component neither on the snapshot profile, neither on the DST. Three eigenvalues are at the threshold level but none of them has an imaginary part as large as we obtained for the bound-state. At this time, the function is just linear waves modulated by the initial soliton remnant by without soliton or quasi-soliton behaviour. Then, progressively, interferences start to occur between overlapping waves and a localized structure grows close to $x - \pi = \pi$, corresponding to $x \equiv 0[2\pi]$. This position, which is unique in the periodic system, correspond to where the initial waves are created. The growth of the localized structure ends at $t = 6.267$, when the DST spectrum is made of a single eigenvalue with a maximum imaginary part. At this

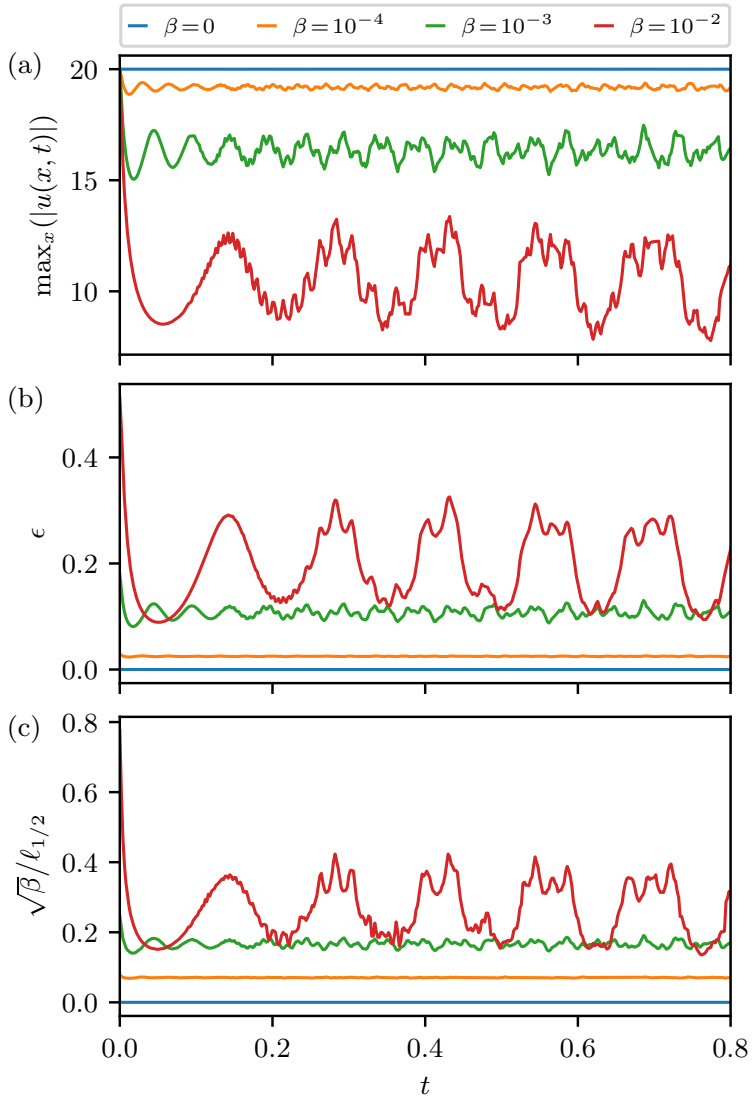


Figure 2.18: **Time evolution for different $\beta$ of three quantities:** (a) **the quasi-soliton amplitude,** (b) **the deviation of 1D-SHE interaction Hamiltonian from the 1D-SHE one,** (c) **the ratio of characteristics integrable and non-integrable lengths. -** These three quantities have similar evolutions. For $\beta = 0$, they are all constant in time and equal at their value for the NLSE. For $\beta > 0$, they oscillate in time around a mean value which drifts away from the $\beta = 0$ value. This drift represents the non-integrability effect which get more important with $\beta$.

time, the linear waves have been grouped into one main peak, modeled with a very good agreement by a sech function, and side secondary lobes. After this maximum, a second eigenvalue rises from zero while the main one goes down in the complex plane, both with the same real part. This evolution strongly reminds us the bound-state behaviour. Once they have the same imaginary part, their real parts change symmetrically around $-2$. This spectrum is illustrated FIGURE 2.20 and the corresponding two solitonic structures are visible on the snapshot and on the $(x - t)$ plot. These two eigenvalues will slowly go down and disappear. This is consistent with the $(x - t)$ plot, where this structure

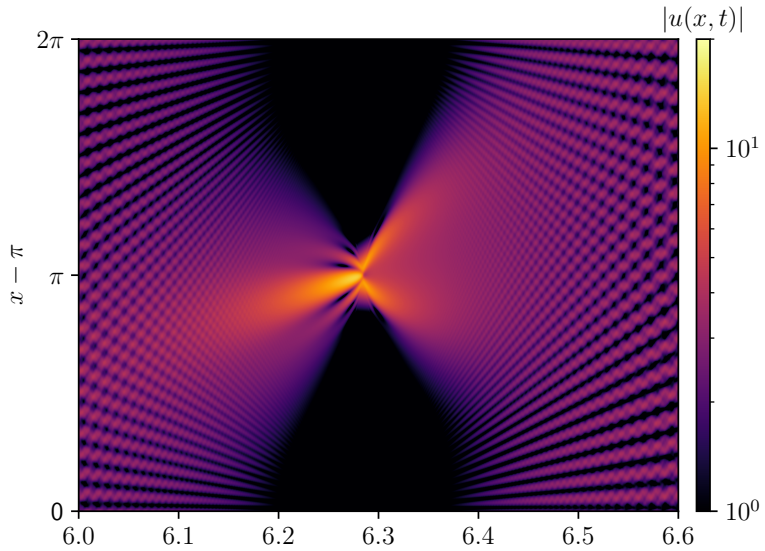


Figure 2.19: **Spatio-temporal dynamics of the system around the solitonic re-appearance -** At $t = 6$, the system is mostly made of waves modulated by the trace of the initial soliton. As the system evolve, the soliton trace grows until all the wave-action in the system is concentrated in a localized structure with a central main peak and side lobes. This structure quickly breaks into two smaller ones propagating with opposite speeds which slowly disintegrate into waves.

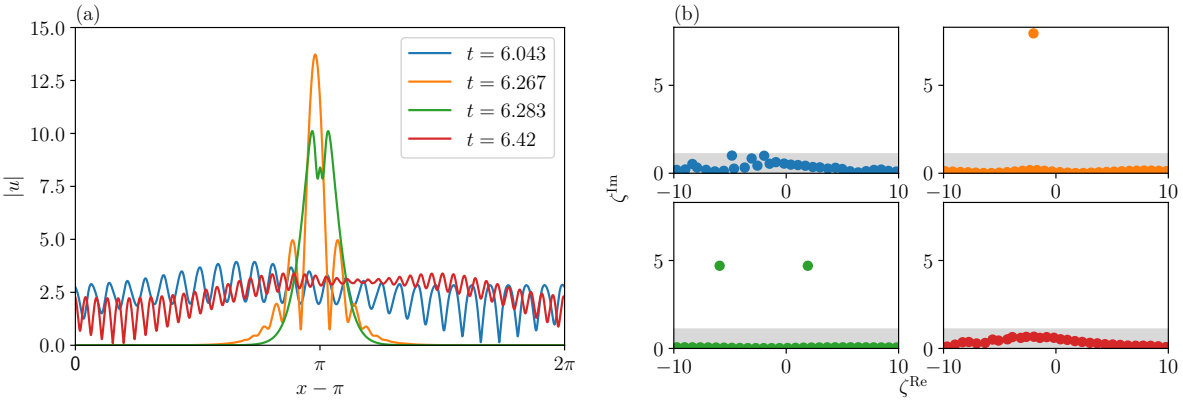


Figure 2.20: **Evolution of the function profile** (a) **and DST spectrum** (b) **during the re-localization of the function -** The "condensation" occurs for modulated waves defined by a spectrum with few eigenvalues barely at the threshold, and it creates a localized structure with a main sech-profiled peak and side smaller lobes. This state is characterized by an unique eigenvalue. This structure quickly breaks into two contra-propagating sech-profiles also seen on the DST spectrum. Finally, the function will radiate waves again and disintegrates again into a wave state without any DST eigenvalue.

radiates waves. At $t = 6.42$, the system is back into only waves, observation supported by the DST spectrum with no eigenvalues above the threshold. We can consider that, from $t = 2\pi$, the relaxation of the localized structure just appeared is similar to the relaxation of the initial 1D-NLSE soliton.

We can explain this re-appearance of the localization of the initial condition with the waves created initially. Assuming that the initial pure soliton fully disintegrates into waves, it creates waves of waves-vectors $p \times \Delta k$, with $p \in \mathbb{Z}$ and $\Delta k = 1$, the Fourier space discretisation in our simulations. With the dispersion relation $\omega_{\mathbf{k}} = \mathbf{k}^2/2$, their group velocity is given by $v_g^p = \frac{\mathrm{d}\omega_{\mathbf{k}_p}}{\mathrm{d}\mathbf{k}^p} = \mathbf{k}_p = p$. Thus, after a time $T$ the wave with wave-vector labelled $p$ has propagated through a distance $d^p = v_g^p \times T = pT$. For the particular case $T = 2\pi$, we find that the $p-$ wave travels a distance $p2\pi$, which is found to be $pL$, with $L = 2\pi$ the length of the periodical box in which we study the 1D-SHE. That implies that after a time $2\pi$, all the waves are back to the position where they were emitted, *ie* $x \equiv 0[2\pi]$. Consequently, the function at $T = 2\pi$ is expected to exhibit a localized structure with non-linear interactions between the waves. Due to non-linear interactions between waves and the initial soliton, the initial solitonic profile can not be exactly recovered. This quasi-recurrence of the initial state can be qualitatively linked with the FPUT problem observations [94].

**Discussion**

To summarize the comparison of evolution with different values of $\beta$, we found that the consequences of the non-integrability increase with the degree of non-integrability. For $\beta$ sufficiently large, these effects are so important that the soliton is disintegrated into linear waves during the initial collapse. The interpretation of the disappearance of the soliton for large $\beta$ is quite sensitive because increasing $\beta$ has three different impacts on the system.

First, we recall the expressions of the quadratic and interaction Hamiltonians $\mathcal{H}_2^{\mathrm{SHE}}$ and $\mathcal{H}_4^{\mathrm{SHE}}$ for the 1D-SHE

$$\mathcal{H}_2^{\mathrm{SHE}} = \int \left|\frac{\partial u}{\partial x}\right|^2 \mathrm{d}x, \quad \mathcal{H}_4^{\mathrm{SHE}} = -\int \frac{1}{2}\left[\left(1 - \beta\frac{\partial^2}{\partial x^2}\right)^{-\frac{1}{2}}|u|^2\right]^2 \mathrm{d}x. \tag{2.10}$$

With these expressions, it is clear that $\mathcal{H}_2^{\mathrm{SHE}}$ does not depend on $\beta$, while $\mathcal{H}_4^{\mathrm{SHE}}$ does. More precisely, for a given function $u(x)$, the non-linear energy is a decreasing function of $\beta$. Reasoning with the initial solitonic state given by $(A = 20, v = 4, s = \pi, \phi = 0)$, which is the same for all $\beta$, it means that the initial total energy decreases with $\beta$ and the non-linear ratio $\chi^{\mathrm{ini}} = |\mathcal{H}_4^{\mathrm{SHE}}(t = 0)|/\mathcal{H}_2^{\mathrm{SHE}}(t = 0)$ decreases with $\beta$. Note that the total energy of this conservative system is determined by its initial value, on the contrary, $\chi$ is left free to evolve. The total energy and initial non-linearity ratio are plotted FIGURE 2.21. Their evolutions with $\beta$ are the ones expected from the discussion above. From this figure we can roughly determine three regimes,

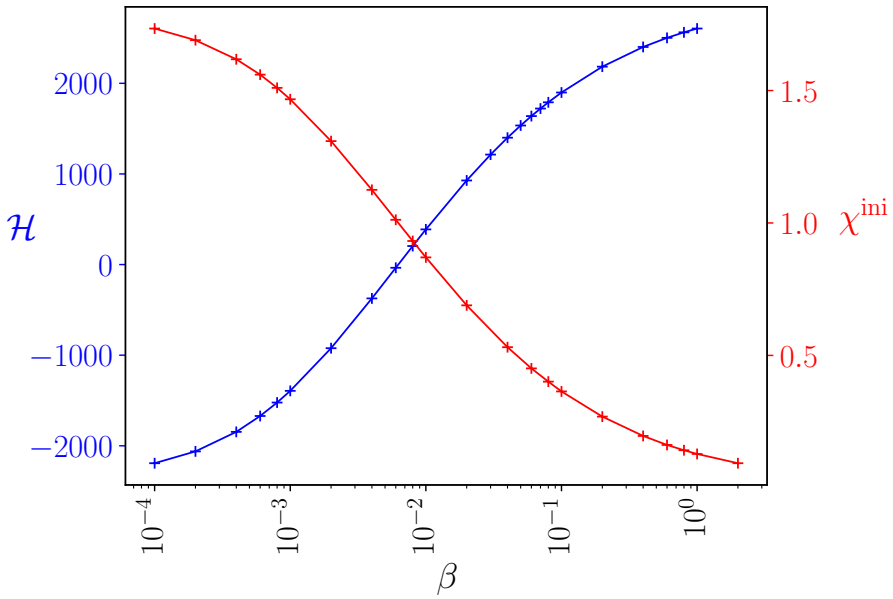


Figure 2.21: **Evolution of the total energy $\mathcal{H}$ and initial non-linearity ratio $\chi^{\text{ini}} = |\mathcal{H}_4^{\text{ini}}|/\mathcal{H}_2^{\text{ini}}$ with $\beta$ -** We can define two extreme regimes, when $\beta$ is small, the system is initially strongly non-linear, which allows the soliton to stay localized into a bound-state. On the contrary, when $\beta$ is large, the system is initially linear, the initial soliton breaks into waves.

- $\beta \simeq 10^{-4} - 10^{-3}$, the total energy is negative and large and the initial non-linearity ratio is large, $\chi^{\text{ini}} \simeq 1.7 - 1.5$. This regime corresponds to the initial soliton only slightly being modified by the non-integrability,
- $\beta - 10^{-2}$, the total energy is nearly null and the initial non-linearity ratio is close to 1. This regime corresponds to the initial soliton being considerably altered by the non-integrability and becoming an observable bound-state,
- $\beta \simeq 10^{-1}-$, the total energy is positive and large and the initial non-linearity ratio is small, $\chi^{\text{ini}} \simeq 0.4 - 0.1$. This regime corresponds to the initial soliton disappearing after the first collapse.

The initial ratio of non-linearity plays an important role because it characterizes the initial pure soliton and solitons need a non-linearity ratio large enough to exist, as the non-linearity must compensate the dispersion. If the linearity is too large, we can assume that the soliton can not be stable, nor the bound-state, because the dispersion is not balanced by the focusing non-linearity. That might explain the collapse of the entire soliton into waves when the initial non-linearity is big, *ie* when $\beta$ is large. This result is consistent with the phase diagram drawn for the quasi-Soliton Turbulence simulations FIGURE 2.6 where we also observe that the bound-state does not appear in systems which are too linear.

Secondly, the larger $\beta$ is, the more non-integrable the equation is. Theoretically, the initial soliton is only stable for the integrable equation ($\beta = 0$), but we can see on $(x - t)$

plots (FIGURE 2.17) that the function stays localized for a small non-integrability perturbation ($\beta \simeq 10^{-2} - 10^{-4}$) while this localization is lost when the non-integrability perturbation is sufficient large ($\beta \simeq 10^{-1} - 1$). To quantify the non-integrability of the 1D-SHE, we define $\epsilon = 1 - \mathcal{H}_4^{\text{SHE}}/\mathcal{H}_4^{\text{NLSE}}$ with $\mathcal{H}_4^{\text{NLSE}}$ the non-linear Hamiltonian of the 1D-NLSE, independant from $\beta$. The expression of $\epsilon$ is chosen to be 0 at $\beta = 0$, *ie* when the 1D-SHE is actually the NLSE. Consequently, $\epsilon$ evaluates the deviation of the 1D-SHE from the 1D-NLSE in a global way as it is defined with the Hamiltonians. Note that this value may vary in time, the conservativeness of the system imposes a total energy constant, but the non-linear component can fluctuate. The evolution of $\epsilon$ for different $\beta$ is plotted FIGURE 2.18(b). For $\beta = 0$, $\epsilon$ is constantly zero, as expected. When $\beta$ increases, $\epsilon$ starts oscillating around a positive mean value, illustrating the deviation from integrability. These oscillations are already seen for very low values of $\beta$ like $10^{-4}$, but they are still weak and around a small value, the system is still close to integrability. When $\beta$ increases, this mean value increases, which represents the system getting more and more non-integrable. We can note that $\epsilon$ oscillates as the same frequency as $\max_x(|u(x,t)|)$.

To study locally the non-integrability, we compare the characteristic length of non-linearity $\sqrt{\beta}$ with the characteristic length of the integrable evolution $\ell_{\frac{1}{2}}$ taken as the mid-amplitude full width of the quasi-soliton found in the evolution. The time series of quantity $\sqrt{\beta}/\ell_{\frac{1}{2}}$ are plotted FIGURE 2.18(c) for different values of $\beta$. For $\beta = 0$ (1D-NLSE) this quantity is constant equal to 0, but for $\beta > 0$ this ratio evolves like $\epsilon$, oscillations for a positive mean value. The development of these oscillations when $\beta$ increases indicates the local non-integrability of the system. As the initial condition is the solution of the integrable equation, it is not surprising to see that it is more unstable when the non-integrability increases. From the consideration of $\epsilon$ and $\sqrt{B}/\ell_{\frac{1}{2}}$, we see that the value of $\beta = 10^{-2}$ chosen for all the simulations presented in this chapter corresponds to a small non-integrability perturbation to the 1D-NLSE, justifying again the use of the DST devised for the 1D-NLSE.

Finally, as the non-integrability of the 1D-SHE changes, its solitonic solution also changes. With the expression of this solution with $\beta$ (1.23), we see that the amplitude evolves as $3/2\ 1/\sqrt{2\beta}$ and the mid-amplitude full-width is $4\,\text{arcosh}(\sqrt{2})\sqrt{\beta} \simeq 3.52\sqrt{\beta}$. When $\beta$ increases, this amplitude decreases and the width increases. For instance, this amplitude is 10.601 for $\beta = 10^{-2}$ and only 1.01 for $\beta = 1$ and the widths are respectively 0.35 and 3.52. Hence, when $\beta$ increases, the solitonic solution of the 1D-SHE is smaller and wider. If we assume that the initial pure soliton relaxes to tend to the solution of the 1D-SHE, that might explain why this relaxation is more pronounced for strong non-integrability. For $\beta = 1$, the solitonic solution has a half-amplitude width of 3.52 bigger than the half of the box length. Thus, it interacts with itself at some point, which might accelerate its disintegration process.

**Summary of the chapter**

- An 1D-NLSE soliton initialized in the 1D-SHE relaxes until a bound-state and emits waves,
- this bound-state appears gradually when the equations gets more non-integrable.
- We assume that the bound-state is an attractor of the system

## 2.7 Conclusion

In this chapter, we have carefully studied the evolution of different initial conditions in the 1D-SHE : a flat-top spectrum, two colliding 1D-SHE solitary waves, two colliding NLSE solitons and a single 1D-NLSE soliton. We conclude that a bound-state (a localized structure with oscillating width and amplitude propagating on top of weakly non-linear waves) acts as a statistical attractor in the 1D-SHE. We have shown that this bound-state requires a certain level of non-linearity to exist in the system.

We characterized the bound-state by a DST spectrum which displays two dominant eigenvalues, whose the imaginary parts oscillate in phase opposition. Its $(\mathbf{k}-\omega)$ spectrum show parallel lines whose slopes correspond to the mean velocity of the bound-state. The bound-states that we have observed in our system are always accompanied by weakly non-linear waves. These are present as a parabola in the $(\mathbf{k}-\omega)$ spectrum. We highlight that both DST and $(\mathbf{k}-\omega)$ spectra are consistent with each other, as it has been found that the frequency of oscillation of the DST eigenvalues corresponds to the secondary lines in the $(\mathbf{k}-\omega)$.

This final state is reached by series of non-elastic collisions between oscillating structures. These non-elastic collisions are allowed by the non-integrability of the 1D-SHE. A phase difference study has been done and leads to the conclusion that the phase difference must be zero for colliding localized structures to merge into a single one. Conversely, two structures colliding in phase opposition undergo an elastic collision.

Finally, we can notice that the DST, originally devised for the integrable 1D-NLSE and here applied to the non-integrable 1D-SHE, gives results qualitatively consistent with the $(x-t)$ dynamics and $(\mathbf{k}-\omega)$ spectrum. The DST spectrum of the bound-state evolves in coherence with the function in the physical space and it correctly tracks the structures during the non-elastic collisions. This observation is an interesting step in applying the DST to non-integrable systems.

# CHAPTER 3

# Cascades in the 1D-SHE

## 3.1 Introduction

In this chapter, we will now focus on the wave turbulence properties of the 1D-SHE. We recall that the limits of this equation, Short-Wave and Long-Wave, correspond respectively to the 1D Schrödinger Newton Equation (1.30) and the 1D Long-Wave Equation (1.28). These equations have been studied in [5]. A key set of results derived in this paper were the KZ cascade spectra of the limits of the 1D-SHE. As it is the case wit KZ spectra, these have a power-law for the wave-action spectrum $n_{\mathbf{k}} = Ck^x$, with $C$ a constant. After a CT to remove the non-resonant four-mode interactions, the KZ spectra were found to be characterized by the scaling exponents $x_{\mathrm{FE}}^{\mathrm{LWE}} = -1$, $x_{\mathrm{FN}}^{\mathrm{LWE}} = -3/4$ for the 1D-LWE and $x_{\mathrm{FE}}^{\mathrm{SNE}} = 7/5$, $x_{\mathrm{FN}}^{\mathrm{SNE}} = 9/5$ for the 1D-SNE. We recall that $x_{\mathrm{FE}}$ and $x_{\mathrm{FN}}$ represent respectively the energy cascade and wave-action cascade KZ spectra. The energy cascade KZ spectrum for the 1D-LWE had to be corrected logarithmically to prevent a divergence of the collision integral while both KZ predictions were found to be invalid for such a divergence. These theoretical predictions were compared to numerical simulations and the predictions for the 1D-SNE were observed in numerics, even though they are invalid. For the 1D-LWE, the comparisons were not conclusive. These simulations showed other interesting behaviours, such as the progressive organization of the system as a unique coherent structure in the 1D-LWE and existence of incoherent structures in 1D-SNE.

For completeness, we mention that turbulence has been studied in the 2D- and 3D-SNE in [25] and for 2D-SHE in [95]. Notice that in these dimensions the four-mode interactions are resonant and there is no need for the CT.

The work presented in this chapter deals with the wave turbulence in the 1D-SHE, ie the complete equation without taking any limit. More precisely, we will consider the 1D-SHE in the SW limit but without assuming the validity of a Taylor expansion of the non-linearity in this limit, with the purpose of having a more precise approach.

To this end, we will follow the method detailed in [95] and derive a reduced model from the 1D-SHE. For reasons that will become clear, we term this new model the Semi-Local Approximation Model (SLAM) fo the 1D-SHE. The SLAM is required as the interaction coefficient of 1D-SHE turns out not to be scale-invariant.

In order for the approximation model to be easier to apply, we will slightly change the expression of the 1D-SHE, which we recall here,

$$i\frac{\partial}{\partial t}u + \frac{1}{2}\frac{\partial^2}{\partial x^2}u + u\left(1 - \beta\frac{\partial^2}{\partial x^2}\right)^{-1}|u|^2 = 0. \tag{3.1}$$

We will change the non-integrability parameter, from $\beta$ to $\Lambda = 1/\beta > 0$. Which this change and a rescaling of the function $u$ as $u \to u\beta^{-\frac{1}{2}}$. The 1D-SHE becomes

$$i\frac{\partial}{\partial t}u + \frac{1}{2}\frac{\partial^2}{\partial x^2}u + u\left(\Lambda - \frac{\partial^2}{\partial x^2}\right)^{-1}|u|^2 = 0. \tag{3.2}$$

We highlight the fact that the rescaling of $u$ does not have any impact on its turbulent properties as we will be mainly interested in the exponent of the wave-action spectrum. The important change is the expression of the four-mode interaction coefficient (1.25) which is now

$${}^{\text{SHE}}T^{\mathbf{k}_1,\mathbf{k}_2}_{\mathbf{k}_3,\mathbf{k}_4} = \frac{-1}{4}\Big(A_{1234} + A_{2134} + A_{1243} + A_{2143}\Big),\ A_{1234} = \frac{1}{(\mathbf{k}_1 - \mathbf{k}_4)(\mathbf{k}_3 - \mathbf{k}_2) + \Lambda}. \tag{3.3}$$

The SWL was previously defined as $k^2 \gg k^{*2}$ with $k^* = 1/\sqrt{\beta}$. With the introduction of $\Lambda$, the SWL is still $k^2 \gg k^{*2}$, but now with $k^* = \sqrt{\Lambda}$. We remind the notation used in this thesis, a vector is denoted with bold variable, for instance $\mathbf{k}$, while its amplitude is denoted without this bold font, for instance $k = |\mathbf{k}|$.

Finally, studying the whole equation appears to be crucial because the KE for the 1D-SNE diverges, and so does the interaction coefficient [95] [25]. Indeed, taking $\Lambda = 0$ in the interaction coefficient for the 1D-SHE (3.3), we get a coefficient which is divergent for $\mathbf{k}_1 = \mathbf{k}_4$. A way to overcome this problem is to study the complete equation 1D-SHE (for which the interaction coefficient is not divergent) and, then, to take the limit $\Lambda \to 0$. The reasoning was illustrated for four-mode interaction coefficient but holds for the six-mode coefficient after carrying out the CT.

This chapter is organized as follows. Section 3.2 presents the approximation model and section 3.3 details its application until the final result. In the section 3.4 we derive the KZ predictions from the result of the SLAM. The sections 3.5 and 3.6 present respectively the numerical scheme to study the turbulence of 1D-SHE and the results of these numerics.

## 3.2 Canonical Transform and approximation models

### 3.2.1 Canonical Transform

As presented in section 1.3.2, for the 1D-SHE, we need to apply a particular CT to remove the four-mode interactions and transfer the interactions to the sixth order, keeping

the canonicity of the equations of motion. The new Hamiltonian has thus the six-mode interaction term :

$$\mathcal{H} = \sum_{\mathbf{k}} \omega_{\mathbf{k}} |b_{\mathbf{k}}|^2 \; + \frac{1}{3} \sum_{1-6} W^{1,2,3}_{4,5,6} \; b_1 b_2 b_3 b_4^* b_5^* b_6^* \; \delta^{1,2,3}_{4,5,6}, \tag{3.4}$$

describing $3 \leftrightarrow 3$ interactions. For convenience, we denote $W^{\mathbf{k}_1,\mathbf{k}_2,\mathbf{k}_3}_{\mathbf{k}_4,\mathbf{k}_5,\mathbf{k}}$ as $W^{1,2,3}_{4,5,\mathbf{k}}$. Similarly, the wave-action densities $n_{\mathbf{k}_i}$ are denoted $n_i$ and the Kronecker delta $\delta^{1,2,3}_{4,5,\mathbf{k}}$ stands for $\delta(\mathbf{k}_1 + \mathbf{k}_2 + \mathbf{k}_3 - \mathbf{k}_4 - \mathbf{k}_5 - \mathbf{k})$. The new interaction coefficient $W^{1,2,3}_{4,5,\mathbf{k}}$ is given by the CT,

$$W^{1,2,3}_{4,5,6} = \frac{1}{24} \sum_{\substack{i,j,k=1 \\ i\neq j\neq k\neq i}}^{3} \sum_{\substack{p,q,r=4 \\ p\neq q\neq r\neq p}}^{6} \left[ \frac{1}{\omega^{i,j}_{r,i+j-r}} - \frac{1}{\omega^{p+q-j,j}_{p.q}} \right] \; {}^{\mathrm{SHE}}T^{i,k}_{r,i+k-r} \; {}^{\mathrm{SHE}}T^{q+p-j,j}_{q,p}, \tag{3.5}$$

and we recall that ${}^{\mathrm{SHE}}T$ is the $2 \leftrightarrow 2$ interaction coefficient for the 1D-SHE, given in (3.3) with $\Lambda$ as a parameter. The explicit computation of this new coefficient gives

$$W^{\mathbf{k}_1,\mathbf{k}_2,\mathbf{k}_3}_{\mathbf{k}_4,\mathbf{k}_5,\mathbf{k}_6} = \frac{1}{48} \sum_{\substack{i,j,m=1 \\ i\neq j\neq k\neq i}}^{3} \sum_{\substack{p,q,r=4 \\ p\neq q\neq r\neq p}}^{6} \mathcal{W}^{i,j,m}_{p,q,r}, \qquad \text{with} \tag{3.6a}$$

$$\mathcal{W}^{i,j,m}_{p,q,r} = \left( \frac{1}{(\mathbf{k}_j - \mathbf{k}_q)(\mathbf{k}_m - \mathbf{k}_q)} + \frac{1}{(\mathbf{k}_i - \mathbf{k}_p)(\mathbf{k}_i - \mathbf{k}_r)} \right) \left( \frac{1}{(\mathbf{k}_j - \mathbf{k}_q)^2 + \Lambda} + \frac{1}{(\mathbf{k}_m - \mathbf{k}_q)^2 + \Lambda} \right) \times \left( \frac{1}{(\mathbf{k}_i - \mathbf{k}_p)^2 + \Lambda} + \frac{1}{(\mathbf{k}_i - \mathbf{k}_r)^2 + \Lambda} \right). \tag{3.6b}$$

The full expression of $W^{\mathbf{k}_1,\mathbf{k}_2,\mathbf{k}_3}_{\mathbf{k}_4,\mathbf{k}_5,\mathbf{k}}$ is the first term $\mathcal{W}^{\mathbf{k}_1,\mathbf{k}_2,\mathbf{k}_3}_{\mathbf{k}_4,\mathbf{k}_5,\mathbf{k}}$ (3.7) plus all the eight swaps among $\{\mathbf{k}_1, \mathbf{k}_2, \mathbf{k}_3\}$ and among $\{\mathbf{k}_4, \mathbf{k}_5, \mathbf{k}\}$.

$$\mathcal{W}^{\mathbf{k}_1,\mathbf{k}_2,\mathbf{k}_3}_{\mathbf{k}_4,\mathbf{k}_5,\mathbf{k}} = \left( \frac{1}{(\mathbf{k}_2 - \mathbf{k}_5)(\mathbf{k}_3 - \mathbf{k}_5)} + \frac{1}{(\mathbf{k}_1 - \mathbf{k}_4)(\mathbf{k}_1 - \mathbf{k})} \right) \left( \frac{1}{(\mathbf{k}_2 - \mathbf{k}_5)^2 + \Lambda} + \frac{1}{(\mathbf{k}_3 - \mathbf{k}_5)^2 + \Lambda} \right) \times \left( \frac{1}{(\mathbf{k}_1 - \mathbf{k}_4)^2 + \Lambda} + \frac{1}{(\mathbf{k}_1 - \mathbf{k})^2 + \Lambda} \right). \tag{3.7}$$

This $W$ coefficient is *a priori* divergent for pairs $\mathbf{k}_i = \mathbf{k}_p$. However, on the resonant manifold, we can check that $W = 0$ in the limit $\Lambda \to \infty$ (up to the $\frac{1}{\Lambda^2}$ term). Indeed, this limit corresponds to the NLSE which is integrable and, thus, does not have any resonances at any order. In 1D, the resonance conditions can be geometrically satisfied for sextexts, which implies that the six-mode coefficients $W$ must be 0 to prevent the existence of resonant sextets.

### 3.2.2 The need for an approximation model

Now that we have the interaction coefficient for the full 1D-SHE, we have the complete collision integral of the KE (3.10). However, the expression of $W^{1,2,3}_{4,5,\mathbf{k}}$ prevents the direct application of the ZT to obtain the KZ prediction. Indeed, for both the ZT and the dimensional derivation, we need the interaction coefficient scale to be invariant, *ie* it has to be characterized by a homogeneity coefficient $\gamma \in \mathbb{R}$ such as

$$W^{\lambda\mathbf{k}_1,\lambda\mathbf{k}_2,\lambda\mathbf{k}_3}_{\lambda\mathbf{k}_4,\lambda\mathbf{k}_5,\lambda\mathbf{k}_6} = \lambda^{\gamma} W^{\mathbf{k}_1,\mathbf{k}_2,\mathbf{k}_3}_{\mathbf{k}_4,\mathbf{k}_5,\mathbf{k}_6}. \tag{3.8}$$

For the 1D-NLSE, 1D-LWE and 1D-SNE, the respective four-mode interaction coefficients are scale invariant [5] and, thus, so are the six-mode coefficients. Due to the $\Lambda$ term, this coefficient is not scale invariant for the 1D-SHE. Consequently, we can not predict a KZ spectrum from the exact KE of the SHE. That is why we will apply an approximation model to simplify this system and derive KZ predictions.

### 3.2.3 Approximation Models

In the Differential Approximation Model (DAM), one assumes that all the interacting wave-vectors are very close to each other. This is known as the assumption of superlocality. This greatly simplifies the KE and Dyachenko et al. [96] showed that the KE turns into an Ordinary Differential Equation, which is much easier to integrate. This simplification conserves the structure of the equation and particularly the conserved quantities, linear energy and wave-action, and the solutions, KZ or RJ. For systems, like the 1D-SHE, exhibiting a dual cascade behaviour, the DAM will link the wave-action spectrum $n_{\mathbf{k}}(t)$ with a non-linear operator $R(n_{\mathbf{k}}(t))$ [25]

$$\frac{\partial n_{\mathbf{k}}}{\partial t} = R(n_{\mathbf{k}}), \tag{3.9}$$

The expression of $R$ depends on the system studied.

The DAM has been applied to the 2D and 3D NLSE [96], to Boltzmann gas [97] and to Kelvin Waves [35]. The DAM allows one to easily obtain the KZ spectra and to check their convergence and the signs of the corresponding fluxes. The DAM is very useful as it reduces the KE to an ODE, but the underlying assumption of superlocality is strong and may be too restricting for certain systems.

The Semi-Local Approximation Model (SLAM) assumes a less restrictive condition : the dynamics are dominated by interactions for which pairs of wave-vectors are very close to each other. This new assumption increases the number of systems it can be applied to. However, the final result obtained by SLAM is not as concise at the DAM as it still contains, at least, one integral. Concretely, the SLAM gives an expression for $Q(k)$ the wave-action flux from which we can derive the KZ spectra of the system. For instance, the SLAM has been applied to the 1D-SHE in 2D and 3D by Skipp et al. [95] which provided the derivation of KZ predictions.

The physical difference between DAM and SLAM is the locality of the interactions. By assuming that all the interacting wave-vectors are almost equal, DAM represents local interactions. This model is even called the *super-local* model because of this precise hypothesis.

The SLAM is more appropriate than the DAM for the 1D-SHE, but in the Short Wave Limit $\Lambda \ll k^2$ only. Indeed, in this limit, some terms of the six-mode interaction coefficient (3.6) are sharply peaked as $\mathbf{k}_r \to \mathbf{k}_q$ if $\Lambda \ll (\mathbf{k}_r - \mathbf{k}_q)^2$. Having dominant terms in $W$ does not require all the wave-vectors equal together, implying that the DAM is not adapted. This motivates us to apply the SLAM instead of the DAM. In the SLAM, the pairings which maximize the interaction coefficient link each vector of the triplet $\{\mathbf{k}_1, \mathbf{k}_2, \mathbf{k}_3\}$ with one of $\{\mathbf{k}_4, \mathbf{k}_5, \mathbf{k}_6\}$. That means an in-coming mode and an out-going mode in the resonant picture, see FIGURE 3.1. To conclude, the SLAM is adapted to our system with the resonances of the six-mode interaction and is less restrictive than the DAM. Hence, we will study the turbulent behaviour with the help of the SLAM.

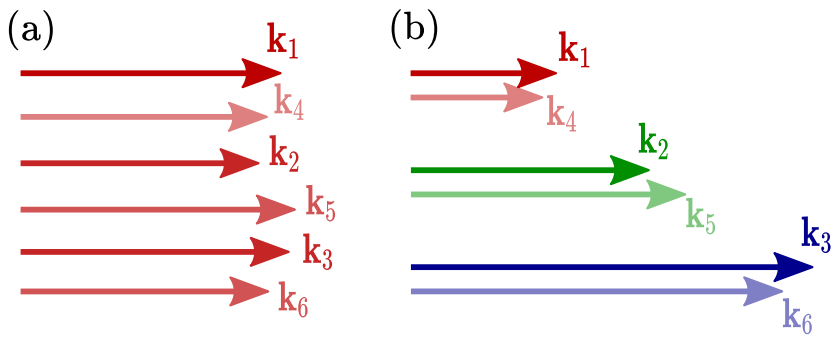


Figure 3.1: **Illustration of the approximation models for a six-mode interaction, DAM** (a) **and SLAM** (b) - The DAM assumes that all the wave-vectors are close while the SLAM only regroup them in pairs. In our work, we used the SLAM.

**Summary of the section**

- The complete 1D-SHE will be studied in the SWL with the SLAM.
- In the SLAM, we assume that the interacting wave-vectors are grouped in pairs.

## 3.3 The Semi-Local Approximation Model

With the 1D-SHE now characterized by six-mode interactions, the weak Wave-Turbulence theory shows that it verifies the generic Kinetic Equation (KE) for six-mode interactions [51] given by

$$\frac{\partial n_{\mathbf{k}}}{\partial t} = 24\pi \int \left|W^{1,2,3}_{4,5,\mathbf{k}}\right|^2 \left[\frac{1}{n_{\mathbf{k}}} + \frac{1}{n_5} + \frac{1}{n_4} - \frac{1}{n_1} - \frac{1}{n_2} - \frac{1}{n_3}\right] \times n_1 n_2 n_3 n_4 n_5 n_{\mathbf{k}}\ \delta^{1,2,3}_{4,5,\mathbf{k}}\ \delta(\omega^{1,2,3}_{4,5,\mathbf{k}})\ \mathrm{d}\mathbf{k}_1\,\mathrm{d}\mathbf{k}_2\,\mathrm{d}\mathbf{k}_3\,\mathrm{d}\mathbf{k}_4\,\mathrm{d}\mathbf{k}_5. \tag{3.10}$$

The Kronecker delta $\delta(\omega^{1,2,3}_{4,5,\mathbf{k}})$ stands for $\delta(\omega_1+\omega_2+\omega_3-\omega_4-\omega_5-\omega_{\mathbf{k}})$ and $\delta^{1,2,3}_{4,5,\mathbf{k}}$ for $\delta^{\mathbf{k}_1,\mathbf{k}_2,\mathbf{k}_3}_{\mathbf{k}_4,\mathbf{k}_5,\mathbf{k}}$.

The goal of the SLAM is to obtain an expression for the wave-action flux $Q$ (depending for now on the wave-vector $\mathbf{k}$) under the assumption of semi-locality. To this end, we introduce a test-function $\varphi_{\mathbf{k}} = \varphi(\mathbf{k})$ and consider the integral

$$\int \varphi_{\mathbf{k}} \frac{\partial n_{\mathbf{k}}}{\partial t} \mathrm{d}\mathbf{k}. \tag{3.11}$$

### 3.3.1 Symmetries and choice of pairing

The KE (3.10) is symmetrical for swaps of indexes inside $\{\mathbf{k}_1, \mathbf{k}_2, \mathbf{k}_3\}$ or between $\mathbf{k}_4$ and $\mathbf{k}_5$. With the $\mathbf{k}-$integration, $\mathbf{k}$ becomes a dummy variable like the $\mathbf{k}_i$. The integral (3.11) is now symmetrical with respect to indexes swaps between modes in $\{\mathbf{k}_1, \mathbf{k}_2, \mathbf{k}_3\}$, between modes in $\{\mathbf{k}_4, \mathbf{k}_5, \mathbf{k}\}$ and with respect to the change $\mathbf{k}_1, \mathbf{k}_2, \mathbf{k}_3 \leftrightarrow \mathbf{k}_4, \mathbf{k}_5, \mathbf{k}$. Thus, the integral (3.11) can be written

$$\int \varphi_{\mathbf{k}} \frac{\partial n_{\mathbf{k}}}{\partial t} \mathrm{d}\mathbf{k} = 4\pi \int \left|W^{1,2,3}_{4,5,\mathbf{k}}\right|^2 \left[\frac{1}{n_{\mathbf{k}}} + \frac{1}{n_5} + \frac{1}{n_4} - \frac{1}{n_1} - \frac{1}{n_2} - \frac{1}{n_3}\right] n_1 n_2 n_3 n_4 n_5 n_{\mathbf{k}} \times \left[\varphi_{\mathbf{k}} + \varphi_5 + \varphi_4 - \varphi_3 - \varphi_2 - \varphi_1\right] \delta^{1,2,3}_{4,5,\mathbf{k}}\ \delta(\omega^{1,2,3}_{4,5,\mathbf{k}})\ \mathrm{d}\mathbf{k}_1\,\mathrm{d}\mathbf{k}_2\,\mathrm{d}\mathbf{k}_3\,\mathrm{d}\mathbf{k}_4\,\mathrm{d}\mathbf{k}_5\mathrm{d}\mathbf{k}. \tag{3.12}$$

Applying the SLAM means grouping the six wave-vectors in three pairs, each pair containing an incoming vector and an output vector. With the symmetries of equation (3.12) and six-mode interaction coefficient(3.6), we can study one particular pairing and assume that the other ones will give the same result by symmetry. Six pairings are possible, resulting in a multiplicative factor of 6. We will consider the pairing

$$\mathbf{k}_1 \approx \mathbf{k}_4,\ \ \mathbf{k}_2 \approx \mathbf{k}_5,\ \ \mathbf{k}_3 \approx \mathbf{k}. \tag{3.13}$$

We will denote $\mathbf{p} = \mathbf{k}_1 - \mathbf{k}_4$ and $\mathbf{q} = \mathbf{k}_2 - \mathbf{k}_5$, with $p \ll k_1, k_4$, $q \ll k_2, k_5$. The goal of the SLAM is to reduce the number of variables of integration.

### 3.3.2 Approximations for the resonance conditions

Before starting the whole computation of the integral, we will see how the SLAM assumption and the pairing (3.13) simplify the resonance conditions encrypted in the Kronecker delta $\delta^{1,2,3}_{4,5,\mathbf{k}}$ and $\delta\left(\omega^{1,2,3}_{4,5,\mathbf{k}}\right)$.

First, we have $\mathbf{k}_1+\mathbf{k}_2+\mathbf{k}_3-\mathbf{k}_4-\mathbf{k}_5-\mathbf{k} = \mathbf{p}+\mathbf{q}+(\mathbf{k}_3-\mathbf{k})$. Given that, the Kronecker delta $\delta^{1,2,3}_{4,5,\mathbf{k}}$ imposes $\mathbf{k}_3 - \mathbf{k} = -\mathbf{p} - \mathbf{q}$ on the resonant manifold. This result does not

assume any expansion in powers of $p$ nor $q$.

Then, let us consider the $\delta\left(\omega^{1,2,3}_{4,5,\mathbf{k}}\right)$ with the $\mathbf{k}-$condition respected. Given the dispersion relation $\omega_{\mathbf{k}} = \mathbf{k}^2/2$, we have $\omega^{1,2,3}_{4,5,\mathbf{k}} = [(\mathbf{k}_1 - \mathbf{k}_4)(\mathbf{k}_1 + \mathbf{k}_4) + (\mathbf{k}_2 - \mathbf{k}_5)(\mathbf{k}_2 + \mathbf{k}_5) + (\mathbf{k}_3 - \mathbf{k})(\mathbf{k}_3 + \mathbf{k})]/2$. We apply the resonance condition $\mathbf{k}_3 - \mathbf{k} = -\mathbf{p} - \mathbf{q}$ and we obtain, to the lowest order in $p$ and $q$, $\omega^{1,2,3}_{4,5,\mathbf{k}} = \mathbf{p}(\mathbf{k}_1 - \mathbf{k}) + \mathbf{q}(\mathbf{k}_2 - \mathbf{k})$. Thus, in the first order of $p$ and $q$, $\delta(\omega^{1,2,3}_{4,5,\mathbf{k}}) = \delta(\mathbf{p}(\mathbf{k}_1 - \mathbf{k}) + \mathbf{q}(\mathbf{k}_2 - \mathbf{k}))$ under the SLAM assumptions and with the $\mathbf{k}$-condition verified. If we want to write $\mathbf{q} = -\mathbf{p}\frac{\mathbf{k}_1 - \mathbf{k}}{\mathbf{k}_2 - \mathbf{k})}$, we need to keep in mind that $\delta(\mathbf{p}(\mathbf{k}_1 - \mathbf{k}) + \mathbf{q}(\mathbf{k}_2 - \mathbf{k})) = \frac{1}{|\mathbf{k}_2 - \mathbf{k}|}\delta(\mathbf{q} + \mathbf{p}\frac{\mathbf{k}_1 - \mathbf{k}}{\mathbf{k}_2 - \mathbf{k}})$

The six initial integration variables $\mathbf{k}_1, \mathbf{k}_2, \mathbf{k}_3, \mathbf{k}_4, \mathbf{k}_5, \mathbf{k}$ were changed into $\mathbf{k}_1, \mathbf{p}, \mathbf{k}_2, \mathbf{q}, \mathbf{k}_3, \mathbf{k}$ and, with the $\mathbf{k}-$ and $\omega-$ Kronecker delta's, we can reduce equation 3.12 to an integration over four variables $\mathbf{k}_1, \mathbf{k}_2, \mathbf{k}$ and $\mathbf{p}$.

### 3.3.3 Approximation for $W$

As we said before, we work with the pairing $\mathbf{k}_1 \approx \mathbf{k}_4$, $\mathbf{k}_2 \approx \mathbf{k}_5, \mathbf{k}_3 \approx \mathbf{k}$ in the SWL $\Lambda \ll \mathbf{k}^2$. Among the nine terms of $W^{1,2,3}_{4,5,\mathbf{k}}$, six are resonant for a given pairing, while the others can be neglected. For instance, the component $\mathcal{W}^{1,2,3}_{4,5,\mathbf{k}}$ (3.14) is resonant because each of the three terms in bracket contain at least one resonant term (highlighted in yellow) while the component $\mathcal{W}^{1,2,3}_{5,4,\mathbf{k}}$ (3.15) has no resonant term for the chosen pairing and will be neglected for this choice of pairings and in the SWL $\Lambda \ll \mathbf{k}^2$.

$$\mathcal{W}^{1,2,3}_{4,5,\mathbf{k}} = \left(\frac{1}{(\mathbf{k}_2 - \mathbf{k}_5)(\mathbf{k}_3 - \mathbf{k}_5)} + \frac{1}{(\mathbf{k}_1 - \mathbf{k}_4)(\mathbf{k}_1 - \mathbf{k})}\right)\left(\frac{1}{(\mathbf{k}_2 - \mathbf{k}_5)^2 + \Lambda} + \frac{1}{(\mathbf{k}_3 - \mathbf{k}_5)^2 + \Lambda}\right) \times \left(\frac{1}{(\mathbf{k}_1 - \mathbf{k}_4)^2 + \Lambda} + \frac{1}{(\mathbf{k}_1 - \mathbf{k})^2 + \Lambda}\right) \tag{3.14}$$

$$\mathcal{W}^{1,2,3}_{5,4,\mathbf{k}} = \left(\frac{1}{(\mathbf{k}_2 - \mathbf{k}_4)(\mathbf{k}_3 - \mathbf{k}_4)} + \frac{1}{(\mathbf{k}_1 - \mathbf{k}_5)(\mathbf{k}_1 - \mathbf{k})}\right)\left(\frac{1}{(\mathbf{k}_2 - \mathbf{k}_4)^2 + \Lambda} + \frac{1}{(\mathbf{k}_3 - \mathbf{k}_4)^2 + \Lambda}\right) \times \left(\frac{1}{(\mathbf{k}_1 - \mathbf{k}_5)^2 + \Lambda} + \frac{1}{(\mathbf{k}_1 - \mathbf{k})^2 + \Lambda}\right), \tag{3.15}$$

From now we forget the non-resonant terms and only consider the resonant ones. We can make these latter terms explicit by writing them component as function of $\mathbf{p}$ and $\mathbf{q}$, keeping $\mathbf{k}_1, \mathbf{k}_2$ and $\mathbf{k}$. For $\mathcal{W}^{1,2,3}_{4,5,\mathbf{k}} = \mathcal{W}^{\mathbf{k}_1,\mathbf{k}_2,\mathbf{k}_3}_{\mathbf{k}_4,\mathbf{k}_5,\mathbf{k}}$, it gives, on the resonant manifold,

$$\mathcal{W}^{\mathbf{k}_1,\mathbf{k}_2,\mathbf{k}_3}_{\mathbf{k}_4,\mathbf{k}_5,\mathbf{k}} = \mathcal{W}^{\mathbf{k}_1,\mathbf{k}_2,\mathbf{k}_3}_{\mathbf{k}_1-\mathbf{p},\mathbf{k}_2-\mathbf{q},\mathbf{k}} = \left(\frac{1}{\mathbf{q}(\mathbf{k}-\mathbf{k}_2-\mathbf{p})}+\frac{1}{\mathbf{p}(\mathbf{k}_1-\mathbf{k})}\right)\left(\frac{1}{\mathbf{q}^2+\Lambda}+\frac{1}{(\mathbf{k}-\mathbf{k}_2-\mathbf{p})^2+\Lambda}\right) \times\left(\frac{1}{\mathbf{p}^2+\Lambda}+\frac{1}{(\mathbf{k}_1-\mathbf{k})^2+\Lambda}\right). \tag{3.16}$$

We recall again that for the SLAM we place ourselvs in the SWL, *ie* $\Lambda \ll k^2$. Thus, still assuming the pairing above, we have $p^2, q^2, \Lambda \ll (\mathbf{k}_i-\mathbf{k}_j)^2$, with $\mathbf{k}_i$ and $\mathbf{k}_j$ not paired. We can simplify $\mathcal{W}^{1,2,3}_{4,5,\mathbf{k}}$, keeping only the resonant terms in the last two brackets

$$\mathcal{W}^{\mathbf{k}_1,\mathbf{k}_2,\mathbf{k}_3}_{\mathbf{k}_1-\mathbf{p},\mathbf{k}_2-\mathbf{q},\mathbf{k}} \simeq \left(\frac{1}{\mathbf{q}(\mathbf{k}-\mathbf{k}_2-\mathbf{p})}+\frac{1}{\mathbf{p}(\mathbf{k}_1-\mathbf{k})}\right)\frac{1}{\mathbf{q}^2+\Lambda}\ \frac{1}{\mathbf{p}^2+\Lambda}. \tag{3.17}$$

We develop the first bracket to the first order in $\frac{p}{|\mathbf{k}-\mathbf{k}_2|} \ll 1$ to have

$$\mathcal{W}^{\mathbf{k}_1,\mathbf{k}_2,\mathbf{k}_3}_{\mathbf{k}_1-\mathbf{p},\mathbf{k}_2-\mathbf{q},\mathbf{k}} \simeq \left(\frac{1}{\mathbf{q}(\mathbf{k}-\mathbf{k}_2)}+\frac{\mathbf{p}}{\mathbf{q}}\frac{1}{(\mathbf{k}-\mathbf{k}_2)^2}+\frac{1}{\mathbf{p}(\mathbf{k}_1-\mathbf{k})}\right)\frac{1}{\mathbf{q}^2+\Lambda}\ \frac{1}{\mathbf{p}^2+\Lambda}. \tag{3.18}$$

Another component of $W^{1,2,3}_{4,5,\mathbf{k}}$ is proportional to $\frac{1}{\mathbf{q}^2+\Lambda}\ \frac{1}{\mathbf{p}^2+\Lambda}$, namely $\mathcal{W}^{2,1,3}_{5,4,\mathbf{k}}$, to which we can apply the same procedure

$$\begin{aligned}\mathcal{W}^{2,1,3}_{5,4,\mathbf{k}} = \mathcal{W}^{\mathbf{k}_2,\mathbf{k}_1,\mathbf{k}_3}_{\mathbf{k}_5,\mathbf{k}_4,\mathbf{k}} =& \left(\frac{1}{(\mathbf{k}_1-\mathbf{k}_4)(\mathbf{k}_3-\mathbf{k}_4)}+\frac{1}{(\mathbf{k}_2-\mathbf{k}_5)(\mathbf{k}_2-\mathbf{k})}\right)\left(\frac{1}{(\mathbf{k}_1-\mathbf{k}_4)^2+\Lambda}+\frac{1}{(\mathbf{k}_3-\mathbf{k}_4)^2+\Lambda}\right) \\ &\times\left(\frac{1}{(\mathbf{k}_2-\mathbf{k}_5)^2+\Lambda}+\frac{1}{(\mathbf{k}_2-\mathbf{k})^2+\Lambda}\right) \\ \mathcal{W}^{\mathbf{k}_2,\mathbf{k}_1,\mathbf{k}_3}_{\mathbf{k}_2-\mathbf{q},\mathbf{k}_1-\mathbf{p},\mathbf{k}} \simeq& \left(\frac{1}{\mathbf{p}(\mathbf{k}-\mathbf{k}_1-\mathbf{q})}+\frac{1}{\mathbf{q}(\mathbf{k}_2-\mathbf{k})}\right)\frac{1}{\mathbf{p}^2+\Lambda}\ \frac{1}{\mathbf{q}^2+\Lambda}\end{aligned} \tag{3.19}$$

$$\mathcal{W}^{\mathbf{k}_2,\mathbf{k}_1,\mathbf{k}_3}_{\mathbf{k}_2-\mathbf{q},\mathbf{k}_1-\mathbf{p},\mathbf{k}} \simeq \left(\frac{1}{\mathbf{p}(\mathbf{k}-\mathbf{k}_1)}+\frac{\mathbf{q}}{\mathbf{p}}\frac{1}{(\mathbf{k}-\mathbf{k}_1)^2}+\frac{1}{\mathbf{q}(\mathbf{k}_2-\mathbf{k})}\right)\frac{1}{\mathbf{p}^2+\Lambda}\ \frac{1}{\mathbf{q}^2+\Lambda} \tag{3.20}$$

We understand that these two components are linked because they are both resonant to the same couples $\mathbf{k}_1 \approx \mathbf{k}_4$ and $\mathbf{k}_2 \approx \mathbf{k}_4$. Taking both components $\mathcal{W}^{1,2,3}_{4,5,\mathbf{k}}$ and $\mathcal{W}^{2,1,3}_{5,4,\mathbf{k}}$ together, the lowest order terms cancel and we have

$$\mathcal{W}^{1,2,3}_{4,5,\mathbf{k}} + \mathcal{W}^{2,1,3}_{5,4,\mathbf{k}} \simeq \left(\frac{\mathbf{p}}{\mathbf{q}}\frac{1}{(\mathbf{k}-\mathbf{k}_2)^2}+\frac{\mathbf{q}}{\mathbf{p}}\frac{1}{(\mathbf{k}-\mathbf{k}_1)^2}\right)\frac{1}{\mathbf{p}^2+\Lambda}\ \frac{1}{\mathbf{q}^2+\Lambda} \tag{3.21}$$

Finally, we use the relation between $\mathbf{p}$ and $\mathbf{q}$ found with the $\omega-$ Kronecker delta : $\frac{\mathbf{q}}{\mathbf{p}} = -\frac{\mathbf{k}-\mathbf{k}_1}{\mathbf{k}-\mathbf{k}_2}$.

$$\begin{aligned}\mathcal{W}^{1,2,3}_{4,5,\mathbf{k}} + \mathcal{W}^{2,1,3}_{5,4,\mathbf{k}} &\simeq \left( -\frac{\mathbf{k}-\mathbf{k}_2}{\mathbf{k}-\mathbf{k}_1}\frac{1}{(\mathbf{k}-\mathbf{k}_2)^2} - \frac{\mathbf{k}-\mathbf{k}_1}{\mathbf{k}-\mathbf{k}_2}\frac{1}{(\mathbf{k}-\mathbf{k}_1)^2}\right) \frac{1}{\mathbf{p}^2+\Lambda}\ \frac{1}{\mathbf{p}^2(\frac{\mathbf{k}-\mathbf{k}_1}{\mathbf{k}-\mathbf{k}_2})^2+\Lambda} \\ \mathcal{W}^{1,2,3}_{4,5,\mathbf{k}} + \mathcal{W}^{2,1,3}_{5,4,\mathbf{k}} &\simeq -2\left(\frac{1}{\mathbf{k}-\mathbf{k}_2}\frac{1}{\mathbf{k}-\mathbf{k}_1}\right) \frac{1}{\mathbf{p}^2+\Lambda}\ \frac{1}{\mathbf{p}^2(\frac{\mathbf{k}-\mathbf{k}_1}{\mathbf{k}-\mathbf{k}_2})^2+\Lambda}\end{aligned} \tag{3.22}$$

The same reasoning goes for the four other resonant components $\mathcal{W}$, the latter can be paired based on the two resonant wave-vector couples they represent. The consideration of the six resonant components gives the expression for the full six-mode interaction coefficient $W^{1,2,3}_{4,5,\mathbf{k}}$ keeping only the resonant components, denoted $W_{\mathrm{r}}$ :

$$\begin{aligned}W_{\mathrm{r}}(\mathbf{k}_1,\mathbf{k}_2,\mathbf{k},\mathbf{p},\mathbf{q}) \simeq &\left(\frac{\mathbf{p}}{\mathbf{q}}\frac{1}{(\mathbf{k}-\mathbf{k}_2)^2} + \frac{\mathbf{q}}{\mathbf{p}}\frac{1}{(\mathbf{k}-\mathbf{k}_1)^2}\right) \frac{1}{\mathbf{p}^2+\Lambda}\ \frac{1}{\mathbf{q}^2+\Lambda} \\ &- \left(\frac{1}{(\mathbf{k}_1-\mathbf{k}_2)^2} + \frac{\mathbf{q}}{\mathbf{p}+\mathbf{q}}\frac{1}{(\mathbf{k}-\mathbf{k}_1)^2} + \frac{\mathbf{p}}{\mathbf{q}}\frac{1}{(\mathbf{k}_1-\mathbf{k}_2)^2}\right) \frac{1}{\mathbf{q}^2+\Lambda}\ \frac{1}{(\mathbf{p}+\mathbf{q})^2+\Lambda} \\ &- \left(\frac{1}{(\mathbf{k}_1-\mathbf{k}_2)^2} + \frac{\mathbf{p}}{\mathbf{p}+\mathbf{q}}\frac{1}{(\mathbf{k}-\mathbf{k}_2)^2} + \frac{\mathbf{q}}{\mathbf{p}}\frac{1}{(\mathbf{k}_1-\mathbf{k}_2)^2}\right) \frac{1}{(\mathbf{p}+\mathbf{q})^2+\Lambda}\ \frac{1}{\mathbf{p}^2+\Lambda}\end{aligned} \tag{3.23}$$

We recall here that this is the resonant expression for $W$ under the assumption of only one pairing.

$$\begin{aligned}W_{\mathrm{r}}(\mathbf{k}_1,\mathbf{k}_2,\mathbf{k},\mathbf{p}) \simeq &-2\left(\frac{1}{\mathbf{k}-\mathbf{k}_2}\frac{1}{\mathbf{k}-\mathbf{k}_1}\right) \frac{1}{\mathbf{p}^2+\Lambda}\ \frac{1}{\mathbf{p}^2(\frac{\mathbf{k}-\mathbf{k}_1}{\mathbf{k}-\mathbf{k}_2})^2+\Lambda} \\ &-2\left(\frac{1}{\mathbf{k}_1-\mathbf{k}_2}\frac{1}{\mathbf{k}_1-\mathbf{k}}\right) \frac{1}{\mathbf{p}^2(\frac{\mathbf{k}_1-\mathbf{k}_2}{\mathbf{k}-\mathbf{k}_2})^2+\Lambda}\ \frac{1}{\mathbf{p}^2(\frac{\mathbf{k}-\mathbf{k}_1}{\mathbf{k}-\mathbf{k}_2})^2+\Lambda} \\ &-2\left(\frac{1}{\mathbf{k}_2-\mathbf{k}_1}\frac{1}{\mathbf{k}_2-\mathbf{k}}\right) \frac{1}{\mathbf{p}^2(\frac{\mathbf{k}_1-\mathbf{k}_2}{\mathbf{k}-\mathbf{k}_2})^2+\Lambda}\ \frac{1}{\mathbf{p}^2+\Lambda}\end{aligned} \tag{3.24}$$

### 3.3.4 Computation

Now that we have dealt with all the terms in the integral $\int \varphi_{\mathbf{k}}\, \dot{n}_{\mathbf{k}}\, \mathrm{d}\mathbf{k}$, we can start its computation, starting from equation (3.12).

$$\begin{aligned}\int \varphi_{\mathbf{k}} \frac{\partial n_{\mathbf{k}}}{\partial t}\mathrm{d}\mathbf{k} = 4\pi \int |W^{1,2,3}_{4,5,\mathbf{k}}|^2\ &\delta\Big((\mathbf{k}_1-\mathbf{k}_4)+(\mathbf{k}_2-\mathbf{k}_5)+(\mathbf{k}_3-\mathbf{k})\Big) \\ &2\delta\Big((\mathbf{k}_1-\mathbf{k}_4)(\mathbf{k}_1+\mathbf{k}_4)+(\mathbf{k}_2-\mathbf{k}_5)(\mathbf{k}_2+\mathbf{k}_5)+(\mathbf{k}_3-\mathbf{k})(\mathbf{k}_3+\mathbf{k})\Big)\ n_1n_2n_3n_4n_5n_{\mathbf{k}} \\ \times\left[\frac{1}{n_1}+\frac{1}{n_2}+\frac{1}{n_3}-\frac{1}{n_4}-\frac{1}{n_5}-\frac{1}{n_{\mathbf{k}}}\right]&\Big[\varphi_1+\varphi_2+\varphi_3-\varphi_4-\varphi_5-\varphi_{\mathbf{k}}\Big]\ \mathrm{d}\mathbf{k}_1\mathrm{d}\mathbf{k}_2\mathrm{d}\mathbf{k}_3\mathrm{d}\mathbf{k}_4\mathrm{d}\mathbf{k}_5\mathrm{d}\mathbf{k}\end{aligned} \tag{3.25}$$

Now, we change the integration variables from $\mathbf{k}_{1-5}, \mathbf{k}$ to $\mathbf{k}_{1-3}, \mathbf{p}, \mathbf{q}, \mathbf{k}$ with $p \ll k_1, k_4$ and $q \ll k_2, k_5$.

$$\begin{aligned}\int \varphi_{\mathbf{k}} \frac{\partial n_{\mathbf{k}}}{\partial t} \mathrm{d}\mathbf{k} = 4\pi \int |W^{\mathbf{k}_1,\mathbf{k}_2,\mathbf{k}_3}_{\mathbf{k}_1-\mathbf{p},\mathbf{k}_2-\mathbf{q},\mathbf{k}}|^2 \; \delta\Big(\mathbf{p}+\mathbf{q}+(\mathbf{k}_3-\mathbf{k})\Big) \\ 2\delta\Big(\mathbf{p}(2\mathbf{k}_1-\mathbf{p})+\mathbf{q}(2\mathbf{k}_2-\mathbf{q})+(\mathbf{k}_3-\mathbf{k})(\mathbf{k}_3+\mathbf{k})\Big) \; \times n_1 n_2 n_3 n_{\mathbf{k}_1-\mathbf{p}} n_{\mathbf{k}_2-\mathbf{q}} n_{\mathbf{k}} \\ \times \left[\frac{1}{n_1}+\frac{1}{n_2}+\frac{1}{n_3}-\frac{1}{n_{\mathbf{k}_1-\mathbf{p}}}-\frac{1}{n_{\mathbf{k}_2-\mathbf{q}}}-\frac{1}{n_{\mathbf{k}}}\right] \\ \times \Big[\varphi_1+\varphi_2+\varphi_3-\varphi_{\mathbf{k}_1-\mathbf{p}}-\varphi_{\mathbf{k}_2-\mathbf{q}}-\varphi_{\mathbf{k}}\Big] \; \mathrm{d}\mathbf{k}_1 \mathrm{d}\mathbf{k}_2 \mathrm{d}\mathbf{k}_3 \mathrm{d}\mathbf{p} \mathrm{d}\mathbf{q} \mathrm{d}\mathbf{k}\end{aligned} \tag{3.26}$$

We perform Taylor expansions in $p$ and in $q$ for the $\frac{1}{n_i}$ and the $\varphi_i$ terms. For conciseness, the derivations $\partial./\partial\mathbf{k_i}$ will be denoted $\partial_{\mathbf{k}_i}$

$$\begin{aligned}\int \varphi_{\mathbf{k}} \frac{\partial n_{\mathbf{k}}}{\partial t} \mathrm{d}\mathbf{k} = 4\pi \int |W^{\mathbf{k}_1,\mathbf{k}_2,\mathbf{k}_3}_{\mathbf{k}_1-\mathbf{p},\mathbf{k}_2-\mathbf{q},\mathbf{k}}|^2 \; \delta\Big(\mathbf{p}+\mathbf{q}+(\mathbf{k}_3-\mathbf{k})\Big) \\ 2\delta\Big(\mathbf{p}(2\mathbf{k}_1-\mathbf{p})+\mathbf{q}(2\mathbf{k}_2-\mathbf{q})+(\mathbf{k}_3-\mathbf{k})(\mathbf{k}_3+\mathbf{k})\Big) \; \times n_1 n_2 n_3 n_{\mathbf{k}_1-\mathbf{p}} n_{\mathbf{k}_2-\mathbf{q}} n_{\mathbf{k}} \\ \times \left[\mathbf{p}\partial_{\mathbf{k}_1}\frac{1}{n_1}+\mathbf{q}\partial_{\mathbf{k}_2}\frac{1}{n_2}+\left(\frac{1}{n_3}-\frac{1}{n_{\mathbf{k}}}\right)\right]\left[p\partial_{\mathbf{k}_1}\varphi_1+q\partial_{\mathbf{k}_2}\varphi_2+\Big(\varphi_3-\varphi_{\mathbf{k}}\Big)\right] \; \mathrm{d}\mathbf{k}_1 \mathrm{d}\mathbf{k}_2 \mathrm{d}\mathbf{k}_3 \mathrm{d}\mathbf{p} \mathrm{d}q \mathrm{d}\mathbf{k}\end{aligned} \tag{3.27}$$

We remove the $\mathbf{k}_3$ integration by using the $\mathbf{k}$ Kronecker delta which sets $\mathbf{k}_3 = \mathbf{k}-\mathbf{p}-\mathbf{q}$.

$$\begin{aligned}\int \varphi_{\mathbf{k}} \frac{\partial n_{\mathbf{k}}}{\partial t} \mathrm{d}\mathbf{k} = 4\pi \int |W^{\mathbf{k}_1,\mathbf{k}_2,\mathbf{k}-\mathbf{p}-\mathbf{q}}_{\mathbf{k}_1-\mathbf{p},\mathbf{k}_2-\mathbf{q},\mathbf{k}}|^2 \; 2\delta\Big(\mathbf{p}(2\mathbf{k}_1-\mathbf{p})+\mathbf{q}(2\mathbf{k}_2+\mathbf{q})+(-\mathbf{p}-\mathbf{q})(2\mathbf{k}-\mathbf{p}-\mathbf{q})\Big) \\ \times n_1 n_2 n_{\mathbf{k}-\mathbf{p}-\mathbf{q}} n_{\mathbf{k}_1-\mathbf{p}} n_{\mathbf{k}_2-\mathbf{q}} n_{\mathbf{k}} \left[\mathbf{p}\partial_{\mathbf{k}_1}\frac{1}{n_1}+\mathbf{q}\partial_{\mathbf{k}_2}\frac{1}{n_2}+\left(\frac{1}{n_{\mathbf{k}-\mathbf{p}-\mathbf{q}}}-\frac{1}{n_{\mathbf{k}}}\right)\right] \\ \times \Big[\mathbf{p}\partial_{\mathbf{k}_1}\varphi_1+\mathbf{q}\partial_{\mathbf{k}_2}\varphi_{\mathbf{k}_2}+\Big(\varphi_{\mathbf{k}-\mathbf{p}-\mathbf{q}}-\varphi_{\mathbf{k}}\Big)\Big] \; \mathrm{d}\mathbf{k}_1 \mathrm{d}\mathbf{k}_2 \mathrm{d}\mathbf{k}_3 \mathrm{d}\mathbf{p} \mathrm{d}q \mathrm{d}\mathbf{k}\end{aligned} \tag{3.28}$$

We perform a new Taylor expansion in $|\mathbf{p}+\mathbf{q}| \ll k$ and we expand the $\omega$ Kronecker delta up to the $p^1, q^1$ terms.

$$\begin{aligned}\int \varphi_{\mathbf{k}} \frac{\partial n_{\mathbf{k}}}{\partial t} \mathrm{d}\mathbf{k} = 4\pi \int |W^{\mathbf{k}_1,\mathbf{k}_2,\mathbf{k}-\mathbf{p}-\mathbf{q}}_{\mathbf{k}_1-\mathbf{p},\mathbf{k}_2-\mathbf{q},\mathbf{k}}|^2 \; \delta\Big(\mathbf{p}(\mathbf{k}_1-\mathbf{k})+\mathbf{q}(\mathbf{k}_2-\mathbf{k})\Big) \; \times n_1 n_2 n_{\mathbf{k}-\mathbf{p}-\mathbf{q}} n_{\mathbf{k}_1-\mathbf{p}} n_{\mathbf{k}_2-\mathbf{q}} n_{\mathbf{k}} \\ \times \left[\mathbf{p}\partial_{\mathbf{k}_1}\frac{1}{n_1}+\mathbf{q}\partial_{\mathbf{k}_2}\frac{1}{n_2}+(-\mathbf{p}-\mathbf{q})\partial_{\mathbf{k}}\frac{1}{n_{\mathbf{k}}}\right] \\ \times \Big[\mathbf{p}\partial_{\mathbf{k}_1}\varphi_1+\mathbf{q}\partial_{\mathbf{k}_2}\varphi_2+(-\mathbf{p}-\mathbf{q})\partial_{\mathbf{k}}\varphi_{\mathbf{k}}\Big] \; \mathrm{d}\mathbf{k}_1 \; \mathrm{d}\mathbf{k}_2 \; \mathrm{d}\mathbf{p} \; \mathrm{d}\mathbf{q} \; \mathrm{d}\mathbf{k}\end{aligned} \tag{3.29}$$

$$\begin{aligned}\int \varphi_{\mathbf{k}} \frac{\partial n_{\mathbf{k}}}{\partial t} \mathrm{d}\mathbf{k} = 4\pi \int |W^{\mathbf{k}_1,\mathbf{k}_2,\mathbf{k}-\mathbf{p}-\mathbf{q}}_{\mathbf{k}_1-\mathbf{p},\mathbf{k}_2-\mathbf{q},\mathbf{k}}|^2 \, \delta\Big(\mathbf{p}(\mathbf{k}_1-\mathbf{k}) + \mathbf{q}(\mathbf{k}_2-\mathbf{k})\Big) \; \times n_1 n_2 n_{\mathbf{k}-\mathbf{p}-\mathbf{q}} n_{\mathbf{k}_1-\mathbf{p}} n_{\mathbf{k}_2-\mathbf{q}} n_{\mathbf{k}} \\ \times \left[\mathbf{p}\left(\partial_{\mathbf{k}_1}\frac{1}{n_1} - \partial_{\mathbf{k}}\frac{1}{n_{\mathbf{k}}}\right) + \mathbf{q}\left(\partial_{\mathbf{k}_2}\frac{1}{n_2} - \partial_{\mathbf{k}}\frac{1}{n_{\mathbf{k}}}\right)\right] \\ \times \left[\mathbf{p}\left(\partial_{\mathbf{k}_1}\varphi_1 - \partial_{\mathbf{k}}\varphi_{\mathbf{k}}\right) + \mathbf{q}\left(\partial_{\mathbf{k}_2}\varphi_2 - \partial_{\mathbf{k}}\varphi_{\mathbf{k}}\right)\right] \mathrm{d}\mathbf{k}_1 \, \mathrm{d}\mathbf{k}_2 \, \mathrm{d}\mathbf{p} \, \mathrm{d}q \, \mathrm{d}\mathbf{k}\end{aligned} \tag{3.30}$$

We now remove the $\mathbf{q}-$integration by using the $\omega$ Kronecker function with $\delta(\mathbf{p}(\mathbf{k}_1 - \mathbf{k})\mathbf{p} + \mathbf{q}(\mathbf{k}_2 - \mathbf{k})) = |\mathbf{k}_2 - \mathbf{k}|^{-1}\delta(\mathbf{p}\frac{\mathbf{k}_1-\mathbf{k}}{\mathbf{k}_2-\mathbf{k}} + \mathbf{q})$. At this point, the interaction coefficient is $W_{\mathrm{r}}(\mathbf{k}_1, \mathbf{k}_2, \mathbf{k}, \mathbf{p})$, written in (3.24).

$$\begin{aligned}\int \varphi_{\mathbf{k}} \frac{\partial n_{\mathbf{k}}}{\partial t} \mathrm{d}\mathbf{k} = 4\pi \int |W_{\mathrm{r}}(\mathbf{k}_1, \mathbf{k}_2, \mathbf{k}, \mathbf{p})|^2 \, \frac{1}{|\mathbf{k}_2 - \mathbf{k}|} \; \times n_1 n_2 n_{\mathbf{k}-\mathbf{p}\frac{\mathbf{k}_2-\mathbf{k}_1}{\mathbf{k}_2-\mathbf{k}}} n_{\mathbf{k}_1-\mathbf{p}} n_{\mathbf{k}_2-\mathbf{p}\frac{\mathbf{k}-\mathbf{k}_1}{\mathbf{k}_2-\mathbf{k}}} n_{\mathbf{k}} \\ \times \mathbf{p}\left[\left(\partial_{\mathbf{k}_1}\frac{1}{n_1} - \partial_{\mathbf{k}}\frac{1}{n_{\mathbf{k}}}\right) + \frac{\mathbf{k}-\mathbf{k}_1}{\mathbf{k}_2-\mathbf{k}}\left(\partial_{\mathbf{k}_2}\frac{1}{n_2} - \partial_{\mathbf{k}}\frac{1}{n_{\mathbf{k}}}\right)\right] \\ \times \mathbf{p}\left[\left(\partial_{\mathbf{k}_1}\varphi_1 - \partial_{\mathbf{k}}\varphi_{\mathbf{k}}\right) + \frac{\mathbf{k}-\mathbf{k}_1}{\mathbf{k}_2-\mathbf{k}}\left(\partial_{\mathbf{k}_2}\varphi_2 - \partial_{\mathbf{k}}\varphi_{\mathbf{k}}\right)\right] \mathrm{d}\mathbf{k}_1 \, \mathrm{d}\mathbf{k}_2 \, \mathrm{d}\mathbf{p} \, \mathrm{d}\mathbf{k}\end{aligned} \tag{3.31}$$

To to stay at the lower order in $p$, the Taylor expansions of $n_{\mathbf{k}_i - \infty\mathbf{p}}$ are done to the first order, in $p^0$.

$$\begin{aligned}\int \varphi_{\mathbf{k}} \frac{\partial n_{\mathbf{k}}}{\partial t} \mathrm{d}\mathbf{k} = 4\pi \int |W_{\mathrm{r}}(\mathbf{k}_1, \mathbf{k}_2, \mathbf{k}, \mathbf{p})|^2 \, \frac{1}{|\mathbf{k}_2 - \mathbf{k}|} \; \times n_1^2 n_2^2 n_{\mathbf{k}}^2 \\ \times \mathbf{p}^2\left[\left(\partial_{\mathbf{k}_1}\frac{1}{n_1} - \partial_{k}\frac{1}{n_{\mathbf{k}}}\right) + \frac{\mathbf{k}-\mathbf{k}_1}{\mathbf{k}_2-\mathbf{k}}\left(\partial_{\mathbf{k}_2}\frac{1}{n_2} - \partial_{\mathbf{k}}\frac{1}{n_{\mathbf{k}}}\right)\right] \\ \times \left[\left(\partial_{\mathbf{k}_1}\varphi_1 - \partial_{\mathbf{k}}\varphi_{\mathbf{k}}\right) + \frac{\mathbf{k}-\mathbf{k}_1}{\mathbf{k}_2-\mathbf{k}}\left(\partial_{\mathbf{k}_2}\varphi_2 - \partial_{\mathbf{k}}\varphi_{\mathbf{k}}\right)\right] \mathrm{d}\mathbf{k}_1 \, \mathrm{d}\mathbf{k}_2 \, \mathrm{d}\mathbf{p} \, \mathrm{d}\mathbf{k}\end{aligned} \tag{3.32}$$

Now we can integrate this with respect to $\mathbf{p}$, and define the function $f = f(\mathbf{k}_1, \mathbf{k}_2, \mathbf{k})$ such as

$$\int_{-\infty}^{\infty} |W_{\mathrm{r}}(\mathbf{k}_1, \mathbf{k}_2, \mathbf{k}, \mathbf{p})|^2 \mathbf{p}^2 \, \mathrm{d}\mathbf{p} = \frac{1}{\Lambda^{\frac{5}{2}}} f(\mathbf{k}_1, \mathbf{k}_2, \mathbf{k}). \tag{3.33}$$

Since the integrand $|W|^2\mathbf{p}^2$ is a positive function, its integral, and thus $f$, is also a positive function, as $\Lambda$ is positive by assumption. Its full expression is given in Appendix B. We then multiply the obtained expression by six in order to take into account the other pairings that the one used for the computation.

$$\int \varphi_{\mathbf{k}} \frac{\partial n_{\mathbf{k}}}{\partial t} \mathrm{d}\mathbf{k} = 24\pi \frac{1}{\Lambda^{\frac{5}{2}}} \iiint f(\mathbf{k}_1, \mathbf{k}_2, \mathbf{k}) \frac{1}{|\mathbf{k}_2 - \mathbf{k}|} n_1^2 n_2^2 n_{\mathbf{k}}^2 \left[ \left( \partial_{\mathbf{k}_1} \frac{1}{n_1} - \partial_{\mathbf{k}} \frac{1}{n_k} \right) + \frac{\mathbf{k} - \mathbf{k}_1}{\mathbf{k}_2 - \mathbf{k}} \left( \partial_{\mathbf{k}_2} \frac{1}{n_2} - \partial_k \frac{1}{n_{\mathbf{k}}} \right) \right] \times \left[ \left( \partial_{\mathbf{k}_1} \varphi_1 - \partial_{\mathbf{k}} \varphi_k \right) + \frac{\mathbf{k} - \mathbf{k}_1}{\mathbf{k}_2 - \mathbf{k}} \left( \partial_{\mathbf{k}_2} \varphi_2 - \partial_{\mathbf{k}} \varphi_k \right) \right] \mathrm{d}\mathbf{k}_1 \, \mathrm{d}\mathbf{k}_2 \, \mathrm{d}\mathbf{k} \tag{3.34}$$

The next computations do not represent any physical concept nor approximation, so we detail them in Appendix A and we only present the last steps. We obtain

$$\frac{\partial n_{\mathbf{k}}}{\partial t} = 24\pi \frac{1}{\Lambda^{\frac{5}{2}}} \partial_{\mathbf{k}} \int V_{\mathbf{k}}^{\mathbf{k}_1, \mathbf{k}_2} \left[ n_2^2 n_{\mathbf{k}}^2 \, 2 \frac{\mathbf{k} - \mathbf{k}_2}{-\mathbf{k}_1 + \mathbf{k}_2} \partial_{\mathbf{k}_1} n_1 + n_1^2 n_2^2 \, \partial_{\mathbf{k}} n_{\mathbf{k}} \right] \mathrm{d}\mathbf{k}_1 \mathrm{d}\mathbf{k}_2. \tag{3.35}$$

$V_{\mathbf{k}}^{\mathbf{k}_1, \mathbf{k}_2}$ is a function which can be interpreted as an interaction coefficient. Its expression is given in Appendix B but we recall here some important properties

$$V_{\mathbf{k}}^{\mathbf{k}_1, \mathbf{k}_2} = V_{\mathbf{k}}^{\mathbf{k}_2, \mathbf{k}_1} \ , \quad V_{\mathbf{k}_2}^{\mathbf{k}_1, \mathbf{k}} = \frac{(\mathbf{k} - \mathbf{k}_1)^2}{(\mathbf{k}_2 - \mathbf{k}_1)^2} V_{\mathbf{k}}^{\mathbf{k}_1, \mathbf{k}_2} \ , \quad \forall \mathbf{k}_1, \mathbf{k}_2, \mathbf{k} \in \mathbb{R}, \, V_{\mathbf{k}}^{\mathbf{k}_1, \mathbf{k}_2} > 0, \tag{3.36}$$

and particularly, $V$ is scale-invariant. We now recall that the action flux $Q(\mathbf{k}$ satisfies the continuity equation for the wave-action 3.37(a), which, by comparison to 3.35, gives the final expression for $Q(\mathbf{k})$ 3.37(b). Together, the continuity equation 3.37(a) and the expression for the wave-action flux 3.37(b) constitute the SLAM.

$$\frac{\partial n_{\mathbf{k}}}{\partial t} = -\frac{\partial Q}{\partial \mathbf{k}} \tag{3.37a}$$

$$Q(\mathbf{k}) = -\frac{24\pi}{\Lambda^{5/2}} \int \frac{V_{\mathbf{k}}^{1,2}}{\mathbf{k}_2 - \mathbf{k}_1} \left[ (\mathbf{k} - \mathbf{k}_2) n_{\mathbf{k}}^2 n_2^2 \frac{\partial n_1}{\partial \mathbf{k}_1} + (\mathbf{k}_1 - \mathbf{k}) n_{\mathbf{k}}^2 n_1^2 \frac{\partial n_2}{\partial \mathbf{k}_2} + (\mathbf{k}_2 - \mathbf{k}_1) n_1^2 n_2^2 \frac{\partial n_{\mathbf{k}}}{\partial \mathbf{k}} \right] \mathrm{d}\mathbf{k}_1 \mathrm{d}\mathbf{k}_2 \tag{3.37b}$$

The SLAM considerably reduced the complexity of the collision integral as $Q$ is now only an integral over two variables, while the original collision integral of the six-mode KE was an integral over five variables.

We can notice here that $n_{\mathbf{k}}$ and $Q$ depend on the wave-number $\mathbf{k}$ and not on its norm $k$. If we assume that the system is isotropic, the wave-action spectrum $n$ should be independent of $\mathrm{sgn}(\mathbf{k})$ and only depend on its norm, namely $n_{\mathbf{k}} = n_{\mathbf{k}}(k)$. With the continuity equation (3.37), that would imply that we can define a symmetric flux $Q_s(k) = \mathrm{sgn}(\mathbf{k}) Q(\mathbf{k})$ such that $\partial n_{\mathbf{k}} / \partial t = -\partial Q_s / \partial k$.

### 3.3.5 Verifications

We first verify that the integrand of $Q(\mathbf{k})$ does not diverge for $\mathbf{k}_1 = \mathbf{k}_2$ or $\mathbf{k}_{1,2} = \mathbf{k}$. This is ensured by the square-bracket term which cancels the divergences of the coefficient $V$.

#### Verification of the Rayleigh-Jeans spectrum

We now check than the Rayleigh-Jeans spectrum defined in section 1.3.4 $n_{\mathbf{k}}^{\mathrm{RJ}} = T/(\mu + \omega_{\mathbf{k}}) = T/(\mu + \frac{1}{2}\mathbf{k}^2)$, is actually a solution of the SLAM (3.37). In the limit $T, \mu \to \infty$ with the ratio $T/\mu$ finite, we obtain the equipartition of particles only with $n_{\mathbf{k}}^{\mathrm{RJ}} \propto k^0$, denoted $x_{\mathrm{TN}} = 0$. The other limit $\mu = 0$ corresponds to the equipartition of energy only. The spectrum obtained is $n_{\mathbf{k}}^{\mathrm{RJ}} \propto k^{-2}$, denoted $x_{\mathrm{TE}} = -2$. These two spectra must be stationary states of the system.

Straightforward computations show that both $n_{\mathbf{k}} = Ck^0$ and $Ck^2$ cancel exactly the square bracket in the integral of the flux and thus, are indeed stationary states of the system. RJ spectrum being a stationary state was expected and thus, stands as a first verification of our final expression of $Q_{\mathbf{k}}$.

#### Conservation of the energy $E$

As said when we introduced the weak WT framework, the total wave-action $\mathcal{N} = \int n_{\mathbf{k}} \mathrm{d}\mathbf{k}$ and the energy $E = \int \omega_{\mathbf{k}} n_{\mathbf{k}} \mathrm{d}\mathbf{k}$ are exactly conserved by the original KE. Thus, we need to verify that they are indeed conserved quantities in the SLAM. Indeed, the SLAM is supposed to keep the structure of the equation, and consequently must conserve the invariants of the original KE.

The final equation of the SLAM (3.37) is a continuity equation for $n_{\mathbf{k}}$ so the conservation of $\mathcal{N}$ is ensured. For $E$, we need to check its conservation by computing explicitly $\partial E/\partial t$,

$$\frac{\partial E}{\partial t} = \int_{-\infty}^{+\infty} \omega_{\mathbf{k}} \frac{\partial n_{\mathbf{k}}}{\partial t} \mathrm{d}\mathbf{k} = -\int \omega_{\mathbf{k}} \frac{\partial Q}{\partial \mathbf{k}} \mathrm{d}\mathbf{k}. \tag{3.38}$$

Integrating by parts, we obtain

$$\frac{\partial E}{\partial t} = -\Big[\omega_{\mathbf{k}} Q\Big]_{-\infty}^{+\infty} + \int \mathbf{k} Q \ \mathrm{d}\mathbf{k}. \tag{3.39}$$

The square bracket is taken to be null as we assume that the wave-action flux tends to 0 for very large wave-numbers. The integral can be written with the expression of $Q$ (3.37) found with the SLAM

$$\frac{\partial E}{\partial t} = \frac{24\pi}{\Lambda^{5/2}} \int \frac{\mathbf{k} V_{\mathbf{k}}^{1,2}}{\mathbf{k}_2 - \mathbf{k}_1} \left[ (\mathbf{k} - \mathbf{k}_2) n_{\mathbf{k}}^2 n_2^2 \frac{\partial n_1}{\partial \mathbf{k}_1} + (\mathbf{k}_1 - \mathbf{k}) n_{\mathbf{k}}^2 n_1^2 \frac{\partial n_2}{\partial \mathbf{k}_2} + (\mathbf{k}_2 - \mathbf{k}_1) n_1^2 n_2^2 \frac{\partial n_{\mathbf{k}}}{\partial \mathbf{k}} \right] \mathrm{d}\mathbf{k}_1 \mathrm{d}\mathbf{k}_2 \mathrm{d}\mathbf{k}. \tag{3.40}$$

As $\mathbf{k}$ is now an integration variable along with $\mathbf{k}_1$ and $\mathbf{k}_2$, we can use the symmetries $\mathbf{k} \leftrightarrow \mathbf{k}_1$ and $\mathbf{k} \leftrightarrow \mathbf{k}_2$ to compute the integral. We split this integral in three equal parts, leaving the first one unchanged and performing the swap of variables $\mathbf{k} \leftrightarrow \mathbf{k}_1$ and $\mathbf{k} \leftrightarrow \mathbf{k}_2$ in the second and third respectively. The arguments of coefficient $V$ will be modified but we can go back to $V_{\mathbf{k}}^{1,2}$ with the property of the coefficient $V$

$$V_{\mathbf{p}_1}^{\mathbf{p}_3,\mathbf{p}_2} = \left(\frac{\mathbf{p}_3 - \mathbf{p}_2}{\mathbf{p}_2 - \mathbf{p}_1}\right)^2 V_{\mathbf{p}_3}^{\mathbf{p}_1,\mathbf{p}_2} \tag{3.41}$$

and with the symmetry of $V$ with respect to its two upper indices, we can write

$$\frac{\partial E}{\partial t} = \frac{24\pi}{3\Lambda^{5/2}} \int \left\{ \frac{\mathbf{k}}{\mathbf{k}_2 - \mathbf{k}_1} + \frac{\mathbf{k}_1(\mathbf{k} - \mathbf{k}_2)}{(\mathbf{k}_2 - \mathbf{k}_1)^2} + \frac{\mathbf{k}_2(\mathbf{k} - \mathbf{k}_1)}{(\mathbf{k}_2 - \mathbf{k}_1)^2} \right\} V_{\mathbf{k}}^{1,2} \times \left[ (\mathbf{k} - \mathbf{k}_2) n_{\mathbf{k}}^2 n_2^2 \frac{\partial n_1}{\partial \mathbf{k}_1} + (\mathbf{k}_1 - \mathbf{k}) n_{\mathbf{k}}^2 n_1^2 \frac{\partial n_2}{\partial \mathbf{k}_2} + (\mathbf{k}_2 - \mathbf{k}_1) n_1^2 n_2^2 \frac{\partial n_{\mathbf{k}}}{\partial \mathbf{k}} \right] \mathrm{d}\mathbf{k}_1 \mathrm{d}\mathbf{k}_2 \mathrm{d}\mathbf{k}.$$

The factorization of the braces term shows that is null, implying that $\partial E/\partial t = 0$. Consequently, we have verified that the 1D-SLAM conserves exactly the linear energy, as expected.

**Summary of the section**

- By applying the SLAM to our system, we obtain an expression of the wave-action flux and its continuity equation with the wave-action spectrum.
- The results of the SLAM are verified : the Rayleigh-Jeans spectrum solution and the conservation of the energy $E$ are satisfied.

## 3.4 KZ predictions

Before deriving the KZ spectra $n_{\mathbf{k}} \propto k^x$ for wave-action and energy cascades, let us summarize their properties with the wave-action and energy fluxes $Q_s(k,x)$ and $P_s(k,x)$

$$\text{wave} - \text{action cascade}, x_{\mathrm{FN}} \quad \text{such as } Q_s(k, x_{\mathrm{FN}}) \propto k^0, \quad P_s(k, x_{\mathrm{FN}}) = 0 \tag{3.42a}$$

$$\text{energy cascade}, x_{\mathrm{FE}} \quad \text{such as } P_s(k, x_{\mathrm{FE}}) \propto k^0, \quad Q_s(k, x_{\mathrm{FE}}) = 0 \tag{3.42b}$$

These equalities just signify that for the cascade of a quantity, the flux of this quantity is a constant while the flux of the other quantity is null.

### 3.4.1 KZ predictions via dimensional analysis

Thanks to the SLAM, we now have an expression for the wave-action flux $Q(\mathbf{k})$

$$Q(\mathbf{k}) = -\frac{24\pi}{\Lambda^{5/2}} \int \frac{V_{\mathbf{k}}^{1,2}}{\mathbf{k}_2 - \mathbf{k}_1} \left[ (\mathbf{k} - \mathbf{k}_2) n_{\mathbf{k}}^2 n_2^2 \frac{\partial n_1}{\partial \mathbf{k}_1} + (\mathbf{k}_1 - \mathbf{k}) n_{\mathbf{k}}^2 n_1^2 \frac{\partial n_2}{\partial \mathbf{k}_2} + (\mathbf{k}_2 - \mathbf{k}_1) n_1^2 n_2^2 \frac{\partial n_{\mathbf{k}}}{\partial \mathbf{k}} \right] \mathrm{d}\mathbf{k}_1 \mathrm{d}\mathbf{k}_2 \tag{3.43}$$

With this expression of $Q(\mathbf{k})$ and power-law spectra $n_{\mathbf{k}} = Ck^x$, we can regroup all the $\mathbf{k}$-dependances to identify the power $x$ which makes it $\mathbf{k}$-independant. Such a power would make the wave-action flux scale-independent, it would thus correspond to the wave-action cascade $x_{\mathrm{FN}}$. To this end, we set the change of variable $\mathbf{k}_1 \to \mathbf{s}_1 = \mathbf{k}_1/\mathbf{k}$ and $\mathbf{k}_2 \to \mathbf{s}_2 = \mathbf{k}_2/\mathbf{k}$ which creates non-dimensional variables $\mathbf{s}_{1,2}$. Similarly as the $\mathbf{k}$-variables, their norms will be denoted $s_{1,2}$. This method corresponds to applying Zakharov Transform (ZT).

The coefficient $V_{\mathbf{k}}^{1,2} = V_{\mathbf{k}}^{\mathbf{k}_1,\mathbf{k}_2}$ is scale-invariant, contrary to the initial six-mode coefficient $W$, and we have

$$V_{\mathbf{k}}^{1,2} = V_{\mathbf{k}}^{\mathbf{s}_1\mathbf{k},\mathbf{s}_2\mathbf{k}} = \frac{1}{k^5} V_1^{\mathbf{s}_1,\mathbf{s}_2}. \tag{3.44}$$

After computations, the change of variables $(\mathbf{k}_1, \mathbf{k}_2) \to (\mathbf{s}_1, \mathbf{s}_2)$ gives

$$Q(\mathbf{k}) = -k^{5x-4}\mathrm{sgn}(\mathbf{k})\frac{24\pi C^5 x}{\Lambda^{5/2}} \int \frac{V_1^{\mathbf{s}_1,\mathbf{s}_2}}{\mathbf{s_2} - \mathbf{s_1}} \left[(1-\mathbf{s}_2)s_2^{2x}s_1^{x-1}\mathrm{sgn}(\mathbf{s}_1) + (\mathbf{s}_1 - 1)s_1^{2x}s_2^{x-1}\mathrm{sgn}(\mathbf{s}_2) + (\mathbf{s}_2 - \mathbf{s}_1)s_1^{2x}s_2^{2x}\right] \mathrm{d}\mathbf{s}_1\mathrm{d}\mathbf{s}_2, \tag{3.45}$$

which allows us to write the symmetric flux $Q_s(k) = \mathrm{sign}(\mathbf{k})Q(\mathbf{k})$ the following way

$$\boxed{Q_s = k^{5x-4}I(x)}, \qquad \text{with} \tag{3.46a}$$

$$I(x) = -\frac{24\pi C^5 x}{\Lambda^{5/2}} \int \frac{V_1^{\mathbf{s}_1,\mathbf{s}_2}}{\mathbf{s_2} - \mathbf{s_1}} \left[(1-\mathbf{s}_2)s_2^{2x}s_1^{x-1}\mathrm{sgn}(\mathbf{s}_1) + (\mathbf{s}_1 - 1)s_1^{2x}s_2^{x-1}\mathrm{sgn}(\mathbf{s}_2) + (\mathbf{s}_2 - \mathbf{s}_1)s_1^{2x}s_2^{2x}\right] \mathrm{d}\mathbf{s}_1\mathrm{d}\mathbf{s}_2 \tag{3.46b}$$

as the product of a power of the modulus $k$ and a dimensionless double integral $I(x)$ which only depends on the exponent $x$. With the definition of the wave-action spectrum $x_{\mathrm{FN}}$ making $Q_s$ $k$-independent, we obtain the dimensional prediction for the wave-action spectrum $x_{\mathrm{FN}} = 4/5$. For this prediction to really correspond to a KZ spectrum, $x_{\mathrm{FN}} = 4/5$ has to cancel the symmetric energy flux $P_s$ and the integral $I(x_{\mathrm{FN}} = 4/5)$ must be finite for this spectrum to be local. The symmetric energy flux $P_s = P_s(k)$ can be derived from $Q_s$ with their respective definitions. From (1.48) and $\omega_{\mathbf{k}} = \mathbf{k}^2/2$ independent of $t$, we can write

$$\omega_k \frac{\partial Q_s}{\partial k} = \frac{\partial P_s}{\partial k} \quad \text{which gives} \quad P_s(k) = k^2 Q_s/2 - \int_0^k k' Q_s(k')\, dk' \tag{3.47}$$

After an integration by parts, we get

$$\boxed{P_s = \frac{k^{5x-2}(5x-4)}{10x-4} I(x)} \tag{3.48}$$

with the same function $I(x)$ as for $Q_s$. We can check that $P_s(x_{\mathrm{FN}} = 4/5) = 0$ provided again that $I(x_{\mathrm{FN}} = 4/5)$ is finite, which could show that no energy is cascading during the wave-action cascade. To answer this question, we need to characterize the integral $I(x)$ and determine its interval of convergence. The detailed computations are presented in Appendix D and we only present here the result :

$$I(x) \text{ convergent } \Leftrightarrow 0 \leq x < \frac{3}{4} \quad \text{or} \quad x = -2. \tag{3.49}$$

We recall here that $x = 0$ and $-2$ are special powers corresponding to the RJ spectrum. The wave-action KZ spectrum $x_{\text{FN}} = 4/5$ is not included in the convergence interval, $Q_s(x_{\text{FN}})$ and $P_s(x_{\text{FN}})$ are not finite and, thus, the wave-action spectrum is not local. This means that the cascade of wave-action is done by non-local interactions occurring when both variables $s_1, s_2$ go to $\infty$ (see Appendix D). This problem requires a non-local analysis which will be performed later.

The other KZ spectrum expected in the 1D-SHE system is the energy spectrum $x_{\text{FE}}$, which makes the energy flux $P_s(k, x_{\text{FE}})$ independent from $k$ and cancels the wave-action flux $Q_s(k, x_{\text{FE}})$. Given the expression (3.48) of $P_s$, $x_{\text{FE}} = 2/5$ makes the energy flux proportional to $k^0$ and thus gives the KZ prediction for the energy cascade. However, this corresponds to $P_s(x_{\text{FE}}) = -2I(2/5)/0$, which is divergent unless $I(2/5) = 0$. The precise computation of $I(2/5)$ with the help of Zakharov Transforms, detailed in Appendix C, shows indeed that it is equal to 0. The value of the energy flux for the energy KZ spectrum is thus finite and its precise value can be computed thanks to the L'Hôpital's rule which gives $P_s(x_{\text{FE}}) = -I'(2/5)/5$ but the computation of $I'(2/5)$ is really difficult, even for `Mathematica`. The computation of the signs of the fluxes will be done in the next section.

With this result of $I(2/5) = 0$, we directly have $Q_s(k, x_{\text{FE}}) = 0$, the wave-action flux is null during the cascade of energy. Consequently, $x_{\text{FE}} = 2/5$ verifies all the conditions to be a KZ spectrum of the SLAM, the energy flux is independent from $k$ and finite and the wave-action flux is null. Furthermore, the convergence study of $I(x)$ showed that the KZ prediction for energy cascade $x_{\text{FE}} = 2/5$ is local.

We can notice that these predictions are significantly different from the ones obtained for the short-wave equation in [5] ; $x_{\text{FN}}^{\text{SWE}} = 9/5$ for the inverse wave-action cascade, compared to $x_{\text{FN}} = 4/5$ here, and $x_{\text{FE}}^{\text{SWE}} = 7/5$ for the direct energy cascade, compared to $x_{\text{FE}} = 2/5$ obtained here. For both cascades, we obtain an exponent smaller by one.

### 3.4.2 Conclusion and signs of fluxes

The Figure 3.2 plots the symmetric energy and waves-action fluxes $P_s$ and $Q_s$ as functions of $x$. On the $x$-axis, we present the exponents $x$ corresponding to the RJ spectra and KZ predictions. The fluxes are plotted with the help of two rules. First, the RJ spectra are characterized by null fluxes, so $P_s$ and $Q_s$ are 0 for $x_{\text{TN}}$ and $x_{\text{TE}}$. The KZ spectra spectra are defined by the flux of one quantity and the absence of flux for the other one. For instance, for the wave-action spectrum at $x = x_{\text{FN}}$, corresponding to cascading wave-action, we should have $Q_s \neq 0$ and $P_s = 0$. Conversely, at $x = x_{\text{FE}}$, we should have $Q_s = 0$ and $P_s \neq 0$. Secondly, we expect some asymptotic behaviours for the fluxes for $x \to \pm\infty$. For $x \to -\infty$, the spectrum is concentrated in low wave-numbers. It is natural to assume that both fluxes are positive to spread the invariants to large wave-numbers. On the contrary, for $x \to +\infty$, we expect $P_s, Q_s < 0$ because the spectrum is

highly increasing for large $k$. With these two rules and the continuity of $P_s$ and $Q_s$, we can draw qualitatively $P_s(x)$ and $Q_s(x)$ in FIGURE 3.2.

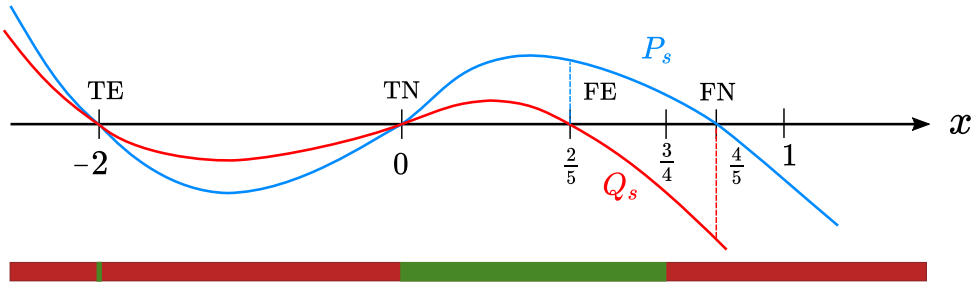


Figure 3.2: **Energy and wave-action fluxes $P_s$ and $Q_s$ against the power-law exponent $x$** - We conclude from this graph that the $P_s(x = x_{\text{FE}}) > 0$ and $Q_s(x = x_{\text{FN}}) < 0$, *ie* the energy cascade is direct and the wave-action cascade is inverse. However, strictly, we can not draw the fluxes outside of their convergence interval highlighted in green in the color bar below the graph. The red parts denotes the interval on which the fluxes diverge.

Plotting $P_S$ and $Q_s$ for all the exponents $x$ assumes that the fluxes are defined for all these values, *ie* that the integral $I(x)$ convergences for all $x$. We have showed that it is not the case. Then, we need to plot the fluxes only for the values of $x$ for which it is defined. This is done FIGURE 3.3.

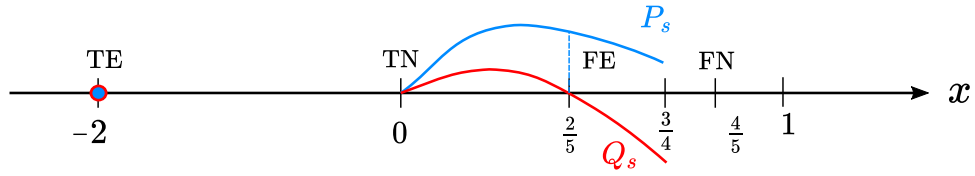


Figure 3.3: **Energy and wave-action fluxes $P_s$ and $Q_s$ against the power-law exponent $x$ on their convergence interval** - $Q_s$ is null only for $x = 0$ and $x_{\text{FE}} = 2/5$ and we know that it goes to $-\infty$ for the largest $x$ possible, so $Q'(x = 2/5) < 0$, from which we conclude $P(x = 2/5) > 0$.

With the plot of $Q_s(x)$, we can find the sign of $P_s(x_{\text{FE}} = 2/5)$. Indeed, we know that in the interval $0 \leq x < 3/4$, $Q_s$ is only null for $x = x_{\text{FE}} = 2/5$. From this we can conclude that $Q'(x = 2/5) < 0$, which directly gives $I'(2/5) < 0$. Finally, the L'Hôpital's rule gave us $P_s(x_{\text{FE}}) = -I'(2/5)/5$, which finally imply $P_s(x_{\text{FE}}) > 0$, as represented in FIGURE 3.3. A positive energy flux at the energy cascade KZ spectrum indicates that the energy cascade is direct, towards large $k$, which is in accordance with the Fjørtoft argument section 1.3.4. We can then assume that the wave-action KZ cascade would be inverse if it was local, which is consistent with $Q_s(x = x_{\text{FN}}) < 0$ observed in FIGURE 3.2, but outside the convergence interval.

To this point, with the expression of $Q_s$ given by the SLAM, we found an energy KZ spectrum prediction $x_{\rm FE} = 2/5$, which was found to correspond to a direct cascade with the study of $P_s(x)$. Additionally , this spectrum is physically viable because the corresponding energy flux is finite. On the contrary, the wave-action KZ spectrum prediction $x_{\rm FN} = 4/5$ turns out to be unphysical because its wave-action flux is not finite. As said previously, we will deal with this issue by analysing the system in the $s_1, s_2 \gg 1$ limit, where the integral $I(x)$ is divergent for the KZ wave-action cascade prediction $x_{\rm FN} = 4/5$ (see Appendix D).

### 3.4.3 Non-local analysis

Let us get back to the expression of the wave-action flux $Q_s(k)$ with dimensional variables $k_{1,2}$ in the limit $k_1, k_2 \gg k$, which corresponds to the UV limit where the integral $I$ is divergent for $x_{\rm FN} = 4/5$. Namely, we re-write $Q_s(k)$ with the expression (3.37b) of $Q$ in this limit. We get

$$Q_s(k) = -24\pi \frac{\operatorname{sgn}\mathbf{k}}{\Lambda^{\frac{5}{2}}} \iint_{k\ll k_{1,2}} V_{\mathbf{k}}^{\mathbf{k}_1,\mathbf{k}_2} \left[ 2n_2^2 n_{\mathbf{k}}^2 \, \frac{-\mathbf{k}_2}{-\mathbf{k}_1+\mathbf{k}_2} \frac{\partial n_1}{\partial \mathbf{k}_1} + n_{k_1}^2 n_{k_2}^2 \frac{\partial n_{\mathbf{k}}}{\partial \mathbf{k}} \right] d\mathbf{k}_1 d\mathbf{k}_2. \quad (3.50)$$

Notice that we have used the $\mathbf{k}_1 \leftrightarrow \mathbf{k}_2$ symmetry to regroup the first two terms in (3.37b). The interaction coefficient $V_{\mathbf{k}}^{\mathbf{k}_1,\mathbf{k}_2}$ can be expanded in this $k_1, k_2 \gg k$ limit. To the first order we have

$$V_{\mathbf{k}}^{\mathbf{k}_1,\mathbf{k}_2} = V_0^{\mathbf{k}_1,\mathbf{k}_2} + \mathcal{O}\Big(\frac{k_1}{k}, \frac{k_2}{k}\Big). \quad (3.51)$$

(notice in Appendix B that $\mathbf{k}$ always appears compared to $\mathbf{k}_{1,2}$). This new coefficient $V_0^{\mathbf{k}_1,\mathbf{k}_2}$ has important properties, due to the third wave-vector considered null,

$$V_0^{\mathbf{k}_1,\mathbf{k}_2} > 0, \quad V_0^{-\mathbf{k}_1,\mathbf{k}_2} = V_0^{\mathbf{k}_1,-\mathbf{k}_2} \text{ and } V_0^{\mathbf{k}_1,\mathbf{k}_2} = V_0^{-\mathbf{k}_1,-\mathbf{k}_2}. \quad (3.52)$$

We can show (see appendix E) that these properties make the integral of the first term of the RHS of (3.50) null. We are left with only the integral of the second term, proportional to $\operatorname{sign}(\mathbf{k})\frac{\partial n_{\mathbf{k}}}{\partial \mathbf{k}} = \frac{\partial n_{\mathbf{k}}}{\partial k}$, *ie*

$$Q_s(k) = -D\partial_k n_{\mathbf{k}}, \quad \text{with } D = \frac{24\pi}{\Lambda^{\frac{5}{2}}} \int_{k\ll k_{1,2}} V_0^{\mathbf{k}_1,\mathbf{k}_2} \, n_1^2 n_2^2 \, d\mathbf{k}_1 d\mathbf{k}_2. \quad (3.53)$$

With the definition of the symmetric wave-action flux $\partial n_{\mathbf{k}}/\partial t = -\partial Q_s/\partial k$, we obtain a diffusion equation

$$\frac{\partial n_{\mathbf{k}}}{\partial t} = -\frac{\partial Q_s}{\partial k} = D\frac{\partial^2 n_{\mathbf{k}}}{\partial k^2} \quad (3.54)$$

for which the coefficient $D$ can play the role of a diffusion coefficient because its positive sign is ensured by the property $V_0^{\mathbf{k}_1,\mathbf{k}_2} > 0$. This diffusion equation can be solved, for a symmetric wave-action spectrum $n_{\mathbf{k}} = n_{\mathbf{k}}(k)$, for the inverse wave-action cascade as

$$n_{\mathbf{k}} = \frac{-Q_s}{D}k = \frac{|Q_s|}{D}k, \quad (3.55)$$

where we have used that $Q_s = \text{const.} < 0$ for the inverse cascade (obtained with the reasoning of FIGURE 3.2). This wave-action spectrum is characterized by the exponent $x = 1$, obtained by a non-local study of the UV divergence of the integral $I(x)$ when both integrated variables tend to infinity. As the integral was divergent and the spectrum non-local for $x > 3/4$, it is consistent to obtain $x = 1$ from our non-local study. Finally it is also consistent to have the integral in the coefficient $D$ dominated by the UV behaviour, $k_{1,2} \gg k$. We want to highlight that this spectrum has been derived with a non-local analysis and, thus, is a non-local spectrum. That means that the interactions between wave-vectors are not constrained to neighbouring wave-vectors, but can represent interactions between wave-vectors considerably different.

**Summary of the section**

- With the obtained expression of the wave-action flux, we derive the predictions for the KZ cascade spectra. Their exponent are $x_{\text{FE}} = 2/5$ for the direct energy cascade spectrum and $x_{\text{FN}} = 4/5$ for the inverse wave-action cascade spectrum.
- The locality analysis shows that the KZ energy cascade spectrum is local while the KZ wave-action cascade spectrum is not.
- Then, we do a non-local analysis for the wave-action cascade, which predicts a non-local spectrum, with the exponent 1.

## 3.5 Numerical set-up

KZ spectra may be observed in forced and dissipative systems when the dissipation exactly matches the forcing. To take into account this, we add new terms to the solved 1D-SHE written with $\Lambda$ :

$$i\frac{\partial}{\partial t}u+\frac{1}{2}\frac{\partial^2}{\partial x^2}u+\left(\Lambda-\frac{\partial^2}{\partial x^2}\right)^{-1}|u|^2+\underbrace{\alpha\Big(-\nabla^2\Big)^{\alpha_{\text{pow}}}u+\nu\Big(-\nabla^2\Big)^{\nu_{\text{pow}}}u}_{Du}=\underbrace{\sum_{\mathbf{k}}f_{\mathbf{k}}\eta_{\mathbf{k}}(t)}_{F} \quad (3.56)$$

with $D = \alpha(-\nabla^2)^{\alpha_{\text{pow}}} + \nu(-\nabla^2)^{\nu_{\text{pow}}}$ the dissipation operator and $F$ the forcing term.

The equation (3.56) is solved with a pseudo-spectral code for a 1D system with length $L = 2\pi$ with periodical conditions. The number of grid points is still $N = 2^{12} = 4096$ with $dx = 1.5 \times 10^{-3}$. To accelerate the simulations, we allow ourselves to increase the time step $dt$ to $10^{-6}$ which resolves up to $k_{\text{max}} \simeq 1500$ with the CFL-like condition(2.3). This is acceptable because higher modes will be dissipated.

### 3.5.1 Dissipation

We choose particular signs for the dissipation Laplacian constants : $\alpha_{\text{pow}} < 0$ and $\nu_{\text{pow}} > 0$. With this convention, the $\alpha$-term represents the dissipation at low $k$ (hypo-viscosity) and the $\nu$-term the dissipation at large $k$ (hyperviscosity). The strength of these dissipation can be tuned by the coefficients $\alpha$ and $\nu$, to ensure a sufficiently large inertial range. We also implemented a dissipation for the zero mode to make sure that this component is null. The dissipation at low $k$ prevents the formation of flat condensate in the system.

### 3.5.2 Forcing

We use a stochastic forcing around a forcing mode $k_f$. For $k \in [\![k_f - dk_f, k_f + dk_f]\!]$, we set a forcing with a fixed norm and random phases, random both in space and in time. This corresponds to

$$f_{\mathbf{k}} = \begin{cases} \text{const. for } k \in [\![k_f - dk_f, k_f + dk_f]\!] \\ 0 \text{ else} \end{cases} \tag{3.57a}$$

$$\eta_{\mathbf{k}}(t) = \exp i\phi_{\mathbf{k}}, \quad \phi_{\mathbf{k}}(t) \in \mathcal{N}(0,1) \tag{3.57b}$$

in equation (3.56). Both the dissipation and the forcing are set to make the simulations symmetrical in $\mathbf{k} \leftrightarrow -\mathbf{k}$ and thus, the system will be considered isotropic in average. The time average is required to average over the random phases which are different between positive and negative $\mathbf{k}$.

The choice of $k_f$ selects the cascade we want to observe. For instance, to study the Direct Cascade (DC) we set the forcing at low $k$, near to the hypoviscosity domain. Doing that, we allow a large direct inertial range in order to observe the cascade, in accordance with the Fjørtoft argument. Inversely, to study the Inverse Cascade (IC), we set the forcing at large $k$. However, as we will see later, choosing $k_f$ too large creates localized structures which stop the cascade.

With forcing and dissipation, the system is not conservative anymore, so the total energy $\mathcal{H}$ (asymptotically equal to the quadratic energy $E$ in weak WT) and wave-action $\mathcal{N}$ can now evolve. We expect these quantities to end up converging to a constant, with fluctuations, as the system converges towards a statistical steady state. The goal is to compare this steady state with the theoretical predictions given by the SLAM and the non-local theory.

$$n_{\mathbf{k}} \propto k^{\frac{2}{5}} \text{ for energy cascade according to the SLAM} \tag{3.58a}$$

$$n_{\mathbf{k}} \propto k^{1} \text{ for wave} - \text{action cascade according to the non} - \text{local analysis} \tag{3.58b}$$

We again highlight that $n_{\mathbf{k}} \propto k^{2/5}$ corresponds to a local KZ spectrum while $n_{\mathbf{k}} \propto k^1$ corresponds to a non-local spectrum.

### 3.5.3 Short-Wave Limit and weak Wave Turbulence : choice of parameters

We need to choose $\Lambda$ in order to have $k^2 \gg k^{*2}$ inside the inertial range for both Direct and Inverse Cascades. This is the condition to be in the Short-Wave Limit (SWL), and this hypothesis has been used to derived the theoretical predictions. To this end, we would like to take $k^*$ as small as possible, corresponding to small $\Lambda = k^{*2}$. Unfortunately, we saw with preliminary simulations that having a very small value for $\Lambda$ slowed down the cascades until they froze entirely : the cascades do not evolve at all if $\Lambda$ is too small, all other parameters fixed. These two effects make the choice of $\Lambda$ crucial to observe cascades in the SWL. For the simulations of Direct and Inverse Cascades, we have chosen $\Lambda = 1$, which gives $k^* = 1$. With this value, the SWL condition $k^2 \gg k^{*2}$ is valid for $k \gtrsim 10$.

**Summary of the section**

- We will perform simulations of the forced and dissipating 1D-SHE, in order to study cascade of invariants.
- These simulations will be realized with the parameter $k^* = 1$ to have the SWL condition respected in the inertial range.

## 3.6 Results of simulations

### 3.6.1 Direct Cascade

To study the Direct Cascade (DC), the forcing is set close to the hypo-viscosity at low $k$ with $k_\mathrm{f} = 16$ and a thin forcing width $dk_f = 2$. The forcing amplitude is chosen to be $f_\mathbf{k} = 100$ and is applied to an initially null function. The dissipation coefficients are $\alpha^{\mathrm{pow}} = -4, \alpha = 2 \times 10^6$, $\nu^{\mathrm{pow}} = 2, \nu = 1 \times 10^{-46}$. The FIGURE 3.4 presents the time series of total energy $\mathcal{H}$ (assumed to be the quadratic energy $E$) and wave-action $\mathcal{N}$ which show a statistically steady state for $t > 150$, characterized by large oscillations around mean values $\langle \mathcal{H} \rangle_\mathrm{s} = 2.26 \times 10^{10}$ and $\langle \mathcal{N} \rangle_\mathrm{s} = 4.96 \times 10^5$. This steady state is characterized by a dissipation of almost of all the wave-action injected, with the injection rate $Q_\mathrm{f} = 8 \times 10^4$ being very close to the dissipation rate $Q_- + Q_+ = 7.856 \times 10^4$. Consequently, we consider the steady state established for $t > 150$ and we perform the steady state averages for these times.

Before plotting the wave-action spectrum, we remind that we consider the symmetric wave-action spectrum, computed as $n_\mathbf{k}(k) = n_\mathbf{k} + n_{-\mathbf{k}}$, given that the forcing not does favour positive or negative $\mathbf{k}$. The wave-action spectrum $n_\mathbf{k}$ averaged in the steady state for the DC is presented FIGURE 3.5. The wave-action spectrum which we plot is the symmetric spectrum We need to remark that no clear slope can be observed in the inertial range, only a general tendency, even if, for almost a decade, the spectrum has a steep and defined slope. This general tendency is globally well modeled by the KZ prediction $n_\mathbf{k} \propto k^{2/5}$, which is an argument in favor of the the KZ prediction. However, the KZ

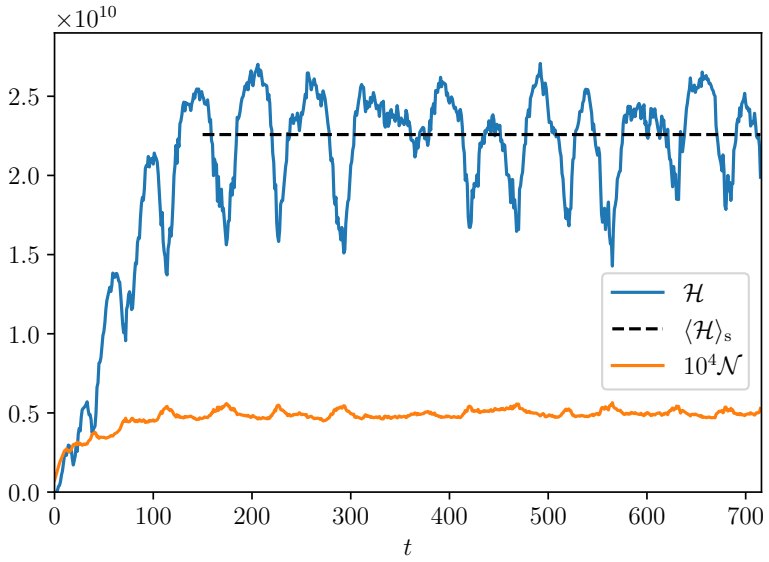


Figure 3.4: **Evolution of total energy $\mathcal{H}$ and wave-action $\mathcal{N}$ for the Direct Cascade -** The steady state is characterized by statistically steady total quantities.

prediction also appears to fit the observed spectrum outside the inertial range, for the entire $k$-range $k_- \simeq 3 \lesssim k \lesssim k_f = 16$. This can be more easily observed in the FIGURE 3.8. This observation has two drawbacks. First, assuming that the part $k < 16$ of the spectrum corresponds to cascade of energy implies an *inverse* cascade of energy, which is contradictory with the Fjørtoft argument. Besides, in this $k-$range, the short-wave condition is less respected than in the inertial range.

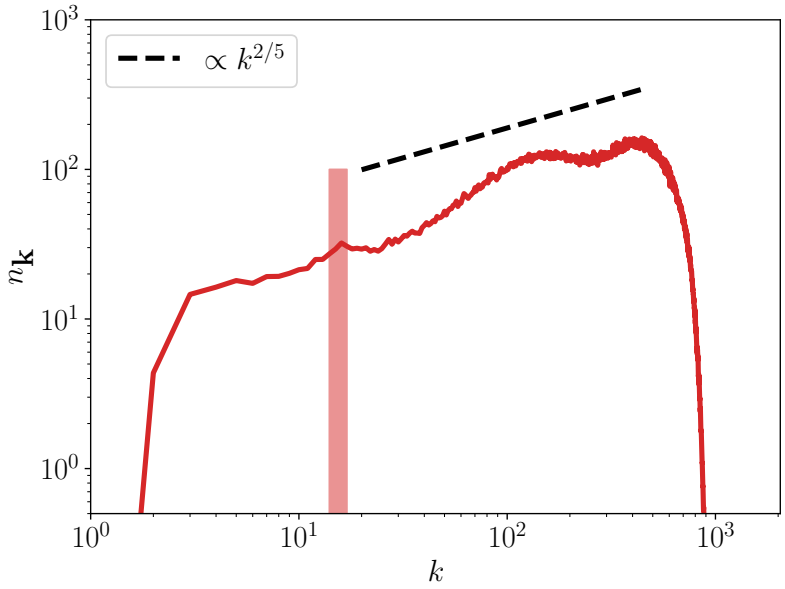


Figure 3.5: **Wave-action spectrum averaged in the steady state for the Direct Cascade -** The KZ prediction $n_{\mathbf{k}} \propto k^{2/5}$ is in accordance with the mean slope of the spectrum in the full $k$-range, but it does not model the inertial range very well.

This wave-action spectrum is compared to the flux $P_s$ of quadratic energy $E$. We notice that $P_s$ is averaged to zero in the inertial range for $k$ up to $\simeq 200$ and oscillates around a value assumed to be zero for $k \gtrsim 200$. During these oscillations, the flux is positive and negative with a comparable number of iterations. For a direct KZ energy cascade, we expect the energy flux to be positive and constant over the inertial range. That implies that the system does not exhibit an energy cascade. However, zooming around the forcing scale $k_f = 16$, we observe a small bump of $P_s$ (see the inset of FIGURE 3.5) which could be interpreted as a positive flux of energy but very locally around the forcing scale, as it only stands for $k = 16$ and 17. With this very narrow region, conclusions are hard to draw but this could correspond to the expected positive and constant value of $P_s$. The energy flux averaged to zero could be explained by the energy being mainly dominated by the interaction Hamiltonian.

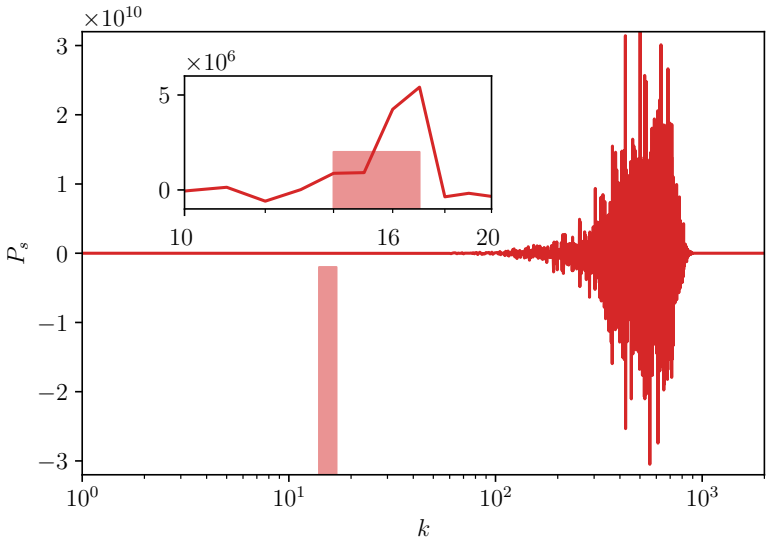


Figure 3.6: **Energy flux $P_s$ averaged for the Direct Cascade steady state** - The flux is not constant in the inertial range, contrarily as expected for an energy spectrum.

The $(x-t)$ plot of the reached steady state is given FIGURE 3.7(a), with $t_f = 176$ a time when the steady state is already established. First, notice the difference of amplitudes of $|u|$ between this DC steady state and the previous dynamics of conservative systems. This difference of two orders of magnitude is explained by the forcing applied to the system. The whole box is filled up with localized structures, which we call *filaments*, with different speeds. Each filament propagates in almost straight lines. The whole system is filled up by filaments with negative speed while a few have positive speed. These groups of filaments will be denoted *Incoherent Solitons* (IS), as a reference to recent works [98] [99]. Inside this envelope, some filaments propagate with velocities different from the mean velocity of the envelope, while staying bound together. The solitonic behaviour is mostly visible on the negative-speed structure which keeps a constant speed and the same envelope size. This division of the main structure (incoherent solitons) in independant smaller sub-structures (filaments) is the main difference with a proper soliton, as defined in (1.10). Indeed, the incoherent solitons are called incoherent because their profile in the $x$-space

is not exactly constant in time. The mean speed of these filaments is $\overline{v_-} \simeq -475$. On top of these filaments, few filaments propagate with positive speeds which mean value is $\overline{v_+} \simeq 115$. The steady state of DC thus shows a clear asymmetry with more filaments with negative speeds.

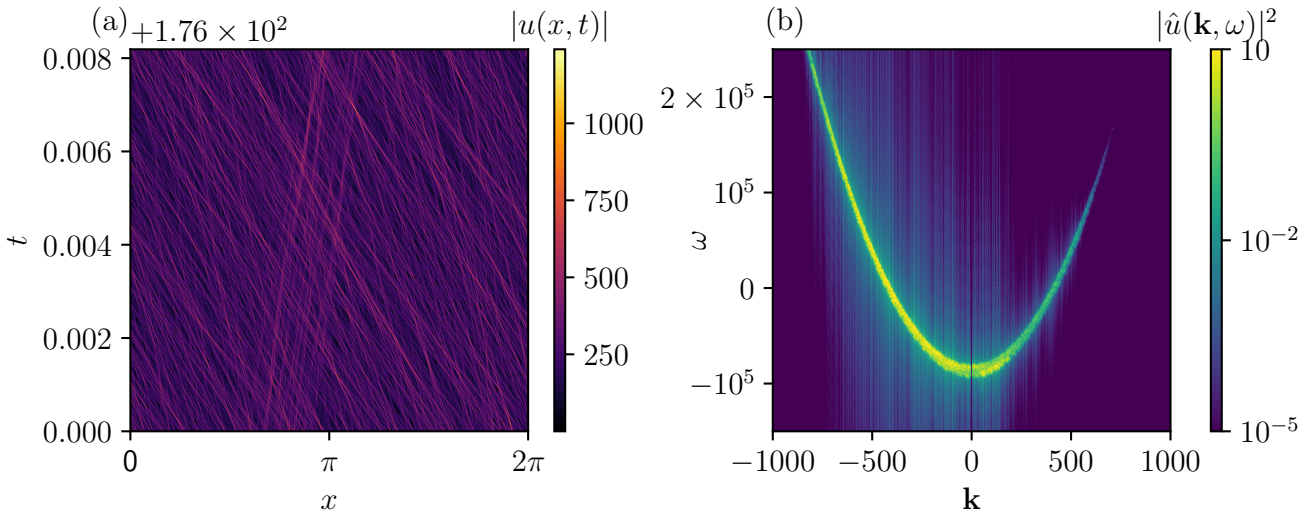


Figure 3.7: $(x-t)$ **dynamics** (a) **and** $(\mathbf{k}-\omega)$ **spectrum** (b) **of the DC simulation of the steady state -** Filaments propagate in the box with a majority with negative speed. A few filaments propagate with a positive speed and can form an Incoherent Soliton. This asymmetry is observed in the $(\mathbf{k}-\omega)$ spectrum which only contains a narrow parabola.

This asymmetry is also clearly visible on the $(\mathbf{k}-\omega)$ plot FIGURE 3.7(b) where the energy is organized as an asymmetric parabola which stands for the linear dispersion $\omega_{\mathbf{k}} = \mathbf{k}^2/2$ of linear waves. Filtering around $\mathbf{k} = 0$, we find that the $\mathbf{k} > 0$ branch of the parabola stands for only 10% of the total mean wave-action during the time interval. Notice than the parabola is considerably shifted away from the $\omega = 0$ axis towards negative values. This large shift is due to the large amplitude of the field. Finally, notice that no straight lines are present in the $(\mathbf{k}-\omega)$ spectrum, which indicates that nor solitons nor any coherent structures propagate in the system. Indeed, assuming that the maximum of $|u|$ is actually a soliton, the corresponding straight line would be found at $\omega^* = (\overline{v_-}^2 - A^2_{\max})/2 \simeq -6.7 \times 10^5$. The output period $dt_o = 2 \times 10^{-6}$ have been chosen to resolve the frequencies up to $\omega_{\max} = \pm 1.5 \times 10^6$ and no straight lines have been observed, suggesting the absence of solitons in the system. This absence is important because solitons are incompatible with the weak Wave Turbulence. Finally, we can remark that the energy is very concentrated around the parabola, which indicates that the system is weakly non-linear.

The observed asymmetry in $\mathbf{k} \leftrightarrow -\mathbf{k}$ was not expected because the forcing is applied with the same amplitude for positive and negative $\mathbf{k}$ and the only difference is the forcing phase which is random and thus, can be different for positive and negative $\mathbf{k}$. Such asymmetry has already been observed for the short-wave limit of the 1D-SHE [5] and we suggest it can be associated with an instability of the 1D-SHE breaking the symmetry.

We assume this asymmetry will be cancelled by considering different realisations of the same simulation.

As described in [99], the existence of IS is not compatible with a KZ wave-action spectrum because it prevents the cascade in the **k**-space. As there is only one IS in positive **k**, we study the asymmetry of the system by plotting in FIGURE 3.8 the wave-action spectrum $n_{\mathbf{k}}$ for positive and negative **k** separately. It appears that the spectrum for positive **k** decreases in large $k$ for smaller values than the spectrum for negative **k**. Precisely, $n_{\mathbf{k}}(\mathbf{k} > 0)$ starts to diminish at $\mathbf{k} \simeq 120$, which is close to the velocity (and so the wave-number) of the IS observed in the $(x - t)$ dynamics ($\overline{v_+} \simeq -115$). Consequently, we could suggest that the IS prevents the wave-action from cascading towards $\mathbf{k} > 120$, which may explain the asymmetry of the system. Nonetheless, we can not explain the creation of the IS. Notice that the $\mathbf{k} < 0$ spectrum displays a clear power-law, whose exponent is measured to be 4/5.

Given that nothing in the forcing scheme selects a special direction between $\mathbf{k} > 0$ and $\mathbf{k} < 0$, we will continue to compare our theoretical predictions to the symmetric spectrum $n_{\mathbf{k}}+n_{-\mathbf{k}}$. However, we need to keep in mind the actual asymmetry observed in the system. The results of the Inverse Cascade simulation will show that we can still consider $n_{\mathbf{k}}+n_{-\mathbf{k}}$.

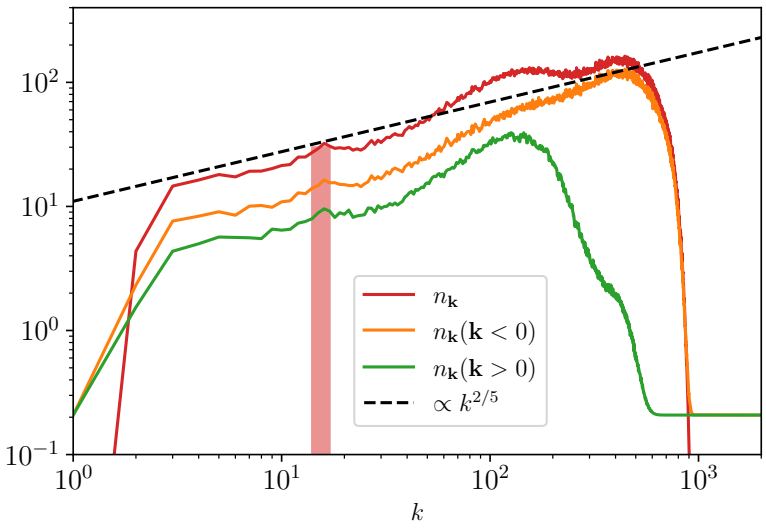


Figure 3.8: **Wave-action spectrum for positive and negative k for the DC steady state -** We observe the asymmetry in the spectra, which may be explained by the IS in $\mathbf{k} > 0$ stopping the cascade.

The FIGURE 3.9 presents the Probability Density Function of the mean real-space intensity $I = |u|^2$, averaged in the time interval displayed in FIGURE 3.7(a). This PDF is fitted by a straight line, characteristic of a gaussian field. This model is very accurate up to $I/\langle I \rangle \simeq 8$. Very high amplitude events are more present in the system than in a gaussian field. This latter deviation from the gaussian statistics shows the intermittency of the studied field. Such tails have been observed developing from a Gaussian initial state in 1D-NLSE [100].

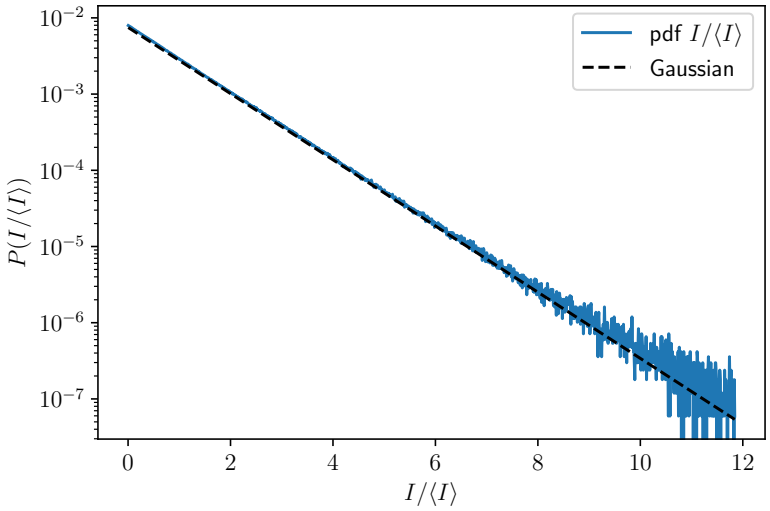


Figure 3.9: **PDF of the averaged intensity $I/\langle I\rangle$ averaged in the DC steady state -** For low amplitudes, the gaussian models fits well the data while we observe more large-amplitude events than expected for a gaussian field.

### 3.6.2 Inverse Cascade

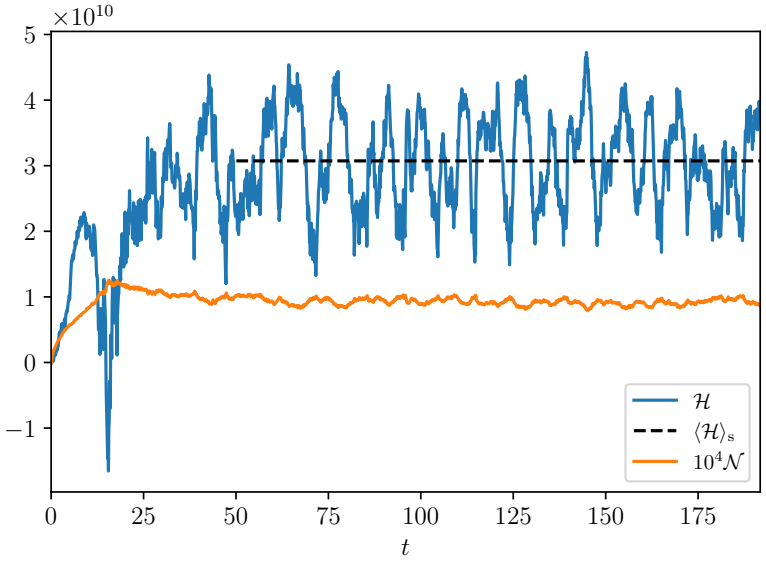


Figure 3.10: **Evolution of the total energy $\mathcal{H}$ for the inverse cascade -**The steady state is characterized by statistically steady total energy and wave-action.

Next, we study the Inverse Cascade (IC) by forcing at large $k$, leaving space for the inverse wave-action cascade to develop towards low $k$, with $k_f = 100, dk = 2$ and a forcing amplitude $f_{\mathbf{k}} = 120$. The dissipation coefficients are $\alpha^{\text{pow}} = -4, \alpha = 2 \times 10^7$,

$\nu^{\text{pow}} = 2, \nu = 1 \times 10^{-36}$. The FIGURE 3.10 presents the time evolution of $\mathcal{H}$ and $\mathcal{N}$. After a transitional state, both quantities exhibit oscillatory behaviours. These oscillations show a statistically steady state with an averaged energy $\langle \mathcal{H} \rangle_{\text{s}} = 3.07 \times 10^{10}$, with the average taken from $t = 50$ to the end of the simulation. We suppose the system to be in a statistically steady state for $t > 50$ and all steady-state averages will be done in this time range. This steady state is characterized by quite large amplitude of oscillations for $\mathcal{H}$. This steady state is also described by the dissipation rate of wave-action in both low and large $k$, respectively $Q_-$ and $Q_+$ which is theoretically equal to the wave-action injection rate $Q_{\text{f}}$. In this IC simulation, the forcing parameters give $Q_{\text{f}} = 11.52 \times 10^4$ and this wave-action injected is almost dissipated because $Q_- + Q_+ = 9.84 \times 10^4$. That indicates that almost all the wave-action injected is dissipated.

The wave-action spectrum $n_{\mathbf{k}}$ averaged in this steady state is presented as the blue curve in FIGURE 3.11. The wave-action is injected at $k_f = 100$ and cascades in both directions in $k$-space. For inverse cascade, the inertial range is in between the low-$k$ dissipation and the forcing scale, *ie* $k_- \simeq 4 \lesssim k \lesssim k_f \simeq 100$. Between dissipations, we can observe that the wave-action spectrum can be modeled with an overall good accuracy with a power-law $n_{\mathbf{k}} = k^1$. This exponent is the one predicted by the non-local theory. We recall that the exponent 1 was found in the Short-Wave Limit $k^2/k^{*2} \gg 1$, with $k^* = 1$. In the lowest limit of the inertial range ($k \simeq 5$), this ratio equal 25, which may be delicate to be considered larger than 1, but which represents the minimum value of this ratio in the inertial range. For instance, at $k = 90$, near the high-$k$ end of the inertial range, this ratio is $8.1 \times 10^3$, which satisfies much better the SWL condition. Near the hypo-viscosity dissipation, so where the SWL is the less respected, the spectrum accumulates until the dissipation is large enough to dissipate it. As for the DC, the expected power-law model $n_{\mathbf{k}} \propto k$ is of good accuracy even for $k > k_f$, which is out of the inertial range for the inverse cascade. More precisely, the $k-$range for this model to fit the spectrum better is the whole range $k_- < k < k_+$. Finally, we can notice that the KZ prediction $n_{\mathbf{k}} \propto k^{4/5}$ is not observed, which is consistent as it was shown non-local.

We compare this spectrum with the wave-action flux $Q_s$ in lin-log scale in FIGURE 3.12. We recall that the spectrum $n_{\mathbf{k}} \propto k$ was derived with the non-local analysis under the assumption that the flux $Q_s$ is independent from $k$ and negative. This constancy requires a time-average in the steady state. In the inertial range, $Q_s$ is constant at $Q_s \simeq -10^{-5}$, which validates the assumption made for the non-local analysis. In the weak WT theory, this negative and constant wave-action flux would correspond to an inverse wave-action cascade, according to the Fjørtoft argument.

To be precise, in the inertial range, the flux is not exactly constant near $k_f$, but exhibits some oscillations. We verified that these oscillations were indeed numerical artefacts by reducing the window for the time average and observing that these oscillations were present for smaller $k$. Even with this slightly oscillating behavior in the inertial range, the clear discontinuity of the $k$-averaged flux at $k_f$ shows the independence of $Q_s$ from $k$ in the inertial range.

To characterize the reached steady state, in FIGURE 3.13(a) we plot the spatio-

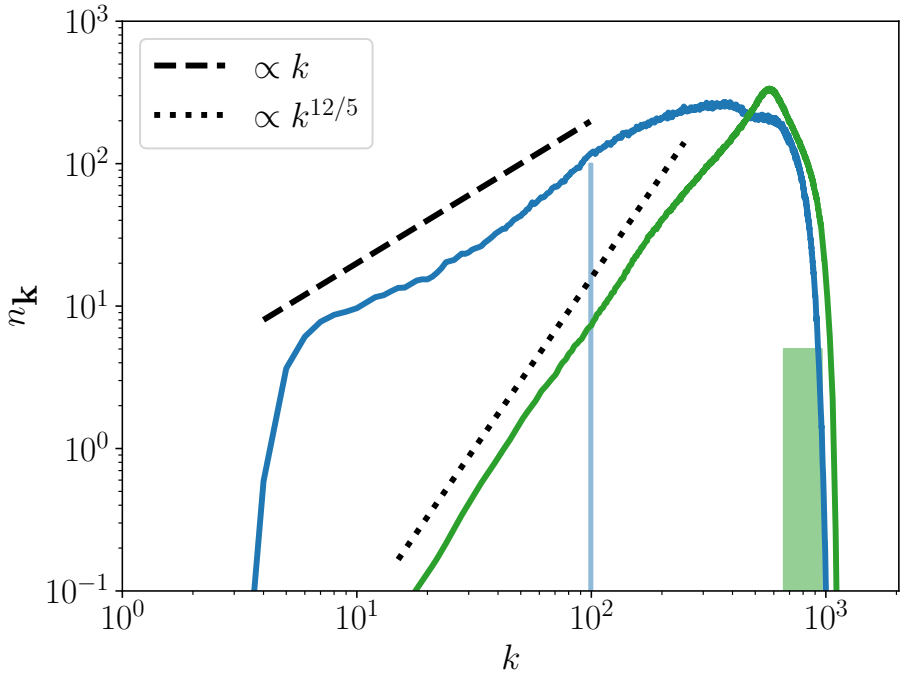


Figure 3.11: **Wave action spectrum averaged in the steady state for two Inverse Cascade simulations -** The blue curve represents the spectrum for the forcing $k_f = 100, dk = 2$ (light blue rectangle) and the green curve the spectrum for the forcing $k_f = 812, dk = 150$ (light green rectangle). Each spectrum is modelled by a power-law function.

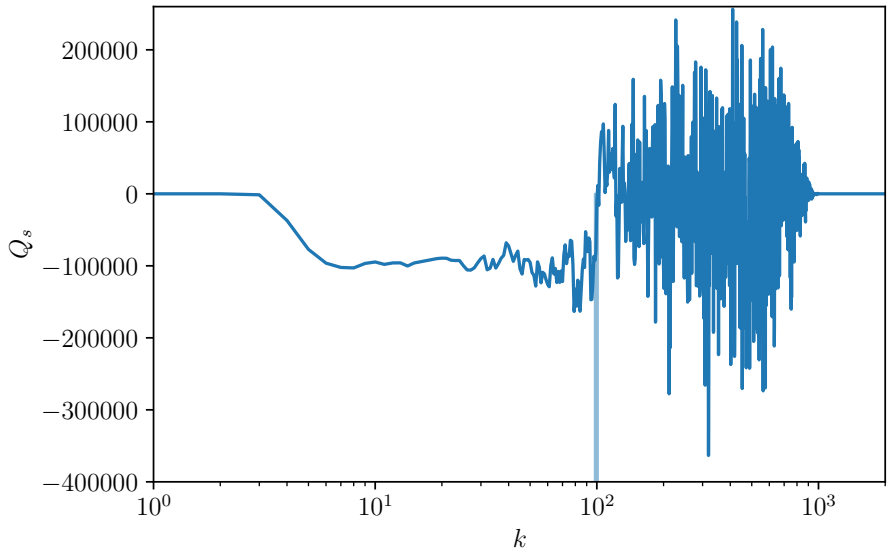


Figure 3.12: **Wave-action flux $Q_s$ averaged for the Inverse Cascade steady state** - The flux is constant in the inertial range, confirming the hypothesis made for the non-local analysis.

temporal dynamics of the system starting at $t_f = 191.8$. The box is crossed by many filaments organized in a narrow and well-definite IS with a negative speed $\overline{v_-} \simeq -250$ and a wider one, less easy to delimit, with a positive speed $v_+ \simeq 500$. Note that the

rest of the space is filled by the similar filament but less concentrated and not organized into a bigger structure. This dynamics also exhibits an asymmetry as the majority of the filaments have a positive speed.

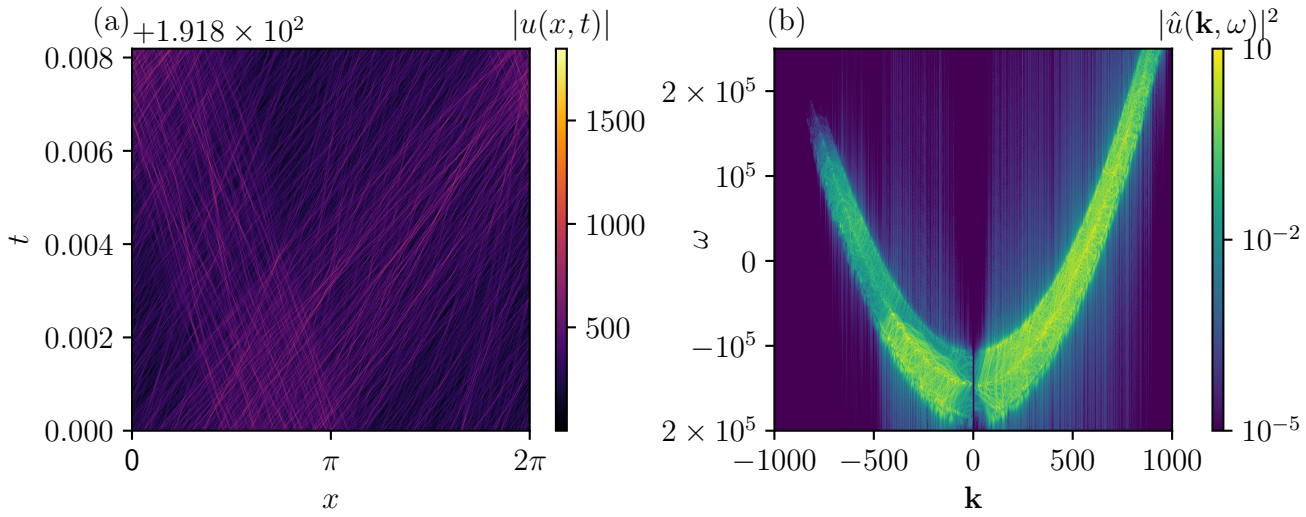


Figure 3.13: $(x-t)$ **dynamics** (a) and $(\mathbf{k}-\omega)$ **spectrum** (b) **of the IC simulation steady state -** In this steady state, the IS's are more recognizable than they were for the DC but one, the one with a negative speed, is still easier to identify. In the $(\mathbf{k}-\omega)$ spectrum, the parabola is wide, showing a quite important non-linearity.

The $(\mathbf{k}-\omega)$ spectrum $|\hat{u}(\mathbf{k},\omega)|^2$ of this $(x-t)$ plot is presented Figure 3.13(b). The first observation is the clear asymmetry with respect to $\mathbf{k}=0$. The spectrum shows more energy for positive $\mathbf{k}$, which was expected from the bigger number of filaments with a positive speed in the $(x-t)$ plot. The spectrum organizes around a parabola widened by "hairy" structures. These hairy structures decorate the parabola differently from the decorations observed for the interaction between a bound-state and linear waves. The width of the parabola represents the non-linearity of the waves in the system, the more non-linear the waves, the wider the dispersion relation. In this Inverse Cascade simulation, the important width of the parabola indicates a non-linearity ratio which can not be considered negligible to 1. Contrary to the quasi-Soliton Turbulence case (see section2.3), these non-linearities stacked around the linear waves do not peel off from this parabola to become real solitons. Finally, we can notice that for $\mathbf{k}<0$, the branch of the parabola with less energy, the decorations are more important for small $k$ and below the parabola, exactly like for the parabola in the DC simulation.

The asymmetry with respect to $\mathbf{k} = 0$ is here not a problem for the study of the cascade. Indeed, the clear IS observed with a negative speed $\overline{v_-} \simeq -250$ is characterized by the wave-vector $\mathbf{k} \simeq -250$ and, thus, does not lie in the inertial range $k \lesssim k_f = 100$. Consequently, this IS does not prevent the inverse cascade to occur. We have verified this, by comparing $n_{\mathbf{k}}, n_{\mathbf{k}}(\mathbf{k} > 0)$ and $n_{\mathbf{k}}(\mathbf{k} < 0)$. We observe that in the inertial range, the spectra are very close for $\mathbf{k} > 0$ and $\mathbf{k} < 0$. Once again, we do not know why an IS has grown in the system. We still assume it might be linked with an instability of the 1D-SHE. Repeating this simulation and averaging over the random phases of the forcing might shed light on this observation. Particularly, it would be interesting to see if the IS still develop for the same sign of $\mathbf{k}$.

We also characterize the steady state by the Probability Density Function (PDF) of the intensity $I = |u|^2$ in the physical space, see FIGURE 3.14. This PDF is averaged in time during the time window of the $(x - t)$ plot 3.13(a). We compare the obtained plot to the PDF expected for a Gaussian field. We can notice a slight lack of mean-intensity events ($I \gtrsim 3.5\langle I \rangle$) in the system compared to the Gaussian field, as well as a quite bigger number of large events ($I > 8\langle I \rangle$), as in the DC steady state.

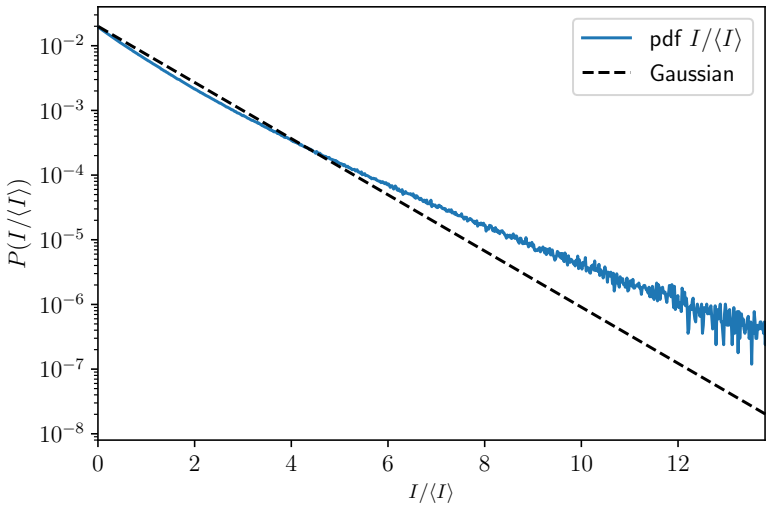


Figure 3.14: **PDF of the wave intensity for the IC -** The system contains more large-amplitude events than expected for the gaussian field.

We found that the IC was very sensitive to the characteristics of the forcing. For instance, in FIGURE 3.11 we present another spectrum, obtained with another forcing, $k_f = 812, dk = 150$ and $f_{\mathbf{k}} = 5$ while keeping the same dissipation coefficients. The spectrum displays a power-law behaviour of exponent 12/5, which is different from the KZ and non-local predictions. The $(x - t)$ dynamics of the steady state is presented FIGURE 3.15(a) from $t_f = 375.2$ where we can clearly see two IS propagating. Contrary to the dynamics previously detailed, here, the IS are easily distinguishable from the rest of the function, see a profile FIGURE 3.16(a). They have the same modulus of speed, showing here the symmetry $\mathbf{k} \leftrightarrow -\mathbf{k}$ of the system, of 582 and -555. These speeds are found very close to the group velocity $v_g = \partial\omega_{\mathbf{k}}/\partial\mathbf{k} \simeq 573$ computed for the scale where the wave-

action spectrum is maximum (see the green curve in FIGURE 3.11). The symmetry of the system can also be seen in the $(\mathbf{k}-\omega)$ spectrum FIGURE 3.15(b) where both branches of the parabola are decorated in the same types of hairy structures. Moreover, the slopes of the decorating straight lines starting from the $\mathbf{k}=0$ are measured at $\simeq 602$ and $\simeq -588$, close to the speed of the IS. We can thus suggest that these decorations represent the filaments inside the IS.

In FIGURE 3.16(b), we present the DST spectrum of the function at $t = t_f + 0.002$. The eigenvalues are organized as two branches around $\zeta^{\mathrm{Re}} \simeq \pm 250$, positions which correspond to speeds near 500. This is assuming that the ratio between velocity and real part is still close to -2, which has been observed in the study of solitons in the 1D-SHE with $\beta = 10^{-2}$ (we recall the value of $\beta = 1$ used in these simulations). These speeds are quite close to the speeds of the IS, so we can suggest that the branches of eigenvalues are the DST signatures of the IS. However, we need to specify that the ratio between the amplitude of the soliton and the imaginary part of the corresponding eigenvalue is found at $\simeq 1.3$ is lower than the value of 2 given for the 1D-NLSE and even lower than the value $\simeq 1.5$ found in the previous chapter. Here, with $\beta = 1$, the non-integrability parameter is bigger, which can explain the worse correspondence of the DST. Each individual eigenvalue slightly moves in time but the global branch structure stands. This is very similar to the filaments in $(x-t)$ dynamics having changing speeds while the IS has a constant speed. All these results indicate that DST might still be a consistent tool to study the forced and dissipating systems, in the same was as it as been shown interesting to study real systems [90]. However, we need to specify that, compared to the last section, we had to multiply by four the number of points used in the DST algorithm to have a spectrum independent of this number of points, showing that this system is more complex to study than the collisions of solitary waves with $\beta = 10^{-2}$.

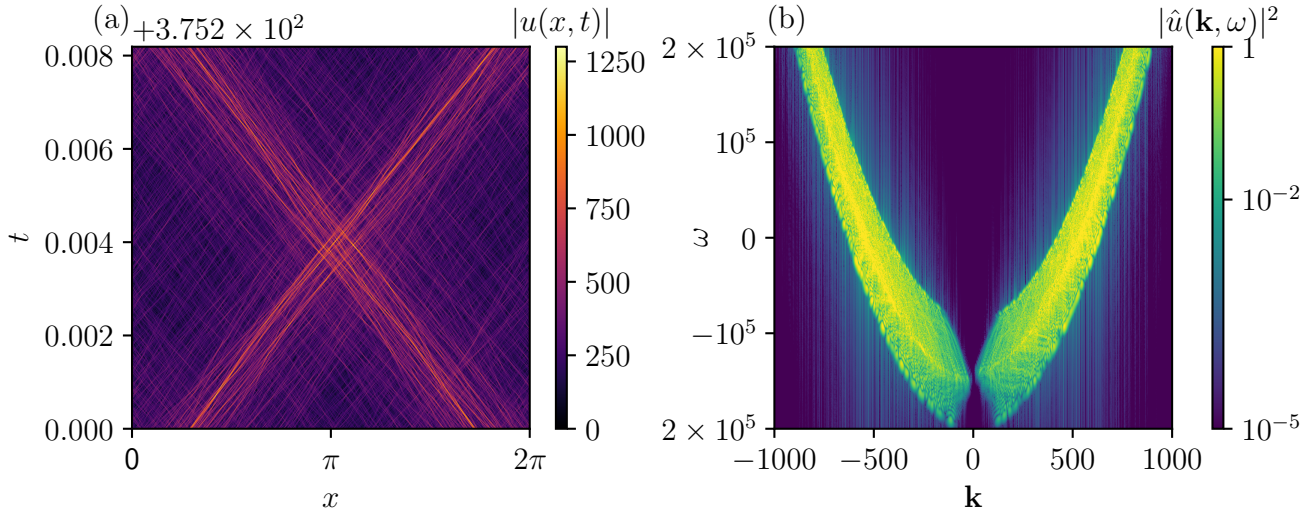


Figure 3.15: $(x-t)$ **dynamics** (a) and $(\mathbf{k}-\omega)$ **spectrum** (b) **of an IC simulation steady state displaying large IS -** The IS are clearly identified on the $(x-t)$ dynamics as well as the straight decorations of the parabola for small $k$.

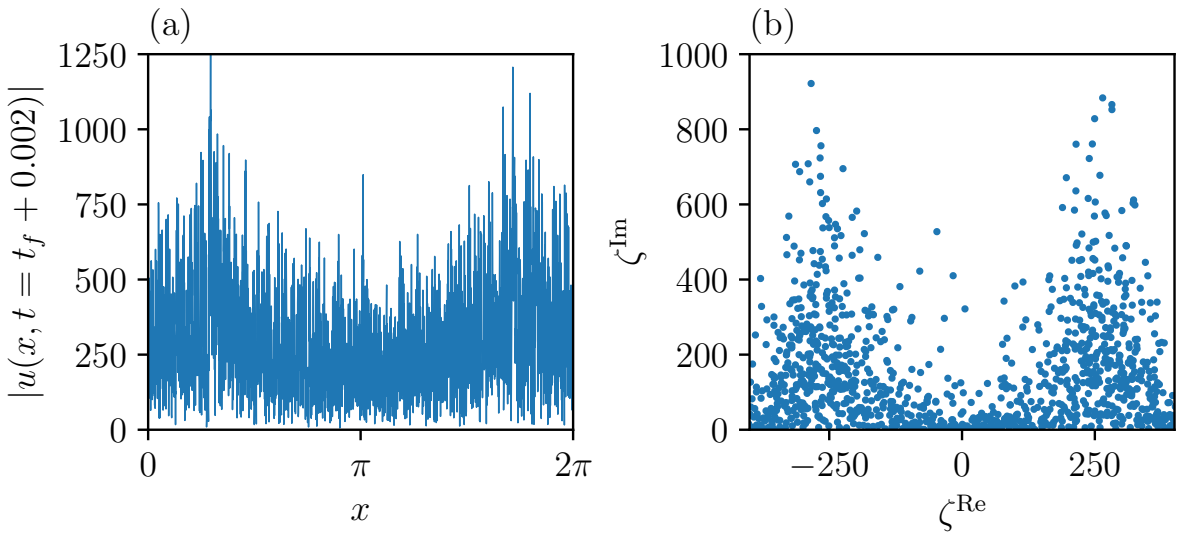


Figure 3.16: **Function profile** (a) **and associated DST spectrum** (b) **-** The two IS are recognizable on the profile of $|u|$ and may be associated with the branches of eigenvalues with the consistent mean real parts.

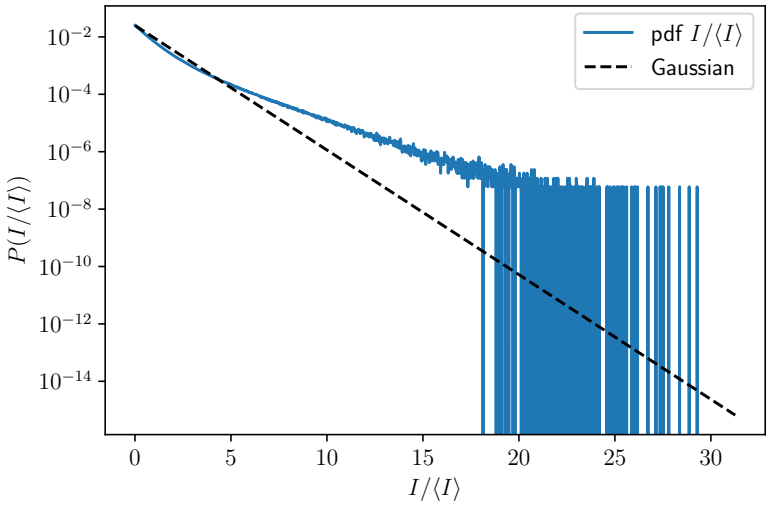


Figure 3.17: **PDF of the averaged wave intensity in the IC steady state displaying IS -** The number of large-amplitude events is considerably larger than for a gaussian field, due to the IS while we observe a lack of small-to-intermediate amplitude events compared to a gaussian field.

### 3.6.3 Impact of the non-integrability over the Incoherent Solitons

To study how the properties of the IS evolve with the non-integrability of the equation, we set a set of simulations for the forced and dissipating 1D-SHE defined with $\beta$ to really identify the role of the non-integrability. We recall the 1D-SHE with $\beta$, to which we add the same dissipative $Du$ and forcing $F$ terms as for the DC and IC simulations.

$$i\frac{\partial}{\partial t}u + \frac{1}{2}\frac{\partial^2}{\partial x^2}u + u\left(1-\beta\frac{\partial^2}{\partial x^2}\right)^{-1}|u|^2 + Du = F. \tag{3.59}$$

The parameters of the set of parameters are, $k_f = 512, dk = 2$ and $f_{\mathbf{k}} = 20$ for the forcing and $\alpha^{\text{pow}} = -4, \alpha = 2\times10^6$, $\nu^{\text{pow}} = 8, \nu = 5\times10^{-51}$ for the dissipation.

In FIGURE 3.18, we compare the spatio temporal dynamics of the steady state reached for different $\beta$. The system has been re-centered around $x = 0$, thanks to periodic boundaries, for simplicity. The first observation is the same qualitative behaviour for the four systems. For all values of $\beta$, the systems contains two incoherent solitons with speeds $\overline{v_\pm} \simeq \pm512$, corresponding to the forcing scale. This observation has been made for all the values of $\beta$ tested and not showed here. In all the cases, the two IS seem to collide elastically but the short scale of times studied may prevents the observation of inelastic collisions. In previous observation of IS [98], the ISs created by Modulational Instability (MI) from a constant field were found to collide ineslatically to finally create a main IS.

The main different between these dynamics is the width of these IS. When $\beta$ increases, the IS are wider and contain more filaments. For instance, for $\beta = 0.05$, the IS are very narrow and contain only a few filaments with very close speeds. With the physical meaning of $\beta$, this observation can be interpreted as the IS being more developed in a strongly non-integrable system.

The steady states are also characterized by their spectral dynamics with the $(\mathbf{k}-\omega)$ plots presented FIGURE 3.19. All these spectra are organized around parabola, representing for the linear waves, and none of them have obvious straight lines, testifying the absence of solitons or solitary waves. For the four $\beta$ presented, the parabola is wide, representing the non-linearity of the system. However, the nature of this width depends on $\beta$. For $\beta = 0.05$, the closest system to integrability, the $(\mathbf{k}-\omega)$ spectrum consists of two vertically displaced parabolae decorated by straight lines of slope $\pm \simeq 512$ running between them. The slopes of these decorating lines corresponding to physical velocities, these lines may correspond to the filaments inside the ISs which have these velocities. We can denote that these lines are present from $k \gtrsim 0$ to $k \simeq 900$. Although some of these straight lines can be seen for $\beta = 0.2$, the decorations of the parabola are more complex for large $\beta$, see for example the curved lines for $\beta = 2$ which decorate the parabola. These structures represent the complexity of the wide ISs but the exact signification is still to be found. We can also observe a clear asymmetry for $\beta = 0.2$ in the parabola itself, the value at $k = 0$ being different for the positive and negative $k$ parabola. The spatio-temporal spectrum is qualitatively different for $\beta = 10$ as the energy is still concentrated around the forcing mode $k_f = 512$ and has not cascaded towards $k \simeq 0$. This observation is consistent with the slowing-down of the dynamics for small $\Lambda$ (linked with $\beta$ as $\Lambda = 1/\beta$) reported in section 3.5.3.

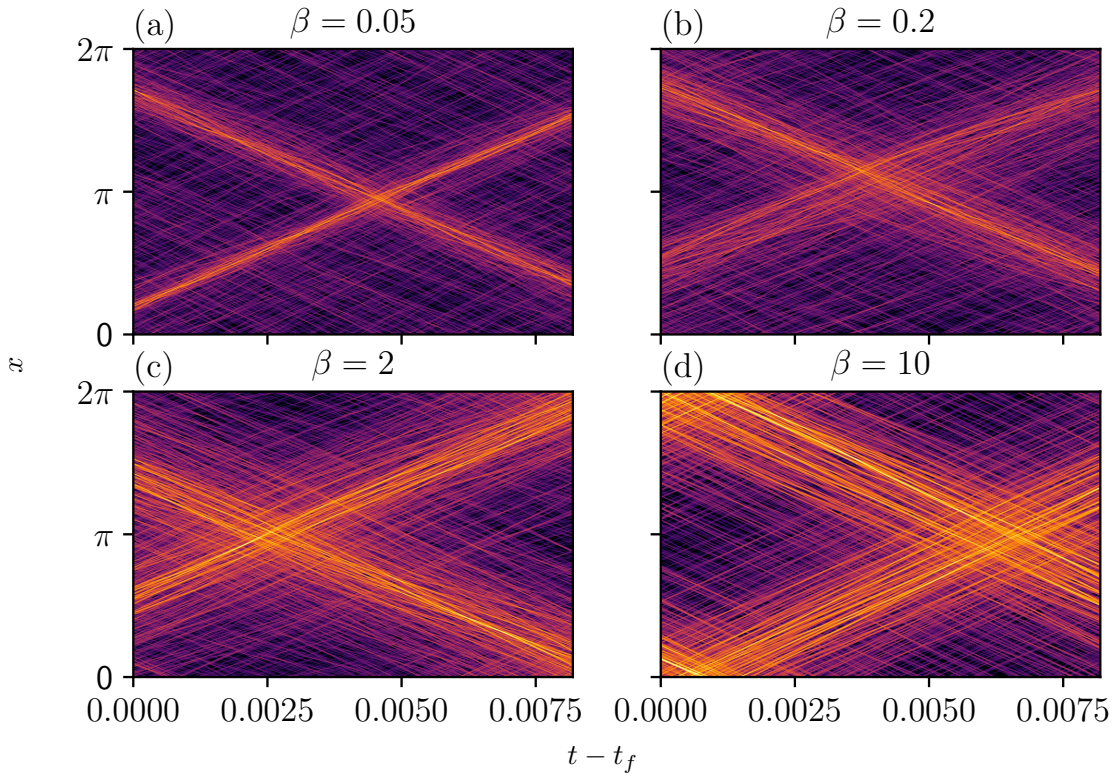


Figure 3.18: **Comparison of steady state** $(x - t)$ **dynamics for different** $\beta$ **-** We observe that for all $\beta$ the ISs created have the same speeds, corresponding here to the forcing scale. However, the widths of the ISs depend on $\beta$ : the larger $\beta$, the wider the ISs.

We support this observation by plotting the time-averaged $k$- spectrum $\langle\ |\hat{u}_k(t)|^2\ \rangle_t$ for the four values of $\beta$ Figure 3.20. The averages have been computed over the time window of the $(x-t)$ plots Figure 3.18. The four spectra are centered around the forcing scale and are qualitatively similar. They are supported by a finite range of $\mathbf{k}$, larger for smaller $\beta$. Picozzi et al [98] have observed this for the final big IS they found. Precisely, the spectrum they present in their article is symmetric around $\mathbf{k} = 0$ as the IS has a null speed. We can precise that this is not possible in our case because the friction dissipation forces the spectrum to be 0 at $\mathbf{k} = 0$. The spectra supported by larger range of $\mathbf{k}$ appear to correspond to more narrow IS in the real space. Naively, this can be interpreted by the by the relation $\Delta x \Delta k \sim 1$, characteristic of the Fourier Transform.

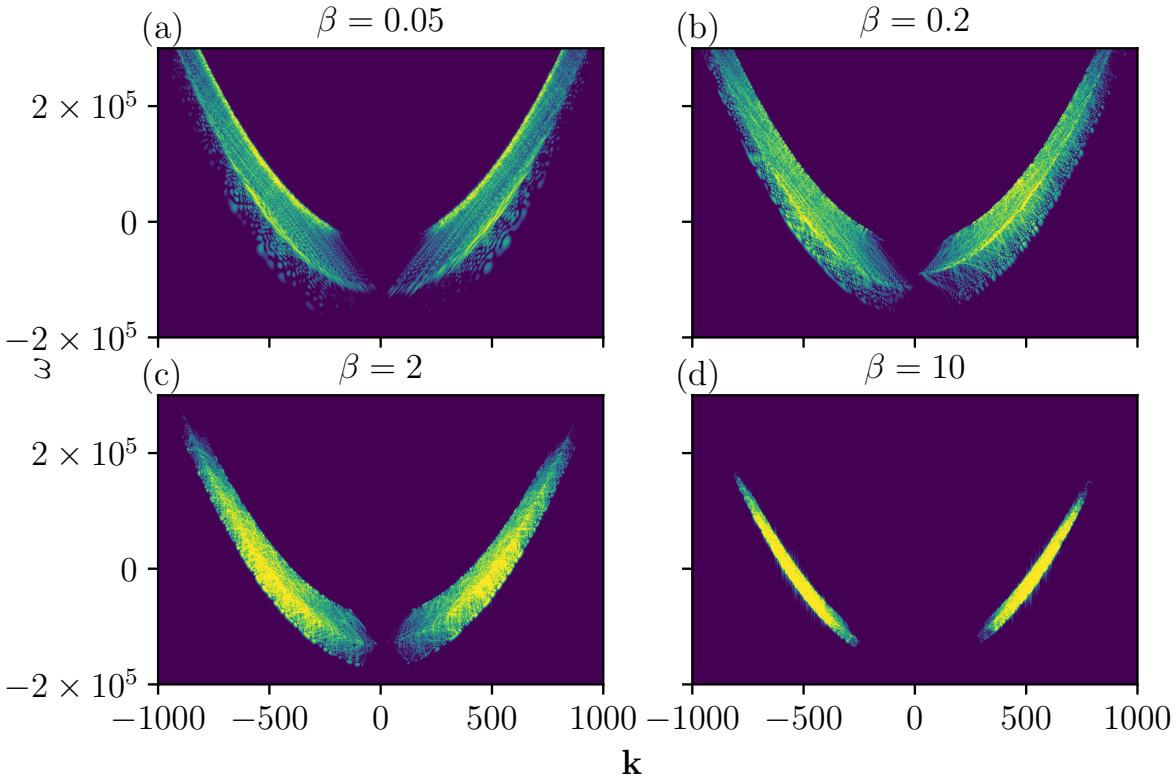


Figure 3.19: **Comparison of steady states ($\mathbf{k} - \omega$) spectra for different $\beta$ -** We observe that for very small $\beta$ the parabola is decorated with straight lines of slope equal to the speed of the ISs. For $\beta = 2$, these decorations are not more sophisticated. For $\beta = 10$ the energy is still concentrated around $k_f$.

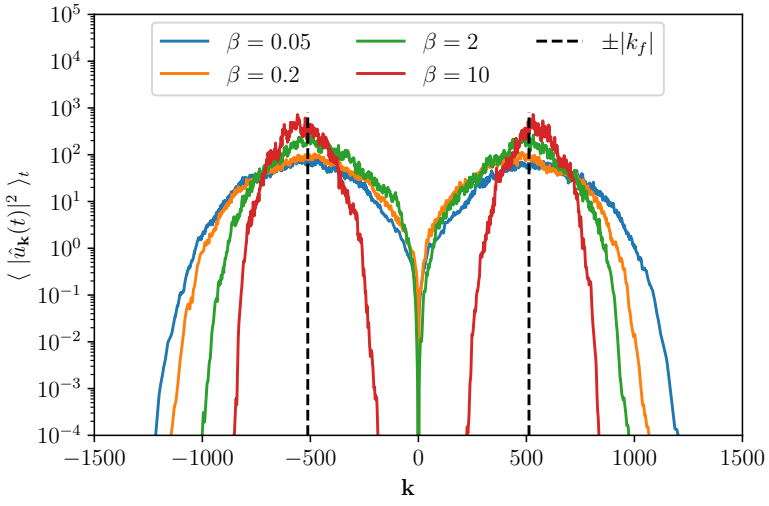


Figure 3.20: **Comparison of time-averaged $k$-spectrum for different $\beta$ -** The four spectra are centered around the forcing scales $\pm k_f$ and have qualitatively the same shape. Note that when $\beta$ increases, the energy does not cascade effectively in the $\mathbf{k}$-space.

**Summary of the section**

- The Direct energy Cascade and Inverse wave-action Cascade predictions are tested against the numerical results.
- In Inverse Cascade, the non-local prediction is of good accordance with the obtained while or the Direct Cascade there is also an accordance, but less obvious. In both cases, the predictions show an overall good correspondence for the whole $k$-range.
- The inverse cascade simulations sometimes display Incoherent Solitons, an envelope propagating like a soliton but with smaller structures propagating inside it.
- For the Direct Cascade simulation, an Incoherent Soliton lies in the inertial range for $\mathbf{k} > 0$, which creates an asymmetry for the spectrum.

## 3.7 Conclusion

In this chapter, we studied the turbulent behaviour of the one-dimensional Schrödinger-Helmholtz Equation in the Short-Wave Limit. We developed a reduced model of the wave kinetics, the Semi-Local Approximation Model, by assuming that the interacting wave-vectors are closely paired in Fourier space. Considering the complete Schrödinger-Helmholtz equation is necessary because the Short-Wave Equation leads to a divergent Kinetic Equation. With the SLAM, we were able to derive an expression for the wave-action flux, which allows us to derive Kolmogorov-Zakharov spectra for the cascades of energy and wave-action. The energy cascade was found to be local while the wave-action cascade is not. We derived a non-local analysis an obtained a non-local spectrum.

Then, these theoretical predictions were tested against numerical simulations of forced and dissipative systems. The numerics spectrum for the Direct Cascade does not exhibit clearly the expected power-law but for the Inverse Cascade, the non-local prediction models with a good accordance the numerics results. In both cascades we can observe a global correspond over the full $k$-range. Finally, Incoherent Solitons have been found under particular conditions. These structures, already mentioned in the literature, were characterized for our system. We can notice that for the Direct Cascade, the Incoherent Soliton spectra signature appears inside the inertial range, which creates an asymmetry for the wave-action spectrum.

# General Conclusion

**Existence of an attractor for the 1D-SHE**

We have established the existence of a statistical attractor of the 1D-SHE. We have prepared the system with different types of initial conditions (flat-top spectrum, two localized structures or a single 1D-NLSE soliton) and all these systems were observed to convergence towards a single structure oscillating in amplitude and in width, propagating among a sea of weakly non-linear waves. This coherent final state can not exist if the system is too linear.

This final state, which we call a bound-state, has been precisely characterized with the DST spectrum (with the DST framework introduced for the 1D-NLSE) displaying two dominant eigenvalues. These two eigenvalues have correlated evolutions : their imaginary parts oscillate with the same frequency, and in phase opposition. This evolution is also correlated with the evolution of the maximum of the function, which we suppose to be the amplitude of the bound-state. We also computed the $(\mathbf{k}-\omega)$ spectrum of this bound-state and we conclude that the bound-state is represented by three parallel lines, with the same slope. This slope corresponds to the speed of the bound-state.

That these two spectral signatures are consistent with each other, and they capture the frequency characteristics of the bound-state. This bound-state was found to depend on the non-integrability parameter, as they do not appear in systems too far away from integrability. Finally, this study has shown that the DST is a reliable tool for the 1D-SHE as it qualitatively follows the dynamics well. The work we have presented in this thesis opens a wide variety of perspectives. We will finish this manuscript by detailing some of them.

Finally, we have also found a criterion to distinguish between elastic and non-elastic collisions of localized structures in the 1D-SHE. We suggest that two structures which collide while they are in phase opposition will undergo an elastic collision which does not alter their amplitudes nor their speeds. In order for a collision to be non-elastic and merge the colliding structure into a single one (a bound-state), these in-coming structures must be in phase at the collision.

**Turbulent cascades in the forced and dissipating 1D-SHE**

As the 1D-SHE is not integrable, it can exhibit weak wave turbulence properties that we studied first theoretically and then numerically. The cascading quantities are the positive invariants : the wave-action and the quadratic energy. We studied the equation with its complete form, and in the Short-Wave Limit, because the 1D-SNE, which is the naively Taylor expanded 1D-SHE, causes the Kinetic Equation to diverge. In this limit, given the expression of the interaction coefficient, the dynamics of wave interactions is dominated by situations when the interacting wave-vectors can be paired with almost-identical values. Using this observation, we reduced the 1D-SHE to a reduced model, the Semi-Local Approximation Model which takes into account this observation.

An important result obtained from this model is an expression of the wave-action flux, which makes possible the derivation of the exponents of the Kolmogorov-Zakharov spectra. It turned out that the KZ spectrum of cascading wave-action is non-local and we developed a non-local analysis to obtain a new spectrum. The physically realisable spectra are characterized by exponents $x_{\mathrm{FE}} = 2/5$ for the local cascade of energy and $x_{\mathrm{FN}} = 1$ for the non-local wave-action cascade. The local energy cascade is direct, as expected with the Fjørtoft argument.

These theoretical predictions were then tested against numerical simulations. Forcing and dissipation were added to the 1D-SHE to allow cascade to occur. For both Direct and Inverse Cascades, the theoretical spectra correspond relatively well to the spectra obtained in the inertial range, particularly for the non-local prediction in the inverse cascade which is found close to the numerics. We still noticed that the theoretical predictions are of good accuracy for the whole $k$-range. Finally, some structures, coherent for large scales and incoherent for small scales, have been observed in simulations. These structures are called Incoherent Solitons and developed in coexistence with cascades. Particularly, in the Direct Cascade Simulation, an Incoherent Soliton stops the cascade towards large positive wave-numbers. We have studied the properties of these structures alone but the simulations displaying both cascades and Incoherent Solitons are an example of a system in which the two aspect of turbulence, strong and week, arise and deserve attention in future works.

**Perspectives**

The work presented in this thesis contains results which bring interesting perspectives. We will conclude this manuscript by detailing some of them.

In our study of the propagation of localized structures in the 1D-SHE, we used the DST framework devised for the the integrable 1D-NLSE without modifying it. This DST gave interesting results as it was found to be relevant to study our system. To improve again the precision of this diagnosis, we can consider, in future work, perturbating this DST to take into account the non-integrability of the 1D-SHE, as it is done in [92] for

other non-integrable equations. That would allow us to adapt the DST tool to our given system and may enable more precise results to be obtained. However, we know that the non-integrable nature itself of the 1D-SHE ensures that we will not be able to find a DST devised exactly for the 1D-SHE. We can also consider the use of DST to analyze real data obtained in non-linear optics experiments.

During our work, we identified a bound-state with given initial conditions. We drew a phase-diagram with the different parameters of the initial flat-top simulation but this phase diagram can be completed by new studies for different types of initial conditions. A preliminary result was obtained in the evolutions of an NLSE soliton in 1D-SHE with different $\beta$ : the bound-state does not appear if the non-integrability parameter is too large, with $\mathcal{N}$ fixed. Finally, the phase diagram displayed a transitional state for which the DST spectrum of the bound-state only contains one eigenvalue, and this transitional state was found to depend on the position of the initial spectrum. We only reported this observation and further studies around the transition could enlighten the critical behaviour.

As reported in the manuscript, the cascades observed in the numerics did not display an universal power-law and, thus, we have not clearly observed the predictions derived from the Semi-Local Approximation Model. The latter are still a good model of the spectrum for the entire $k$-range, showing that they are still particular for this system. We only report here the lack of correspondence in the inertial range but we do not have an explanation yet for this observation. Particularly, we do not know why the predictions for an inertial range are also observed outside of this inertial range.

We have discovered that Incoherent Solitons can be created during the Inverse Cascade simulations. Further considerations and more simulations will be necessary to improve our understanding the conditions required for these particular structures to grow. In order to do so, we propose to study quantitatively the link between the non-integrability parameter $\beta$ and the width of the IS. In our work, we have started this study but further work can explore more in detail this aspect of the 1D-SHE Particularly, it could be interesting to derive a Vlasov equation, as done in [98], to model with accuracy their profile in $\mathbf{k}$-space.

Finally, the cascades, expected in a weakly non-linear system, are observed with Incoherent Solitons, which testify that the non-linearity is not so small. This observation requires to develop a more complete theory of optical Wave Turbulence, to take into account both weakly and strongly non-linear waves coexisting in the same systems. For the Direct Cascade, we observed a cascade in the inertial range for negative wave-vectors and an Incoherent Soliton for the inertial range for positive wave-vectors. This dual system requires more attention to understand why the system is so different on each direction while the forcing is statistically equal in both directions. Repeating this simulation and keeping all the parameters constant can allow us to average over the random phases of the forcing and to see whether the Incoherent Soliton will still be observed.

# APPENDIX A

## Details of SLAM computations

We present here the details of the computations leading to the final expression (3.35) of the SLAM integral. We start with equation (3.34)

$$\begin{aligned}
&\int \varphi_{\mathbf{k}} \dot{n}_{\mathbf{k}} \mathrm{d}\mathbf{k} = 24\pi \frac{1}{\Lambda^{\frac{5}{2}}} \int f(\mathbf{k}_1, \mathbf{k}_2, \mathbf{k}) \frac{1}{|\mathbf{k}_2 - \mathbf{k}|} n_1^2 n_2^2 n_{\mathbf{k}}^2 \left[ \left( \partial_1 \frac{1}{n_1} - \partial_{\mathbf{k}} \frac{1}{n_{\mathbf{k}}} \right) + \frac{\mathbf{k} - \mathbf{k}_1}{\mathbf{k}_2 - \mathbf{k}} \left( \partial_2 \frac{1}{n_2} - \partial_{\mathbf{k}} \frac{1}{n_{\mathbf{k}}} \right) \right] \partial_1 \varphi_1 \, \mathrm{d}\mathbf{k}_1 \mathrm{d}\mathbf{k}_2 \mathrm{d}\mathbf{k} \\
&- 24\pi \frac{1}{\Lambda^{\frac{5}{2}}} \int f(\mathbf{k}_1, \mathbf{k}_2, \mathbf{k}) \frac{1}{|\mathbf{k}_2 - \mathbf{k}|} n_1^2 n_2^2 n_{\mathbf{k}}^2 \left[ \left( \partial_1 \frac{1}{n_1} - \partial_{\mathbf{k}} \frac{1}{n_{\mathbf{k}}} \right) + \frac{\mathbf{k} - \mathbf{k}_1}{\mathbf{k}_2 - \mathbf{k}} \left( \partial_2 \frac{1}{n_2} - \partial_{\mathbf{k}} \frac{1}{n_{\mathbf{k}}} \right) \right] \partial_{\mathbf{k}} \varphi_{\mathbf{k}} \, \mathrm{d}\mathbf{k}_1 \mathrm{d}\mathbf{k}_2 \mathrm{d}\mathbf{k} \\
&+ 24\pi \frac{1}{\Lambda^{\frac{5}{2}}} \int f(\mathbf{k}_1, \mathbf{k}_2, \mathbf{k}) \frac{1}{|\mathbf{k}_2 - \mathbf{k}|} n_1^2 n_2^2 n_{\mathbf{k}}^2 \left[ \left( \partial_1 \frac{1}{n_1} - \partial_{\mathbf{k}} \frac{1}{n_{\mathbf{k}}} \right) + \frac{\mathbf{k} - \mathbf{k}_1}{\mathbf{k}_2 - \mathbf{k}} \left( \partial_2 \frac{1}{n_2} - \partial_{\mathbf{k}} \frac{1}{n_{\mathbf{k}}} \right) \right] \frac{\mathbf{k} - \mathbf{k}_1}{\mathbf{k}_2 - \mathbf{k}} \partial_2 \varphi_2 \, \mathrm{d}\mathbf{k}_1 \mathrm{d}\mathbf{k}_2 \mathrm{d}\mathbf{k} \\
&- 24\pi \frac{1}{\Lambda^{\frac{5}{2}}} \int f(\mathbf{k}_1, \mathbf{k}_2, \mathbf{k}) \frac{1}{|\mathbf{k}_2 - \mathbf{k}|} n_1^2 n_2^2 n_{\mathbf{k}}^2 \left[ \left( \partial_1 \frac{1}{n_1} - \partial_{\mathbf{k}} \frac{1}{n_{\mathbf{k}}} \right) + \frac{\mathbf{k} - \mathbf{k}_1}{\mathbf{k}_2 - \mathbf{k}} \left( \partial_2 \frac{1}{n_2} - \partial_{\mathbf{k}} \frac{1}{n_{\mathbf{k}}} \right) \right] \frac{\mathbf{k} - \mathbf{k}_1}{\mathbf{k}_2 - \mathbf{k}} \partial_{\mathbf{k}} \varphi_{\mathbf{k}} \, \mathrm{d}\mathbf{k}_1 \mathrm{d}\mathbf{k}_2 \mathrm{d}\mathbf{k}
\end{aligned} \tag{A.1}$$

and we group together the integrands proportional to $\partial_{\mathbf{k}} \varphi_{\mathbf{k}}$

$$\begin{aligned}
&\int \varphi_{\mathbf{k}} \dot{n}_{\mathbf{k}} \mathrm{d}\mathbf{k} = 24\pi \frac{1}{\Lambda^{\frac{5}{2}}} \int f(\mathbf{k}_1, \mathbf{k}_2, \mathbf{k}) \frac{1}{|\mathbf{k}_2 - \mathbf{k}|} n_1^2 n_2^2 n_{\mathbf{k}}^2 \left[ \left( \partial_1 \frac{1}{n_1} - \partial_{\mathbf{k}} \frac{1}{n_{\mathbf{k}}} \right) + \frac{\mathbf{k} - \mathbf{k}_1}{\mathbf{k}_2 - \mathbf{k}} \left( \partial_2 \frac{1}{n_2} - \partial_{\mathbf{k}} \frac{1}{n_{\mathbf{k}}} \right) \right] \partial_1 \varphi_1 \, \mathrm{d}\mathbf{k}_1 \mathrm{d}\mathbf{k}_2 \mathrm{d}\mathbf{k} \\
&+ 24\pi \frac{1}{\Lambda^{\frac{5}{2}}} \int f(\mathbf{k}_1, \mathbf{k}_2, \mathbf{k}) \frac{1}{|\mathbf{k}_2 - \mathbf{k}|} n_1^2 n_2^2 n_{\mathbf{k}}^2 \left[ \left( \partial_1 \frac{1}{n_1} - \partial_{\mathbf{k}} \frac{1}{n_{\mathbf{k}}} \right) + \frac{\mathbf{k} - \mathbf{k}_1}{\mathbf{k}_2 - \mathbf{k}} \left( \partial_2 \frac{1}{n_2} - \partial_{\mathbf{k}} \frac{1}{n_{\mathbf{k}}} \right) \right] \frac{\mathbf{k} - \mathbf{k}_1}{\mathbf{k}_2 - \mathbf{k}} \partial_2 \varphi_2 \, \mathrm{d}\mathbf{k}_1 \mathrm{d}\mathbf{k}_2 \mathrm{d}\mathbf{k} \\
&- 24\pi \frac{1}{\Lambda^{\frac{5}{2}}} \int f(\mathbf{k}_1, \mathbf{k}_2, k\mathbf{k} \frac{1}{|\mathbf{k}_2 - \mathbf{k}|} n_1^2 n_2^2 n_{\mathbf{k}}^2 \left[ \left( \partial_1 \frac{1}{n_1} - \partial_{\mathbf{k}} \frac{1}{n_{\mathbf{k}}} \right) + \frac{\mathbf{k} - \mathbf{k}_1}{\mathbf{k}_2 - \mathbf{k}} \left( \partial_2 \frac{1}{n_2} - \partial_{\mathbf{k}} \frac{1}{n_{\mathbf{k}}} \right) \right] \frac{\mathbf{k}_2 - \mathbf{k}_1}{\mathbf{k}_2 - \mathbf{k}} \partial_{\mathbf{k}} \varphi_{\mathbf{k}} \, \mathrm{d}\mathbf{k}_1 \mathrm{d}\mathbf{k}_2 \mathrm{d}\mathbf{k}
\end{aligned} \tag{A.2}$$

Then, we perform a change of variable $\mathbf{k}_1 \leftrightarrow \mathbf{k}$ in the first term and $\mathbf{k}_2 \leftrightarrow \mathbf{k}$ in the second term in order to write all the integrands proportional to $\partial_{\mathbf{k}} \varphi_{\mathbf{k}}$

$$\int \varphi_{\mathbf{k}} \dot{n}_{\mathbf{k}} \mathrm{d}\mathbf{k} = 24\pi \frac{1}{\Lambda^{\frac{5}{2}}} \int f(\mathbf{k}, \mathbf{k}_2, \mathbf{k}_1) \frac{1}{|\mathbf{k}_2 - \mathbf{k}_1|} n_1^2 n_2^2 n_{\mathbf{k}}^2 \left[ \left( \partial_{\mathbf{k}} \frac{1}{n_{\mathbf{k}}} - \partial_1 \frac{1}{n_1} \right) + \frac{\mathbf{k}_1 - \mathbf{k}}{\mathbf{k}_2 - \mathbf{k}_1} \left( \partial_2 \frac{1}{n_2} - \partial_1 \frac{1}{n_1} \right) \right] \partial_{\mathbf{k}} \varphi_{\mathbf{k}} \, \mathrm{d}\mathbf{k}_1 \mathrm{d}\mathbf{k}_2 \mathrm{d}\mathbf{k}$$
$$+ 24\pi \frac{1}{\Lambda^{\frac{5}{2}}} \int f(\mathbf{k}_1, \mathbf{k}, \mathbf{k}_2) \frac{1}{|\mathbf{k}_2 - \mathbf{k}|} n_1^2 n_2^2 n_{\mathbf{k}}^2 \left[ \left( \partial_1 \frac{1}{n_1} - \partial_2 \frac{1}{n_2} \right) + \frac{\mathbf{k}_2 - \mathbf{k}_1}{\mathbf{k} - \mathbf{k}_2} \left( \partial_{\mathbf{k}} \frac{1}{n_{\mathbf{k}}} - \partial_2 \frac{1}{n_2} \right) \right] \frac{\mathbf{k}_2 - \mathbf{k}_1}{\mathbf{k} - \mathbf{k}_2} \partial_{\mathbf{k}} \varphi_{\mathbf{k}} \, \mathrm{d}\mathbf{k}_1 \mathrm{d}\mathbf{k}_2 \mathrm{d}\mathbf{k}$$
$$- 24\pi \frac{1}{\Lambda^{\frac{5}{2}}} \int f(\mathbf{k}_1, \mathbf{k}_2, \mathbf{k}) \frac{1}{|\mathbf{k}_2 - \mathbf{k}|} n_1^2 n_2^2 n_{\mathbf{k}}^2 \left[ \left( \partial_1 \frac{1}{n_1} - \partial_{\mathbf{k}} \frac{1}{n_{\mathbf{k}}} \right) + \frac{\mathbf{k} - \mathbf{k}_1}{\mathbf{k}_2 - \mathbf{k}} \left( \partial_2 \frac{1}{n_2} - \partial_{\mathbf{k}} \frac{1}{n_{\mathbf{k}}} \right) \right] \frac{\mathbf{k}_2 - \mathbf{k}_1}{\mathbf{k}_2 - \mathbf{k}} \partial_{\mathbf{k}} \varphi_{\mathbf{k}} \, \mathrm{d}\mathbf{k}_1 \mathrm{d}\mathbf{k}_2 \mathrm{d}\mathbf{k}. \tag{A.3}$$

Then, we isolate all the $\partial_2 \frac{1}{n_2}$ terms

$$\int \varphi_{\mathbf{k}} \dot{n}_{\mathbf{k}} \mathrm{d}\mathbf{k} = 24\pi \frac{1}{\Lambda^{\frac{5}{2}}} \int f(\mathbf{k}, \mathbf{k}_2, \mathbf{k}_1) \frac{1}{|\mathbf{k}_2 - \mathbf{k}_1|} n_1^2 n_2^2 n_{\mathbf{k}}^2 \left[ \left( \partial_{\mathbf{k}} \frac{1}{n_{\mathbf{k}}} - \partial_1 \frac{1}{n_1} \right) + \frac{\mathbf{k}_1 - \mathbf{k}}{\mathbf{k}_2 - \mathbf{k}_1} \left( - \partial_1 \frac{1}{n_1} \right) \right] \partial_k \varphi_k \, \mathrm{d}\mathbf{k}_1 \mathrm{d}\mathbf{k}_2 \mathrm{d}\mathbf{k}$$
$$+ 24\pi \frac{1}{\Lambda^{\frac{5}{2}}} \int f(\mathbf{k}, \mathbf{k}_2, \mathbf{k}_1) \frac{1}{|\mathbf{k}_2 - \mathbf{k}_1|} n_1^2 n_2^2 n_{\mathbf{k}}^2 \frac{\mathbf{k}_1 - \mathbf{k}}{\mathbf{k}_2 - \mathbf{k}_1} \left( \partial_2 \frac{1}{n_2} \right) \partial_{\mathbf{k}} \varphi_{\mathbf{k}} \, \mathrm{d}\mathbf{k}_1 \mathrm{d}\mathbf{k}_2 \mathrm{d}\mathbf{k}$$
$$+ 24\pi \frac{1}{\Lambda^{\frac{5}{2}}} \int f(\mathbf{k}_1, \mathbf{k}, \mathbf{k}_2) \frac{1}{|\mathbf{k}_2 - \mathbf{k}|} n_1^2 n_2^2 n_{\mathbf{k}}^2 \left[ \left( \partial_1 \frac{1}{n_1} \right) + \frac{\mathbf{k}_2 - \mathbf{k}_1}{\mathbf{k} - \mathbf{k}_2} \left( \partial_{\mathbf{k}} \frac{1}{n_{\mathbf{k}}} \right) \right] \frac{\mathbf{k}_2 - \mathbf{k}_1}{\mathbf{k} - \mathbf{k}_2} \partial_{\mathbf{k}} \varphi_{\mathbf{k}} \, \mathrm{d}\mathbf{k}_1 \mathrm{d}\mathbf{k}_2 \mathrm{d}\mathbf{k}$$
$$+ 24\pi \frac{1}{\Lambda^{\frac{5}{2}}} \int f(\mathbf{k}_1, \mathbf{k}, \mathbf{k}_2) \frac{1}{|\mathbf{k}_2 - \mathbf{k}|} n_1^2 n_2^2 n_{\mathbf{k}}^2 \left[ \left( - \partial_2 \frac{1}{n_2} \right) + \frac{\mathbf{k}_2 - \mathbf{k}_1}{\mathbf{k} - \mathbf{k}_2} \left( - \partial_2 \frac{1}{n_2} \right) \right] \frac{\mathbf{k}_2 - \mathbf{k}_1}{\mathbf{k} - \mathbf{k}_2} \partial_{\mathbf{k}} \varphi_{\mathbf{k}} \, \mathrm{d}\mathbf{k}_1 \mathrm{d}\mathbf{k}_2 \mathrm{d}\mathbf{k}$$
$$- 24\pi \frac{1}{\Lambda^{\frac{5}{2}}} \int f(\mathbf{k}_1, \mathbf{k}_2, \mathbf{k}) \frac{1}{|\mathbf{k}_2 - \mathbf{k}|} n_1^2 n_2^2 n_{\mathbf{k}}^2 \left[ \left( \partial_1 \frac{1}{n_1} - \partial_{\mathbf{k}} \frac{1}{n_{\mathbf{k}}} \right) + \frac{\mathbf{k} - \mathbf{k}_1}{\mathbf{k}_2 - \mathbf{k}} \left( - \partial_{\mathbf{k}} \frac{1}{n_{\mathbf{k}}} \right) \right] \frac{\mathbf{k}_2 - \mathbf{k}_1}{\mathbf{k}_2 - \mathbf{k}} \partial_{\mathbf{k}} \varphi_{\mathbf{k}} \, \mathrm{d}\mathbf{k}_1 \mathrm{d}\mathbf{k}_2 \mathrm{d}\mathbf{k}$$
$$- 24\pi \frac{1}{\Lambda^{\frac{5}{2}}} \int f(\mathbf{k}_1, \mathbf{k}_2, \mathbf{k}) \frac{1}{|\mathbf{k}_2 - \mathbf{k}|} n_1^2 n_2^2 n_{\mathbf{k}}^2 \frac{\mathbf{k} - \mathbf{k}_1}{\mathbf{k}_2 - \mathbf{k}} \frac{\mathbf{k}_2 - \mathbf{k}_1}{\mathbf{k}_2 - \mathbf{k}} \partial_2 \frac{1}{n_2} \partial_{\mathbf{k}} \varphi_{\mathbf{k}} \, \mathrm{d}\mathbf{k}_1 \mathrm{d}\mathbf{k}_2 \mathrm{d}\mathbf{k}. \tag{A.4}$$

In every integral for which the integral is proportional to $\partial_2 \frac{1}{n_2}$, we change the integration variables $\mathbf{k}_1 \leftrightarrow \mathbf{k}_2$.

$$\begin{aligned}
\int \varphi_{\mathbf{k}} \dot{n}_{\mathbf{k}} \mathrm{d}\mathbf{k} = {} & 24\pi \frac{1}{\Lambda^{\frac{5}{2}}} \int f(\mathbf{k}, \mathbf{k}_2, \mathbf{k}_1) \frac{1}{|\mathbf{k}_2 - \mathbf{k}_1|} n_1^2 n_2^2 n_{\mathbf{k}}^2 \left[ \left( \partial_{\mathbf{k}} \frac{1}{n_{\mathbf{k}}} - \partial_1 \frac{1}{n_1} \right) + \frac{\mathbf{k}_1 - \mathbf{k}}{\mathbf{k}_2 - \mathbf{k}_1} \left( - \partial_1 \frac{1}{n_1} \right) \right] \partial_{\mathbf{k}} \varphi_{\mathbf{k}} \mathrm{d}\mathbf{k}_1 \mathrm{d}\mathbf{k}_2 \mathrm{d}\mathbf{k} \\
& + 24\pi \frac{1}{\Lambda^{\frac{5}{2}}} \int f(\mathbf{k}, \mathbf{k}_1, \mathbf{k}_2) \frac{1}{|\mathbf{k}_1 - \mathbf{k}_2|} n_1^2 n_2^2 n_{\mathbf{k}}^2 \frac{\mathbf{k}_2 - \mathbf{k}}{\mathbf{k}_1 - \mathbf{k}_2} \left( \partial_1 \frac{1}{n_1} \right) \partial_{\mathbf{k}} \varphi_{\mathbf{k}} \mathrm{d}\mathbf{k}_1 \mathrm{d}\mathbf{k}_2 \mathrm{d}\mathbf{k} \\
& + 24\pi \frac{1}{\Lambda^{\frac{5}{2}}} \int f(\mathbf{k}_1, \mathbf{k}, \mathbf{k}_2) \frac{1}{|\mathbf{k}_2 - \mathbf{k}|} n_1^2 n_2^2 n_{\mathbf{k}}^2 \left[ \left( \partial_1 \frac{1}{n_1} \right) + \frac{\mathbf{k}_2 - \mathbf{k}_1}{\mathbf{k} - \mathbf{k}_2} \left( \partial_{\mathbf{k}} \frac{1}{n_{\mathbf{k}}} \right) \right] \frac{\mathbf{k}_2 - \mathbf{k}_1}{\mathbf{k} - \mathbf{k}_2} \partial_{\mathbf{k}} \varphi_{\mathbf{k}} \mathrm{d}\mathbf{k}_1 \mathrm{d}\mathbf{k}_2 \mathrm{d}\mathbf{k} \\
& + 24\pi \frac{1}{\Lambda^{\frac{5}{2}}} \int f(\mathbf{k}_2, \mathbf{k}, \mathbf{k}_1) \frac{1}{|\mathbf{k}_1 - \mathbf{k}|} n_1^2 n_2^2 n_{\mathbf{k}}^2 \left[ \left( - \partial_1 \frac{1}{n_1} \right) + \frac{\mathbf{k}_1 - \mathbf{k}_2}{\mathbf{k} - \mathbf{k}_1} \left( - \partial_1 \frac{1}{n_1} \right) \right] \frac{\mathbf{k}_1 - \mathbf{k}_2}{\mathbf{k} - \mathbf{k}_1} \partial_{\mathbf{k}} \varphi_{\mathbf{k}} \mathrm{d}\mathbf{k}_1 \mathrm{d}\mathbf{k}_2 \mathrm{d}\mathbf{k} \\
& - 24\pi \frac{1}{\Lambda^{\frac{5}{2}}} \int f(\mathbf{k}_1, \mathbf{k}_2, \mathbf{k}) \frac{1}{|\mathbf{k}_2 - \mathbf{k}|} n_1^2 n_2^2 n_{\mathbf{k}}^2 \left[ \left( \partial_1 \frac{1}{n_1} - \partial_{\mathbf{k}} \frac{1}{n_{\mathbf{k}}} \right) + \frac{\mathbf{k} - \mathbf{k}_1}{\mathbf{k}_2 - \mathbf{k}} \left( - \partial_{\mathbf{k}} \frac{1}{n_{\mathbf{k}}} \right) \right] \frac{\mathbf{k}_2 - \mathbf{k}_1}{\mathbf{k}_2 - \mathbf{k}} \partial_{\mathbf{k}} \varphi_{\mathbf{k}} \mathrm{d}\mathbf{k}_1 \mathrm{d}\mathbf{k}_2 \mathrm{d}\mathbf{k} \\
& - 24\pi \frac{1}{\Lambda^{\frac{5}{2}}} \int f(\mathbf{k}_2, \mathbf{k}_1, \mathbf{k}) \frac{1}{|\mathbf{k}_1 - \mathbf{k}|} n_1^2 n_2^2 n_{\mathbf{k}}^2 \frac{\mathbf{k} - \mathbf{k}_2}{\mathbf{k}_1 - \mathbf{k}} \frac{\mathbf{k}_1 - \mathbf{k}_2}{\mathbf{k}_1 - \mathbf{k}} \partial_1 \frac{1}{n_1} \partial_{\mathbf{k}} \varphi_{\mathbf{k}} \mathrm{d}\mathbf{k}_1 \mathrm{d}\mathbf{k}_2 \mathrm{d}\mathbf{k}.
\end{aligned} \tag{A.5}$$

$$\int \varphi_{\mathbf{k}} \dot{n}_{\mathbf{k}} \mathrm{d}\mathbf{k} = 24\pi \frac{1}{\Lambda^{\frac{5}{2}}} \int \mathrm{d}\mathbf{k}_1 \mathrm{d}\mathbf{k}_2 \mathrm{d}\mathbf{k} \; n_1^2 n_2^2 n_{\mathbf{k}}^2 \left[ U_{\mathbf{k}}^{\mathbf{k}_1, \mathbf{k}_2} \partial_1 \frac{1}{n_1} + V_{\mathbf{k}}^{\mathbf{k}_1, \mathbf{k}_2} \partial_{\mathbf{k}} \frac{1}{n_{\mathbf{k}}} \right] \partial_{\mathbf{k}} \varphi_{\mathbf{k}} \tag{A.6}$$

$$\int \varphi_{\mathbf{k}} \dot{n}_{\mathbf{k}} \mathrm{d}\mathbf{k} = -24\pi \frac{1}{\Lambda^{\frac{5}{2}}} \int \mathrm{d}\mathbf{k}_1 \mathrm{d}\mathbf{k}_2 \mathrm{d}\mathbf{k} \left[ n_2^2 n_{\mathbf{k}}^2 \; U_{\mathbf{k}}^{\mathbf{k}_1, \mathbf{k}_2} \partial_1 n_1 + n_1^2 n_2^2 \; V_{\mathbf{k}}^{\mathbf{k}_1, \mathbf{k}_2} \partial_{\mathbf{k}} n_{\mathbf{k}} \right] \partial_{\mathbf{k}} \varphi_{\mathbf{k}}, \tag{A.7}$$

with

$$U_{\mathbf{k}}^{\mathbf{k}_1,\mathbf{k}_2} = -\Big[f(\mathbf{k},\mathbf{k}_2,\mathbf{k}_1)+f(\mathbf{k},\mathbf{k}_1,\mathbf{k}_2)\Big]\frac{1}{|\mathbf{k}_2-\mathbf{k}_1|}\frac{\mathbf{k}_2-\mathbf{k}}{\mathbf{k}_2-\mathbf{k}_1}$$
$$+\Big[f(\mathbf{k}_1,\mathbf{k},\mathbf{k}_2)+f(\mathbf{k}_1,\mathbf{k}_2,\mathbf{k})\Big]\frac{1}{|\mathbf{k}_2-\mathbf{k}|}\frac{\mathbf{k}_2-\mathbf{k}_1}{\mathbf{k}-\mathbf{k}_2}-\Big[f(\mathbf{k}_2,\mathbf{k},\mathbf{k}_1)+f(\mathbf{k}_2,\mathbf{k}_1,\mathbf{k})\Big]\frac{1}{|\mathbf{k}_1-\mathbf{k}|}\frac{\mathbf{k}_1-\mathbf{k}_2}{\mathbf{k}-\mathbf{k}_1}\frac{\mathbf{k}-\mathbf{k}_2}{\mathbf{k}-\mathbf{k}_1}, \tag{A.8}$$

and

$$V_{\mathbf{k}}^{\mathbf{k}_1,\mathbf{k}_2} = f(\mathbf{k},\mathbf{k}_2,\mathbf{k}_1)\frac{1}{|\mathbf{k}_2-\mathbf{k}_1|}+\Big[f(\mathbf{k}_1,\mathbf{k},\mathbf{k_2})+f(\mathbf{k}_1,\mathbf{k}_2,\mathbf{k})\Big]\frac{1}{|\mathbf{k}_2-\mathbf{k}|}\frac{(\mathbf{k}_2-\mathbf{k}_1)^2}{(\mathbf{k}-\mathbf{k}_2)^2}. \tag{A.9}$$

We highlight properties of $V$ which will be important later

$$V_{\mathbf{k}}^{\mathbf{k}_1,\mathbf{k}_2} = V_{\mathbf{k}}^{\mathbf{k}_2,\mathbf{k}_1}\ ,\ \ V_{\mathbf{k}}^{\mathbf{k}_1,\mathbf{k}_2} = \frac{(k_1-k_2)^2}{(k-k_1)^2}V_{\mathbf{k}_2}^{\mathbf{k}_1,\mathbf{k}}\ ,\ \ U_{\mathbf{k}}^{\mathbf{k}_1,\mathbf{k}_2} = 2\frac{\mathbf{k}-\mathbf{k}_2}{-\mathbf{k}_1+\mathbf{k}_2}V_{\mathbf{k}}^{\mathbf{k}_1,\mathbf{k}_2}. \tag{A.10}$$

We now integrate by parts to have integrands from both LHS and RHS proportional to $\varphi_{\mathbf{k}}$

$$\int\varphi_{\mathbf{k}}\dot{n}_{\mathbf{k}}\mathrm{d}\mathbf{k} = 24\pi\frac{1}{\Lambda^{\frac{5}{2}}}\int\mathrm{d}k\mathbf{k}_1\mathrm{d}\mathbf{k}_2\mathrm{d}\mathbf{k}\ \varphi_{\mathbf{k}}\partial_{\mathbf{k}}\left(\left[n_2^2n_{\mathbf{k}}^2\ U_{\mathbf{k}}^{\mathbf{k}_1,\mathbf{k}_2}\partial_1 n_1+n_1^2n_2^2\ V_{\mathbf{k}}^{\mathbf{k}_1,\mathbf{k}_2}\partial_{\mathbf{k}}n_{\mathbf{k}}\right]\right). \tag{A.11}$$

And with $\varphi_k$ being a random test function, we have

$$\dot{n}_{\mathbf{k}} = 24\pi\frac{1}{\Lambda^{\frac{5}{2}}}\partial_{\mathbf{k}}\int\mathrm{d}\mathbf{k}_1\mathrm{d}\mathbf{k}_2\ \left[n_2^2n_{\mathbf{k}}^2\ U_{\mathbf{k}}^{\mathbf{k}_1,\mathbf{k}_2}\partial_1 n_1+n_1^2n_2^2\ V_{\mathbf{k}}^{\mathbf{k}_1,\mathbf{k}_2}\partial_{\mathbf{k}}n_{\mathbf{k}}\right]. \tag{A.12}$$

With the property $U_{\mathbf{k}}^{\mathbf{k}_1,\mathbf{k}_2} = 2\frac{\mathbf{k}-\mathbf{k}_2}{-\mathbf{k}_1+\mathbf{k}_2}\,V_{\mathbf{k}}^{\mathbf{k}_1,\mathbf{k}_2}$, $\partial n_{\mathbf{k}}/\partial t$ becomes

$$\frac{\partial n_{\mathbf{k}}}{\partial t} = 24\pi\frac{1}{\Lambda^{\frac{5}{2}}}\partial_{\mathbf{k}}\int\ V_{\mathbf{k}}^{\mathbf{k}_1,\mathbf{k}_2}\ \left[n_2^2n_{\mathbf{k}}^2\ 2\frac{\mathbf{k}-\mathbf{k}_2}{-\mathbf{k}_1+\mathbf{k}_2}\partial_{\mathbf{k}_1}n_1+n_1^2n_2^2\ \partial_{\mathbf{k}}n_{\mathbf{k}}\right]\mathrm{d}\mathbf{k}_1\mathrm{d}\mathbf{k}_2. \tag{A.13}$$

# APPENDIX B

## Expressions for the SLAM

$$
\begin{aligned}
f(\mathbf{k}_1,\mathbf{k}_2,\mathbf{k}) = {} & \frac{-\pi(\mathbf{k}-\mathbf{k}_2)}{48\Lambda^{\frac{5}{2}}(\mathbf{k}-\mathbf{k}_1)^3(\mathbf{k}+\mathbf{k}_1-2\mathbf{k}_2)^3(\mathbf{k}_1-\mathbf{k}_2)^3(\mathbf{k}-2\mathbf{k}_1+\mathbf{k}_2)^3(-2\mathbf{k}+\mathbf{k}_1+\mathbf{k}_2)^3|\mathbf{k}-\mathbf{k}_2|} \\
& \times \Bigg[ -(\mathbf{k}-\mathbf{k}_1)^3(\mathbf{k}+\mathbf{k}_1-2\mathbf{k}_2)^3\Big(4\mathbf{k}^4+4\mathbf{k}_1^4+2\mathbf{k}_1^3\mathbf{k}_2-5\mathbf{k}_1^2\mathbf{k}_2^2+6\mathbf{k}_1\mathbf{k}_2^3-3\mathbf{k}_2^4+2\mathbf{k}^3(-9\mathbf{k}_1+\mathbf{k}_2) \\
& +\mathbf{k}^2\big(25\mathbf{k}_1^2+4\mathbf{k}_1\mathbf{k}_2-5\mathbf{k}_2^2\big)+\mathbf{k}\big(-18\mathbf{k}_1^3+4\mathbf{k}_1^2\mathbf{k}_2-8\mathbf{k}_1\mathbf{k}_2^2+6\mathbf{k}_2^3\big)\Big) \\
& (\mathbf{k}-\mathbf{k}_2)^3(\mathbf{k}-2\mathbf{k}_1+\mathbf{k}_2)^3\Big(4\mathbf{k}^4+4\mathbf{k}_2^4+2\mathbf{k}_2^3\mathbf{k}_1-5\mathbf{k}_2^2\mathbf{k}_1^2+6\mathbf{k}_2\mathbf{k}_1^3-3\mathbf{k}_1^4+2\mathbf{k}^3(-9\mathbf{k}_1+\mathbf{k}_1) \\
& +\mathbf{k}^2\big(25\mathbf{k}_2^2+4\mathbf{k}_2\mathbf{k}_1-5\mathbf{k}_1^2\big)+\mathbf{k}\big(-18\mathbf{k}_2^3+4\mathbf{k}_2^2\mathbf{k}_1-8\mathbf{k}_2\mathbf{k}_1^2+6\mathbf{k}_1^3\big)\Big) \\
& -(\mathbf{k}_1-\mathbf{k}_2)^3(-2\mathbf{k}+\mathbf{k}_1+\mathbf{k}_2)^3\Big(-3\mathbf{k}^4+4\mathbf{k}_1^4-18\mathbf{k}_1^3\mathbf{k}_2+25\mathbf{k}_1^2\mathbf{k}_2^2-18\mathbf{k}_1\mathbf{k}_2^3+4\mathbf{k}_2^4+6\mathbf{k}^3(\mathbf{k}_1+\mathbf{k}_2) \\
& -\mathbf{k}^2\big(5\mathbf{k}_1^2+8\mathbf{k}_1\mathbf{k}_2+5\mathbf{k}_2^2\big)+2\mathbf{k}\big(\mathbf{k}_1^3+2\mathbf{k}_1^2\mathbf{k}_2+2\mathbf{k}_1\mathbf{k}_2^2+\mathbf{k}_2^3\big)\Big)|\mathbf{k}_1-\mathbf{k}_2|\Bigg]
\end{aligned}
\tag{B.1}
$$

$$
\begin{aligned}
V(\mathbf{k}_1,\mathbf{k}_2,\mathbf{k}) = & \frac{-\pi}{48\Lambda^{\frac{5}{2}}(\mathbf{k}-\mathbf{k}_1)^3(\mathbf{k}+\mathbf{k}_1-2\mathbf{k}_2)^3(\mathbf{k}-\mathbf{k}_2)^3(\mathbf{k}_1-\mathbf{k}_2)(\mathbf{k}-2\mathbf{k}_1+\mathbf{k}_2)^3(-2\mathbf{k}+\mathbf{k}_1+\mathbf{k}_2)^3} \\
\times & \Bigg[ -(\mathbf{k}-\mathbf{k}_1)^3(\mathbf{k}+\mathbf{k}_1-2\mathbf{k}_2)^3\Big(4\mathbf{k}^4-18\mathbf{k}^3\mathbf{k}_1+25\mathbf{k}^2\mathbf{k}_1^2-18\mathbf{k}\mathbf{k}_1^3+4\mathbf{k}_1^4+2(\mathbf{k}+\mathbf{k}_1)(\mathbf{k}^2+\mathbf{k}\mathbf{k}_1+\mathbf{k}_1^2)\mathbf{k}_2 \\
& -(5\mathbf{k}^2+8\mathbf{k}\mathbf{k}_1+5\mathbf{k}_1^2)\mathbf{k}_2^2+6(\mathbf{k}+\mathbf{k}_1)\mathbf{k}_2^3-3\mathbf{k}_2^4\Big)|\mathbf{k}-\mathbf{k}_1|+ \\
& (\mathbf{k}-\mathbf{k}_2)^3(\mathbf{k}+\mathbf{k}_2-2\mathbf{k}_1)^3\Big(4\mathbf{k}^4-18\mathbf{k}^3\mathbf{k}_2+25\mathbf{k}^2\mathbf{k}_2^2-18\mathbf{k}\mathbf{k}_2^3+4\mathbf{k}_2^4+2(\mathbf{k}+\mathbf{k}_2)(\mathbf{k}^2+\mathbf{k}\mathbf{k}_2+\mathbf{k}_2^2)\mathbf{k}_2 \\
& -(5\mathbf{k}^1+8\mathbf{k}\mathbf{k}_2+5\mathbf{k}_2^2)\mathbf{k}_1^2+6(\mathbf{k}+\mathbf{k}_2)\mathbf{k}_1^3-3\mathbf{k}_1^4\Big)|\mathbf{k}-\mathbf{k}_2|+ \\
& (\mathbf{k}_1-\mathbf{k}_2)^3(-2\mathbf{k}+\mathbf{k}_1+\mathbf{k}_2)^3\Big(3\mathbf{k}^4-4\mathbf{k}_1^4+18\mathbf{k}_1^3\mathbf{k}_2-25\mathbf{k}_1^2\mathbf{k}_2^2+18\mathbf{k}_1\mathbf{k}_2^3-4\mathbf{k}_2^4-6\mathbf{k}^3(\mathbf{k}_1+\mathbf{k}_2) \\
& -2\mathbf{k}(\mathbf{k}_1+\mathbf{k}_2)(\mathbf{k}_1^2+\mathbf{k}_1\mathbf{k}_2+\mathbf{k}_2^2)+\mathbf{k}^2(5\mathbf{k}_1^2+8\mathbf{k}_1\mathbf{k}_2+5\mathbf{k}_2^2.\Big)|\mathbf{k}_1-\mathbf{k}_2|\Bigg]
\end{aligned}
\tag{B.2}
$$

# APPENDIX C

## Computation of $I(x_{\mathrm{FE}} = 2/5)$

To compute $I(x_{\mathrm{FE}} = 2/5)$, we apply Zakharov Transforms to the integral $I(x)$, written again below for convenience.

$$I(x) = -\frac{24\pi C^5 x}{\Lambda^{5/2}} \int \frac{V_1^{\mathbf{s}_1,\mathbf{s}_2}}{\mathbf{s_2} - \mathbf{s_1}} \left[(1-\mathbf{s}_2)s_2^{2x}s_1^{x-1}\mathrm{sgn}(\mathbf{s}_1) + (\mathbf{s}_1-1)s_1^{2x}s_2^{x-1}\mathrm{sgn}(\mathbf{s}_2) + (\mathbf{s}_2-\mathbf{s}_1)s_1^{2x}s_2^{2x}\right] \mathrm{d}\mathbf{s}_1\, \mathrm{d}\mathbf{s}_2. \tag{C.1}$$

The integrand of $I(x)$ has three terms. We will apply two Zakharov Transforms to the first and second terms. To the first term, we apply the change of variables $\mathbf{s}_1 = \frac{1}{\tilde{\mathbf{s}}_1}$ and $\mathbf{s}_2 = \frac{\tilde{\mathbf{s}}_2}{\tilde{\mathbf{s}}_1}$ and for the second $\mathbf{s}_1 = \frac{\tilde{\mathbf{s}}_1}{\tilde{\mathbf{s}}_2}$ and $\mathbf{s}_2 = \frac{1}{\tilde{\mathbf{s}}_2}$. We will detail the computations for the first term and deduce the results for the second term.

With the first ZT $\mathbf{s}_1 = \frac{1}{\tilde{\mathbf{s}}_1}$ and $\mathbf{s}_2 = \frac{\tilde{\mathbf{s}}_2}{\tilde{\mathbf{s}}_1}$, $d\mathbf{s}_1 d\mathbf{s}_2$ becomes $|J| d\tilde{\mathbf{s}}_1 d\tilde{\mathbf{s}}_2$ with $J = -\left(\frac{1}{\tilde{\mathbf{s}}_1}\right)^3$ the Jacobian of the change of variables. With $\tilde{\mathbf{s}}_1 \in \mathbb{R}, |J| = \frac{1}{|\tilde{\mathbf{s}}_1|^3}$.

With the change of variables, $V_1^{\mathbf{s}_1,\mathbf{s}_2} = V(\mathbf{s}_1, \mathbf{s}_2, 1)$ becomes $V\left(\frac{1}{\tilde{\mathbf{s}}_1}, \frac{\tilde{\mathbf{s}}_2}{\tilde{\mathbf{s}}_1}, 1\right)$ and with the property $V(\lambda\mathbf{p}, \lambda\mathbf{q}, \lambda\mathbf{k}) = \frac{1}{|\lambda|^5} V(\mathbf{p}, \mathbf{q}, \mathbf{k})$, it finally becomes $|\tilde{\mathbf{s}}_1|^5 V(1, \tilde{\mathbf{s}}_2, \tilde{\mathbf{s}}_1)$. We use another property of $V$, $V(\mathbf{p}_3, \mathbf{p}_2, \mathbf{p}_1) = \left(\frac{\mathbf{p}_3 - \mathbf{p}_2}{\mathbf{p}_2 - \mathbf{p}_1}\right)^2 V(\mathbf{p}_1, \mathbf{p}_2, \mathbf{p}_3)$, to write $V\left(\frac{1}{\tilde{\mathbf{s}}_1}, \frac{\tilde{\mathbf{s}}_2}{\tilde{\mathbf{s}}_1}, 1\right) = |\tilde{\mathbf{s}}_1|^5 V\left(1, \tilde{\mathbf{s}}_2, \tilde{\mathbf{s}}_1\right) = \left(\frac{1-\tilde{\mathbf{s}}_2}{\tilde{\mathbf{s}}_1 - \tilde{\mathbf{s}}_2}\right)^2 |\tilde{\mathbf{s}}_1|^5 V(\tilde{\mathbf{s}}_1, \tilde{\mathbf{s}}_2, 1)$.

$$I(x) = -\frac{24\pi C^5 x}{\Lambda^{5/2}} \int \frac{V_1^{\mathbf{s}_1,\mathbf{s}_2}}{\mathbf{s_2} - \mathbf{s_1}} \left[\underbrace{\mathrm{sgn}(\mathbf{s}_1)(1-\mathbf{s}_2)s_2^{2x}s_1^{x-1}}_{I_1(x)} + \mathrm{sgn}(\mathbf{s}_2)(\mathbf{s}_1-1)s_1^{2x}s_2^{x-1} + (\mathbf{s}_2-\mathbf{s}_1)s_1^{2x}s_2^{2x}\right] \mathrm{d}\mathbf{s}_1 \mathrm{d}\mathbf{s}_2. \tag{C.2}$$

$$I_1(x) = -\frac{24\pi C^5 x}{\Lambda^{5/2}} \int \tilde{\mathbf{s}}_1 |\tilde{\mathbf{s}}_1|^2 \Big(\frac{1-\tilde{\mathbf{s}}_2}{\tilde{\mathbf{s}}_1 - \tilde{\mathbf{s}}_2}\Big)^2 \frac{V_1^{\tilde{\mathbf{s}}_1,\tilde{\mathbf{s}}_2}}{\tilde{\mathbf{s}}_2 - 1} \left[ \mathrm{sgn}(\tilde{\mathbf{s}}_1) \Big(1 - \frac{\tilde{\mathbf{s}}_2}{\tilde{\mathbf{s}}_1}\Big) \Big(\frac{\tilde{s}_2}{\tilde{s}_1}\Big)^{2x} \tilde{s}_1^{1-x} \right] \mathrm{d}\tilde{\mathbf{s}}_1 \mathrm{d}\tilde{\mathbf{s}}_2 \quad \text{(C.3)}$$

$$I_1(x) = -\frac{24\pi C^5 x}{\Lambda^{5/2}} \int \tilde{\mathbf{s}}_1 \tilde{s}_1^{-5x+2} \Big(\frac{1-\tilde{\mathbf{s}}_2}{\tilde{\mathbf{s}}_1 - \tilde{\mathbf{s}}_2}\Big)^2 \frac{V_1^{\tilde{\mathbf{s}}_1,\tilde{\mathbf{s}}_2}}{\tilde{\mathbf{s}}_2 - 1} \left[ \Big(\tilde{\mathbf{s}}_1 - \tilde{\mathbf{s}}_2\Big) \tilde{s}_2^{2x} \tilde{s}_1^{2x} \right] \mathrm{d}\tilde{\mathbf{s}}_1 \mathrm{d}\tilde{\mathbf{s}}_2 \quad \text{(C.4)}$$

$$I_1(x) = -\frac{24\pi C^5 x}{\Lambda^{5/2}} \int V_1^{\tilde{\mathbf{s}}_1,\tilde{\mathbf{s}}_2} \ \tilde{s}_1^{2x} \tilde{s}_2^{2x} \left[ \tilde{s}_1^{-5x+2} \ \tilde{\mathbf{s}}_1 \ \frac{\tilde{\mathbf{s}}_2 - 1}{\tilde{\mathbf{s}}_1 - \tilde{\mathbf{s}}_2} \right] \mathrm{d}\tilde{\mathbf{s}}_1 \mathrm{d}\tilde{\mathbf{s}}_2 \quad \text{(C.5)}$$

The second term $I_2(x)$ can be obtained the same way by applying the second ZT ($\mathbf{s}_1 = \frac{\tilde{\mathbf{s}}_1}{\tilde{\mathbf{s}}_2}$ and $\mathbf{s}_2 = \frac{1}{\tilde{\mathbf{s}}_2}$ ) and is given by

$$I_2(x) = -\frac{24\pi C^5 x}{\Lambda^{5/2}} \int V_1^{\tilde{\mathbf{s}}_1,\tilde{\mathbf{s}}_2} \ \tilde{s}_1^{2x} \tilde{s}_2^{2x} \left[ \tilde{s}_2^{-5x+2} \ \tilde{\mathbf{s}}_2 \ \frac{1-\tilde{\mathbf{s}}_1}{\tilde{\mathbf{s}}_1 - \tilde{\mathbf{s}}_2} \right] \mathrm{d}\tilde{\mathbf{s}}_1 \mathrm{d}\tilde{\mathbf{s}}_2 \quad \text{(C.6)}$$

The third term $I_3(x)$ is left unchanged and we can now write the sum of these three terms

$$I(x) = -\frac{24\pi C^5 x}{\Lambda^{5/2}} \int V_1^{\tilde{\mathbf{s}}_1,\tilde{\mathbf{s}}_2} \ \tilde{s}_1^{2x} \tilde{s}_2^{2x} \left[ \underbrace{\tilde{s}_1^{-5x+2} \ \tilde{\mathbf{s}}_1 \ \frac{1-\tilde{\mathbf{s}}_2}{\tilde{\mathbf{s}}_2 - \tilde{\mathbf{s}}_1} + \tilde{s}_2^{-5x+2} \ \tilde{\mathbf{s}}_2 \ \frac{1-\tilde{\mathbf{s}}_1}{\tilde{\mathbf{s}}_1 - \tilde{\mathbf{s}}_2} + 1}_{S(x)} \right] \mathrm{d}\tilde{\mathbf{s}}_1 \mathrm{d}\tilde{\mathbf{s}}_2. \quad \text{(C.7)}$$

The function $S(x)$ is found to be 0 for $x = 2/5$,

$$\begin{aligned} S\Big(x = \frac{2}{5}\Big) &= \ \tilde{\mathbf{s}}_1 \ \frac{1-\tilde{\mathbf{s}}_2}{\tilde{\mathbf{s}}_2 - \tilde{\mathbf{s}}_1} + \ \tilde{\mathbf{s}}_2 \ \frac{1-\tilde{\mathbf{s}}_1}{\tilde{\mathbf{s}}_1 - \tilde{\mathbf{s}}_2} + 1 \\ &= (\tilde{\mathbf{s}}_1 - \tilde{\mathbf{s}}_2)^{-1} \ \Big( - \tilde{\mathbf{s}}_1(1-\tilde{\mathbf{s}}_2) + \tilde{\mathbf{s}}_2(1-\tilde{\mathbf{s}}_1) + \tilde{\mathbf{s}}_1 - \tilde{\mathbf{s}}_2 \Big) \\ &= 0, \end{aligned} \quad \text{(C.8)}$$

# APPENDIX D

## Convergence of $I(x)$

To study the integrability of $I(x)$, we need to take into account two cases as it is a double integral. Indeed, the limits of one variable $s_{1,2}$ going to 0 or $+\infty$, the other one being fixed, and the limits of both variables tending simultaneously to 0 or $\infty$ are independant and will be tackled separately. We can notice that for the first case we can limit our computations to $s_1 \to 0, \infty$ with $s_2$ fixed thanks to the $\mathbf{s}_1 \leftrightarrow \mathbf{s}_2$ symmetry of $I(x)$.

For convenience, we recall the one-dimensional expression of $I(x)$ with KZ ansatz for the wave-action spectrum

$$I(x) = -\frac{24\pi C^5 x}{\Lambda^{5/2}} \int \frac{V_1^{\mathbf{s}_1,\mathbf{s}_2}}{\mathbf{s_2} - \mathbf{s_1}} \left[\mathrm{sgn}(\mathbf{s}_1)(1-\mathbf{s}_2)s_2^{2x}s_1^{x-1} + \mathrm{sgn}(\mathbf{s}_2)(\mathbf{s}_1-1)s_1^{2x}s_2^{x-1} + (\mathbf{s}_2-\mathbf{s}_1)s_1^{2x}s_2^{2x}\right] \mathrm{d}\mathbf{s}_1\mathrm{d}\mathbf{s}_2. \tag{D.1}$$

Before considering the limits, we recall that the integral $I(x)$ is integrable for $x = -2$ and 0, as it has been checked explicitly as corresponding to the RJ spectrum. These particular values of $x$ are not mentioned while considering the limits but must not be forgotten.

## D.1 Limit $s_1 \ll s_2, 1$

The integrand of $I(x)$ can be split in two expressions, $\frac{V_1^{\mathbf{s}_1,\mathbf{s}_2}}{\mathbf{s}_2-\mathbf{s}_1}$ (independent of $x$) and $\Delta n := \left[\mathrm{sgn}(\mathbf{s}_1)(1-\mathbf{s}_2)s_2^{2x}s_1^{x-1} + \mathrm{sgn}(\mathbf{s}_2)(\mathbf{s}_1-1)s_1^{2x}s_2^{x-1} + (\mathbf{s}_2-\mathbf{s}_1)s_1^{2x}s_2^{2x}\right]$, which asymptotics can be obtained independently.

With `Mathematica`, we get the asymptote of $V_1^{\mathbf{s}_1,\mathbf{s}_2}$ by expanding it in the $s_1 \ll s_2, 1$ limit in the leading order : $V_1^{\mathbf{s}_1,\mathbf{s}_2} \propto \mathbf{s}_1^0$ and similarly for $1/(\mathbf{s}_2 - \mathbf{s}_1) \propto s_1^0$. Thus, we obviously have

$$\frac{V_1^{\mathbf{s}_1,\mathbf{s}_2}}{\mathbf{s}_2-\mathbf{s}_1}\underbrace{\propto}_{s_1\ll s_2,1}\mathbf{s}_1^0 \tag{D.2}$$

In the same limit, $\Delta n$ can be simplified

$$\Delta n=\left[\mathrm{sgn}(\mathbf{s}_1)(1-\mathbf{s}_2)s_2^{2x}s_1^{x-1}+(-\mathrm{sgn}(\mathbf{s}_2)\,s_2^{x-1}+\mathbf{s}_2s_2^{2x})\,s_1^{2x}\right]. \tag{D.3}$$

For $s_1\ll s_2,1$, the dominating term is the one with the smaller power of $s_1$, so the $s_1^{2x}$-term for $x<-1$ and the $s_1^{x-1}$-term for $x>-1$, both terms being equivalent for $x=-1$. Given that $V_1^{\mathbf{s}_1,\mathbf{s}_2}/(\mathbf{s}_2-\mathbf{s}_1)$ has a constant asymptote, we can conclude with the Riemann criteria that, in the $s_1\ll s_2,1$ limit, $I(x)$ is integrable for $x>0$, this condition being the union of the Riemann conditions for both dominating terms.

## D.2 Limit $s_1\gg s_2,1$

For the opposite limit $s_1\to\infty$ with $s_2$ fixed, we use the same method and get the asymptotes $V_1^{\mathbf{s}_1,\mathbf{s}_2}\propto -s_1^{-5}\mathrm{sgn}(\mathbf{s}_1)$ and $1/(\mathbf{s}_2-\mathbf{s}_1)\propto -s_1^{-1}$. Thus, the product behaves like $s_1^{-4}\mathrm{sgn}(\mathbf{s}_1)$. The factor $\Delta n$ now has the expression,

$$\Delta n=\left[\mathrm{sgn}(\mathbf{s}_1)(1-\mathbf{s}_2)s_2^{2x}s_1^{x-1}+\mathrm{sgn}(\mathbf{s}_1)(\mathrm{sgn}(\mathbf{s}_2)s_2^{x-1}-s_2^{2x})\,s_1^{2x+1}\right] \tag{D.4}$$

where we have used $\mathbf{s}_1=\mathrm{sgn}(\mathbf{s}_1)s_1$. In this expression, the dominant terms are the $s_1^{x-1}$-term for $x<-2$ and the $s_1^{2x+1}$-term for $x>-2$. Taking the asymptotes of the different terms in the integrand, we obtain with the Riemann criteria that, in the $s_1\gg s_2,1$ limit, $I(x)$ is convergent for $x<2$.

To this point, we have derived that the integral $I(x)$ is convergent in the interval $0<x<1$ for the limits of only one variable. We now consider the double limits, *ie* when both $s_1$ and $s_2$ go simultaneously to 0 and $\infty$.

## D.3 Limit $s_1,s_2\ll 1$

To study this double limit, we change the variables, from cartesian $\mathbf{s}_1,\mathbf{s}_2$ to polar coordinates $r,\theta$,

$$\mathbf{s}_1=r\cos\theta,\ \mathbf{s}_2=r\sin\theta. \tag{D.5}$$

With this change of variables, the Jacobian $J=r$ of the transformation adds a power of $r$. The simultaneous limits $s_1,s_2\ll 1$ correspond now to $r\ll 1$. The term $V_1^{\mathbf{s}_1,\mathbf{s}_2}/(\mathbf{s}_2-\mathbf{s}_1)$ can be rewritten in terms of $r,\theta$ and studied with `Mathematica` in this limit to obtain its asymptote

$$\frac{V_1^{r\cos\theta,r\sin\theta}}{r(\sin\theta-\cos\theta)}\propto r^1 \tag{D.6}$$

The $\Delta n$ term can also be written for $r, \theta$

$$\Delta n = \{(1 - r\,\sin\theta)\cos\theta\,|\cos\theta|^{x-2}|\sin\theta|^{2x} + (1 - r\,\cos\theta)\sin\theta\,|\sin\theta|^{x-2}|\cos\theta|^{2x}\}r^{3x-1} + (\sin\theta - \cos\theta)|\cos\theta\sin\theta|^{2x}r^{4x+1} \tag{D.7}$$

for which we have used $\mathrm{sgn}(\cos\theta) = \cos\theta|\cos\theta|^{-1}$. In the limit $r \ll 1$, we can simplify $\Delta n$ to get

$$\Delta n = \{\cos\theta\,|\cos\theta|^{x-2}|\sin\theta|^{2x} + \sin\theta\,|\sin\theta|^{x-2}|\cos\theta|^{2x}\}r^{3x-1} + (\sin\theta - \cos\theta)\,|\cos\theta\sin\theta|^{2x}r^{4x+1}\,, \tag{D.8}$$

for which the dominant term is the $r^{4x+1}$-term for $x < -2$ and the $r^{3x-1}$ for $x > -2$. Taking into account the two terms in the integral and the $J = r$ jacobian, the integral is convergent, in the $s_1, s_2 \ll 1$ limit, if $x > -2/3$.

## D.4 Limit $s_1, s_2 \gg 1$

This limit corresponds to $r \gg 1$ and to the following asymptote

$$\frac{V_1^{r\cos\theta, r\sin\theta}}{r(\sin\theta - \cos\theta)} \propto r^{-6} \tag{D.9}$$

Similarly, $\Delta n$ writes

$$\Delta n = \{\sin\theta\cos\theta\,|\cos\theta|^{x-2}|\sin\theta|^{2x} - \cos\theta\sin\theta\,|\sin\theta|^{x-2}|\cos\theta|^{2x}\}r^{3x} + (\sin\theta - \cos\theta)|\cos\theta\sin\theta|^{2x}r^{4x+1}. \tag{D.10}$$

with $r^{3x}$-term dominant for $x < -1$ and $r^{4x+1}$-term for $x > -1$. Putting all these asymptotes with the $r$ jacobian, we obtain that $I(x)$ is convergent for $x < 3/4$ in the $s_1, s_2 \gg 1$ limit.

Grouping the results for the four limits indicates that the integral $I(x)$ is only convergent for $\boxed{0 \leqslant x < 3/4 \text{ or } x = -2}$.

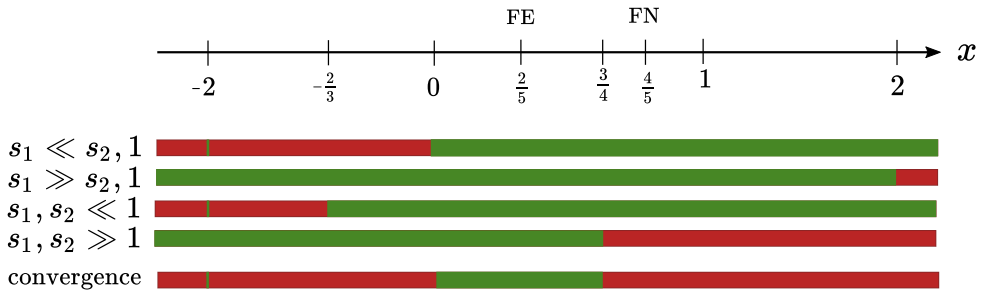

# APPENDIX E

## Non-local analysis

We start from equation (3.50) in the limit $k_1 \gg k$ and $k_2 \gg k$ which implies $V_{\mathbf{k}}^{\mathbf{k}_1,\mathbf{k}_2} = V_0^{\mathbf{k}_1,\mathbf{k}_2}$

$$Q_s(k) = -24\pi \frac{\operatorname{sgn}\mathbf{k}}{\Lambda^{\frac{5}{2}}} \int_{k\ll k_{1,2}} V_0^{\mathbf{k}_1,\mathbf{k}_2} \left[ 2n_{k_2}^2 n_k^2 \, \frac{-\mathbf{k}_2}{-\mathbf{k}_1+\mathbf{k}_2} \frac{\partial n_1}{\partial \mathbf{k}_1} + n_{k_1}^2 n_{k_2}^2 \frac{\partial n_k}{\partial \mathbf{k}} \right] \mathrm{d}\mathbf{k}_1 \mathrm{d}\mathbf{k}_2. \quad \text{(E.1)}$$

We can take $n_k^2$ and $\partial_k n_k$ out of the integral(s)

$$\begin{aligned} Q_s(k) = -24\pi \frac{\operatorname{sgn}\mathbf{k}}{\Lambda^{\frac{5}{2}}} 2n_k^2 \int V_0^{\mathbf{k}_1,\mathbf{k}_2} \; n_{k_2}^2 \; \frac{-\mathbf{k}_2}{-\mathbf{k}_1+\mathbf{k}_2} \frac{\partial n_1}{\partial \mathbf{k}_1} d\mathbf{k}_1 d\mathbf{k}_2 \\ - 4\pi \frac{1}{\Lambda^{\frac{5}{2}}} \frac{\partial n_k}{\partial k} \int V_0^{\mathbf{k}_1,\mathbf{k}_2} n_{k_1}^2 n_{k_2}^2 \mathrm{d}\mathbf{k}_1 \mathrm{d}\mathbf{k}_2, \end{aligned} \quad \text{(E.2)}$$

for shortness we omit the index $k \ll k_{1,2}$ but the presented integrals are indeed computed in this limit. We now denote $B = 2\int \mathrm{d}k_1 \mathrm{d}k_2 \; V_0^{\mathbf{k}_1,\mathbf{k}_2} \; n_{k_2}^2 \; \frac{\mathbf{k}_2}{-\mathbf{k}_1+\mathbf{k}_2} \partial_{\mathbf{k}_1} n_1$, the integral in the first term in the RHS. Notice that this integral does not depend on $\mathbf{k}$. This integral for $\mathbf{k}_1, \mathbf{k}_2 \in \mathbb{R}^2$ will be split in four integrals for the four quadrants of the $(\mathbf{k}_1, \mathbf{k}_2)$ plane :

$$\begin{aligned} \frac{1}{2}B &= \int \; V_0^{\mathbf{k}_1,\mathbf{k}_2} \; n_2^2 \; \frac{\mathbf{k}_2}{-\mathbf{k}_1+\mathbf{k}_2} \partial_{\mathbf{k}_1} n_1 \mathrm{d}\mathbf{k}_1 \mathrm{d}\mathbf{k}_2 \\ \frac{1}{2}B &= \int_{\substack{\mathbf{k}_1>0 \\ \mathbf{k}_2>0}} V_0^{\mathbf{k}_1,\mathbf{k}_2} \; n_2^2 \; \frac{\mathbf{k}_2}{-\mathbf{k}_1+\mathbf{k}_2} \partial_{\mathbf{k}_1} n_1 \mathrm{d}\mathbf{k}_1 \mathrm{d}\mathbf{k}_2 + \int_{\substack{\mathbf{k}_1<0 \\ \mathbf{k}_2>0}} V_0^{\mathbf{k}_1,\mathbf{k}_2} \; n_2^2 \; \frac{\mathbf{k}_2}{-\mathbf{k}_1+\mathbf{k}_2} \partial_{k_1} n_1 \mathrm{d}\mathbf{k}_1 \mathrm{d}\mathbf{k}_2 \\ &+ \int_{\substack{\mathbf{k}_1>0 \\ \mathbf{k}_2<0}} V_0^{\mathbf{k}_1,\mathbf{k}_2} \; n_2^2 \; \frac{\mathbf{k}_2}{-\mathbf{k}_1+\mathbf{k}_2} \partial_{\mathbf{k}_1} n_1 \mathrm{d}\mathbf{k}_1 \mathrm{d}\mathbf{k}_2 + \int_{\substack{\mathbf{k}_1<0 \\ \mathbf{k}_2<0}} V_0^{\mathbf{k}_1,\mathbf{k}_2} \; n_2^2 \; \frac{\mathbf{k}_2}{-\mathbf{k}_1+\mathbf{k}_2} \partial_{\mathbf{k}_1} n_1 \mathrm{d}\mathbf{k}_1 \mathrm{d}\mathbf{k}_2 \end{aligned} \quad \text{(E.3)}$$

We then perform change of variables, respectively $\mathbf{k}_1 \to -\mathbf{k}_1$ in the second integral, $\mathbf{k}_2 \to -\mathbf{k}_2$ in the third and both in the fourth, to have all the integrals defined on the positive quadrant $(\mathbf{k}_1 > 0, \mathbf{k}_2 > 0)$

$$\frac{1}{2}B = \int_{\substack{\mathbf{k}_1>0\\ \mathbf{k}_2>0}} V_0^{\mathbf{k}_1,\mathbf{k}_2}\ n_2^2\ \frac{\mathbf{k}_2}{-\mathbf{k}_1+\mathbf{k}_2}\partial_{\mathbf{k}_1} n_1 \mathrm{d}\mathbf{k}_1\mathrm{d}\mathbf{k}_2 - \int_{\substack{\mathbf{k}_1>0\\ \mathbf{k}_2>0}} V_0^{-\mathbf{k}_1,\mathbf{k}_2}\ n_2^2\ \frac{\mathbf{k}_2}{+\mathbf{k}_1+\mathbf{k}_2}\partial_{\mathbf{k}_1} n_1 \mathrm{d}\mathbf{k}_1\mathrm{d}\mathbf{k}_2$$
$$- \int_{\substack{\mathbf{k}_1>0\\ \mathbf{k}_2>0}} V_0^{\mathbf{k}_1,-\mathbf{k}_2}\ n_2^2\ \frac{\mathbf{k}_2}{-\mathbf{k}_1-\mathbf{k}_2}\partial_{\mathbf{k}_1} n_1 \mathrm{d}\mathbf{k}_1\mathrm{d}\mathbf{k}_2 + \int_{\substack{\mathbf{k}_1>0\\ \mathbf{k}_2>0}} V_0^{-\mathbf{k}_1,-\mathbf{k}_2}\ n_2^2\ \frac{\mathbf{k}_2}{+\mathbf{k}_1-\mathbf{k}_2}\partial_{\mathbf{k}_1} n_1 \mathrm{d}\mathbf{k}_1\mathrm{d}\mathbf{k}_2 \tag{E.4}$$

$$\frac{1}{2}B = \iint_{\substack{k_1>0\\ k_2>0}} n_2^2\,\partial_{\mathbf{k}_1} n_1 \left[\ \frac{\mathbf{k}_2}{-\mathbf{k}_1+\mathbf{k}_2}\Big(V_0^{\mathbf{k}_1,\mathbf{k}_2} - V_0^{-\mathbf{k}_1,-\mathbf{k}_2}\Big) + \frac{\mathbf{k}_2}{\mathbf{k}_1+\mathbf{k}_2}\Big(V_0^{\mathbf{k}_1,-\mathbf{k}_2} - V_0^{-\mathbf{k}_1,\mathbf{k}_2}\Big)\right]\mathrm{d}\mathbf{k}_1\mathrm{d}\mathbf{k}_2 \tag{E.5}$$

With the properties of $V_0^{\mathbf{k}_1,\mathbf{k}_2}$, we obtain $B = 0$.

The equation (E.2) thus becomes

$$Q_s(k) = -24\pi \frac{1}{\Lambda^{\frac{5}{2}}} \frac{\partial n_k}{\partial k} \int_{k\ll k_{1,2}} V_0^{\mathbf{k}_1,\mathbf{k}_2} n_{k_1}^2 n_{k_2}^2 \mathrm{d}\mathbf{k}_1\mathrm{d}\mathbf{k}_2. \tag{E.6}$$

# Bibliography


[1] M. Kamalian, J. E. Prilepsky, S. T. Le, and S. K. Turitsyn, "Periodic nonlinear Fourier transform for fiber-optic communications, Part I: theory and numerical methods," Optics Express, vol. 24, pp. 18353–18369, Aug. 2016. Publisher: Optica Publishing Group.

[2] G. Arora, R. Rani, and H. Emadifar, "Numerical solutions of nonlinear schrodinger equation with applications in optical fiber communication," Optik, vol. 266, p. 169661, 2022.

[3] S. Nazarenko and M. Onorato, "Wave turbulence and vortices in Bose–Einstein condensation," Physica D: Nonlinear Phenomena, vol. 219, pp. 1–12, July 2006.

[4] D. Proment, S. Nazarenko, and M. Onorato, "Quantum turbulence cascades in the Gross-Pitaevskii model," Physical Review A, vol. 80, p. 051603, Nov. 2009. Publisher: American Physical Society.

[5] J. Laurie, U. Bortolozzo, S. Nazarenko, and S. Residori, "One-dimensional optical wave turbulence: Experiment and theory," Physics Reports, vol. 514, pp. 121–175, May 2012.

[6] A. Picozzi, J. Garnier, T. Hansson, P. Suret, S. Randoux, G. Millot, and D. N. Christodoulides, "Optical wave turbulence: Towards a unified nonequilibrium thermodynamic formulation of statistical nonlinear optics," Physics Reports, vol. 542, pp. 1–132, Sept. 2014.

[7] P. Suret, A. Tikan, F. Bonnefoy, F. Copie, G. Ducrozet, A. Gelash, G. Prabhudesai, G. Michel, A. Cazaubiel, E. Falcon, G. El, and S. Randoux, "Nonlinear Spectral Synthesis of Soliton Gas in Deep-Water Surface Gravity Waves," Physical Review Letters, vol. 125, p. 264101, Dec. 2020. Publisher: American Physical Society.

[8] C. Sulem and P.-L. Sulem, The nonlinear Schrödinger equation: self-focusing and wave collapse, vol. 139. Springer Science & Business Media, 2007.

[9] V. Zakharov and A. Shabat, "Exact Theory of Two-dimensional Self-focusing and One-dimensional Self-modulation of Waves in Nonlinear Media," Journal of Experimental and Theoretical Physics, 1970.

[10] C. S. Gardner, J. M. Greene, M. D. Kruskal, and R. M. Miura, "Method for Solving the Korteweg-deVries Equation," Physical Review Letters, vol. 19, pp. 1095–1097, Nov. 1967. Publisher: American Physical Society.

[11] I. S. Chekhovskoy, O. V. Shtyrina, M. P. Fedoruk, S. B. Medvedev, and S. K. Turitsyn, "Nonlinear Fourier Transform for Analysis of Coherent Structures in Dissipative Systems," in 2019 Conference on Lasers and Electro-Optics Europe & European Quantum Electronics Conference (CLEO/Europe-EQEC), pp. 1–1, June 2019.

[12] A. A. Gelash and D. S. Agafontsev, "Strongly interacting soliton gas and formation of rogue waves," Physical Review E, vol. 98, p. 042210, Oct. 2018. Publisher: American Physical Society.

[13] P. Suret, S. Randoux, A. Gelash, D. Agafontsev, B. Doyon, and G. El, "Soliton Gas: Theory, Numerics and Experiments," Apr. 2023. arXiv:2304.06541 [nlin, physics:physics].

[14] P. D. Lax, "Integrals of nonlinear equations of evolution and solitary waves," Communications on Pure and Applied Mathematics, vol. 21, no. 5, pp. 467–490, 1968.

[15] S. Randoux, P. Suret, A. Chabchoub, B. Kibler, and G. El, "Nonlinear spectral analysis of Peregrine solitons observed in optics and in hydrodynamic experiments," Physical Review E, vol. 98, no. 2, 2018.

[16] P. Suret, M. Dufour, G. Roberti, G. El, F. Copie, and S. Randoux, "Soliton refraction by an optical soliton gas," Physical Review Research, vol. 5, p. 42002, Oct. 2023.

[17] S. K. Turitsyn, J. E. Prilepsky, S. T. Le, S. Wahls, L. L. Frumin, M. Kamalian, and S. A. Derevyanko, "Nonlinear Fourier transform for optical data processing and transmission: advances and perspectives," Optica, vol. 4, pp. 307–322, Mar. 2017. Publisher: Optica Publishing Group.

[18] S. Novikov, S. Manakov, L. P. Pitaevsky, and V. E. Zakharov, Theory of Solitons: The Inverse Scattering Method. 1984.

[19] V. B. Matveev and M. A. Salle, Darboux Transformations and Solitons. 1992.

[20] J. S. Russel, "Report on waves," 14th Meeting of the British Association for the Advancement of Science, pp. 311–390, 1844.

[21] N. J. Zabusky and M. D. Kruskal, "Interaction of "solitons" in a collisionless plasma and the recurrence of initial states," Phys. Rev. Lett., vol. 15, pp. 240–243, Aug 1965.

[22] R. Hirota, "Exact solution of the sine-gordon equation for multiple collisions of solitons," Journal of the Physical Society of Japan, vol. 33, pp. 1459–1463, 1972.

[23] M. A. Kawser, M. A. Akbar, M. A. Khan, and H. A. Ghazwani, "Exact soliton solutions and the significance of time-dependent coefficients in the Boussinesq equation: theory and application in mathematical physics," Scientific Reports, vol. 14, p. 762, Jan. 2024.

[24] Y. S. Kivshar and B. Luther-Davies, "Dark optical solitons: physics and applications," Physics Reports, vol. 298, pp. 81–197, May 1998.

[25] J. Skipp, V. L'vov, and S. Nazarenko, "Wave turbulence in self-gravitating Bose gases and nonlocal nonlinear optics," Physical Review A, vol. 102, p. 043318, Oct. 2020. Publisher: American Physical Society.

[26] M. D. I. Castillo, J. J. Sánchez-Mondragón, and S. Stepanov, "Formation of steady-state cylindrical thermal lenses in dark stripes," Optics Letters, vol. 21, pp. 1622–1624, Oct. 1996. Publisher: Optica Publishing Group.

[27] R. Bekenstein, R. Schley, M. Mutzafi, C. Rotschild, and M. Segev, "Optical simulations of gravitational effects in the Newton–Schrödinger system," Nature Physics, vol. 11, pp. 872–878, Oct. 2015.

[28] T. Roger, C. Maitland, K. Wilson, N. Westerberg, D. Vocke, E. M. Wright, and D. Faccio, "Optical analogues of the Newton-Schrödinger equation and boson star evolution," Nature Communications, vol. 7, p. 13492, 2016.

[29] C. Conti, M. Peccianti, and G. Assanto, "Route to nonlocality and observation of accessible solitons," Physical Review Letters, vol. 91, no. 7, p. 073901, 2003.

[30] M. Peccianti, C. Conti, and G. Assanto, "Optical modulational instability in a nonlocal medium," Phys. Rev. E, vol. 68, no. 2, p. 025602, 2003.

[31] J. Jia and J. Lin, "Solitons in nonlocal nonlinear Kerr media with exponential response function," Optics express, vol. 20, pp. 7469–79, Mar. 2012.

[32] M. Onorato, A. R. Osborne, M. Serio, D. Resio, A. Pushkarev, V. E. Zakharov, and C. Brandini, "Freely Decaying Weak Turbulence for Sea Surface Gravity Waves," Physical Review Letters, vol. 89, p. 144501, Sept. 2002. Publisher: American Physical Society.

[33] E. Falcon and N. Mordant, "Experiments in Surface Gravity-Capillary Wave Turbulence," Annual Review of Fluid Mechanics, vol. 54, pp. 1–25, Jan. 2022. arXiv:2107.04015 [nlin, physics:physics].

[34] C. Garrett and W. Munk, "Internal Waves in the Ocean," Annual Review of Fluid Mechanics, vol. 11, pp. 339–369, Jan. 1979. Publisher: Annual Reviews.

[35] G. Boffetta, A. Celani, D. Dezzani, J. Laurie, and S. Nazarenko, "Modeling Kelvin Wave Cascades in Superfluid Helium," Journal of Low Temperature Physics, vol. 156, pp. 193–214, Sept. 2009. arXiv:0911.1916 [nlin].

[36] B. Bigot, S. Galtier, and H. Politano, "An anisotropic turbulent model for solar coronal heating," Astronomy amp; Astrophysics, vol. 490, p. 325–337, Sept. 2008.

[37] J. P. Laurie, Six-wave systems in one-dimensional wave turbulence. phd, University of Warwick, Sept. 2010.

[38] G. Düring, C. Josserand, and S. Rica, "Weak turbulence for a vibrating plate: Can one hear a kolmogorov spectrum?," Phys. Rev. Lett., vol. 97, p. 025503, Jul 2006.

[39] L. F. Richardson and G. T. Walker, "Atmospheric diffusion shown on a distance-neighbour graph," Proceedings of the Royal Society of London. Series A, vol. 110, no. 756, pp. 709–737, 1926. Publisher: Royal Society.

[40] A. N. Kolmogorov, "The local structure of turbulence in incompressible viscous fluid for very large Reynolds numbers," Doklady Akademiia Nauk SSSR, vol. 30, pp. 301–305, 1941. Publisher: Royal Society.

[41] A. N. Kolmogorov, "Dissipation of energy in the locally isotropic turbulence," Doklady Akademiia Nauk SSSR, vol. 32, p. 16, 1941. Publisher: Royal Society.

[42] R. Fjørtoft, "On the Changes in the Spectral Distribution of Kinetic Energy for Twodimensional, Nondivergent Flow," Tellus, vol. 5, no. 3, pp. 225–230, 1953. _eprint: https://onlinelibrary.wiley.com/doi/pdf/10.1111/j.2153-3490.1953.tb01051.x.

[43] R. H. Kraichnan, "Inertial Ranges in Two-Dimensional Turbulence," The Physics of Fluids, vol. 10, pp. 1417–1423, July 1967.

[44] G. Boffetta and R. E. Ecke, "Two-Dimensional Turbulence," 2011.

[45] G. Boffetta, "Energy and enstrophy fluxes in the double cascade of two-dimensional turbulence," Journal of Fluid Mechanics, vol. 589, pp. 253–260, Oct. 2007.

[46] G. Boffetta and S. Musacchio, "Evidence for the double cascade scenario in two-dimensional turbulence," Physical Review E, vol. 82, p. 016307, July 2010. Publisher: American Physical Society.

[47] V. E. Zakharov, "Stability of periodic waves of finite amplitude on the surface of a deep fluid," Journal of Applied Mechanics and Technical Physics, vol. 9, no. 2, pp. 190–194, 1972.

[48] J. Laurie, V. S. L'vov, S. Nazarenko, and O. Rudenko, "Interaction of Kelvin waves and nonlocality of energy transfer in superfluids," Physical Review B, vol. 81, p. 104526, Mar. 2010. Publisher: American Physical Society.

[49] S. Nazarenko and S. Lukaschuk, "Wave Turbulence on Water Surface," Annual Review of Condensed Matter Physics, vol. 7, pp. 61–88, Mar. 2016. Publisher: Annual Reviews.

[50] C. Connaughton, C. Josserand, A. Picozzi, Y. Pomeau, and S. Rica, "Condensation of classical nonlinear waves," Physical Review Letters, vol. 95, Dec. 2005.

[51] S. Nazarenko, Wave Turbulence, vol. 825 of Lecture Notes in Physics. Berlin, Heidelberg: Springer, 2011.

[52] V. E. Zakharov, "Weak turbulence in media with a decay spectrum," Journal of Applied Mechanics and Technical Physics, vol. 6, pp. 22–24, July 1965.

[53] S. Nazarenko and B. Quinn, "Triple cascade behavior in quasigeostrophic and drift turbulence and generation of zonal jets," Phys. Rev. Lett., vol. 103, p. 118501, Sep 2009.

[54] V. Zakharov and N. N. Filonenko, "Energy Spectrum for Stochastic Oscillations of the Surface of a Liquid," Apr. 1967.

[55] V. E. Zakharov and N. N. Filonenko, "Weak turbulence of capillary waves," Journal of Applied Mechanics and Technical Physics, vol. 8, pp. 37–40, Sept. 1967.

[56] A. Pushkarev and V. Zakharov, "Turbulence of capillary waves — theory and numerical simulation," Physica D: Nonlinear Phenomena, vol. 135, pp. 98–116, Jan. 2000.

[57] A. N. Pushkarev and V. E. Zakharov, "Turbulence of capillary waves," Physical Review Letters, vol. 76, pp. 3320–3323, Apr. 1996.

[58] K. Hasselmann, "Weak-Interaction Theory of Ocean Waves," 1967.

[59] Y. Toba, "Local balance in the air-sea boundary processes," 1972.

[60] O. M. Phillips, "The equilibrium range in the spectrum of wind-generated waves," Journal of Fluid Mechanics, vol. 4, pp. 426–434, Aug. 1958.

[61] C. Garrett and W. Munk, "Space-time scales of internal waves: A progress report," Journal of Geophysical Research (1896-1977), vol. 80, no. 3, pp. 291–297, 1975. _eprint: https://onlinelibrary.wiley.com/doi/pdf/10.1029/JC080i003p00291.

[62] Y. V. Lvov and E. G. Tabak, "Hamiltonian Formalism and the Garrett-Munk Spectrum of Internal Waves in the Ocean," Physical Review Letters, vol. 87, p. 168501, Oct. 2001. Publisher: American Physical Society.

[63] Y. V. Lvov, K. L. Polzin, and E. G. Tabak, "Energy Spectra of the Ocean's Internal Wave Field: Theory and Observations," Physical Review Letters, vol. 92, p. 128501, Mar. 2004. Publisher: American Physical Society.

[64] G. Davis, T. Jamin, J. Deleuze, S. Joubaud, and T. Dauxois, "Succession of Resonances to Achieve Internal Wave Turbulence," Physical Review Letters, vol. 124, p. 204502, May 2020.

[65] E. Kozik and B. Svistunov, "Scale-Separation Scheme for Simulating Superfluid Turbulence: Kelvin-Wave Cascade," Physical Review Letters, vol. 94, p. 025301, Jan. 2005. Publisher: American Physical Society.

[66] E. V. Kozik and B. V. Svistunov, "Theory of Decay of Superfluid Turbulence in the Low-Temperature Limit," Journal of Low Temperature Physics, vol. 156, pp. 215–267, Sept. 2009.

[67] T. B. Benjamin and J. E. Feir, "The disintegration of wave trains on deep water part 1. theory," Journal of Fluid Mechanics, vol. 27, no. 3, p. 417–430, 1967.

[68] T. B. Benjamin, "Instability of periodic wavetrains in nonlinear dispersive systems," Proc. R. Soc. Lond. A, vol. 299, no. 3, pp. 59–76, 1967.

[69] A. R. Osborne, M. Onorato, and M. Serio, "The nonlinear dynamics of rogue waves and holes in deep-water gravity wave trains," Physics Letters A, vol. 275, no. 5, pp. 386–393, 2000.

[70] M. Peccianti, C. Conti, and G. Assanto, "Optical modulational instability in a nonlocal medium," Physical Review E, vol. 68, p. 025602, Aug. 2003. Publisher: American Physical Society.

[71] V. E. Zakharov, "Kinetic equation for solitons," Zh. Eksp. Teor. Fiz, vol. 60, pp. 993–1000.

[72] A. Gelash, D. Agafontsev, V. Zakharov, G. El, S. Randoux, and P. Suret, "Bound state soliton gas dynamics underlying the spontaneous modulational instability," Phys. Rev. Lett., vol. 123, p. 234102, Dec 2019.

[73] V. E. Zakharov, A. N. Pushkarev, S. V. F, and Y. V. V, "Soliton turbulence," Pis'ma Zh. Eksp. Teor. Fiz, vol. 48, pp. 79–82, 1988.

[74] U. Bortolozzo, J. Laurie, S. Nazarenko, and S. Residori, "Optical wave turbulence and condensation of light," Journal of the Optical Society of America B, vol. 26, p. 2280, Dec. 2009. arXiv:0904.2552 [physics].

[75] B. Rumpf and A. C. Newell, "Coherent Structures and Entropy in Constrained, Modulationally Unstable, Nonintegrable Systems," Physical Review Letters, vol. 87, p. 054102, July 2001. Publisher: American Physical Society.

[76] R. Jordan, B. Turkington, and C. L. Zirbel, "A mean-field statistical theory for the nonlinear Schrödinger equation," Physica D: Nonlinear Phenomena, vol. 137, pp. 353–378, Mar. 2000.

[77] R. Jordan and C. Josserand, "Self-organization in nonlinear wave turbulence," Phys. Rev. E, vol. 61, pp. 1527–1539, Feb 2000.

[78] S. A. Orszag, "Numerical Methods for the Simulation of Turbulence," The Physics of Fluids, vol. 12, pp. II–250, Dec. 1969. Num Pages: II-257.

[79] D. Gottlieb and S. A. Orszag, Numerical Analysis of Spectral Methods. Society for Industrial and Applied Mathematics, 1977.

[80] G. Krstulovic and M. Brachet, "Dispersive bottleneck delaying thermalization of turbulent bose-einstein condensates," Physical Review Letters, vol. 106, Mar. 2011.

[81] S. Cox and P. Matthews, "Exponential time differencing for stiff systems," Journal of Computational Physics, vol. 176, pp. 430–455, 03 2002.

[82] J. Yang, Nonlinear Waves in Integrable and Nonintegrable Systems. Society for Industrial and Applied Mathematics, 2010.

[83] D. S. Agafontsev, A. A. Gelash, R. I. Mullyadzhanov, and V. E. Zakharov, "Bound-state soliton gas as a limit of adiabatically growing integrable turbulence," Chaos, Solitons & Fractals, vol. 166, p. 112951, Jan. 2023.

[84] S. Randoux, P. Suret, and G. El, "Inverse scattering transform analysis of rogue waves using local periodization procedure," Scientific Reports, vol. 6, p. 29238, July 2016. Number: 1 Publisher: Nature Publishing Group.

[85] G. Boffetta and A. R. Osborne, "Computation of the direct scattering transform for the nonlinear Schroedinger equation," Journal of Computational Physics, vol. 102, pp. 252–264, Oct. 1992.

[86] I. Mullyadzhanov, A. Gudko, R. Mullyadzhanov, and A. Gelash, "Numerical direct scattering transform for breathers," July 2023. arXiv:2308.04568 [nlin].

[87] M. J. Ablowitz and J. F. Ladik, "Nonlinear differential–difference equations and Fourier analysis," Journal of Mathematical Physics, vol. 17, pp. 1011–1018, June 1976.

[88] M. J. Ablowitz and J. F. Ladik, "A Nonlinear Difference Scheme and Inverse Scattering," Studies in Applied Mathematics, vol. 55, pp. 213–229, Sept. 1976.

[89] L. Fache, F. Bonnefoy, G. Ducrozet, F. Copie, F. Novkoski, G. Ricard, G. Roberti, E. Falcon, P. Suret, G. El, and S. Randoux, "Interaction of soliton gases in deep-water surface gravity waves," Sept. 2023. arXiv:2309.09604 [nlin].

[90] S. Sugavanam, M. K. Kopae, J. Peng, J. E. Prilepsky, and S. K. Turitsyn, "Analysis of laser radiation using the Nonlinear Fourier transform," Nature Communications, vol. 10, p. 5663, Dec. 2019. Number: 1 Publisher: Nature Publishing Group.

[91] Y. Zhou, G. Zhou, Y. Qin, S. Fu, A. P. T. Lau, and K. K. Y. Wong, "Unveiling laser radiation of multiple optical solitons by nonlinear fourier transform," Laser & Photonics Reviews, vol. 17, no. 7, p. 2200731, 2023.

[92] Y. S. Kivshar and B. A. Malomed, "Dynamics of solitons in nearly integrable systems," Reviews of Modern Physics, vol. 61, pp. 763–915, Oct. 1989.

[93] E. A. Kuznetsov, A. V. Mikhailov, and I. A. Shimokhin, "Nonlinear interaction of solitons and radiation," Physica D: Nonlinear Phenomena, vol. 87, pp. 201–215, Oct. 1995.

[94] E. Fermi, J. Pasta, and S. Ulam, "Studies of nonlinear problems. i," Fermi, Collected Papers, vol. 2, no. 210, pp. 977–988, 1955.

[95] J. Skipp, J. Laurie, and S. Nazarenko, "An effective semilocal model for wave turbulence in two-dimensional nonlinear optics," Proceedings of the Royal Society A, vol. 479, July 2023.

[96] S. Dyachenko, A. C. Newell, A. Pushkarev, and V. E. Zakharov, "Optical turbulence: weak turbulence, condensates and collapsing filaments in the nonlinear Schr6dinger equation," Optical turbulence.

[97] D. Proment, M. Onorato, P. Asinari, and S. Nazarenko, "Warm cascade states in a forced-dissipated Boltzmann gas of hard spheres," Physica D: Nonlinear Phenomena, vol. 241, pp. 600–615, Mar. 2012.

[98] A. Picozzi and J. Garnier, "Incoherent Soliton Turbulence in Nonlocal Nonlinear Media," Physical Review Letters, vol. 107, p. 233901, Nov. 2011. Publisher: American Physical Society.

[99] J. Garnier, K. Baudin, A. Fusaro, and A. Picozzi, "Incoherent localized structures and hidden coherent solitons from the gravitational instability of the Schrödinger-Poisson equation," Physical Review. E, vol. 104, p. 054205, Nov. 2021.

[100] S. Randoux, P. Walczak, M. Onorato, and P. Suret, "Nonlinear random optical waves: Integrable turbulence, rogue waves and intermittency," Physica D: Nonlinear Phenomena, vol. 333, pp. 323–335, 2016. Dispersive Hydrodynamics.